frontiers | Research Topics

Advances in new combinational therapies for treatment of MDR pathogens

Edited by
Sanket Kaushik, Sanjit Kumar and Biswajit Mishra

Coordinated by
Anshul Chaudhary

Published in
Frontiers in Cellular and Infection Microbiology

ISSN 1664-8714
ISBN 978-2-8325-7147-7
DOI 10.3389/978-2-8325-7147-7

Generative AI statement
Any alternative text (Alt text) provided alongside figures in the articles in this ebook has been generated by Frontiers with the support of artificial intelligence and reasonable efforts have been made to ensure accuracy, including review by the authors wherever possible. If you identify any issues, please contact us.

About Frontiers

Frontiers is more than just an open access publisher of scholarly articles: it is a pioneering approach to the world of academia, radically improving the way scholarly research is managed. The grand vision of Frontiers is a world where all people have an equal opportunity to seek, share and generate knowledge. Frontiers provides immediate and permanent online open access to all its publications, but this alone is not enough to realize our grand goals.

Frontiers journal series

The Frontiers journal series is a multi-tier and interdisciplinary set of open-access, online journals, promising a paradigm shift from the current review, selection and dissemination processes in academic publishing. All Frontiers journals are driven by researchers for researchers; therefore, they constitute a service to the scholarly community. At the same time, the *Frontiers journal series* operates on a revolutionary invention, the tiered publishing system, initially addressing specific communities of scholars, and gradually climbing up to broader public understanding, thus serving the interests of the lay society, too.

Dedication to quality

Each Frontiers article is a landmark of the highest quality, thanks to genuinely collaborative interactions between authors and review editors, who include some of the world's best academicians. Research must be certified by peers before entering a stream of knowledge that may eventually reach the public - and shape society; therefore, Frontiers only applies the most rigorous and unbiased reviews. Frontiers revolutionizes research publishing by freely delivering the most outstanding research, evaluated with no bias from both the academic and social point of view. By applying the most advanced information technologies, Frontiers is catapulting scholarly publishing into a new generation.

What are Frontiers Research Topics?

Frontiers Research Topics are very popular trademarks of the *Frontiers journals series*: they are collections of at least ten articles, all centered on a particular subject. With their unique mix of varied contributions from Original Research to Review Articles, Frontiers Research Topics unify the most influential researchers, the latest key findings and historical advances in a hot research area.

Find out more on how to host your own Frontiers Research Topic or contribute to one as an author by contacting the Frontiers editorial office: frontiersin.org/about/contact

Advances in new combinational therapies for treatment of MDR pathogens

Topic editors
Sanket Kaushik — Amity University Jaipur, India
Sanjit Kumar — Guru Ghasidas Vishwavidyalaya, India
Biswajit Mishra — Brown University, United States

Topic coordinator
Anshul Chaudhary — The Scripps Research Institute, United States

Citation
Kaushik, S., Kumar, S., Mishra, B., Chaudhary, A., eds. (2025). *Advances in new combinational therapies for treatment of MDR pathogens*.
Lausanne: Frontiers Media SA. doi: 10.3389/978-2-8325-7147-7

Table of contents

frontiers | Frontiers in Cellular and Infection Microbiology

TYPE Editorial
PUBLISHED 04 November 2025
DOI 10.3389/fcimb.2025.1709379

OPEN ACCESS

EDITED BY
Costas C. Papagiannitsis,
University of Thessaly, Greece

REVIEWED BY
Vijay Singh Gondil,
University of Rochester Medical Center, United States

*CORRESPONDENCE
Sanket Kaushik
skaushik@jpr.amity.edu

RECEIVED 20 September 2025
ACCEPTED 21 October 2025
PUBLISHED 04 November 2025

CITATION
Kumar S, Mishra B, Chaudhary A and Kaushik S (2025) Editorial: Advances in new combinational therapies for treatment of MDR pathogens.
Front. Cell. Infect. Microbiol. 15:1709379.
doi: 10.3389/fcimb.2025.1709379

Editorial: Advances in new combinational therapies for treatment of MDR pathogens

Sanjit Kumar[1], Biswajit Mishra[2], Anshul Chaudhary[3] and Sanket Kaushik[4]*

[1]Guru Ghasidas Vishwavidyalaya, Bilaspur, India, [2]Brown University, Providence, RI, United States, [3]University of California, San Diego, La Jolla, CA, United States, [4]Amity University Rajasthan, Jaipur, India

KEYWORDS

MDR, combinational therapeutic strategy, nanoparticle, synergistic effect, ESKAPE bacteria

Editorial on the Research Topic
Advances in new combinational therapies for treatment of MDR pathogens

Multidrug-resistant (MDR) pathogens pose an urgent challenge due to genetic change, misuse of antibiotics, and biofilm production, working against standard treatments. To seek solutions, recent progress has focused on combinational approaches that combine multiple methodologies for greater effectiveness (Elshobary et al., 2025; Kain et al., 2025). Nanotechnology-based delivery systems offer improvements in drug stability and targeting, while natural products offer potential synergistic efficacy with currently available antibiotics (Islam et al., 2025). Treatments are also evolving with photodynamic therapy and immunotherapeutic approaches, as well as the new use of computational drug design and epitope-based vaccines (Haldiya et al., 2024; Thiruppathi et al., 2024). In so doing, these combined or integrated innovations together comprise a unified response to the issues surrounding the impending MDR crisis globally.

This Research Topic aims to give a concise overview of new combinational strategies for treatment of MDR pathogens. By integrating natural products, nanotechnology, computational screening, and vaccine design, the goal is to highlight promising interventions that not only combat resistant pathogens but also enhance therapeutic outcomes and minimize resistance development.

Tanu et al. in a mini review, highlight how photodynamic therapy (PDT), uses a photosensitizer, light and oxygen to produce reactive oxygen species (ROS), has the potential to address already established resistance mechanisms to treatment. PDT is a treatment modality that proves broadly effective against a variety of pathogens *in vivo* due to its ability to penetrate biofilms, generate an immune response, and produce local antimicrobial effects while being considered overall quite safe. Recent advances in antimicrobial blue light and the introduction of next-generation photosensitizers lend support to the PDT approach for the treatment of infectious diseases.

There are several studies that have conducted primary research and reported the use of nanotechnology for the treatment of MDR pathogens. For example, a SabiWhite-loaded

ethosome-based topical delivery system was reported to have a vesicle size, entrapment efficiency and zeta potential of 184.4nm, 92.5% and -13.50mV, respectively. The efficacy of the delivery system was optimized to show sustained release (93.12% over 24 hrs) and demonstrated efficacies of 36.17% *in-vivo* edema reduction, relative to Diclofenac gel (41.92%) and no evidence of irritation was observed after 120 days of storage (Shi et al.). Once again, garlic derived AgNPs (15–20 nm), had strong antimicrobial activity against a MDR pathogen, *Escherichia fergusonii*, which has been described as a relevant clinical pathogen and has a 24% prevalence in wound infections, Furthermore, AgNPs produced inhibition zone findings of 28 ± 0.5 mm, a minimum inhibitory concentration (MIC) of 100 mg/mL and compromised the bacterial cell membrane through oxidative stress. The synergy assays showed strong interactions with the antibiotic, ciprofloxacin (FIC index = 0.37) and time-kill assays indicated that bacteria were cleared rapidly by the AgNP when used in combination (Abdelkhalig et al.).

Natural resources also showed the ability to treat diseases. Extracts from the desert plant Indian Borage showed strong antimicrobial, antioxidant (IC50 = 71.97 μg/mL) and anti-inflammatory properties. Interestingly, when mixed with amikacin, over 50% of resistant isolates became sensitive. In mouse models, the combination of amikacin and extract resulted in less pulmonary lesion and splenic damage than antibiotic therapy alone (Safwat et al.). Essential oils isolated from *Cissampelos oppositifolia* that also contain α-pinene, δ-carene, and caryophyllene were also very synergistic with antibiotics. δ-Carene was tested as having MICs of 0.04 mg/mL against MRSA and 0.05 mg/mL against *E. coli*. Time-kill assays indicated that the bacteria were killed in 2–4 h with amoxicillin or erythromycin. FTIR/UV spectra data indicated that there were structural changes, and molecular docking showed good binding with antibiotics (Zhao et al.).

Computational studies broadened the treatment landscape by virtually screening natural products against the metallo-β-lactamase VIM-1 of *Pseudomonas aeruginosa*, which afforded 4 inhibitors (CNP0390322, CNP03905695, CNP0079056, CNP0338283) with superior docked scores and stable interactions in a one-microsecond molecular dynamics simulation, which may restore β-lactam activity (Ardawi et al.).

With the advancement of Immunotherapeutic approaches the discovery of Staphylococcal Protein A (SpA) epitopes resulted in the construction of a multi-epitope which resulted in high bindin affinities to HLA, and TLR-4 interactions which may indicate viable vaccine candidates against MRSA (Zhou et al.). Likewise, analysis of non-structural proteins of the hepatitis C virus identified 27 CTL epitopes, three of which were more than 90% conserved and exhibited significantly strong immunogenic responses after docking to HLA-A*02:01 and TLR-3, indicating they are reasonable vaccine candidates (Tudi et al.).

Finally, Shang et al. discussed how microbial natural products further demonstrated their value in antibiotic discovery. *Streptomyces kanamyceticus*, which was obtained from a soil source, exhibited antimicrobial activity with inhibition zones as great of 30 mm, with MIC values from 20 to 70 μg/mL. Maximal production of metabolites was achieved through media optimization with glucose and soybean meal at a nutrient concentration of 10 g/L. This was further evidence of the value of microbial sources for new antibiotics.

Conclusion

Overall, these nine submissions reflect the changing paradigm of MDR therapy; moving away from antibiotics solely, towards combinative approaches that incorporate a variety of disciplines. Both PDT, nanocarriers, silver nanoparticles, and essential oil can function as immediate translational options, while bioinformatics-based inhibitor discovery and epitope-based vaccines are probable options for the future. Plant-derived extract and microbial metabolites also reiterate the value of natural products as resistance modulators. Altogether, these developments reaffirm that the future of combating MDR treatments will be deducing a combination: where a natural compound, an independently smart delivery system, and even immunology-based interventions act side-by-side, in addition to antibiotics, to outsmart evolving resistance to aid in improved global health.

Author contributions

SKu: Writing – review & editing. BM: Formal Analysis, Writing – review & editing. AC: Project administration, Writing – review & editing. SKa: Conceptualization, Writing – original draft.

Conflict of interest

The authors declare that the research was conducted in the absence of any commercial or financial relationships that could be construed as a potential conflict of interest.

Generative AI statement

The author(s) declare that no Generative AI was used in the creation of this manuscript.

Any alternative text (alt text) provided alongside figures in this article has been generated by Frontiers with the support of artificial intelligence and reasonable efforts have been made to ensure accuracy, including review by the authors wherever possible. If you identify any issues, please contact us.

Publisher's note

References

Elshobary, M. E., Badawy, N. K., Ashraf, Y., Zatioun, A. A., Masriya, H. H., Ammar, M. M., et al. (2025). Combating antibiotic resistance: mechanisms, multidrug-resistant pathogens, and novel therapeutic approaches: an updated review. *Pharmaceuticals* 18, 402. doi: 10.3390/PH18030402

Haldiya, A., Kain, H., Dubey, S., Punde, S. K., Gupta, P. K. P., Srivastava, V. K., et al. (2024). Investigating Sortase A inhibitory potential of herbal compounds using integrated computational and biochemical approaches. *Acta Tropica* 260, 107430. doi: 10.1016/J.ACTATROPICA.2024.107430

Islam, S., Ahmed, M. M. S., Islam, M. A., Hossain, N., and Chowdhury, M. A. (2025). Advances in nanoparticles in targeted drug delivery–A review. *Results Surfaces Interfaces* 19, 100529. doi: 10.1016/J.RSURFI.2025.100529

Kain, H., Gupta, E., Sharma, P., Haldiya, A., Srivastava, V. K., Neeraj, R. R. K., et al. (2025). Rolling down the pilus formation of gram-positive bacteria: underlining the importance of Sortase C as a drug target. *Biofouling* 41, 1–19. doi: 10.1080/08927014.2024.2426167

Thiruppathi, J., Vijayan, V., Park, I. K., Lee, S. E., and Rhee, J. H. (2024). Enhancing cancer immunotherapy with photodynamic therapy and nanoparticle: making tumor microenvironment hotter to make immunotherapeutic work better. *Front. Immunol.* 15. doi: 10.3389/FIMMU.2024.1375767

frontiers | Frontiers in Cellular and Infection Microbiology

TYPE Original Research
PUBLISHED 07 November 2024
DOI 10.3389/fcimb.2024.1480987

OPEN ACCESS

EDITED BY
Sanket Kaushik,
Amity University Jaipur, India

REVIEWED BY
Mukesh Kumar,
All India Institute of Medical Sciences, India
Satyajeet Das,
Institute of Microbial Technology (CSIR), India

*CORRESPONDENCE
Maimaitiaili Tuerxun
tuerxun0235@163.com

RECEIVED 15 August 2024
ACCEPTED 04 October 2024
PUBLISHED 07 November 2024

CITATION
Tudi M, Sawuti A, Abudurusuli M, Wu C, Chen X, Ailimu G, Wulayin K and Tuerxun M (2024) Epitope-based therapeutic targets in HCV genotype 1 non-structural proteins: a novel strategy to combat emerging drug resistance.
Front. Cell. Infect. Microbiol. 14:1480987.
doi: 10.3389/fcimb.2024.1480987

Epitope-based therapeutic targets in HCV genotype 1 non-structural proteins: a novel strategy to combat emerging drug resistance

Mireayi Tudi, Adili Sawuti, Maimaitituerhong Abudurusuli, Chao Wu, Xiaoyu Chen, Gulimire Ailimu, Kuerbannisa Wulayin and Maimaitiaili Tuerxun*

Department of Infectious Diseases, The First People's Hospital of Kashi Prefecture, Kashi, China

Introduction: The hepatitis C virus (HCV) poses a major global health challenge, with its non-structural proteins being essential for viral replication and pathogenesis. Mutations in these proteins significantly contribute to drug resistance, necessitating innovative therapeutic strategies. This study aims to identify epitope-based therapeutic targets in the non-structural proteins of HCV genotype 1, employing in-depth in silico tools to counteract emerging drug resistance.

Methods: We retrieved approximately 250 sequences of each non-structural protein from the NCBI database, capturing a broad spectrum of variability and sequence alignments, variability analysis and physicochemical property analysis were conducted. We utilized the TEPITOOL server by IEDB to predict cytotoxic T lymphocyte (CTL) epitopes. Following this, we assessed the efficiency of TAP transport and proteasomal cleavage using IEDB's combined predictor tool. The epitopes were selected based on conservancy analysis, immunogenicity, allergenicity, and presence in non-glycosylated regions, ensuring high predictive scores and suitability as vaccine candidates. Epitopes were docked with the HLA-A*02:01 allele and Toll-like receptor-3 using the ClusPro server. The immune response potential of the epitopes was evaluated through *in-silico* immune stimulation.

Results: The study identified 27 potential CTL epitopes from the non-structural proteins, including NS3, NS4a, NS4b, NS5a, and NS5b. Out of these, three lead epitopes demonstrated high conservation (>90%), strong binding affinities to HLA-A*02:01 and TLR-3, and robust immune response potential. These epitopes also showed favorable characteristics such as being non-allergenic and non-glycosylated.

Conclusion: This comprehensive *in-silico* analysis provides a promising foundation for developing an epitope-based vaccine targeting HCV non-structural proteins, offering a novel approach to overcoming drug resistance in HCV treatment.

KEYWORDS

drug resistance, epitopes, hepatitis C, HLA allele, non-structural proteins

1 Introduction

Hepatitis C virus (HCV) is a leading cause of chronic liver disease, affecting approximately 58 million people worldwide, with 1.5 million new infections occurring annually (Kenfack-Momo et al., 2024). Chronic HCV infection can lead to severe liver conditions, including cirrhosis and hepatocellular carcinoma (HCC), significantly contributing to global morbidity and mortality with over 3,50,000 fatalities each year (Organization, W. H. 2019). Among the six genotypes of HCV (1 to 6), genotype 1 is the most prevalent and poses a considerable challenge due to its high propensity for developing resistance to antiviral therapies (Shen et al., 2023). The primary treatment for HCV involves direct-acting antivirals (DAAs), which target specific non-structural proteins of the virus, such as NS3/4A protease, NS5A, and NS5B polymerase (Dobrowolska et al., 2024). These DAAs have revolutionized HCV treatment, achieving high cure rates. However, the emergence of resistance-associated substitutions (RASs) in the HCV genome remains a significant obstacle, diminishing the efficacy of these drugs and necessitating the development of alternative therapeutic strategies (Xiong and Guo, 2024). Non-structural proteins of HCV, including NS3, NS4a, NS4b, NS5a, and NS5b, are crucial for the viral life cycle and are common targets for DAAs (Ramos et al., 2023). Mutations in these proteins can lead to resistance, underscoring the need for novel approaches to counteract this challenge. For instance, the NS3/4A protease is crucial for processing the HCV polyprotein, which is essential for viral replication. Similarly, NS5A plays a role in viral replication and assembly, while NS5B functions as an RNA-dependent RNA polymerase, which is vital for the replication of the viral genome (Izhari, 2023). The pivotal roles of these proteins in the HCV life cycle make them prime candidates for targeted therapeutic interventions. Epitope-based vaccines offer a promising approach to overcoming drug resistance in HCV. These vaccines are designed to elicit a robust and specific immune response against conserved regions of the virus, thereby enhancing the immune system's ability to control and clear the virus, even in the presence of drug-resistant variants (Cowton et al., 2021). The strategy involves identifying short sequences of amino acids (epitopes) that are recognized by cytotoxic T lymphocytes (CTLs). CTLs play a critical role in controlling viral infections by targeting and destroying infected cells, making them a key component in the fight against HCV. The HLA-A*02:01 allele is one of the most prevalent human leukocyte antigen (HLA) class I molecules, known for its effective presentation of viral epitopes to CTLs (Wang et al., 2020). Predicting HLA-A*02:01 restricted epitopes from HCV non-structural proteins is, therefore, a strategic approach for developing potent vaccines. *In-silico* methods provide an efficient means of identifying potential epitopes, enabling the screening of extensive viral sequences and predicting epitopes with high binding affinity to HLA molecules (Sohail et al., 2021). The advancements in bioinformatics, have propelled vaccine science into a new era, introducing a contemporary, innovative, and highly practical approach to developing next-generation robust immunogens (Shawan et al., 2023). The methodology has previously been employed for developing vaccines against various pathogens like Influenza virus, Trypanosoma cruzi, Ebola and Dengue viruses and several others (Martinelli, 2022).

In this study, we aim to develop an epitope-based therapeutic strategy specifically targeting the non-structural proteins of HCV genotype-1 (Cowton et al., 2021). We hypothesize that by identifying HLA-A*02:01 restricted epitopes from NS3, NS4a, NS4b, NS5a, and NS5b proteins, we can formulate a vaccine that elicits a potent CTL response. This response would be capable of targeting and eliminating HCV-infected cells, thus providing a robust defense against the virus, even in the presence of drug-resistant mutations. By focusing on conserved regions within these non-structural proteins, we aim to create a vaccine candidate that not only prevents infection but may also offer therapeutic benefits. This includes enhancing the immune system's ability to control and clear the virus, particularly in individuals infected with drug-resistant HCV variants. The outcomes of this research could pave the way for novel vaccine designs, contributing to the global effort to eradicate HCV and mitigate the impact of drug resistance.

2 Methodology

2.1 HCV non-structural proteins sequence retrieval and physicochemical properties analysis

The non-structural protein sequences for NS3, NS4a, NS4b, NS5a and NS5b of HCV genotype-1 were retrieved from NCBI database https://www.ncbi.nlm.nih.gov/. To capture a comprehensive view of the protein variations, we downloaded approximately 250 sequences from diverse regions, ensuring a broad representation of genetic variability. The inclusion Criteria for selecting the target sequences were: Genotype specificity: Sequences must belong to HCV genotype 1, as verified through BLAST analysis https://blast.ncbi.nlm.nih.gov/Blast.cgi; Protein specificity: Only sequences corresponding to the non-structural proteins NS3, NS4a, NS4b, NS5a, and NS5b were included; Sequence completeness: Full-length protein sequences were selected to ensure comprehensive analysis. Geographic diversity: Sequences were chosen to represent a broad range of geographic regions to capture genetic variability; and lastly Quality and annotation: Sequences must be well-annotated with minimal ambiguous bases, ensuring high-quality data. The exclusion criteria included Incomplete Sequences: Partial or truncated sequences were excluded to avoid incomplete data representation; Non-genotype 1 sequences: Any sequence not verified as belonging to HCV genotype 1 through BLAST analysis was excluded.; Low-quality sequences: Sequences with poor annotation, high levels of ambiguity, or those lacking sufficient metadata were excluded; Redundant sequences: Duplicates or highly similar sequences were excluded to avoid redundancy and ensure a diverse dataset; and Recombinant strains: Sequences identified as potential recombinants were excluded to maintain focus on standard genotype 1 variations. Initially, the sequences underwent BLAST analysis to confirm their identity and similarity. Subsequently, the aligned sequences were subjected to multiple sequence alignment using the COBALT tool (https://www.ncbi.nlm.nih.gov/tools/cobalt/re_cobalt.cgi) (Papadopoulos and Agarwala, 2007). This

alignment was essential for identifying conserved and variable regions within the proteins. The physicochemical properties of the proteins like theoretical pI, mol. wt, extinction coefficient, estimated half-life, instability index, and grand average of hydropathicity (GRAVY) were then assessed using the PROTPARAM tool (https://web.expasy.org/protparam/) (Gasteiger et al., 2005).

2.2 Prediction of CTL epitopes using multiple algorithms

Initially, the amino acid sequences of each non-structural protein were analyzed using the TEPITOOL server (https://tools.iedb.org/tepitool/) by IEDB, one of the most advanced and up-to-date tools for epitope prediction (Paul et al., 2016). This tool enabled the identification of top-scoring epitopes based on their potential to elicit a CTL response. Following this, the top-scoring epitopes with percentile rank ≤ 1 were further evaluated for their efficient TAP transport and C-terminal proteasomal cleavage. This analysis was performed using the combined TAP transport and MHC class-I predictor tool provided by IEDB, which integrates these processes to predict the likelihood of an epitope being effectively presented on the surface of infected cells (Tenzer et al., 2005). TAP transport and proteasomal cleavage analysis are essential for evaluating the potential of epitopes as CTL targets. These processes are critical because proteasomal cleavage ensures that the epitope is processed and presented by the MHC, while TAP transport facilitates the transfer of these processed peptides into the endoplasmic reticulum for MHC loading. Both assessments are key to determining whether an epitope can be effectively recognized by CTLs.

2.3 Selection of promising epitopes

The initially identified epitopes were further refined based on several criteria to ensure their suitability for vaccine development.

2.4 Conservancy

Epitopes were examined for conservancy using the IEDB conservancy analysis tool (Bui et al., 2007). Epitopes demonstrating greater than 90% conservancy were selected for further analysis. Targeting conserved regions within the non-structural proteins of HCV genotype-1 is crucial because these regions are less likely to undergo mutations, which minimizes immune evasion and ensures the effectiveness of the vaccine against various viral strains, including drug-resistant ones.

2.5 Immunogenicity

The VaxiJen v2.0 server was utilized to evaluate the immunogenicity of the selected epitopes, effectively distinguishing between non-antigenic and antigenic epitopes (Doytchinova and Flower, 2007). Non-immunogenic epitopes were discarded. This was carried out in view that most of the peptides are less immunogenic, thus it becomes important to screen the epitopes for their immunogenicity.

2.6 Allergenicity

The remaining epitopes were evaluated for allergenicity using the AllerTOP v2.0 server (https://www.ddg-pharmfac.net/AllerTOP/method.html) (Dimitrov et al., 2014). Epitopes identified as allergenic were excluded.

2.7 Glycosylation

Epitopes were also checked for the presence of glycosylation sites using the NetNGlyc 1.0 server (https://services.healthtech.dtu.dk/services/NetNGlyc-1.0/) (Gupta and Brunak, 2001). Epitopes located in glycosylated regions were omitted to avoid potential issues with epitope processing and presentation.

The final list comprised epitopes that met all the criteria: high predictive scores, efficient TAP transport, proteasomal cleavage, conservancy, immunogenicity, non-allergenicity, and location in non-glycosylated regions. These promising epitopes were selected for further analysis.

2.8 Epitopes 3D structure and physicochemical analysis

The physicochemical properties of the epitopes as discussed in the methodology section were determined using the ProtParam server. The secondary structure of the epitopes was also analyzed. This analysis provided insights into the alpha helices, beta strands, and coils within the epitope structures, which are crucial for understanding their stability and potential interactions.

2.9 Evaluation of high-affinity CTL epitopes for HLA-A*02:01

The epitopes were further assessed for their affinity to the HLA-A*02:01 allele. To achieve this, the epitopes were modelled using the PEPFOLD 2.0 server (https://bioserv.rpbs.univ-paris-diderot.fr/services/PEP-FOLD/), which is a *de novo* tool for predicting the 3D structure of peptides between 9 and 36 amino acids in length (Shen et al., 2014). The secondary structural properties were also noted for all the epitopes as provided by the PEPFOLD server. PEPFOLD 2.0 uses Hidden Markov Models and performs simulations to generate the most representative conformations based on energy and population metrics. The predicted 3D structures of the epitopes were docked with the HLA-A*02:01 allele using the ClusPro server (Kozakov et al., 2017). ClusPro evaluates balanced docking energies, which include the

combination of van der Waals interactions, electrostatics, and desolvation contributions, to predict the binding affinity of each epitope. The 3D model of HLA Class-I allele: HLA-A*02:01 was obtained from Protein Data Bank (PDB ID: 1QEW).

2.10 Optimization of epitopes through binding to the TLR-3 membrane receptor

To evaluate the immunogenic potential of the epitopes, their binding affinity to Toll-like receptor-3 (TLR-3) was further analyzed. The structure of the TLR-3 receptor was obtained from the Protein Data Bank (PDB ID: 7C76). The selected epitopes were docked with the TLR-3 receptor to evaluate their binding interactions. This step was crucial to ensure that the epitopes not only bind effectively to the HLA-A*02:01 allele but also engage with the TLR-3 receptor, which is vital for the innate immune response.

2.11 Immune simulation by lead epitopes

The immune response elicited by the lead epitope candidates, particularly the cytotoxic T-cell response, was assessed through *in-silico* immune simulations utilizing an ImmSim server (Rapin et al., 2010). The immune simulations were conducted using advanced *in-silico* tools with over 100 simulation steps. This comprehensive simulation aimed to model the immune response dynamics over time. The primary focus was on evaluating the cytotoxic T-cell response, which is crucial for targeting and eliminating HCV-infected cells. These immune simulations helped predict the potential effectiveness of the selected epitopes in generating a robust and targeted immune response, thereby validating their suitability as candidates for an epitope-based therapeutic strategy against HCV genotype-1.

3 Results

3.1 Target non-structural proteins

Approximately 250 protein sequences for each of the HCV non-structural proteins (NS3, NS4a, NS4b, NS5a, and NS5b) were retrieved in FASTA format from the NCBI database. These sequences represented a wide range of variability and geographical regions. The sequences were initially aligned using the protein BLAST tool from NCBI. The aligned sequences were then processed using the COBALT multiple sequence alignment tool. The COBALT alignment allowed us to visualize the sequences based on a frequency-based difference method. In this method, residues in a column are scored based on their representation in the column's frequency profile. Rarely occurring residues are highlighted darkly, and columns with any degree of mismatch are also highlighted (Supplementary Figure S1). The physicochemical properties of these proteins were analyzed using the ProtParam tool. These analyses provided insights into various parameters such as molecular weight, theoretical pI etc, which are summarized in Supplementary Table S1. This comprehensive sequence alignment and physicochemical analysis laid the foundation for the subsequent identification and evaluation of potential epitopes.

3.2 HLA-A*02:01 targeting epitopes prediction

Epitopes targeting the HLA-A*02:01 allele were predicted using the TEPITOOL server, specifically focusing on 9-mer epitopes. The top-scoring epitopes were selected based on a consensus percentile rank of ≤1, ensuring high predictive accuracy. We employed the IEDB-recommended method for epitope prediction, which utilizes the default selection of predictors. This approach leverages the best available methods for a given MHC molecule, including artificial neural networks (ANN), stabilizing membrane models (SMM), and combinatorial libraries (CombLib) whenever applicable. Following the initial prediction, the selected epitopes were further evaluated for their likelihood of undergoing proteasomal cleavage and TAP transport. For this analysis, the sequences were evaluated using the Combined Predictor tool from IEDB, which integrates Proteasomal Cleavage, TAP Transport, and MHC Class I assessments. This comprehensive tool combines predictors for proteasomal processing, TAP transport, and MHC binding to deliver an overall score that indicates each peptide's potential as a T cell epitope. This dual approach effectively led to the identification of potential epitopes characterized by high percentile ranks and favorable conditions for proteasomal cleavage, thereby enhancing their suitability as candidates for further development in an epitope-based therapeutic strategy (Table 1).

3.3 Epitopes screening

The identified epitopes using the above-mentioned epitope prediction tools underwent a rigorous screening process based on several immunological parameters. Initially, the epitopes were assessed for conservancy, with only those exhibiting greater than 90% conservancy selected for further evaluation. The conserved epitopes were then subjected to immunogenicity testing using the VaxiJen v2.0. Non-immunogenic epitopes (below threshold 0.4) identified in this analysis were eliminated from consideration. The immunogenic epitopes were further subjected to allergenicity testing. The allergenic epitopes identified were also excluded from the final selection. Lastly, the epitopes were screened for their presence in glycosylation sites. Epitopes located in glycosylated regions were also eliminated from the list. As a result of this comprehensive screening process, we identified a set of epitopes that met the following criteria: high percentile scores, likelihood of undergoing proteasomal cleavage, high conservancy, immunogenicity, non-allergenicity, and non-glycosylation. The final predictions included two epitopes from NS3, two from NS4a, two from NS4b, thirteen from NS5a, and eight from NS5b (Table 1).

10.3389/fcimb.2024.1480987

TABLE 1 Most promising epitopes predicted in each non-structural protein.

Non-structural protein	Epitope	Sequence	Conservancy	Vaxijen Score
NS3	E1	LVLNPSVAA	100%	0.5
	E2	VLNPSVAAT	100%	0.66
NS4a	E3	VLVGGVLAA	100%	0.43
	E4	AIIPDREVL	100%	0.58
NS4b	E5	GVAGALVAF	100%	0.48
	E6	RVTAILSSL	100%	0.49
NS5a	E7	GLGWAGWLL	83.6%	0.86
	E8	YVGGVEHRL	83.60%	1.16
	E9	ALSTGLLHL	100%	0.77
	E10	GLWSFSLLL	99.6%	0.6
	E11	SMMAFSAAL	83.6%	0.45
	E12	FVVSGLVGA	96.8%	0.8
	E13	GILSPGALV	83.6%	0.43
	E14	KVSARLLTL	97.2%	0.61
	E15	FQYSPAQRV	99.6%	0.43
	E16	GIVAPTMLV	97.2%	0.51
	E17	YLFNWAVKT	95.6%	0.68
	E18	LLLFVGVGL	88%	1.23
	E19	FVGVGLFLL	88%	0.95
NS5b	E20	SLLRHHNLV	100%	0.5
	E21	VTFDRLQVL	99.6%	0.53
	E22	VLDSHYQDV	98.4%	0.81
	E23	KVKANLLSV	100%	0.83
	E24	KAVAHINSV	97.6%	0.64
	E25	IMFAPTLWA	100%	0.71
	E26	YLFNWAVRT	100%	0.69
	E27	LLLAAGVGI	100%	0.83

E1-E27 are the epitope codes given along with their sequence.

3.4 Epitopes affinity to HLA allele and TLR-3

The top-scoring epitopes were subjected to molecular docking analysis with the HLA-A02:01 allele using the ClusPro server (Figure 1). The 3D model of the HLA-A02:01 allele was extracted from the PDB, which includes a 9-mer melanoma-associated antigen-3 (MAA-3) complexed with the HLA-A*02:01 allele. Before docking, the retrieved 3D model underwent energy minimization and was prepared by removing the MAA-3 peptide, along with water molecules and other heteroatoms. All the epitopes were successfully docked in the active site of the HLA-A02:01 allele showing varying degrees of docking energy scores (Figures 1, 2). In addition, the epitopes were also docked with TLR-3 in order to examine the affinities of epitopes towards immune receptors. The docked energy scores and docking patterns were examined and noted (Figures 1, 3). Previously several studies have also utilized the ClusPro tool for studying molecular interactions between epitope and HLA molecules for vaccine development (Chauhan et al., 2021; Dubey et al., 2024). This analysis highlighted the potential of the epitopes to engage effectively with key immune components, supporting their candidacy for further development in an epitope-based therapeutic strategy. In addition, the secondary structural properties of the epitopes as provided by the Pepfold server were also examined (Figure 4).

10.3389/fcimb.2024.1480987

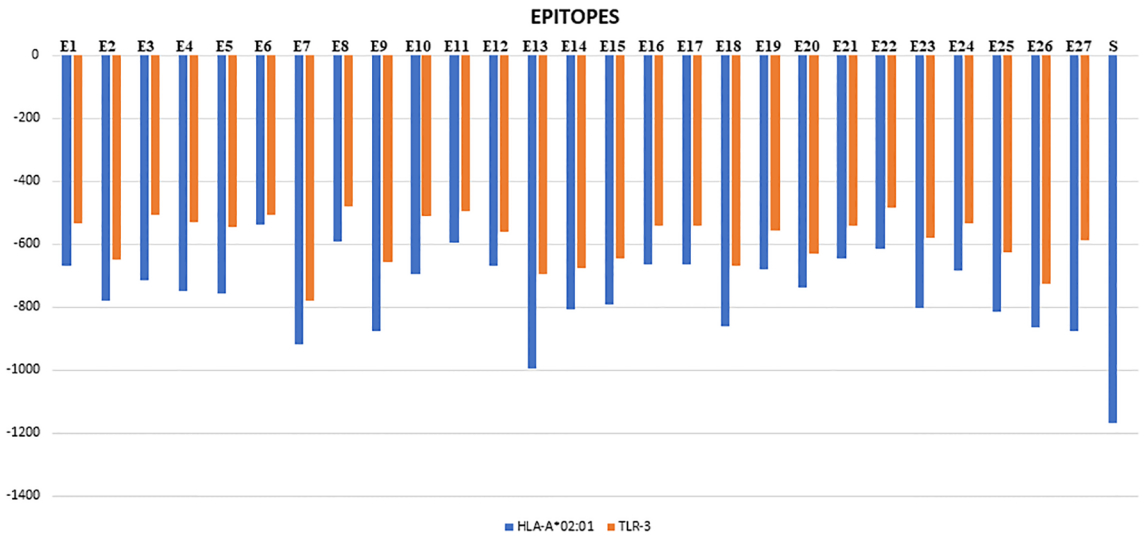

FIGURE 1
Bar graph representing the docking energies of epitopes (E1-E27) with HLA-A*02:01 allele and TLR-3 represented by blue and orange bars respectively. Std is the standard MAA-3 peptide.

3.5 Immune simulation analysis

The top five epitopes with the highest affinities to the HLA-A*02:01 allele and TLR-3 i.e. epitopes E7, E9, E13, E14 and E27 underwent immune simulation analysis. Among these, epitopes E9, E13 and E27 demonstrated the strongest potential for activating cytotoxic T cells (Figure 5). This analysis facilitated the identification of lead epitopes that possess high affinities to both

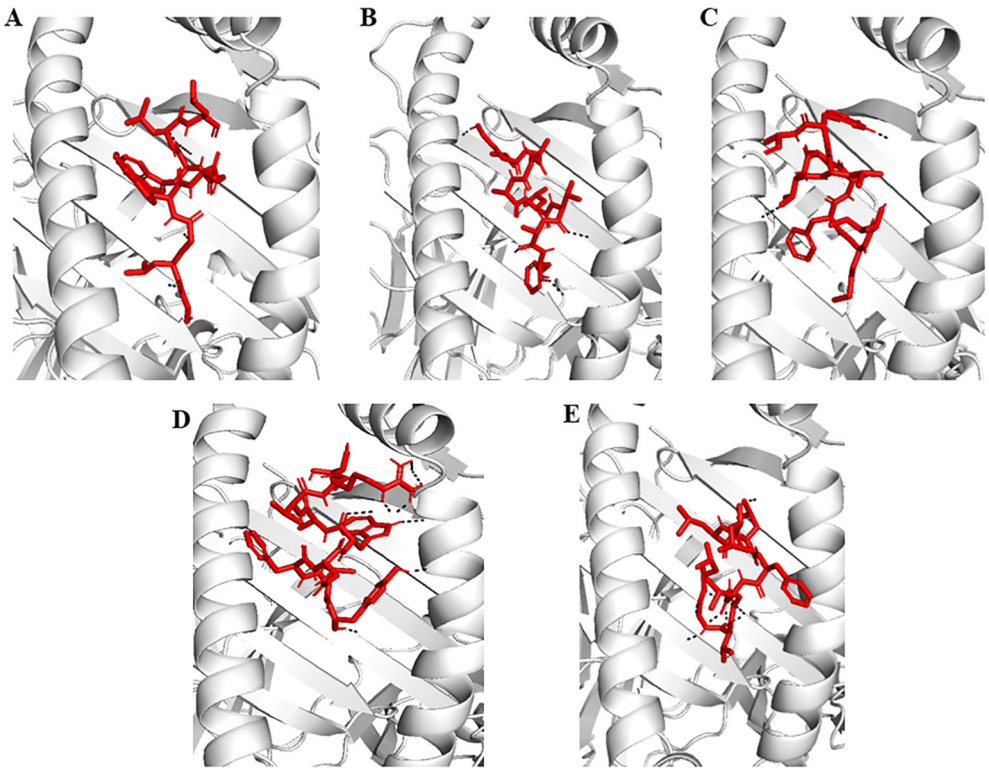

FIGURE 2
Representation of molecular docking pattern of epitopes with HLA-A*02:01 allele. The allele is represented in white (cartoon) and epitopes in red (sticks). The H-bonds formed are represented in black dashes. **(A–E)** are the epitopes E7, E9, E13, E14 and E27 respectively.

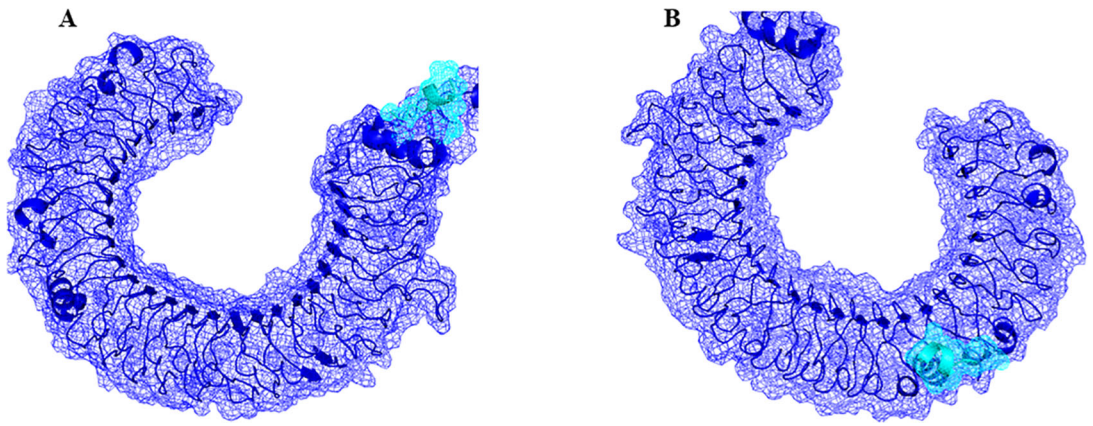

FIGURE 3
Cartoon representation of epitopes E7 **(A)** and E 13 **(B)** (cyan) with TLR-3 (dark blue).

HLA and TLR, as well as key immunological characteristics: they are conserved, non-allergenic, immunogenic, non-glycosylated, and capable of inducing a robust cytotoxic T cell response.

4 Discussion

Hepatitis C virus (HCV) remains a significant global health challenge, primarily due to its ability to develop drug resistance, particularly in genotype-1, which is the most prevalent worldwide (Kenfack-Momo et al., 2024). Direct-acting antiviral (DAA) treatments achieve a cure rate of over 95% in individuals with chronic HCV infection. Nevertheless, for some patients where the treatment is unsuccessful, resistance-associated substitutions (RASs) may emerge, reducing retreatment options and increasing the potential for the transmission of resistant viruses (Howe et al., 2022). Our study aimed to develop an epitope-based therapeutic strategy specifically targeting the non-structural proteins of HCV genotype-1 to combat this rising resistance. The overall workflow employed for epitope screening is represented in Figure 6. Immuno-informatics is essential in vaccine development as it enables the identification of potential epitopes and the prediction of immune responses. This computational approach streamlines the design of effective vaccines against infectious diseases (Oli et al., 2020). Previous studies have successfully employed immuno-informatics for epitope prediction across various disease contexts, including cancers (Rizarullah et al., 2024), viral pathogens

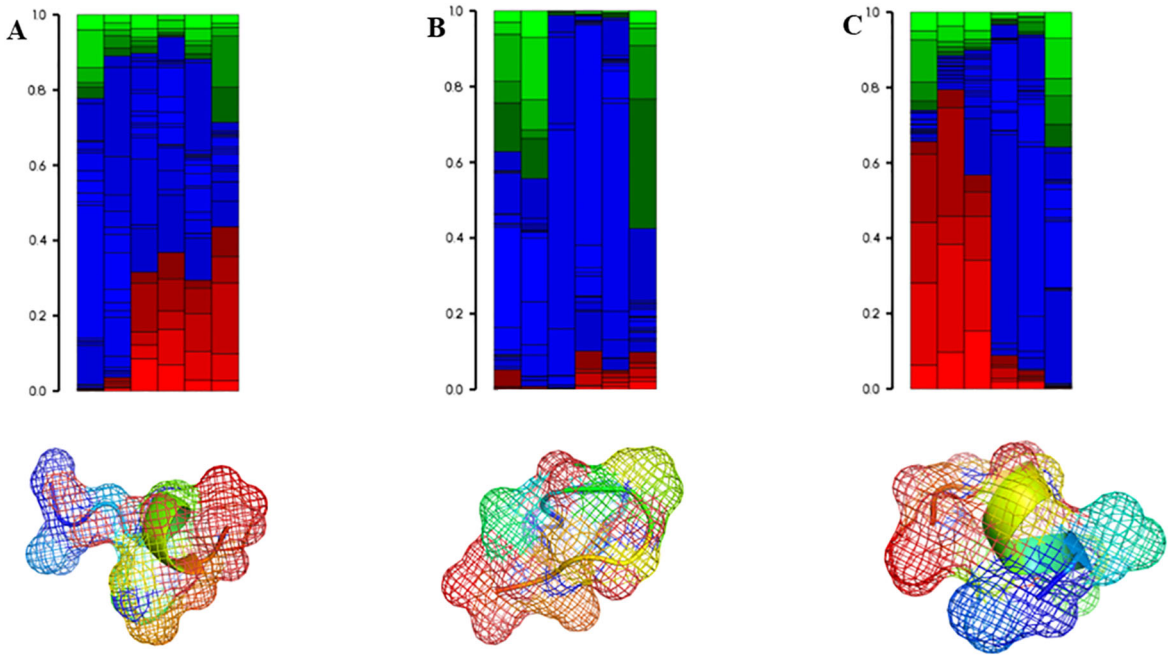

FIGURE 4
Secondary structural properties red: helical, green: extended and blue: coil of the top 3 lead epitopes. In addition, the 3D models of the epitopes are also represented in cartoons and mesh formats. **(A–C)** represent epitopes E7, E13 and E27.

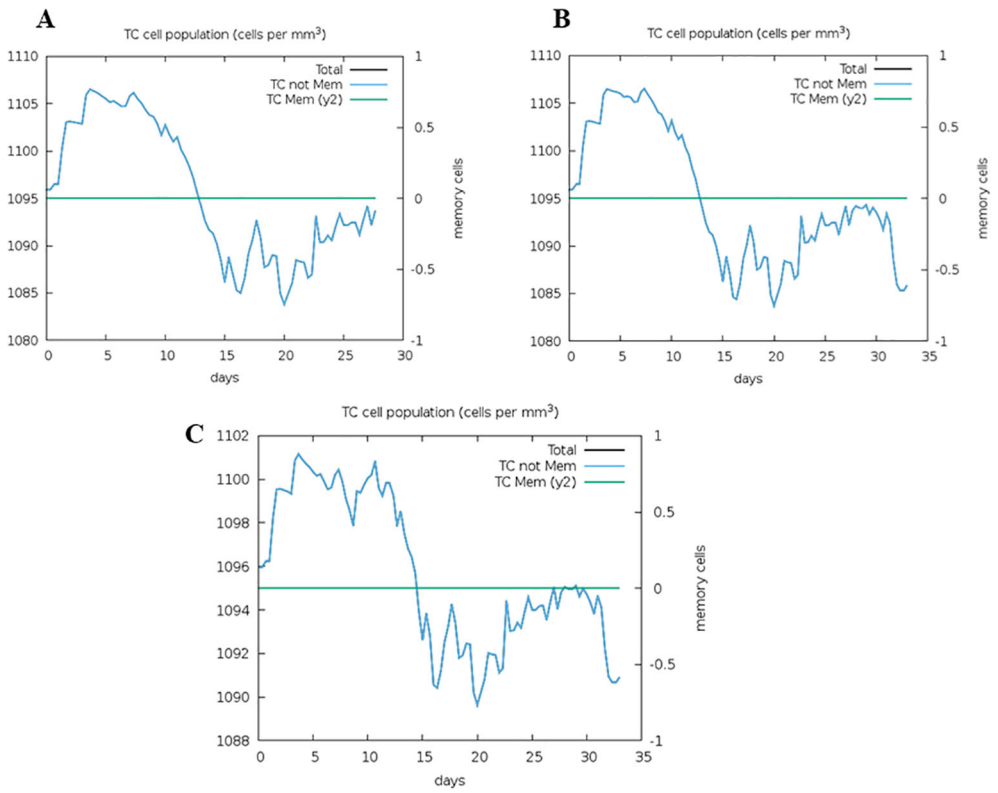

FIGURE 5
Immune simulation analysis of the epitopes E7 **(A)**, E13 **(B)** and E27 **(C)**. The capacity to induce the activation of cytotoxic T cells was investigated.

(Chauhan and Singh, 2020), and antimicrobial-resistant pathogens (Muteeb et al., 2024). By leveraging comprehensive immuno-informatics analyses, we identified 27 lead epitopes distributed across the targeted non-structural proteins: two from NS3, two from NS4a, two from NS4b, thirteen from NS5a, and eight from NS5b. Each of these epitopes exhibited high conservancy (>90%), non-allergenic properties, and robust immunogenicity, positioning them as promising candidates for vaccine development. Notably, our top five epitopes demonstrated significant binding affinities to both the HLA-A*02:01 allele and the TLR-3 receptor, further validating their potential as effective immunogens. The integration of multiple algorithms for predicting T cell epitopes has been shown to enhance predictive accuracy, evident in our selection process. This comprehensive methodology aligns with the practices highlighted in recent studies, such as Kumar et al (Kumar et al., 2021), who predicted CTL epitopes against SARS-CoV-2. Their approach involved multiple sequence alignments for conservancy analysis, the application of various epitope prediction algorithms, and a rigorous immune filtration process to screen effective T-cell epitopes. Furthermore, our findings resonate with those of Dobrowolska et al (Dobrowolska et al., 2024), who emphasized the importance of targeting conserved regions within viral proteins to elicit more effective and durable immune responses, especially in populations facing high rates of drug resistance. By focusing on conserved regions and employing a multi-faceted predictive strategy, our study aims to ensure that the identified epitopes can elicit strong and lasting immune responses. In comparison to earlier studies, such as that by Chauhan et al (Chauhan et al., 2018), which identified both B and T cell epitopes against Indian HCV genotype 3a using an immuno-informatics approach, our study stands out by utilizing a diverse range of global sequences. This broader dataset enhances the applicability and relevance of our findings across different populations and HCV strains. Moreover, our results suggest that the identified epitopes could form the foundation for a vaccine capable of not only preventing HCV infection but also inducing robust T cell-mediated responses against drug-resistant variants. We meticulously considered drug resistance mutations during the epitope screening process, ensuring that our selected epitopes remain relevant in the context of evolving viral strains. As highlighted by Izhari (2023), the continuously evolving nature of HCV necessitates ongoing monitoring of viral mutations and their effects on epitope presentation. Thus, continuous surveillance of circulating HCV strains will be vital in ensuring the long-term efficacy of any developed vaccine strategy. By integrating computational predictions with ongoing clinical and epidemiological studies, we can enhance our understanding of HCV dynamics and improve vaccine design strategies, ultimately contributing to more effective interventions against this persistent global health threat.

4.1 Limitations and future directions

While this study presents promising findings, the *in-silico* predictions must be validated through experimental and clinical

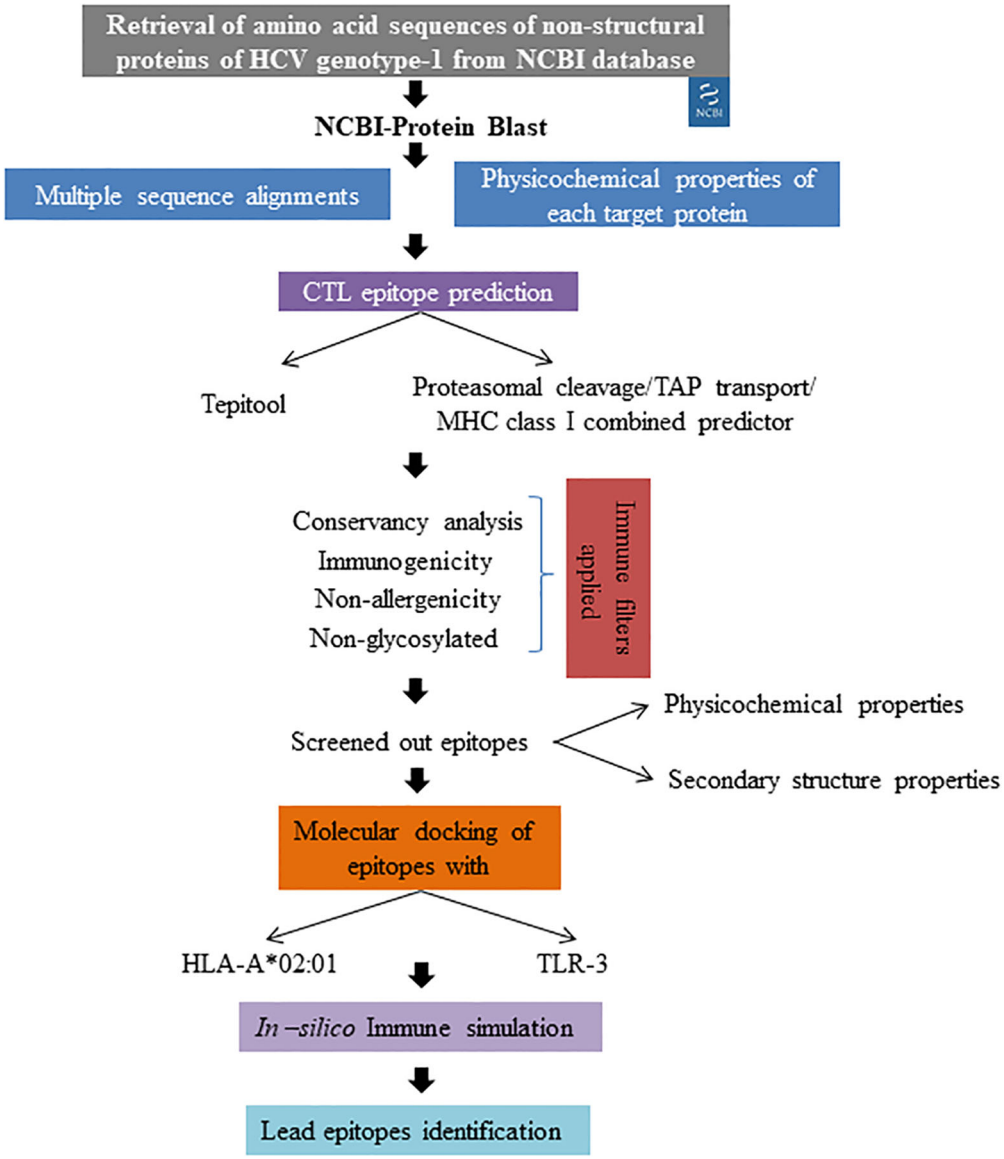

FIGURE 6
Overall methodology applied for lead epitope identification.

studies. The identified epitopes should undergo further validation in preclinical settings, such as *in vitro* and *in vivo* immune response assays. Additionally, continuous monitoring of HCV mutations remains essential to ensure the ongoing relevance of the selected epitopes against emerging strains. Future research should focus on integrating these findings with population-based studies to determine the efficacy of these epitopes in diverse HCV-infected populations.

5 Conclusion

This study successfully identified lead epitopes targeting the non-structural proteins of HCV genotype-1, demonstrating high conservancy, non-allergenic properties, and robust immunogenicity. Our findings underscore the potential of these epitopes as candidates for vaccine development, particularly in combating drug-resistant variants. The top epitopes showed significant binding affinities to HLA-A*02:01 and TLR-3, validating their roles as effective immunogens. By employing a comprehensive immuno-informatics approach, we laid the groundwork for developing an epitope-based vaccine that could elicit strong cytotoxic T-cell responses. The reliance on computational predictions necessitates validation through experimental approaches, such as *in vitro* and *in vivo* studies, to confirm the immunogenic potential of the identified epitopes. Future research should focus on these experimental validations, as well as expanding the analysis to include a broader range of HCV genotypes and variants. Ongoing monitoring of HCV mutations will be essential to ensure the long-term efficacy of the identified epitopes and any

future vaccine strategies. Ultimately, our research contributes to the advancement of effective therapeutic options against HCV infection and resistance.

Data availability statement

The datasets presented in this study can be found in online repositories. The names of the repository/repositories and accession number(s) can be found below: https://www.ncbi.nlm.nih.gov.

Author contributions

MiT: Conceptualization, Investigation, Writing – original draft, Writing – review & editing. AS: Investigation, Methodology, Writing – original draft, Writing – review & editing. MA: Formal analysis, Investigation, Project administration, Writing – original draft, Writing – review & editing. CW: Data curation, Formal analysis, Writing – original draft, Writing – review & editing. XC: Conceptualization, Formal analysis, Visualization, Writing – original draft, Writing – review & editing. GA: Investigation, Writing – original draft, Writing – review & editing. KW: Writing – original draft, Writing – review & editing. MaT: Investigation, Project administration, Resources, Writing – original draft, Writing – review & editing.

Funding

The author(s) declare that no financial support was received for the research, authorship, and/or publication of this article.

Conflict of interest

The authors declare that the research was conducted in the absence of any commercial or financial relationships that could be construed as a potential conflict of interest.

Publisher's note

Supplementary material

The Supplementary Material for this article can be found online at: https://www.frontiersin.org/articles/10.3389/fcimb.2024.1480987/full#supplementary-material

References

Bui, H.-H., Sidney, J., Li, W., Fusseder, N., and Sette, A. (2007). Development of an epitope conservancy analysis tool to facilitate the design of epitope-based diagnostics and vaccines. *BMC Bioinf.* 8, 1–6. doi: 10.1186/1471-2105-8-361

Chauhan, V., Rungta, T., Rawat, M., Goyal, K., Gupta, Y., and Singh, M. P. (2021). Excavating SARS-coronavirus 2 genome for epitope-based subunit vaccine synthesis using immunoinformatics approach. *J. Cell. Physiol.* 236, 1131–1147. doi: 10.1002/jcp.29923IF:4.5Q1

Chauhan, V., and Singh, M. P. (2020). Immuno-informatics approach to design a multi-epitope vaccine to combat cytomegalovirus infection. *Eur. J. Pharm. Sci.* 147, 105279. doi: 10.1016/j.ejps.2020.105279

Chauhan, V., Singh, M. P., and Ratho, R. K. (2018). Identification of T cell and B cell epitopes against Indian HCV-genotype-3a for vaccine development-An in silico analysis. *Biologicals* 53, 63–71. doi: 10.1016/j.biologicals.2018.02.003

Cowton, V. M., Owsianka, A. M., Fadda, V., Ortega-Prieto, A. M., Cole, S. J., Potter, J. A., et al. (2021). Development of a structural epitope mimic: An idiotypic approach to HCV vaccine design. *NPJ Vaccines* 6, 1–10. doi: 10.1038/s41541-020-00269-1

Dimitrov, I., Bangov, I., Flower, D. R., and Doytchinova, I. (2014). AllerTOP v. 2—a server for in silico prediction of allergens. *J. Mol. Modeling* 20, 1–6. doi: 10.1007/s00894-014-2278-5

Dobrowolska, K., Brzdęk, M., Rzymski, P., Flisiak, R., Pawłowska, M., Janczura, J., et al. (2024). Revolutionizing hepatitis C treatment: next-gen direct-acting antivirals. *Expert Opin. Pharmacotherapy.* 25(7): P-833–852. doi: 10.1080/14656566.2024.2358139

Doytchinova, I. A., and Flower, D. R. (2007). VaxiJen: a server for prediction of protective antigens, tumour antigens and subunit vaccines. *BMC Bioinf.* 8, 1–7. doi: 10.1186/1471-2105-8-4

Dubey, S. K., Mishra, M. K., Khan, F., Nahid, A., and Kumar, A. (2024). An immunoinformatics study to explore HTL epitopes for fungal pathogen Aspergillus lentulus. *J. Proteins Proteom.* 15, 15–27. doi: 10.1007/s42485-023-00125-5

Gasteiger, E., Hoogland, C., Gattiker, A., Duvaud, S. E., Wilkins, M. R., Appel, R. D., et al. (2005). "Protein identification and analysis tools on the ExPASy server," in *The Proteomics Protocols Handbook*, ed. J. M. Walker (Berlin: Springer), 571–607. doi: 10.1385/1-59259-890-0:571

Gupta, R., and Brunak, S. (2001). Prediction of glycosylation across the human proteome and the correlation to protein function. *Biocomputing* 2002, P310–320.

Howe, A. Y., Rodrigo, C., Cunningham, E. B., Douglas, M. W., Dietz, J., Grebely, J., et al. (2022). Characteristics of hepatitis C virus resistance in an international cohort after a decade of direct-acting antivirals. *JHEP Rep.* 4, 100462. doi: 10.1016/j.jhepr.2022.100462

Izhari, M. A. (2023). Molecular mechanisms of resistance to direct-acting antiviral (DAA) drugs for the treatment of hepatitis C virus infections. *Diagnostics* 13, 3102. doi: 10.3390/diagnostics13193102

Kenfack-Momo, R., Ngounoue, M. D., Kenmoe, S., Takuissu, G. R., Ebogo-Belobo, J. T., Kengne-Ndé, C., et al. (2024). Global epidemiology of hepatitis C virus in dialysis patients: A systematic review and meta-analysis. *PloS One* 19, e0284169. doi: 10.1371/journal.pone.0284169

Kozakov, D., Hall, D. R., Xia, B., Porter, K. A., Padhorny, D., Yueh, C., et al. (2017). The ClusPro web server for protein–protein docking. *Nat. Protoc.* 12, 255–278. doi: 10.1038/nprot.2016.169

Kumar, N., Admane, N., Kumari, A., Sood, D., Grover, S., Prajapati, V. K., et al. (2021). Cytotoxic T-lymphocyte elicited vaccine against SARS-CoV-2 employing immunoinformatics framework. *Sci. Rep.* 11, 7653. doi: 10.1038/s41598-021-86986-6

Martinelli, D. D. (2022). In silico vaccine design: A tutorial in immunoinformatics. *Healthcare Analytics.* 2, 100044. doi: 10.1016/j.health.2022.100044

Muteeb, G., Rehman, M. T., Pani, B., and Khan, R. H. (2024). Novel drug-designing approaches to combat antimicrobial resistance. *Front. Media SA*. doi: 10.3389/fmolb.2023.1342702

Oli, A. N., Obialor, W. O., Ifeanyichukwu, M. O., Odimegwu, D. C., Okoyeh, J. N., Emechebe, G. O., et al. (2020). Immunoinformatics and vaccine development: an overview. *ImmunoTargets Ther.*, 13–30. doi: 10.2147/ITT.S241064

Organization, W. H (2019). *Progress report on HIV, viral hepatitis and sexually transmitted infections 2019: accountability for the global health sector strategies 2016–2021* (World Health Organization).

Papadopoulos, J. S., and Agarwala, R. (2007). COBALT: constraint-based alignment tool for multiple protein sequences. *Bioinformatics* 23, 1073–1079. doi: 10.1093/bioinformatics/btm076

Paul, S., Sidney, J., Sette, A., and Peters, B. (2016). TepiTool: a pipeline for computational prediction of T cell epitope candidates. *Curr. Protoc. Immunol.* 114, 18.19. doi: 10.1002/0471142735.2016.114.issue-1

Ramos, D., Pinto, M., Sousa Coutinho, R., Silva, C., Quina, M., Gomes, J. P., et al. (2023). Looking at the Molecular Target of NS5A Inhibitors throughout a Population Highly Affected with Hepatitis C Virus. *Pathogens* 12, 754. doi: 10.3390/pathogens12060754

Rapin, N., Lund, O., Bernaschi, M., and Castiglione, F. (2010). Computational immunology meets bioinformatics: the use of prediction tools for molecular binding in the simulation of the immune system. *PloS One* 5, e9862. doi: 10.1371/journal.pone.0009862

Rizarullah,, Aditama, R., Giri-Rachman, E. A., and Hertadi, R. (2024). Designing a novel multiepitope vaccine from the human papilloma virus E1 and E2 proteins for Indonesia with immunoinformatics and molecular dynamics approaches. *ACS Omega* 9, 16547–16562. doi: 10.1021/acsomega.4c00425

Shawan, M. M. A. K., Sharma, A. R., Halder, S. K., Arian, T. A., Shuvo, M. N., Sarker, S. R., et al. (2023). Advances in computational and bioinformatics tools and databases for designing and developing a multi-epitope-based peptide vaccine. *Int. J. Pept. Res. Ther.* 29, 60. doi: 10.1007/s10989-023-10535-0

Shen, C., Jiang, X., Li, M., and Luo, Y. (2023). Hepatitis virus and hepatocellular carcinoma: recent advances. *Cancers* 15, 533. doi: 10.3390/cancers15020533

Shen, Y., Maupetit, J., Derreumaux, P., and Tufféry, P. (2014). Improved PEP-FOLD approach for peptide and miniprotein structure prediction. *J. Chem. Theory Comput.* 10, 4745–4758. doi: 10.1021/ct500592m

Sohail, M. S., Ahmed, S. F., Quadeer, A. A., and Mckay, M. R. (2021). In silico T cell epitope identification for SARS-CoV-2: Progress and perspectives. *Advanced Drug Delivery Rev.* 171, 29–47. doi: 10.1016/j.addr.2021.01.007

Tenzer, S., Peters, B., Bulik, S., Schoor, O., Lemmel, C., Schatz, M., et al. (2005). Modeling the MHC class I pathway by combining predictions of proteasomal cleavage, TAP transport and MHC class I binding. *Cell. Mol. Life Sci. CMLS*, 62, 1025–1037. doi: 10.1007/s00018-005-4528-2

Wang, C., Xiong, C., Hsu, Y.-C., Wang, X., and Chen, L. (2020). Human leukocyte antigen (HLA) and cancer immunotherapy: HLA-dependent and-independent adoptive immunotherapies. *Ann. Blood* 5:14. doi: 10.21037/aob-20-27

Xiong, H., and Guo, J. (2024). Key points for the management of hepatitis C in the era of pan-genotypic direct-acting antiviral therapy. *Explor. Digestive Dis.* 3, 226–240. doi: 10.37349/edd

frontiers | Frontiers in Cellular and Infection Microbiology

TYPE Original Research
PUBLISHED 28 November 2024
DOI 10.3389/fcimb.2024.1481656

OPEN ACCESS

EDITED BY
Sanjit Kumar,
Guru Ghasidas Vishwavidyalaya, India

REVIEWED BY
Prakash Shukla,
VIT University, India
Afreen Anjum,
Guru Ghasidas University, India

*CORRESPONDENCE
Xinli Pang
Pangxinli2024@163.com
Vipasha Sharma
sharma.vipasha@gmail.com

†These authors share first authorship

‡These authors have contributed equally to this work and share last authorship

RECEIVED 16 August 2024
ACCEPTED 28 October 2024
PUBLISHED 28 November 2024

CITATION
Zhao K, Jiang Y, Dev K, He X, Sharma V and Pang X (2024) Terpenoids as principal bioactive compound of *Cissampelos oppositifolia* essential oils: enhancing synergistic efficacy with conventional antibiotics.
Front. Cell. Infect. Microbiol. 14:1481656.
doi: 10.3389/fcimb.2024.1481656

Terpenoids as principal bioactive compound of *Cissampelos oppositifolia* essential oils: enhancing synergistic efficacy with conventional antibiotics

Kexin Zhao[1†], Yurong Jiang[2†], Kamal Dev[3], Xin He[2], Vipasha Sharma[4*‡] and Xinli Pang[2*‡]

[1]Department of Respiratory Medicine, Shenzhen Children's Hospital, Shenzhen, Guangdong, China, [2]Shenzhen People's Hospital (The Second Clinical Medical College, Jinan University; The First Affiliated Hospital, Southern University of Science and Technology)., Shenzhen, Guangdong, China, [3]Department of Pharmacology and Toxicology, Wright State University, Dayton, OH, United States, [4]University Institute of Biotechnology, Chandigarh University, Mohali, India

Background: The rise of antibiotic resistance imposes the search for novel antimicrobial strategies as natural products or its combination with antibiotics. This study investigates the synergistic effects of terpenoids from *Cissampelos oppositifolia* (*C. oppositifolia*) essential oil in combination with antibiotics against *Escherichia coli* (*E. coli*) and *Staphylococcus aureus* (*S. aureus*). The aims were to evaluate the antimicrobial efficacy, analyze functional group modifications and assess molecular interaction.

Methods: Essential oil was extracted from *C. oppositifolia* by hydro-distillation. The EO was analyzed for terpenoid content via Thin Layer Chromatography (TLC). Antimicrobial activity was assessed using the disc diffusion method and Minimum Inhibitory Concentration determinations (MIC) by broth dilution followed by bactericidal essay (Time-killing). FTIR and UV spectroscopy were employed to detect functional group modifications in terpenoid-antibiotic combinations. Molecular docking studies assessed interaction energies between terpenoids and antibiotics.

Results: TLC identified α-pinene, δ-carene, and caryophyllene in the EO. δ-Carene exhibited the highest synergy with antibiotics, showing the lowest MIC of 0.04 mg/mL against *S. aureus* ATCC-43300 and 0.05 mg/mL against *E. coli* MTCC-739. Time-kill assays demonstrated that α-pinene, δ-carene, and caryophyllene achieved complete bacterial eradication by 4 hours in combination with amoxicillin against *E. coli*, and by 2 hours against *S. aureus* in combination with erythromycin. FTIR analysis revealed peak shifts at 1599, 1774, and 2259 cm^{-1} for amoxicillin + α-pinene, and new peaks at 1648 and 1287 cm^{-1} for δ-carene + erythromycin. UV spectra indicated potential complex formations. Docking studies showed δ-carene's strong interaction with erythromycin and amoxicillin, with interaction energies of -96.10 and -87.75 kcal/mol, respectively.

Conclusion: Terpenoids from *C. oppositifolia* enhance the antimicrobial efficacy of antibiotics. Functional group modifications and complex formations suggest that these interactions may contribute to synergistic effects. These findings support the potential use of terpenoid-antibiotic combinations in overcoming antibiotic resistance and warrant further investigation into their mechanisms of action.

KEYWORDS

terpenoids, antibiotics, synergy, spectroscopy, docking studies

1 Introduction

The global incidence of microbial infectious diseases is rising (Masyita et al., 2022; Salvi et al., 2022; Baker et al., 2022), significantly impacted by the increasing prevalence of microbial drug resistance to current antimicrobial agents (Salam et al., 2023). This resistance results in multidrug-resistant microbes causing widespread infections. This is linked to higher morbidity and mortality rates of about 4.95 million people who died by drug-resistant infections among 1.27 million deaths by antibiotic resistance in 2019 (Antimicrobial Resistance Collaborators, 2022). The growing issue of antibiotic resistance and the higher recurrence rates of common infections are straining healthcare systems and societies (Ali et al., 2024). Predictions indicate that by 2050, the mortality attributable to antimicrobial resistance may exceed 10 million annually, surpassing that of other major diseases and cancers (de Kraker et al., 2016). Consequently, there is an urgent need for novel antimicrobial agents or the use of a combination of natural remedies with modern antibiotics to treat MDR infections (Konwar et al., 2022). Natural products, particularly those derived from plants, offer a promising avenue for discovering new antimicrobial agents (Cowan, 1999). Medicinal plants have been used throughout history for their therapeutic properties, with essential oils (EOs) being one of the most prominent natural products and so catching the attention of researchers globally (Nasim et al., 2022; Chaachouay and Zidane, 2024). EOs are concentrated hydrophobic liquids derived from plants, known as rich sources of bioactive compounds with antimicrobial, antiviral, antioxidant, anti-inflammatory, and other pharmacological effects. Plants produce these chemicals to protect themselves, contributing to their color, aroma, and flavor. Essential oils, as key secondary metabolites, are responsible for many of these pharmaceutical properties (Masyita et al., 2022; Salvi et al., 2022). EOs are found in the cytoplasm of specific plant cell secretions in various plant organs, including secretory hairs or trichomes, epidermal cells, internal secretory cells, and secretory pockets (Gersbach, 2002). These oils are complex mixtures that may contain over 300 different compounds. They consist of organic volatile compounds, generally of low molecular weight below 300 g/mol (Dhifi et al., 2016; de Sousa et al., 2023). These Eos consistent compounds belong to various chemical classes: alcohols, ethers or oxides, aldehydes, ketones, esters, amines, amides, phenols, heterocycles, and mainly the terpenes. Alcohols, aldehydes, and ketones offer a wide variety of aromatic notes, such as fruity ((E)-nerolidol), floral (Linalool), citrus (Limonene), herbal (γ-selinene), etc. Among all chemical components of EOs, terpenes and terpenoids have been comprehensively studied and reported to play key roles in human health (Jugreet et al., 2020; Haro-González et al., 2021). Terpenoids or terpenes are the most structurally varied classes and they are the largest family of compounds of plant products. Previous studies estimated the existence of more than 23,000 known terpenoid compounds, including monoterpenes, sesquiterpene, carotenoids, tetraterpenes, diterpenes, tocopherol, phytol, steroids and hormones (Masyita et al., 2022). The monoterpenes and sesquiterpene are the most dominant terpenoids present in the Eos. These compounds contribute to the flavor and aroma of plants but they have therapeutic potential (Proshkina et al., 2020). The monoterpenes and sesquiterpene oxygenated derivatives of terpenes are recognized for their ability to combat both antibiotic-susceptible and resistant bacteria. They act primarily by disrupting microbial cell membranes, inhibiting protein synthesis, and interfering with DNA replication (Masyita et al., 2022). Compounds such as carvacrol, carvone, eugenol, geraniol, and thymol have demonstrated antibacterial properties against pathogens including *Staphylococcus aureus*. *C. oppositifolia* is a traditional medicinal plant widely used in various cultures for its therapeutic properties. Known for its rich phytochemical profile, it contains essential oils abundant in terpenoids, particularly α-pinene, δ-carene, and caryophyllene, which are recognized for their antimicrobial, anti-inflammatory, and antioxidant activities (Shang et al., 2024). Historically, the plant has been employed in herbal medicine to treat ailments such as fevers, respiratory disorders, and infections (Sharma et al., 2021). Recent studies highlight its potential in modern medicine, especially in enhancing the efficacy of conventional antibiotics, making it a promising candidate for further research in phytotherapy and drug development (Mahizan

et al., 2019). These terpenoids have shown potential in enhancing the effectiveness of conventional antibiotics through synergistic interactions. This study aims to investigate the principal bioactive terpenoids in the essential oils of *C. oppositifolia* and their role in improving antibiotic efficacy. By exploring these interactions, the research seeks to contribute to the development of more effective antimicrobial strategies and address the growing challenge of drug-resistant infections.

2 Methods

The present study was conducted in accordance with the biosafety regulations of the university. *Escherichia coli* MTCC-739 and *Staphylococcus aureus* ATCC-43300 were obtained from the Institute of Microbial Technology (IMTECH), Chandigarh. The research was approved by the university's research committee.

2.1 Plant material and antimicrobial property screening

A total of 72 plant specimens (Supplementary Table 1), including *C. oppositifolia*, were collected from two locations in Himachal Pradesh, India: Solan (altitude 1350 m, temperature 20-30°C, humidity 55-68%) and Shimla (altitude 2202 m, temperature 12-25°C, humidity 62-80%). The specimens, comprising leaves, buds, flowers, and tubers, were identified and verified using the herbarium at Dr Y.S. Parmar University of Horticulture and Forestry, Nauni, Himachal Pradesh. The collected specimens were washed with water and surface-sterilized using 1% hydrogen peroxide (H_2O_2), followed by rinsing with autoclaved distilled water to remove any residual H_2O_2, as per an established protocol in our laboratory. The surface-sterilised plant material was then dried in an oven at 40°C until completely desiccated. The dried material was ground into a fine powder using an electronic mixer grinder (Sharma and Mishra, 2019). Among the specimens, *C. oppositifolia* extract exhibited significantly higher antimicrobial activity, as shown in our published data. Phytochemical analysis of the extracts revealed the presence of various bioactive compounds, including phenols, terpenoids, flavonoids, tannins, coumarins, glycosides, and alkaloids. EOs were subsequently extracted from *C. oppositifolia* and further investigated for this study.

2.2 Extraction of essential oil

The EOs were extracted using an environmentally friendly hydro-distillation method (Abbas et al., 2022) and calculated by Extract Yield (%)= (Weight of starting material/Weight of extract obtained)×100. Fresh leaves and inflorescence of *C. oppositifolia* were subjected to hydro-distillation using a Clevenger apparatus. Two hundred grams of chopped plant material were placed in a round-bottom flask, and 400 mL of distilled water was added. The mixture underwent hydro-distillation for 3 hours. Afterwards, the organic phase was dried over sodium sulphate, and filtered, and the solvent was evaporated to dryness. The volatile oil was then stored at 4°C until analysis. This method combines extraction and steam distillation into a single process, which reduces trial time, saves solvents, simplifies equipment, and facilitates operation. While the extraction rate is relatively low, the essential oil obtained is of high purity. However, the process involves high temperatures, which may lead to the volatilization or oxidation of certain components in the EOs. The method primarily collects insoluble EOs, resulting in the loss of water-soluble components and, consequently, a lower extraction yield. The extracted oil is still a multi-component composite essential oil, making it challenging to achieve selective extraction and complete purity.

2.3 Extraction of terpenoids

The EOs were further processed to isolate terpenoids using TLC (Jiang et al., 2016). Initially, a small quantity of the essential oil was dissolved in a minimal amount of an extraction solvent, typically a mixture of hexane and ethyl acetate in a 7:3 ratio. This solution was then placed onto a pre-coated silica gel TLC plate, which had been activated by heating at 110°C for 30 minutes. The TLC plate was placed in a development chamber containing a mobile phase of hexane and ethyl acetate (7:3 ratio), allowing the solvent front to rise to about 3/4th of the plate's height. After development, the TLC plate was removed from the chamber and air-dried. Visualization of the terpenoids was achieved by observing the plate under UV light at 254 nm and 365 nm, where terpenoids typically have fluorescence. For further visualization, the plate was sprayed with anisaldehyde-sulfuric acid reagent and heated at 110°C for 10 minutes, revealing distinct colored bands corresponding to the terpenoids. The retention factor (Rf) values of these bands were calculated and compared with known standards to identify the specific terpenoids present in the essential oil α-pinene, δ-carene, and caryophyllene. The results were documented by photographing the TLC plates and noting the colors and Rf values of the terpenoid spots.

2.4 Antimicrobial and synergistic effect of α-pinene, δ-carene, caryophyllene

2.4.1 Antimicrobial susceptibility testing

The antimicrobial susceptibility of the terpenoids—α-pinene, δ-carene, and caryophyllene, was assessed using the disc diffusion method (Gupta et al., 2023). Each compound was dissolved in dimethyl sulfoxide (DMSO) at a concentration of 0.75 mg/mL and stored in sterile centrifuge tubes at 4°C to reduce volatilization. For the susceptibility tests, the stock solutions were further diluted to 0.25 mg/mL, with 0.25% DMSO serving as the control. Bacterial inoculation was standardized to a concentration of 0.5 McFarland (1.5×10^5 CFU/mL) by spectrophotometric measurement at 625 nm, ensuring an optical density of 0.06. The terpenoids were tested against *E. coli* MTCC-739 and *S. aureus* ATCC-43300. Standard antibiotics, amoxicillin (30 µg) and erythromycin (15 µg) were included for comparison, both individually and in combination with each terpenoid. Mueller-Hinton agar plates were inoculated and incubated at 37°C for 18-20 hours. Antimicrobial activity was evaluated by measuring the zone of

inhibition around each disc. Compounds that exhibited significant antimicrobial activity were selected for further determination of MIC.

2.4.2 Minimum inhibitory concentration determination

MIC values were determined using the microdilution method (Kowalska-Krochmal and Dudek-Wicher, 2021), with concentrations of each terpenoid ranging from 0.25 to 0.002 mg/mL. Assays were conducted individually for each microorganism to prevent cross-interaction due to volatilization. All tests were performed in triplicate, and results were interpreted according to the CLSI-M100 guidelines (Clinical & Laboratory Standards Institute, 1999).

2.4.3 Time-kill study

A 24-hour time-kill curve study was performed according to CLSI document M26-A guidelines (M26-A Methods for Determining Bactericidal Activi.pdf, 2024). The terpenoids were evaluated at MIC, 2xMIC, and 4xMIC concentrations, with a negative control consisting of Mueller-Hinton broth, 0.25% DMSO, and bacterial inoculum. Bacterial suspensions were prepared as previously described, and the samples were incubated at 35°C for 24 hours. At intervals of 0, 2, 4, 8, 12, and 24 hours, 10 µL of each sample was diluted in 990 µL of 0.9% sterile saline, and 100 µL of this dilution was plated onto Mueller-Hinton agar. Plates were incubated for 24 hours at 35°C, after which colony-forming units (CFU) were manually counted. The counts were multiplied by 1000 to determine CFU/mL, and these values were transformed into a logarithmic scale to generate time-kill curves. A bactericidal effect was defined as a ≥ 3 $\log_{10}$ reduction in CFU from the initial count.

2.5 FTIR spectra of terpenoids and combination with antibiotics

FTIR spectroscopy was employed to investigate the molecular interactions between terpenoids (α-pinene, δ-carene, and caryophyllene) and antibiotics-amoxicillin and erythromycin. Terpenoids and antibiotics were prepared in solution, and FTIR spectra were recorded over the range of 4000–400 cm^{-1} using an ATR accessory for liquid samples and KBr pellets for solid samples. The spectra were analyzed for characteristic peaks and shifts to identify functional groups and potential interactions. Comparison of the spectra of individual terpenoids with their combinations with antibiotics revealed changes in peak positions or intensities, providing insights into molecular interactions and potential synergistic effects.

2.6 UV spectrophotometer spectra of terpenoids and combinations with antibiotics

UV spectrophotometry was utilized to analyze the absorbance characteristics of terpenoids-α-pinene, δ-carene, and caryophyllene and their combinations with antibiotics-amoxicillin and erythromycin. Solutions of each terpenoid and antibiotic were prepared at a concentration of 0.1 mg/mL in methanol or acetonitrile. Combined samples were also prepared by mixing equal volumes of the terpenoid and antibiotic solutions. Using a UV-visible spectrophotometer, spectra were recorded over the range of 200–400 nm. The baseline spectrum of the solvent was first recorded to correct for any background absorbance. Each sample was then analyzed to identify characteristic absorbance peaks and any shifts or changes when terpenoids were combined with antibiotics. These changes provided insights into the interactions between the compounds and their potential synergistic effects.

2.8 Docking study of combinations of terpenoids with antibiotics

The chemical structures of the selected terpenoids α-pinene, δ-carene, and caryophyllene and antibiotics-erythromycin and amoxicillin were first retrieved from the PubChem database-https://pubchem.ncbi.nlm.nih.gov/in.sdf format and converted to.pdb format using OpenBabel. These ligands were then subjected to energy minimization using the MMFF94 force field to obtain their most stable conformations, with protonation states adjusted and any missing hydrogens added.

3 Results

Of 71 plant *C. oppositifolia* extracts that showed interesting antimicrobial potential, further essential oil was extracted. The EO by hydro-distillation method yielded 1.2% by weight of the starting plant material. The purity of the extracted oil was measured at 95%, but the process led to the loss of approximately 10% of volatile components and the oxidation of some sensitive compounds. The oil primarily contained insoluble components, with a reduction of 15% in water-soluble substances. Despite these losses, the EO maintained a high degree of purity and was suitable for further analysis.

3.1 Terpenoids and antibiotics

The TLC analysis of the EO from *C. oppositifolia* revealed the presence of several terpenoids, including monoterpenes- α-pinene, δ-carene, and sesquiterpene-caryophyllene (Figure 1). These terpenoids were identified based on their characteristic retention factor (Rf) values compared to known standards. The terpenoids were tested in combination with two antibiotics, amoxicillin and erythromycin (Figure 1).

3.2 Antimicrobial susceptibility

The antimicrobial screening results for *S. aureus* ATCC-43300 and *E. coli* MTCC-739 demonstrated varying degrees of efficacy for the essential oil terpenoids and their combinations with antibiotics

10.3389/fcimb.2024.1481656

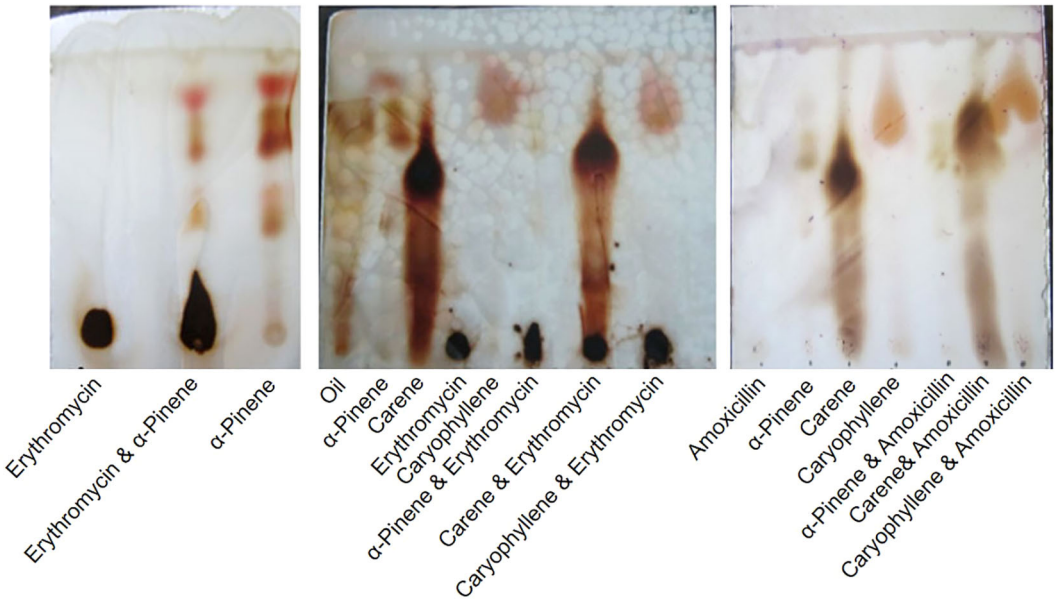

FIGURE 1
Thin Layer Chromatography (TLC) Analysis of Terpenoids from *Cissampelos oppositifolia* Extracts and Their Combination with Antibiotics.

(Table 1). For *S. aureus* ATCC-43300, erythromycin alone yielded a zone of inhibition of 7 ± 0.2 mm. When tested individually, α-pinene also showed a zone of 7 ± 0.2 mm, while δ-carene and caryophyllene produced zones of 10 ± 0.2 mm and 8 ± 0.2 mm, respectively. The combination of terpenoids with erythromycin enhanced the inhibitory effect, with α-pinene + erythromycin producing a zone of 10 ± 0.2 mm, δ-carene + erythromycin showing the largest zone of 11 ± 0.2 mm, and caryophyllene + erythromycin yielding 8 ± 0.2 mm. Among these, δ-carene exhibited the most significant synergistic effect with erythromycin against *S. aureus*. For E. coli MTCC-739, amoxicillin alone resulted in a zone of inhibition of 4 ± 0.2 mm. The individual terpenoids showed improved activity, with α-pinene, δ-carene, and caryophyllene producing zones of 9 ± 0.2 mm, 11 ± 0.2 mm, and 7 ± 0.2 mm, respectively. Combinations of terpenoids with amoxicillin led to further enhanced inhibition: α-pinene + amoxicillin resulted in a zone of 12 ± 0.2 mm, δ-carene + amoxicillin showed a zone of 11 ± 0.2 mm, and caryophyllene + amoxicillin achieved 8 ± 0.2 mm. The combination of α-pinene with amoxicillin exhibited the most significant synergistic effect against *E. coli*.

3.2.1 MICs of terpenoids

MICs of the compounds were evaluated for both *S. aureus* ATCC-43300 and *E. coli* MTCC-739. The results are presented in Table 2. α-Pinene exhibited a MIC of 0.08 mg/mL against S. aureus ATCC-43300 and 0.06 mg/mL against E. coli MTCC-739, indicating a moderate inhibitory effect. δ-carene showed the lowest MIC values, with 0.04 mg/mL for *S. aureus* ATCC-43300 and 0.05 mg/mL for *E. coli* MTCC-739, suggesting a stronger antimicrobial activity compared to the other compounds. Caryophyllene had MICs of 0.07 mg/mL against *S. aureus* ATCC-43300 and 0.08 mg/mL against *E. coli* MTCC-739, reflecting its effective but slightly less potent activity. Erythromycin had an MIC of 0.5 mg/mL against *S. aureus* ATCC-43300, while amoxicillin showed an MIC of 0.5 mg/mL against *E. coli* MTCC-739. These results highlight the varying levels of effectiveness of the terpenoids and antibiotics against the tested bacterial strains.

3.2.2 Time killing

he time-kill assay was conducted to assess the antimicrobial efficacy of α-pinene, δ-carene, and caryophyllene against *E. coli* MTCC-739 and *S. aureus* ATCC-43300, both individually and in combination with amoxicillin or erythromycin (Figures 2A, B). All treatments began with an initial bacterial load of 5 $\log_{10}$ CFU/ml at time zero. In the case of *E. coli*, during the first hour, α-pinene, δ-carene, and caryophyllene alone showed varying antibacterial activity, with bacterial counts reducing to 4, 0, and 6 $\log_{10}$ CFU/ml, respectively. Amoxicillin alone did not reduce the bacterial load at this early stage. By the second hour, α-Pinene and δ-carene maintained complete bacterial killing (0 $\log_{10}$ CFU/ml), while caryophyllene remained less effective, with a count of 6 $\log_{10}$ CFU/ml. Amoxicillin alone continued to show no reduction. By the four-hour mark, all treatments, including the combinations of α-pinene + amoxicillin, δ-carene + amoxicillin, and caryophyllene + amoxicillin, achieved a complete bacterial kill, maintaining a 0 $\log_{10}$ CFU/ml count. This bactericidal effect persisted through 8, 12, and 24 hours, indicating the potent efficacy of these compounds, particularly when combined with amoxicillin. A similar pattern was observed in *S. aureus* ATCC-43300. After 1 hour, α-Pinene and δ-carene alone reduced the bacterial load to 4 $\log_{10}$ CFU/ml, while caryophyllene alone led to an increase in the bacterial count to 6 $\log_{10}$ CFU/ml. Erythromycin alone showed no significant reduction, but the combinations of α-pinene + erythromycin and δ-carene +

10.3389/fcimb.2024.1481656

TABLE 1 Antimicrobial activity of terpenoids alone and in combination with antibiotics against *Staphylococcus aureus* ATCC-43300 and *Escherichia coli* MTCC-739.

Antibiotic/Terpenoid	*Staphylococcus aureus* ATCC-43300	*Escherichia coli* MTCC-739
	Zone of Inhibition (mm)	Zone of Inhibition (mm)
Erythromycin	7 ± 0.2	–
α-Pinene	7 ± 0.2	9 ± 0.2
Carene	10 ± 0.2	11 ± 0.2
Caryophyllene	8 ± 0.2	7 ± 0.2
α-Pinene + Erythromycin	10 ± 0.2	–
δ-carene + Erythromycin	11 ± 0.2	–
Caryophyllene + Erythromycin	8 ± 0.2	–
Amoxicillin	–	10± 0.2
α-Pinene + Amoxicillin	–	12 ± 0.2
δ-carene + Amoxicillin	–	11 ± 0.2
Caryophyllene + Amoxicillin	–	8 ± 0.2
Best Synergistic Effect with Erythromycin	δ-carene + Erythromycin	–
Best Synergistic Effect with Amoxicillin	–	- α-Pinene + Amoxicillin

erythromycin completely eradicated the bacteria, achieving 0 $\log_{10}$ CFU/ml. By the second hour, α-Pinene alone eliminated *S. aureus*, while δ-carene reduced the count to 2 $\log_{10}$ CFU/ml. Caryophyllene remained ineffective with 6 $\log_{10}$ CFU/ml, and erythromycin alone was still ineffective. At the four-hour mark, all treatments, except caryophyllene and erythromycin alone, achieved complete bacterial killing. This trend continued through 8, 12, and 24 hours, with α-pinene, δ-carene, and their combinations with erythromycin effectively maintaining a 0 $\log_{10}$ CFU/ml count. In contrast, caryophyllene and erythromycin alone exhibited limited antibacterial activity, with caryophyllene showing no reduction and erythromycin gradually reducing the bacterial load to 4 $\log_{10}$ CFU/ml by 24 hours. These results demonstrate that α-pinene, δ-carene, and their combinations with either amoxicillin or erythromycin exhibit strong bactericidal activity against both *E. coli a*nd *S. aureus*. To further validate these primary results, it is essential to investigate the mode of action of each terpenoid—α-pinene, δ-carene, and caryophyllene—by studying their effects on bacterial cell wall integrity. This can be done through assays designed to assess cell wall disruption, which would provide insights into the bactericidal mechanisms of these compounds. By evaluating how these terpenoids interact with bacterial cell walls, we can better understand whether their antimicrobial efficacy stems from cell wall destruction.

TABLE 2 Minimum Inhibitory Concentrations (mg/mL) of the terpenoids.

Compound	*S. aureus* ATCC-43300	*E. coli* MTCC-739
α-Pinene	0.08	0.06
Carene	0.04	0.05
Caryophyllene	0.07	0.08
Erythromycin	0.5	N/A
Amoxicillin	N/A	0.5

3.3 FTIR spectroscopy

The FTIR spectra analysis of antibiotics and terpenoids (Supplementary Figure 1) revealed significant modifications in the functional groups when combined, suggesting potential synergistic interactions. The overlay spectra for the combinations were analyzed. For the amoxicillin + α-Pinene combination, distinct peak shifts were observed at 1599, 1774, and 2259 cm^{-1} (Figure 3A). Similarly, the combination of α-Pinene with Amoxicillin showed a peak shift at 1715 cm^{-1} (Figure 3B). The combination of amoxicillin with caryophyllene exhibited peak shifts at 1599 and 1774 cm^{-1} (Figure 3C). Notably, the overlay of caryophyllene with amoxicillin resulted in similar peak modifications as seen with carene, at 1599 and 1774 cm^{-1} (Figure 3D). In contrast, the combination of δ-carene with erythromycin generated new peaks at 1648 and 1287 cm^{-1}, indicating a different interaction pattern (Figure 3E). Furthermore, the overlay of caryophyllene with amoxicillin led to the disappearance of the amoxicillin peaks at 1599 and 1774 cm^{-1}, while no modifications were observed in the caryophyllene and erythromycin combination (Figure 3F). These spectral changes suggest that the combination of terpenoids with antibiotics results in functional group modifications, which could be responsible for the observed synergistic effects in antimicrobial activity.

10.3389/fcimb.2024.1481656

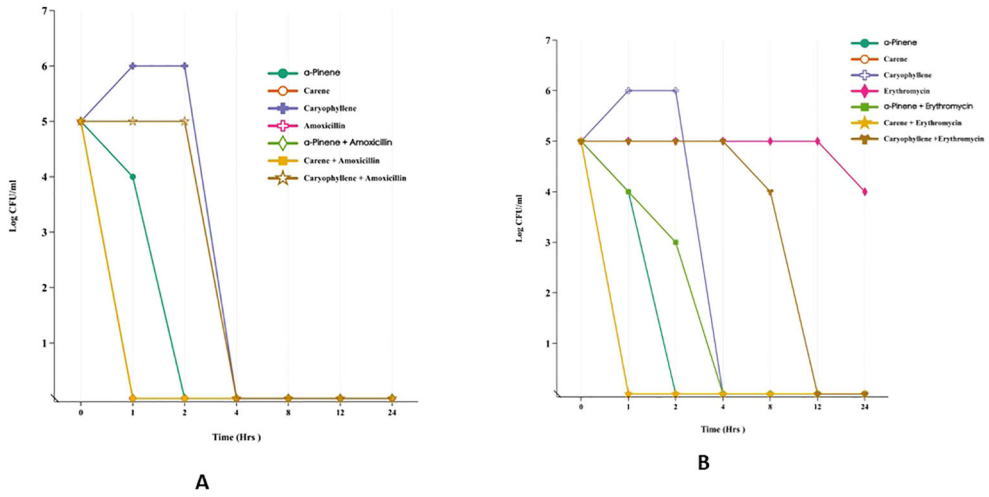

FIGURE 2
Time-Kill Assay of Terpenoids and Their Combinations with Antibiotics Against *E. coli* MTCC-739 **(A)** and *S. aureus* ATCC-43300 **(B)**.

3.4 UV spectrophotometer

Notable changes in the UV spectra were observed when terpenoids were mixed with antibiotics, suggesting possible interactions or alterations in the molecular structure of the components. In the combination of amoxicillin with α-Pinene (Figure 4A), significant shifts in the absorption peaks were noted, indicating potential interactions that may alter the electronic environment of the molecules. These shifts could be indicative of changes in the conjugation of the antibiotic's chromophore when combined with the terpenoid. Similarly, the combination of erythromycin with α-Pinene (Figure 4B) also showed noticeable peak shifts, further supporting the possibility of complex formation between these molecules. When amoxicillin was combined with δ-

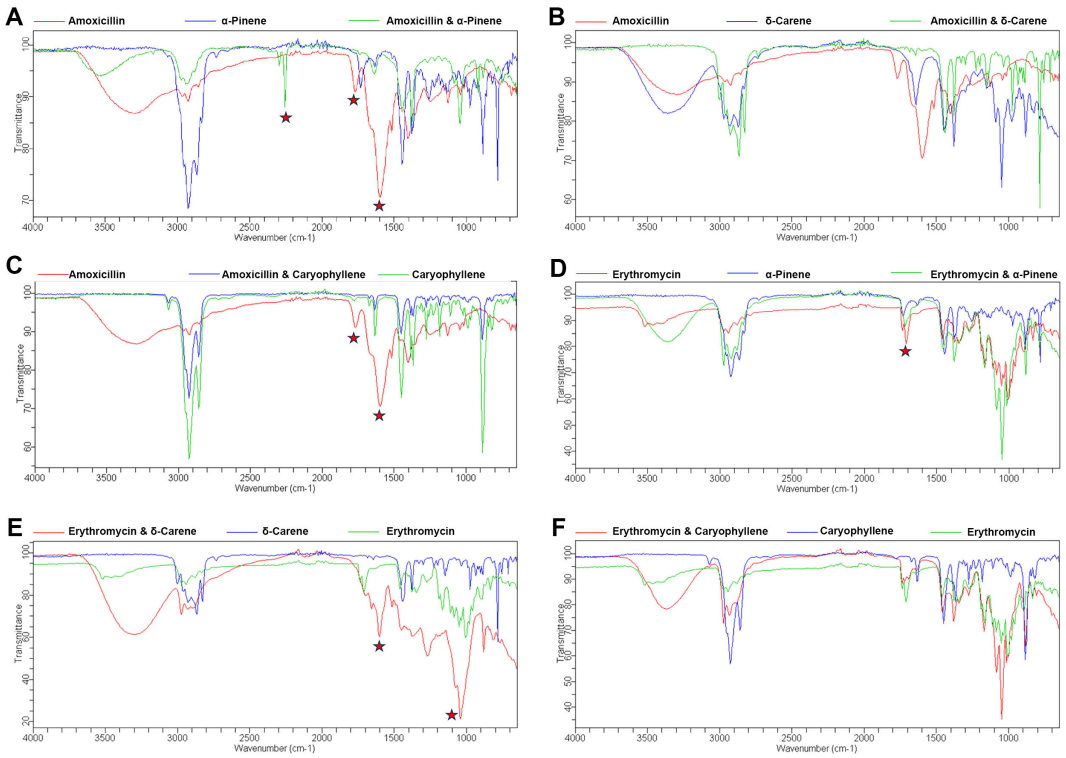

FIGURE 3
FTIR Spectroscopy Analysis of Functional Group Modifications in Terpenoid-Antibiotic Combinations. **(A)** Amoxicillin + α-Pinene; **(B)** Erythromycin + α-Pinene; **(C)** Amoxicillin + δ-Carene **(D)** Amoxicillin + Caryophyllene **(E)** Erythromycin + δ-Carene **(F)** Erythromycin + Caryophyllene.

10.3389/fcimb.2024.1481656

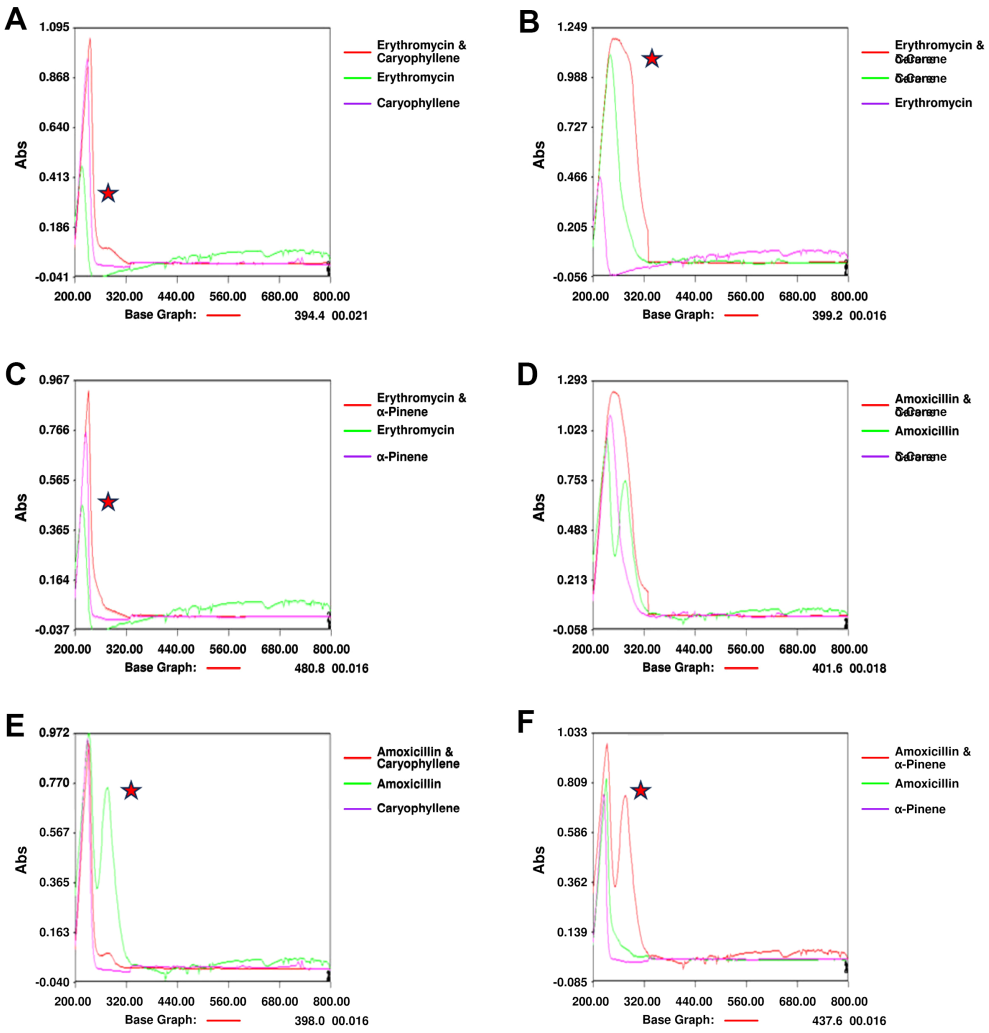

FIGURE 4
UV Spectrophotometry Analysis of Terpenoid-Antibiotic Interactions. **(A)** Amoxicillin + α-Pinene; **(B)** Erythromycin + α-Pinene; **(C)** UV Spectrum of Amoxicillin + δ-Carene; **(D)** Amoxicillin + Caryophyllene; **(E)** UV Spectrum of Erythromycin + δ-Carene; **(F)** Erythromycin + Caryophyllene.

carene (Figure 4C), distinct modifications in the absorption spectra were observed, highlighting potential changes in the molecular interactions. Caryophyllene, when mixed with amoxicillin (Figure 4D), showed similar alterations in the UV spectra, suggesting that the interaction between these molecules may involve modifications in their electronic structures. The combination of δ-carene and erythromycin (Figure 4E) revealed the formation of new absorption peaks, indicating the possible creation of new molecular entities or complexes. Finally, the spectra for caryophyllene and erythromycin (Figure 4F) showed minimal modifications, suggesting that while interactions may occur, they might be less pronounced than with other combinations. Overall, these results suggest that the mixing of terpenoids and antibiotics leads to changes in their UV absorption spectra, which could indicate complex formation or alterations in their molecular structures. These findings provide valuable insights into the potential synergistic effects observed in combination therapies involving these compounds.

3.5 Docking interactions of terpenoids with antibiotics

The docking results suggested the interaction energy values were analyzed to determine the strength of the interactions. Lower (more negative) values of interaction energy indicate stronger interactions. The docking structure for terpenoids- α-pinene, δ-carene and antibiotics- erythromycin, amoxicillin adopted, we have not included caryophyllene for the docking study (Supplementary Figure 2). The highest interaction was observed between δ-carene and erythromycin, with a total interaction energy value of -96.10 kcal/mol, suggesting a strong binding affinity between these two compounds (Figure 5A). This was followed by δ-carene with amoxicillin, which had an interaction energy value of -87.75 kcal/mol, indicating a significant interaction as well (Figure 5B). The α-pinene with erythromycin demonstrated an interaction energy of -83.58 kcal/mol, also reflecting a strong interaction but with amoxicillin had a slightly lower interaction energy value of -74.26

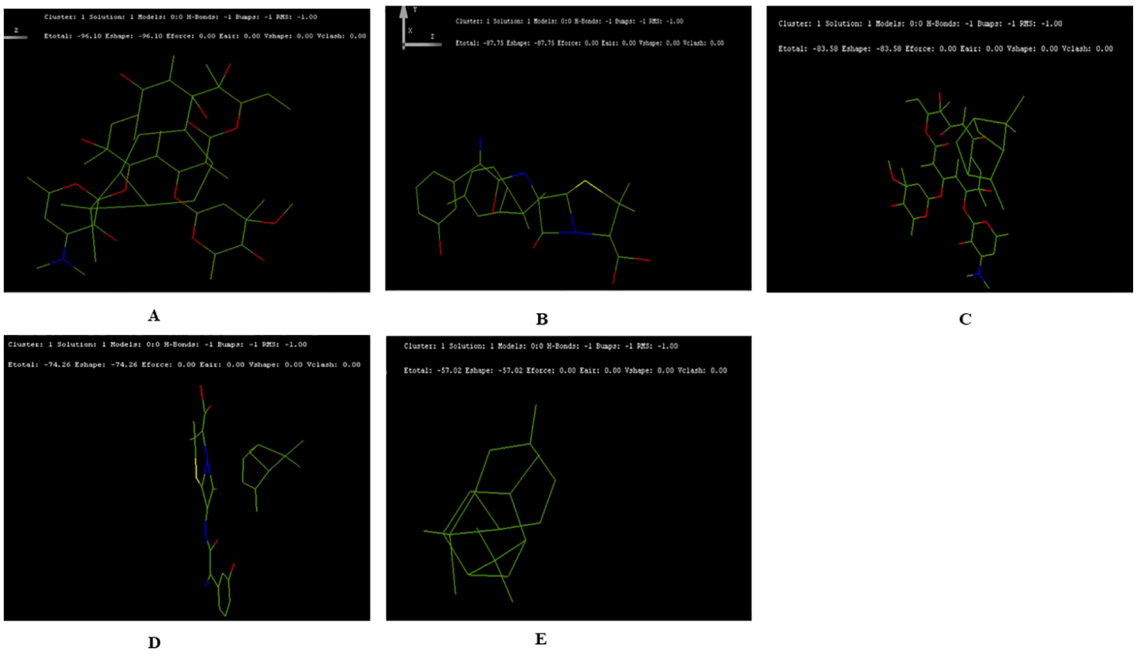

FIGURE 5
Docking Interactions of Terpenoids with Antibiotics Showing the Top Five Binding Conformations. **(A)** δ-Carene with Erythromycin; **(B)** Amoxicillin; **(C)** Docking of α-Pinene with Erythromycin; **(D)** α-Pinene with Amoxicillin **(E)** Docking of α-Pinene with δ-Carene.

kcal/mol (Figures 5C, D). Lastly, the combination of α-pinene with δ-carene displayed an interaction energy of -57.02 kcal/mol, which, although lower compared to the other pairs (Figure 5E). These docking results suggest that δ-carene exhibits the highest potential for interaction with both erythromycin and amoxicillin, which could imply enhanced efficacy or synergistic effects in therapeutic applications involving these combinations.

4 Discussion

The study explores the antimicrobial potential of *C. oppositifolia* EOs and its terpenoid constituents, such as α-pinene, δ-carene, and caryophyllene, in combination with antibiotics like amoxicillin and erythromycin. The findings offer significant insights into their individual and synergistic effects against *S. aureus* and *E. coli*, contributing to our understanding of their potential applications in combating bacterial infections. The essential oil extracted from *C. oppositifolia* yielded 1.2% of the starting plant material, with a high purity of 95%. This extraction efficiency and purity are comparable to other studies on essential oils, which often report similar yields and purities, although minor losses due to volatility and oxidation were noted (Sharma et al., 2021). Despite these losses, the EO's integrity and suitability for further analysis were maintained. The TLC analysis confirmed the presence of key terpenoids—α-pinene, δ-carene, and caryophyllene—in the EO. These findings are consistent with previous research identifying these terpenoids in *C. oppositifolia* and other plant species (Basholli-Salihu et al., 2017; Hanuš and Hod, 2020). The individual antimicrobial activity of these terpenoids demonstrated varying efficacy, with δ-carene showing the most potent effect against both *S. aureus* and *E. coli*. This is in line with other studies reporting δ-carene's significant antimicrobial properties (Swamy et al., 2016; Guimarães et al., 2019). When combined with antibiotics, the terpenoids exhibited synergistic effects. For *S. aureus*, the combination of δ-carene and erythromycin resulted in the largest zone of inhibition, aligning with the findings of synergistic effects between terpenoids and antibiotics observed in similar studies (Mahfouz et al., 2023). Similarly, the combination of α-pinene with amoxicillin showed enhanced inhibition against *E. coli*, highlighting the potential for these combinations to improve therapeutic efficacy. The MIC values revealed that δ-carene had the lowest MICs for both bacterial strains, indicating its superior antimicrobial activity. These results are consistent with other studies that have reported δ-carene as a potent antimicrobial agent (Roman et al., 2023). Caryophyllene and α-pinene also demonstrated effective antimicrobial properties, although with higher MIC values compared to δ-carene (Valdivieso-Ugarte et al., 2019). The time-kill assay provided a detailed understanding of the bactericidal effects of the terpenoids and their combinations. All tested compounds, both individually and in combination with antibiotics, were effective in achieving complete bacterial kill at various time points. This is particularly noteworthy for the combination of α-pinene, δ-carene, and amoxicillin, which showed sustained bactericidal activity. Similar trends have been observed in other studies evaluating the time-kill kinetics of terpenoids and antibiotics (da Silva Rivas et al., 2012).

The FTIR and UV spectroscopy analyses revealed significant changes in the functional groups and absorption spectra of the terpenoid-antibiotic combinations. The observed peak shifts and modifications suggest potential interactions or complex formations between these molecules. These findings are supported by other studies that have used FTIR and UV spectroscopy to investigate the interactions between terpenoids and antibiotics (Huang et al., 2022). The presence of new peaks or disappearance of existing ones in the spectra indicates possible changes in the molecular structures or electronic environments, which could contribute to the observed synergistic effects. Docking studies further elucidated the interaction energies between terpenoids and antibiotics. The strongest interactions were observed between δ-carene and erythromycin, with an interaction energy of -96.10 kcal/mol. This suggests a high binding affinity and potential for enhanced therapeutic efficacy. The results align with other docking studies that have explored similar interactions (Zlotnikov et al., 2023). Several limitations should be considered in interpreting these results. First, while the study provides valuable insights into the antimicrobial potential and interactions of the terpenoids and antibiotics, the *in- vitro* nature of the assays may not fully represent the *in-vivo* conditions. The effects observed in laboratory settings may differ from those in a physiological context due to factors such as metabolism and bioavailability. Study focused on a limited number of terpenoids and antibiotics. The inclusion of additional compounds could provide a more comprehensive understanding of potential synergistic effects and interactions. Study did not explore the mechanisms of action of the terpenoids and antibiotics in detail. Additional research, such as assessing bacterial cell wall integrity and intracellular targets, would provide deeper insights into how these compounds exert their antimicrobial effects. FTIR and UV spectroscopy analyses suggest possible interactions, further structural characterization and validation using techniques like NMR and X-ray crystallography could provide more definitive evidence of complex formation and interaction mechanisms.

5 Conclusion

The study demonstrates the significant antimicrobial potential of *C. oppositifolia* terpenoids and their synergistic effects with antibiotics. The results highlight the potential for developing novel combination therapies to enhance antimicrobial efficacy. However, further research is needed to validate these findings *in vivo*, explore additional terpenoid and antibiotic combinations, and elucidate the detailed mechanisms of action.

Data availability statement

The original contributions presented in the study are included in the article/Supplementary Material. Further inquiries can be directed to the corresponding authors.

Author contributions

KZ: Formal analysis, Methodology, Resources, Writing – original draft, Writing – review & editing. YJ: Conceptualization, Investigation, Writing – original draft, Writing – review & editing. KD: Conceptualization, Writing – original draft, Writing – review & editing. XH: Investigation, Methodology, Writing – original draft, Writing – review & editing. VS: Conceptualization, Investigation, Methodology, Project administration, Visualization, Writing – original draft, Writing – review & editing. XP: Investigation, Methodology, Writing – original draft, Writing – review & editing.

Funding

The author(s) declare that no financial support was received for the research, authorship, and/or publication of this article.

Conflict of interest

The authors declare that the research was conducted in the absence of any commercial or financial relationships that could be construed as a potential conflict of interest.

Publisher's note

Supplementary material

The Supplementary Material for this article can be found online at: https://www.frontiersin.org/articles/10.3389/fcimb.2024.1481656/full#supplementary-material

References

Abbas, A., Anwar, F., Alqahtani, S. M., Ahmad, N., Al-Mijalli, S. H., Shahid, M., et al. (2022). Hydro-distilled and supercritical fluid extraction of eucalyptus camaldulensis essential oil: characterization of bioactives along with antioxidant, antimicrobial and antibiofilm activities. *Dose Response* 20, 15593258221125477. doi: 10.1177/15593258221125477

Ali, T., Habib, A., Nazir, Z., Ali, M., and Haque, M. A. (2024). Healthcare challenges in LMICs: addressing antibiotic resistance threats, a call for comprehensive global solutions: an editorial. *Int. J. Surg.* 110, 3085–3087. doi: 10.1097/JS9.0000000000001165

Antimicrobial Resistance Collaborators. (2022). Global burden of bacterial antimicrobial resistance in 2019: a systematic analysis. *Lancet* 399, 629–655. doi: 10.1016/S0140-6736(21)02724-0

M26-A Methods for Determining Bactericidal Activi.pdf. (2024) Available online at: https://clsi.org/media/1462/m26a_sample.pdf (Accessed August 14, 2024).

Baker, R. E., Mahmud, A. S., Miller, I. F., Rajeev, M., Rasambainarivo, F., Rice, B. L., et al. (2022). Infectious disease in an era of global change. *Nat. Rev. Microbiol.* 20, 193–205. doi: 10.1038/s41579-021-00639-z

Basholli-Salihu, M., Schuster, R., Hajdari, A., Mulla, D., Viernstein, H., Mustafa, B., et al. (2017). Phytochemical composition, anti-inflammatory activity and cytotoxic effects of essential oils from three Pinus spp. *Pharm. Biol.* 55 (1), 1553–1560 doi: 10.1080/13880209.2017.1309555

Chaachouay, N., and Zidane, L. (2024). Plant-derived natural products: A source for drug discovery and development. *Drugs Drug Candidates* 3, 184–207. doi: 10.3390/ddc3010011

Clinical & Laboratory Standards Institute. (1999). *CLSI Guidelines*. Available online at: https://clsi.org/ (Accessed March 28, 2024).

Cowan, M. M. (1999). Plant products as antimicrobial agents. *Clin. Microbiol. Rev.* 12, 564–582. doi: 10.1128/CMR.12.4.564

da Silva Rivas, A. C., Lopes, P. M., de Azevedo Barros, M. M., Costa MaChado, D. C., Alviano, C. S., and Alviano, D. S. (2012). Biological activities of α-pinene and β-pinene enantiomers. *Molecules* 17, 6305–6316. doi: 10.3390/molecules17066305

de Kraker, M. E. A., Stewardson, A. J., and Harbarth, S. (2016). Will 10 million people die a year due to antimicrobial resistance by 2050? *PloS Med.* 13, e1002184. doi: 10.1371/journal.pmed.1002184

de Sousa, D. P., Damasceno, R. O. S., Amorati, R., Elshabrawy, H. A., de Castro, R. D., Bezerra, D. P., et al. (2023). Essential oils: chemistry and pharmacological activities. *Biomolecules* 13, 1144. doi: 10.3390/biom13071144

Dhifi, W., Bellili, S., Jazi, S., Bahloul, N., and Mnif, W. (2016). Essential oils' Chemical characterization and investigation of some biological activities: A critical review. *Medicines* 3, 25. doi: 10.3390/medicines3040025

Gersbach, P. V. (2002). The essential oil secretory structures of prostanthera ovalifolia (Lamiaceae). *Ann. Bot.* 89, 255–260. doi: 10.1093/aob/mcf033

Guimarães, A. C., Meireles, L. M., Lemos, M. F., Guimarães, M. C. C., Endringer, D. C., Fronza, M., et al. (2019). Antibacterial activity of terpenes and terpenoids present in essential oils. *Molecules* 24, 2471. doi: 10.3390/molecules24132471

Gupta, N., Bhattacharya, S., Urbanová, K., Dutta, A., Hazra, A. K., Fernández-Cusimamani, E., et al. (2023). Systematic analysis of antimicrobial activity, phytochemistry, and in silico molecular interaction of selected essential oils and their formulations from different Indian spices against foodborne bacteria. *Heliyon* 9, e22480. doi: 10.1016/j.heliyon.2023.e22480

Hanuš, L. O., and Hod, Y. (2020). Terpenes/terpenoids in cannabis: are they important? *Med. Cannabis Cannabinoids* 3, 25–60. doi: 10.1159/000509733

Haro-González, J. N., Castillo-Herrera, G. A., Martínez-Velázquez, M., and Espinosa-Andrews, H. (2021). Clove essential oil (Syzygium aromaticum L. Myrtaceae): extraction, chemical composition, food applications, and essential bioactivity for human health. *Molecules* 26, 6387. doi: 10.3390/molecules26216387

Huang, W., Wang, Y., Tian, W., Cui, X., Tu, P., Li, J., et al. (2022). Biosynthesis investigations of terpenoid, alkaloid, and flavonoid antimicrobial agents derived from medicinal plants. *Antibiotics* 11, 1380. doi: 10.3390/antibiotics11101380

Jiang, Z., Kempinski, C., and Chappell, J. (2016). Extraction and analysis of terpenes/terpenoids. *Curr. Protoc. Plant Biol.* 1, 345–358. doi: 10.1002/cppb.20024

Jugreet, S. B., Suroowan, S., Rengasamy, R. R. K., and Mahomoodally, M. F. (2020). Chemistry, bioactivities, mode of action and industrial applications of essential oils. *Trends Food Sci. Technol.* 101, 89–105. doi: 10.1016/j.tifs.2020.04.025

Konwar, A. N., Hazarika, S. N., Bharadwaj, P., and Thakur, D. (2022). Emerging non-traditional approaches to combat antibiotic resistance. *Curr. Microbiol.* 79, 330. doi: 10.1007/s00284-022-03029-7

Kowalska-Krochmal, B., and Dudek-Wicher, R. (2021). The minimum inhibitory concentration of antibiotics: methods, interpretation, clinical relevance. *Pathogens* 10, 165. doi: 10.3390/pathogens10020165

Mahfouz, A. A., Said, H. S., Elfeky, S. M., and Shaaban, M. I. (2023). Inhibition of Erythromycin and Erythromycin-Induced Resistance among Staphylococcus aureus Clinical Isolates. *Antibiotics (Basel)* 12, 503. doi: 10.3390/antibiotics12030503

Mahizan, N. A., Yang, S.-K., Moo, C.-L., Song, A. A.-L., Chong, C.-M., Chong, C.-W., et al. (2019). Terpene derivatives as a potential agent against antimicrobial resistance (AMR) pathogens. *Molecules* 24, 2631. doi: 10.3390/molecules24142631

Masyita, A., Mustika Sari, R., Dwi Astuti, A., Yasir, B., Rahma Rumata, N., Emran, T. B., et al. (2022). Terpenes and terpenoids as main bioactive compounds of essential oils, their roles in human health and potential application as natural food preservatives. *Food Chem. X* 13, 100217. doi: 10.1016/j.fochx.2022.100217

Nasim, N., Sandeep, I. S., and Mohanty, S. (2022). Plant-derived natural products for drug discovery: current approaches and prospects. *Nucleus (Calcutta)* 65, 399–411. doi: 10.1007/s13237-022-00405-3

Proshkina, E., Plyusnin, S., Babak, T., Lashmanova, E., Maganova, F., Koval, L., et al. (2020). Terpenoids as potential geroprotectors. *Antioxidants* 9, 529. doi: 10.3390/antiox9060529

Roman, S., Voaides, C., and Babeanu, N. (2023). Exploring the sustainable exploitation of bioactive compounds in pelargonium sp.: beyond a fragrant plant. *Plants* 12, 4123. doi: 10.3390/plants12244123

Salam, M., Al-Amin, M., Salam, M. T., Pawar, J. S., Akhter, N., Rabaan, A. A., et al. (2023). Antimicrobial resistance: A growing serious threat for global public health. *Healthcare (Basel)* 11, 1946. doi: 10.3390/healthcare11131946

Salvi, P., Kumar, G., Gandass, N., Kajal,, Verma, A., Rajarammohan, S., et al. (2022). Antimicrobial potential of essential oils from aromatic plant ocimum sp.; A comparative biochemical profiling and in-silico analysis. *Agronomy* 12, 627. doi: 10.3390/agronomy12030627

Shang, Z., Sharma, V., Kumar, T., Dev, K., and Patil, S. (2024). Phytochemical characterization and synergistic antibacterial effects of colebrookea oppositifolia essential oil as adjuvants to modern antibiotics in combating drug resistance. *DDDT* 18, 4601–4614. doi: 10.2147/DDDT.S489517

Sharma, N., Khajuria, V., Gupta, S., Kumar, C., Sharma, A., Lone, N. A., et al. (2021). Dereplication based strategy for rapid identification and isolation of a novel anti-inflammatory flavonoid by LCMS/MS from colebrookea oppositifolia. *ACS Omega* 6, 30241–30259. doi: 10.1021/acsomega.1c01837

Sharma, G., and Mishra, T. (2019). Phytochemical analysis, high-performance liquid chromatography, and ex vivo antioxidant potential of A herbal fruit extract. *Asian J. Pharm. Clin. Res.*, 256–260. doi: 10.22159/ajpcr.2019.v12i2.29760

Swamy, M. K., Akhtar, M. S., and Sinniah, U. R. (2016). Antimicrobial properties of plant essential oils against human pathogens and their mode of action: an updated review. *Evid Based Complement Alternat Med.* 2016, 3012462. doi: 10.1155/2016/3012462

Valdivieso-Ugarte, M., Gomez-Llorente, C., Plaza-Díaz, J., and Gil, Á. (2019). Antimicrobial, antioxidant, and immunomodulatory properties of essential oils: A systematic review. *Nutrients* 11, 2786. doi: 10.3390/nu11112786

Zlotnikov, I. D., Davydova, M. P., Danilov, M. R., Krylov, S. S., Belogurova, N. G., and Kudryashova, E. V. (2023). Covalent conjugates of allylbenzenes and terpenoids as antibiotics enhancers with the function of prolonged action. *Pharmaceuticals* 16, 1102. doi: 10.3390/ph16081102

frontiers | Frontiers in Cellular and Infection Microbiology

TYPE Original Research
PUBLISHED 06 January 2025
DOI 10.3389/fcimb.2024.1500440

OPEN ACCESS

EDITED BY
Biswajit Mishra,
Brown University, United States

REVIEWED BY
Poonam Mudgil,
Charles Sturt University, Australia
Pramodkumar Pyarelal Gupta,
Padmashree Dr. D.Y. Patil University, India

*CORRESPONDENCE
Sandip Patil
sandippatil1309@yahoo.com

†These authors have contributed equally to this work

RECEIVED 23 September 2024
ACCEPTED 10 December 2024
PUBLISHED 06 January 2025

CITATION
Shang Z, Sharma V, Pai L, Kumar T and Patil S (2025) Optimizing the production and efficacy of antimicrobial bioactive compounds from *Streptomyces kanamyceticus* in combating multi-drug-resistant pathogens.
Front. Cell. Infect. Microbiol. 14:1500440.
doi: 10.3389/fcimb.2024.1500440

Optimizing the production and efficacy of antimicrobial bioactive compounds from *Streptomyces kanamyceticus* in combating multi-drug-resistant pathogens

Zifang Shang[1†], Vipasha Sharma[2†], Liu Pai[3], Tarun Kumar[4] and Sandip Patil[4,5*]

[1]Guangdong Engineering Technological Research Centre of Clinical Molecular Diagnosis and Antibody Drugs, Meizhou Academy of Medical Sciences, Meizhou People's Hospital (Huangtang Hospital), Meizhou, China, [2]Department of Biotechnology, University Institute of Biotechnology, Chandigarh University, Mohali, Punjab, India, [3]Department of Haematology and Oncology, Shenzhen Children's Hospital, Shenzhen, China, [4]Mkelly Biotech Pvt Ltd., Mohali, Punjab, India, [5]Paediatric Research Institute, Shenzhen Children's Hospital, Shenzhen, China

Background: The rise of antibiotic-resistant pathogens has intensified the search for novel antimicrobial agents. This study aimed to isolate *Streptomyces kanamyceticus* from local soil samples and evaluate its antimicrobial properties, along with optimizing the production of bioactive compounds.

Methods: Soil samples were collected from local regions, processed, and analysed for Streptomyces strains isolation using morphological characteristics and molecular identification through 16S rRNA gene PCR assay. Antimicrobial activity was assessed against *Escherichia coli*, *Staphylococcus aureus*, *Bacillus subtilis*, and *Candida albicans* using the double-layer method, while Minimum Inhibitory Concentration (MIC) values were determined. The extracted compounds underwent Fourier Transform Infrared Spectroscopy (FTIR) analysis for functional group identification. Optimization of bioactive compound production was performed using a Central Composite Design (CCD) coupled with Partial Least Squares Regression (PLSR).

Results: A total of 25 distinct *Streptomyces* strains were isolated, with seven confirmed as *S. kanamyceticus*. These strains exhibited antimicrobial activity, with inhibition zones reaching 30 mm and MIC values between 20 and 70 µg/mL. The extraction yielded 150-200 mL of bioactive compounds. Optimization studies revealed that a medium containing 10 g/L glucose and 10 g/L glycine max meal maximized antibiotic production.

Conclusion: This study confirmed that *S. kanamyceticus* is a promising source of novel antibiotics. The combination of microbial isolation, antimicrobial testing, and statistical optimization successfully enhanced the production of bioactive compounds, contributing to the search for effective antimicrobial agents against resistant pathogens.

KEYWORDS

***Streptomyces kanamyceticus*, antimicrobial activity, bioactive compounds, optimization, antibiotic resistance**

1 Introduction

The global rise of multidrug-resistant (MDR) pathogens represents a critical public health challenge, with serious implications for healthcare systems worldwide (Kumar et al., 2024). MDR infections have become a major cause of morbidity and mortality, with nearly 700,000 deaths annually, a figure projected to rise to 10 million by 2050 if current trends persist (Tang et al., 2023). This crisis is exacerbated by the indiscriminate use of antibiotics, particularly broad-spectrum antibiotics like cephalosporins, fluoroquinolones, and carbapenems, which have accelerated the emergence of resistant strains (Aslam et al., 2018). About 50% of antibiotics prescribed are either inappropriate or unnecessary, contributing to the rapid development of resistance (Ventola, 2015). The limitations of currently available antibiotics, including penicillin derivatives, tetracyclines, and macrolides, further compound the problem as many first-line treatments are losing efficacy against resistant organisms such as *Escherichia coli*, *Klebsiella pneumoniae*, and *Staphylococcus aureus* (Saxena et al., 2023). This pressing issue highlights the urgent need for novel antimicrobial agents capable of effectively combating MDR pathogens. Despite decades of research, the discovery of new antibiotics has been remarkably slow, with only a handful—such as daptomycin and ceftaroline—introduced in the last 40 years (D'Andrea et al., 2019; Uddin et al., 2021). This stagnation is largely due to the high costs and extended timelines associated with antibiotic development, paired with the limited financial returns from drugs that are typically used only for short durations (Bergkessel et al., 2023). The pharmaceutical industry has largely shifted its focus away from antibiotic development due to the lower profitability of antimicrobial agents. This has resulted in a limited pipeline of novel drugs (Powers, 2004). Furthermore, most recent efforts have yielded only minor improvements on existing therapies, rather than producing innovative breakthrough solutions. The scarcity of new antibiotics has led to an increased reliance on last-resort drugs like colistin and vancomycin (Mondal et al., 2024). Alarmingly, resistance to these vital drugs is also emerging, underscoring the need to explore alternative sources of antimicrobial compounds. Natural products, particularly phytochemicals such as flavonoids, alkaloids, and terpenes, have long been recognized as rich sources of bioactive compounds with therapeutic potential (Riaz et al., 2023). Notably, over 70% of all antibiotics in clinical use, including penicillin and vancomycin, were derived from natural sources. In recent years, research efforts have turned toward underexplored reservoirs such as plant-based compounds and microbial metabolites. Numerous studies have shown the efficacy of phytochemicals like curcumin and berberine in inhibiting bacterial growth, often with lower risks of resistance development compared to synthetic antibiotics (Martens and Demain, 2017). However, despite the promising potential of these natural compounds, large-scale, in-depth research remains limited. Most studies are still in their preliminary stages, and there is a pressing need for more comprehensive investigations on a global scale (Barba-Ostria et al., 2022). One particularly promising source of bioactive compounds is *Streptomyces*, a genus of soil-dwelling bacteria renowned for its ability to produce a wide range of antibiotics, including tetracycline, chloramphenicol, and erythromycin, along with other secondary metabolites like antitumor agents and immunosuppressants (Khan et al., 2023). *Streptomyces* has played a pivotal role in antibiotic discovery, most notably as the source of streptomycin, the first effective treatment for tuberculosis (Quinn et al., 2020). The genus is recognized for producing diverse bioactive compounds with antimicrobial, antifungal, and antitumor properties. Continued exploration of *Streptomyces* species remains essential for the identification of new bioactive compounds (Mazumdar et al., 2023). In this study, we focus on optimizing the production and efficacy of bioactive compounds from *S. kanamyceticus* in combating MDR pathogens. Our objective is to enhance the yield and potency of these compounds using Central Composite Design (CCD) and Partial Least Squares Regression (PLSR) analysis. By doing so, we aim to uncover the potential of *S. kanamyceticus* as a source of novel antimicrobial agents, contributing to the global fight against MDR infections.

2 Methods

2.1 Chemicals

All chemicals, media components, and standard antibiotics utilized in this study were sourced from Hi-Media Pvt. Ltd. and

Sigma-Aldrich Corporation (India). The solvents used throughout the experiments were of analytical or HPLC grade, obtained from SD Fine Chem Limited (India).

2.2 Isolation and characterization of *Streptomyces* species

A total of 10 soil samples were systematically collected from the loacal region in February 2023, specifically at Latitude 30.7333° N and Longitude 76.7794° E. Sampling sites were randomly selected from various distances within the area. To ensure diversity in *Streptomyces* species, soil was collected from five distinct points within a 400 m^2 zone for each habitat. At each point, the top 6 cm of soil was removed using a sterile spatula. Subsequently, 100 to 120 grams of soil from the underlying layer were collected, placed in stomacher sachets, mixed, and homogenized to produce a heterogeneous sample (Mazumdar et al. 2023). All soil samples were collected in sterile containers and stored immediately at 4°C until further processing. To initiate the isolation process, soil samples (1gram) were suspended in sterile saline (9ml), and serial dilutions were spread onto starch-nitrate agar medium, which was supplemented with 50 µg/ml of cycloheximide and 30 µl/ml of nalidixic acid. The agar plates were incubated at 37°C for 5 days. Potentially valuable isolates were identified by selecting grey colonies that secreted pigments. These selected colonies were then streaked onto starch casein nitrate (SCN) agar containing 25 µg/ml cycloheximide and 50 µg/ml rifampicin, with further incubation at 37° C for another 5 days. After incubation, the isolates were characterized based on the International *Streptomyces* Project (ISP) criteria, which included an evaluation of mycelium shape, colour, substrate mycelium, melanin production, and soluble pigment production. Stock cultures of the 20 selected isolates were preserved as spore and mycelial suspensions in 20% glycerol at -20°C for future reference. To confirm the species, morphological assessments were conducted on the 20 isolates. Species confirmation involved performing a PCR assay targeting the 16S rRNA gene using forward primer (5'-AGAGTTTGATCMTGGCTCAG-3') and reverse primer (5'-TACGGYTACCTTGTTACGACTT-3') (Chen et al., 2015). The amplified products were visualized through electrophoresis on a 1.8% agarose gel stained with 0.5 µg/ml ethidium bromide. DNA sequencing of the PCR products was carried out by a commercial service provider (Genentech). The resulting sequences were analyzed using the Basic Local Alignment Search Tool (BLAST) on the National Center for Biotechnology Information (NCBI) platform. These sequences were compared with GenBank database sequences (www.ncbi.nlm.nih.gov), and a phylogenetic tree was constructed to determine evolutionary relationships.

2.3 Primary screening for antimicrobial activity

To identify the optimal medium for antibiotic production, the antimicrobial activity of pure isolates was evaluated using the double-layer method on various ISP agar media. First, different ISP agar media, including ISP2, ISP3, ISP4, and ISP5, were prepared according to standard protocols (Rajeswari et al., 2014). These media were selected to assess the performance of *Streptomyces* under different nutrient conditions. Streptomyces isolates were then inoculated onto the prepared ISP agar media and incubated for a specified period, typically 7 days, to promote optimal growth and antibiotic production. Subsequently, test organisms, including *Escherichia coli* ATCC 25922 (Gram-negative bacterium), *Staphylococcus aureus* ATCC 25923 (Gram-positive bacterium), *Bacillus subtilis* ATCC 19659 (non-pathogenic Gram-positive bacterium), and *Candida albicans* ATCC 60193 (pathogenic yeast), were used to evaluate antimicrobial activity. The plates were then incubated at 37°C for 24 to 48 hours for bacterial strains and at 25°C for 48 to 72 hours for *Candida albicans*. Following incubation, antimicrobial activity was assessed by measuring the zones of inhibition around the Actinomycetes colonies. The measurement of these zones (mm) provided an indication of the antimicrobial effectiveness of the isolates. Larger zones of inhibition signified greater antimicrobial activity. The results were analysed to determine which ISP media supported the highest levels of antimicrobial activity. This comparison facilitated the selection of the most effective medium for optimizing antibiotic production.

2.4 Extraction method for bioactive compounds from *Streptomyces* spp.

To extract bioactive compounds from *Streptomyces* spp., the culture broth was filtered through sterile cheesecloth to remove mycelial debris The filtrate, typically 100 mL, was transferred to a separatory funnel. To this, an equal volume of diethyl ether (Et2O) was added. The mixture was shaken vigorously for 10 minutes to ensure thorough mixing. Afterwards, the mixture was allowed to settle, and the organic layer, which contained the extracted compounds, was carefully separated and collected. Concurrently, the mycelial mass was homogenized with diethyl ether in a mortar and pestle, using approximately 100 mL of solvent for the homogenization. The resulting homogenate was filtered through a fine mesh to obtain the liquid extract. This liquid was then combined with the organic layer from the culture broth extraction. The combined diethyl ether extracts were concentrated using a rotary evaporator at 40°C to remove the solvent (Ibnouf et al., 2022). The concentrated extract was transferred to a clean glass vial and stored at -20°C until further analysis.

2.5 Determination of minimum inhibitory concentration

To determine the MIC of the bioactive compounds extracted from *Streptomyces* spp., the Kirby-Bauer disc diffusion method was utilized. Mueller-Hinton agar plates were prepared for bacterial assays, while Sabouraud Dextrose agar plates were used for fungal assays. The test microorganisms—*Escherichia coli*, *Staphylococcus*

aureus, and *Candida albicans*—were cultured to an appropriate turbidity, specifically a 0.5 McFarland standard, which corresponds to approximately 1.5×10^8 CFU/mL. This turbidity standard ensures consistent inoculum density across different assays. The cultures were then evenly spread onto the surface of the agar plates using a sterile spreader to achieve a uniform lawn of growth. Sterile filter paper discs were impregnated with various concentrations of the concentrated extract. Typically, concentrations ranged from 10 µg, 20 µg, 40µg to 100 µg per disc, though specific concentrations may vary depending on the extract's potency and experimental design. The discs were placed on the inoculated agar plates with sufficient spacing to prevent overlapping inhibition zones. The plates were incubated at 37°C for 24 hours for bacterial strains and at 25°C for 48 to 72 hours for *Candida albicans*. After incubation, the zones of inhibition around the discs were measured in mm (Sharma et al., 2016). The MIC was determined by identifying the lowest concentration of the extract which resulted in a clear zone of inhibition around the disc, indicating effective suppression of microbial growth. This approach provided a quantitative measure of the antimicrobial activity of the extracts against the selected pathogens.

2.6 FTIR analysis of diethyl ether extracts from *Streptomyces* SK-2023-2 and SK-2023-4

The diethyl ether extracts of Streptomyces strains SK-2023-2 and SK-2023-4 were analyzed using Fourier Transform Infrared Spectroscopy (FTIR) to identify functional groups and characterize the chemical composition of the bioactive compounds (Chakraborty et al., 2023). 1 mg of each extract was placed on a clean KBr pellet and thoroughly mixed with about 100 mg of dry KBr powder to form a homogeneous mixture. This mixture was then compressed into a transparent pellet using a hydraulic press at a pressure of 10,000 psi for approximately 5 minutes, ensuring that the pellet was uniform and free from air bubbles. FTIR spectra were recorded using an FTIR spectrometer (ReactIR702L) over the range of 4000 cm^{-1} to 400 cm^{-1}. Each spectrum was acquired at a resolution of 4 cm^{-1}, with 32 scans averaged to enhance the signal-to-noise ratio. The obtained spectra were analyzed to identify characteristic absorption bands corresponding to the functional groups present in the extracts. Peaks were assigned based on comparisons with standard reference spectra and literature values. The spectral data were interpreted to determine the functional groups and possible chemical structures of the bioactive compounds present in the extracts from SK-2023-2 and SK-2023-4.

TABLE 1 Experimental setup for central composite design (CCD) to optimize media components.

Factor	Level -α	Level -1	Level 0	Level +1	Level +α
Glucose (g/L)	5	10	15	20	25
Glycine max (g/L)	5	10	15	20	25
$CaCO_3$ (g/L)	0.5	1	1.5	2	2.5

2.7 Statistical optimization of antimicrobial properties

To identify the optimal concentration and interactions of key media components—glucose, glycine max, and $CaCO_3$—a systematic investigation was performed using a Central Composite Design (CCD) (Ju et al., 2017). The experimental setup is detailed in Table 1, where each factor was evaluated at five different levels: -α, -1, 0, + 1, and +α. Design Expert Software version 13 was utilized to generate a series of 20 experiments, each conducted in triplicate. The average zone of inhibition (mm) was measured as the dependent variable or response. All experiments were prepared and incubated at 28°C and 100 rpm for 5 days.

2.7.1 Statistical analysis and modelling

The data obtained from the CCD experiments were subjected to rigorous analysis of variance (ANOVA). A first-order polynomial equation was fitted through multiple regression analysis to develop an empirical model that quantifies the relationship between the measured response and the independent variables. The empirical model is expressed by the following equation:

$$Y = B0 + B1X_1 + B2X_2 + B3X_3 + B4X1X_2 + B5X1X_3 + B6X_2X_3 + B7X_1^2 + B8X_2^2 + B9X_3^2$$

Where Y represents the predicted response, and B_0 through B_9 are the regression coefficients for the respective variables and interaction terms. The independent variables X_1, X_2, and X_3 correspond to glucose, glycine max, and $CaCO_3$, respectively. The response was further analysed through three-dimensional plots to visualize the effects and interactions of the variables.

2.7.2 Multivariate analysis

A combination of multiple linear regression (MLR) and the white box approach of data modelling was employed, utilizing Partial Least Squares Regression (PLSR) (Kreeger, 2013). This methodology, as discussed in the literature previously aimed to thoroughly understand the correlation between the independent variables (glucose, glycine max, and $CaCO_3$) and the zone of inhibition (dependent variable). PLSR is particularly useful in the presence of multicollinearity among predictor variables, allowing the development of both explanatory and predictive models. Additionally, to ensure the robustness of the developed model, a model assessment technique known as leave-one-out cross-validation was applied. This iterative procedure involves creating a regression model for each sample while excluding it as a test case, and then assessing the prediction outcomes. Through these statistical approaches, the complex relationships between the experimental variables and the antifungal properties were extensively explored.

3 Results

3.1 Identification and characterization of *Streptomyces* spp.

The soil analysis from the site indicated it to be alkaline with a pH of 7.9 and low salinity (EC = 0.15 ds/m). Based on the texture diagram, the soil was classified as sandy loam, characterized by a low clay content (20%), adequate total nitrogen (0.17%), and a moderate level of organic matter (2.98%). The analysis also revealed the presence of exchangeable cations, including potassium (K), magnesium (Mg), aluminium (Al), calcium (Ca), and silicon (Si). Among the mineral elements, oxygen (O), iron (Fe), and silicon (Si) were the most abundant, followed by aluminium, calcium, potassium, and magnesium (Supplementary Table S1). From the soil samples collected across the five locations, 25 morphologically distinct presumptive *Streptomyces* strains were successfully isolated. Out of the 25 isolated strains, 7 were identified as *S. kanamyceticus* based on 16S rRNA sequencing, and their phylogenetic relationships were confirmed through a constructed phylogenetic tree (Figure 1). These 7 isolates were selected for further study and were designated as SK-2023-1 through SK-2023-7.

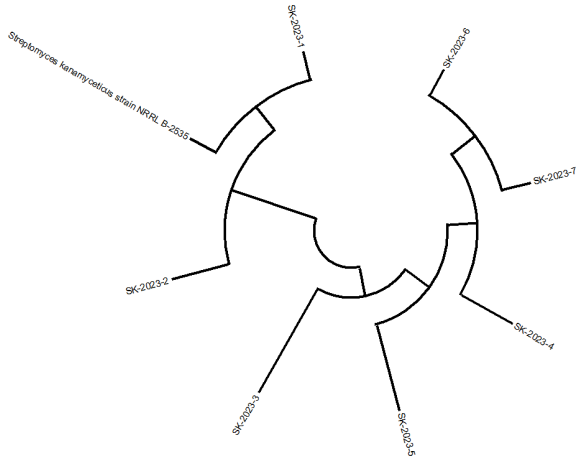

FIGURE 1
Phylogenetic tree of isolated *Streptomyces* spp. based on 16S rRNA sequencing.

3.2 Screening of active *S. kanamyceticus* isolates

The primary screening of the *S. kanamyceticus* isolates against *Escherichia coli* ATCC 25922, *Staphylococcus aureus* ATCC 25923, *Bacillus subtilis* ATCC 19659, and *Candida albicans* ATCC 60193 revealed varied levels of antimicrobial activity (Figure 2). Isolate SK-2023-1 demonstrated inhibition zones of 20 mm, 22 mm, 25 mm, and 25 mm, respectively, against these microorganisms. SK-2023-2 exhibited the highest inhibition for all tested organisms, with 24 mm against *E. coli*, 30 mm against *S. aureus*, 29 mm against *B. subtilis*, and 30 mm against *C. albicans*. Conversely, SK-2023-3 showed the lowest activity, with inhibition zones of 16 mm, 15 mm, 14 mm, and 18 mm, respectively. SK-2023-4 produced strong inhibition, particularly against *C. albicans* (31 mm) and *S. aureus* (28 mm). The antimicrobial activity of SK-2023-5 was moderate, ranging from 15 mm to 20 mm across all pathogens. SK-2023-6 and SK-2023-7 displayed similar levels of activity, with SK-2023-6 showing higher inhibition against *E. coli* (29 mm), while both exhibited strong inhibition against *C. albicans* (27 mm and 31 mm, respectively). These results indicate significant variability in the antimicrobial efficacy of the different *S. kanamyceticus* isolates.

3.3 Extraction and minimum inhibitory concentration

The extraction of bioactive compounds from *Streptomyces* spp. was successfully achieved, yielding approximately 150-200 mL of

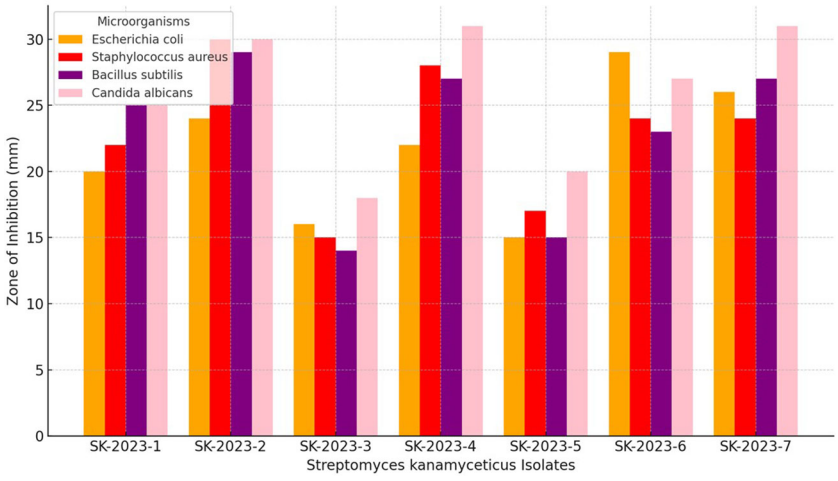

FIGURE 2
Antimicrobial activity profiles of *S. kanamyceticus* isolates against pathogens.

TABLE 2 Minimum inhibitory concentration and zone of inhibition of bioactive compounds against selected pathogens.

Pathogen	Minimum Inhibitory Concentration (µg/ml) and Zone of Inhibition (mm)													
	SK-2023-1		SK-2023-2		SK-2023-3		SK-2023-4		SK-2023-5		SK-2023-6		SK-2023-7	
	(µg/ml)	(mm)	(µg/ml)	(mm)	(µg/ml)	(mm)	(µg/ml)	(mm)	(µg/ml)	(mm)	(µg/ml)	(mm)	(µg/ml)	(mm)
Escherichia coli ATCC25922	40	**	30	**	60	***	50	***	70	**	20	****	25	**
Staphylococcus aureus ATCC 25923	35	***	40	***	70	**	30	****	50	***	60	***	25	**
Bacillus subtilis ATCC 19659	25	**	20	**	50	***	40	***	60	***	30	**	35	**
Candida albicans ATCC 60193	30	**	25	**	65	**	45	***	55	***	20	****	30	****

Note: Indicate zone of inhibition, * =5 mm; ** = 10–19 mm; *** = 20–24 mm; **** = 25 mm. noting that the well diameter was 5 mm.

concentrated extracts suitable for further analysis. The concentrated extracts exhibited distinct colours and viscosities, indicating the presence of various metabolites. Subsequent antibacterial and antifungal activity assays revealed significant antimicrobial potential of the bioactive compounds. The MIC (MIC) and the corresponding Zone of Inhibition were recorded (Table 2). *Escherichia coli* ATCC25922 exhibited a MIC ranging from 20 µg/ml to 70 µg/ml, with zone inhibition measurements varying from non-detectable to substantial inhibition (29 mm). Similarly, *Staphylococcus aureus* ATCC25923 demonstrated MIC values between 25 µg/ml and 70 µg/ml, with zones of inhibition reaching up to 25 mm. *Bacillus subtilis* ATCC 19659 showed an MIC range of 20 µg/ml to 60 µg/ml, while its zone of inhibition varied significantly, reaching a maximum of 23 mm. For the fungal pathogen *Candida albicans* ATCC 60193, the MIC ranged from 20 µg/ml to 65 µg/ml, with inhibition zones also showing substantial variability, peaking at 31 mm. These findings indicated that the bioactive compounds possessed significant antimicrobial activity against both bacterial and fungal pathogens.

3.4 FTIR analysis

The FTIR analysis of the diethyl ether extracts from *Streptomyces* SK-2023-2 and SK-2023-4 revealed distinct spectral profiles, highlighting the presence of various functional groups (Figure 3). The FTIR spectrum of SK-2023-2 displayed characteristic absorption bands at specific wavenumbers (Figure 3A). A prominent peak at 3350 cm^{-1} corresponded to O-H stretching vibrations, indicating the presence of hydroxyl groups. Additionally, peaks at 2920 cm^{-1} and 2850 cm^{-1} indicated C-H stretching of aliphatic compounds, while the absorption band at 1740 cm^{-1} suggested the presence of carbonyl (C=O) groups. Furthermore, peaks at 1600 cm^{-1} and 1450 cm^{-1} were attributed to C=C stretching vibrations, suggesting possible aromatic structures. FTIR spectrum of SK-2023-4 (Figure 3B) exhibited similar absorption features. The presence of O-H stretching was confirmed by a broad peak around 3400 cm^{-1}, while C-H stretching vibrations appeared at 2925 cm^{-1} and 2855 cm^{-1}. The carbonyl group was indicated by a peak at 1715 cm^{-1}. Moreover, peaks at 1610 cm^{-1} and 1490 cm^{-1} were associated with aromatic compounds. The FTIR analysis confirmed the presence of functional groups indicative of diverse bioactive compounds in both extracts, suggesting their potential for further investigation into antimicrobial activities.

3.5 Statistical optimization and modelling

The optimization of antibiotic production was performed using a central composite design (CCD), which included three independent variables: X_1 = glucose, X_2 = glycine max, and X_3 = $CaCO_3$. This design comprised three experimental runs that examined the influence of these factors on the antibiotic yield (Table 3). The highest antibiotic production was achieved in a medium containing (g/L): glucose 10, glycine max 10, and $CaCO_3$ 1, resulting in a zone of inhibition of 30 mm. The statistical model analysed through ANOVA, confirmed the significance of the optimization process with an F-value of 3.18 and a p-value of 0.0427 (Table 4). Three-dimensional response surface plots were generated to illustrate the interaction effects of glucose, glycine max, and $CaCO_3$ concentrations on the zone of inhibition. The results showed that varying two factors at a time, while maintaining the third at the midpoint, significantly impacted antifungal activity against *Candida albicans* (Figures 4A–C). These insights underscored the critical roles of glucose and glycine max concentrations in maximizing the antibiotic yield produced by *Streptomyces* SK-2023-2. The regression equation modelling the zone of inhibition (Y) based on the glucose (X_1), glycine max (X_2), and $CaCO_3$ (X_3) concentrations was as follows:

$$[Y = 26.13 + 3.08X_1 + 2.60X_2 + 0.89X_3 + 2.50X_1X_2 - 0.75X_1X_3 - 5.15X_1^2 - 4.80X_2^2 - 2.33X_3^2]$$

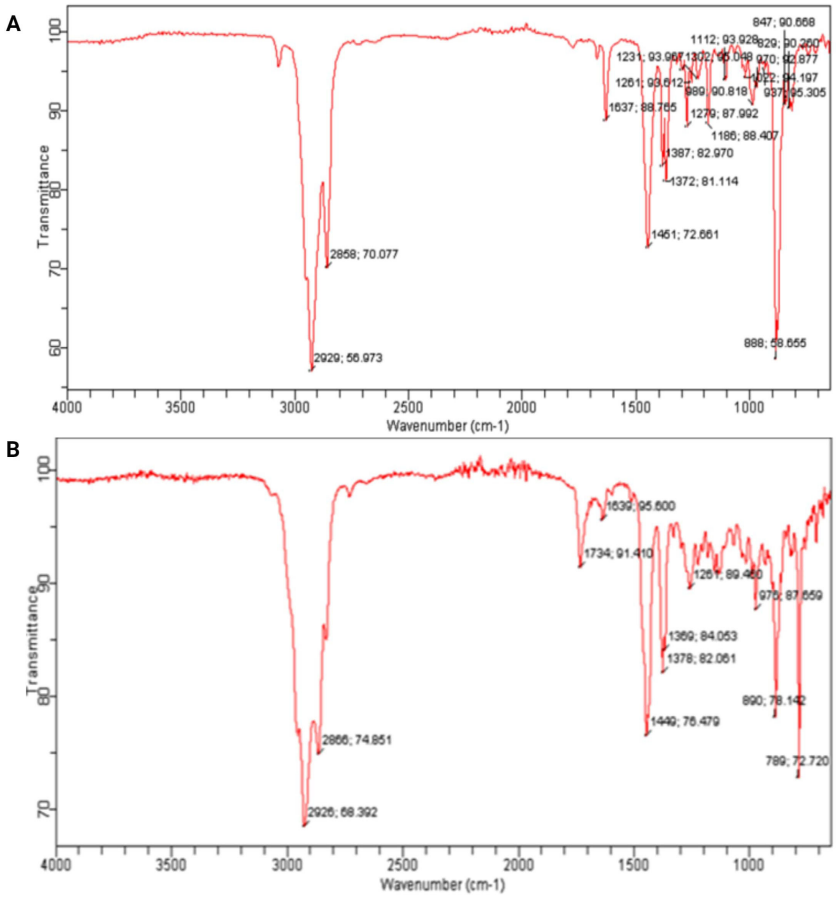

FIGURE 3
FTIR analysis of the diethyl ether extracts from *Streptomyces* SK-2023-2 and SK-2023-4. **(A)** FTIR Spectrum of Diethyl Ether Extract from Streptomyces SK-2023-2; **(B)** FTIR Spectrum of Diethyl Ether Extract from Streptomyces SK-2023-4.

The predictive power of this model highlighted the significant contributions of glucose and glycine max in enhancing antifungal activity, while $CaCO_3$ exerted a moderate effect.

3.6 Multivariate analysis

Partial Least Squares Regression (PLSR) was used to delve deeper into the relationships between the independent variables (glucose, glycine max, and $CaCO_3$) and the zone of inhibition. Variable Importance in Projection (VIP) scores revealed that both glucose and glycine max played critical roles in antimicrobial activity, with VIP scores exceeding 1, indicating high significance (Table 5). In contrast, $CaCO_3$ exhibited a comparatively lower influence on antibiotic production. The correlation circle plot (Figure 5A) illustrated the strong positive correlation between the glucose and glycine max concentrations with the zone of inhibition, while $CaCO_3$ had a more moderate association. Additionally, the VIP plot (Figure 5B) visually confirmed that glycine max exerted the greatest impact, followed by glucose. These findings reinforce the importance of optimizing glucose and glycine max concentrations to maximize antibiotic production. Statistical validation using leave-one-out cross-validation confirmed the robustness of the regression model. The optimization experiments, as summarized in Table 3, showed that the maximum antibiotic production, corresponding to a zone of

TABLE 3 Optimization of antibiotic production using central composite design (CCD).

Run Number	Glucose (g/L)	Glycine Max (g/L)	$CaCO_3$ (g/L)	Zone of Inhibition (mm)
1	10	10	1	30
2	8	12	1.5	28
3	12	8	0.5	27
4	10	10	1	30
5	9	11	1	29
6	11	9	1.2	27.5
7	10	10	1	30
8	7	13	1	26
9	13	7	1	25
10	10	10	1	30

TABLE 4 Analysis of variance (ANOVA) for the optimization model.

Source	Sum of Squares	Degrees of Freedom (df)	Mean Square	F-Value	p-Value
Model	240.15	7	34.31	3.18	0.0427
X_1 (Glucose)	28.44	1	28.44	3.65	0.0619
X_2 (Glycine Max)	22.28	1	22.28	2.86	0.0915
X_3 ($CaCO_3$)	2.52	1	2.52	0.32	0.5776
$X_1 \times X_2$	15.68	1	15.68	2.01	0.1687
$X_1 \times X_3$	3.37	1	3.37	0.43	0.5268
X_1^2	106.45	1	106.45	13.66	0.002
X_2^2	92.16	1	92.16	11.83	0.0033
X_3^2	27.25	1	27.25	3.5	0.0678
Residual	140.89	18	7.83		
Lack of Fit	85.43	11	7.77	0.99	0.5456
Pure Error	55.46	7	7.92		

inhibition of 30 mm, was obtained at 10 g/L glucose, 10 g/L glycine max, and 1 g/L $CaCO_3$. The regression analysis strongly indicated the critical importance of glucose and glycine max in enhancing antibiotic production, as depicted in Figures 2A, B. These results highlight the necessity of fine-tuning these variables to achieve the highest possible antimicrobial efficacy.

4 Discussion

In this study, we characterized the soil environment where *Streptomyces* strains were isolated, noting a pH of 7.9 and a sandy-loam texture conducive to microbial diversity. Our analysis revealed that the soil's nutritional profile, including adequate nitrogen and organic matter, supported the isolation of 25 distinct presumptive *Streptomyces* strains. Using 16S rRNA sequencing, we identified seven strains as *Streptomyces kanamyceticus*. This rigorous identification process underscores the importance of molecular techniques in accurately classifying microbial species, reflecting best practices in microbial ecology (Franco-Duarte et al., 2019). Our findings highlight the potential of these isolates for biotechnological applications, particularly in antibiotic production.

We conducted a primary screening of our *S. kanamyceticus* isolates against several pathogens, revealing significant variability in antimicrobial activity. Notably, isolate SK-2023-2 demonstrated the highest inhibition zones, showcasing its potential for producing bioactive compounds. This observation aligns with previous studies indicating that certain *Streptomyces* species can yield potent antibiotics (Westhoff et al., 2021). Our results suggest that specific isolates may be more effective for therapeutic purposes, emphasizing the need for further investigation into their bioactive metabolites and mechanisms of action, particularly against resistant strains of bacteria. We successfully extracted bioactive compounds from the *Streptomyces* isolates, achieving significant antimicrobial activity as evidenced by MIC values ranging from 20 µg/ml to 70 µg/ml. Our findings, particularly the high activity against *Staphylococcus aureus* and *Candida albicans*, reinforce the notion that *S. kanamyceticus* can produce unique antimicrobial agents.

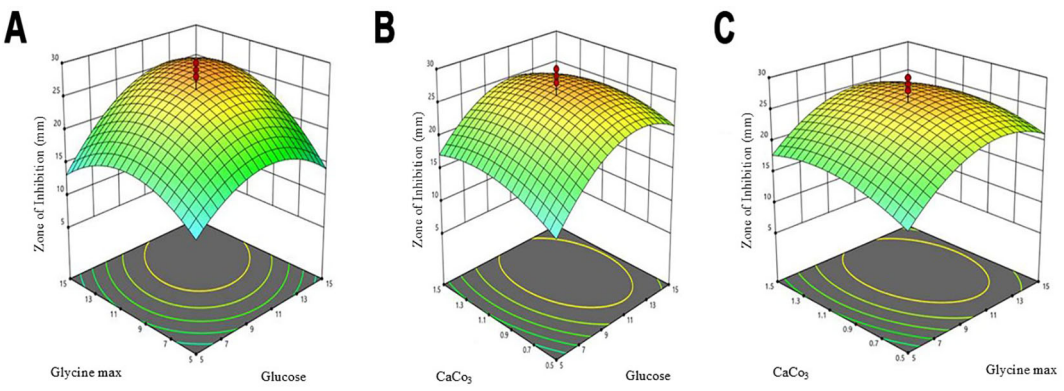

FIGURE 4
Three-dimensional response surface plots for antibiotic production optimization. **(A)** Interactive effects of glucose and soybean meal concentration. **(B)** Interactive effects of soybean meal concentration and $CaCO_3$ concentration. **(C)** Interactive effects of glucose and $CaCO_3$ concentration.

TABLE 5 Regression coefficients and VIP scores for antibiotic production optimization.

Variables	Coefficient Estimate	Standard Error	t-Value	p-Value	VIP Score
Glucose (X_1)	3.08	0.79	3.9	0.0015	1.92
Glycine max (X_2)	2.6	0.75	3.47	0.0028	1.85
$CaCO_3$ (X_3)	0.89	0.64	1.39	0.179	1.05
$X_1 \times X_2$	2.5	0.98	2.55	0.0237	—
$X_1 \times X_3$	-0.75	0.91	-0.82	0.4258	—
X_1^2	-5.15	1.23	-4.19	0.0008	—
X_2^2	-4.8	1.17	-4.1	0.0009	—
X_3^2	-2.33	0.88	-2.65	0.0186	—

This variability in efficacy supports existing literature documenting the diverse bioactive potential of *Streptomyces* extracts (Bhat et al., 2024; Eshboev et al., 2024). The substantial inhibition observed across different pathogens indicates the possibility of developing new therapeutic agents from these isolates, particularly in light of the increasing incidence of antimicrobial resistance.

Our FTIR analysis provided insight into the functional groups present in the extracts from SK-2023-2 and SK-2023-4. The identification of O-H, C-H, and C=O groups suggests a diverse range of bioactive metabolites, including phenolic compounds and terpenoids, which are known for their antimicrobial properties (Wongsa et al., 2022; Rijia et al., 2024). The similarity in spectral profiles between the two isolates indicates shared metabolic pathways for compound production. This finding enhances our understanding of the chemical diversity present in *Streptomyces* extracts and paves the way for further investigations into their antimicrobial mechanisms. We employed a central composite design (CCD) to optimize the production of antimicrobial compounds, demonstrating the significant roles of glucose, glycine max, and $CaCO_3$. The optimization yielded the highest antibiotic production at specific nutrient concentrations, with an F-value of 3.18 and a p-value of 0.0427 indicating the reliability of our findings. This statistical approach not only affirms our methodology but also aligns with other studies utilizing response surface methodology to enhance microbial production (Ju et al., 2017; Hemalatha and Subathra Devi, 2022). Our results underscore the necessity of optimizing nutrient profiles in biotechnological processes, particularly for maximizing the yields of bioactive compounds.

In our multivariate analysis using Partial Least Squares Regression (PLSR), we elucidated the relationships between nutrient concentrations and antimicrobial activity. The high VIP scores for glucose and glycine max reaffirm their critical contributions to antibiotic production. This analysis aligns with existing literature, highlighting the importance of optimizing carbon and nitrogen sources in microbial metabolism (Hattori et al., 2020). The correlation circle plot we generated visually represents these relationships, reinforcing our findings on how nutrient manipulation can significantly impact antimicrobial efficacy. Our statistical validation through leave-one-out cross-validation confirms the robustness of our regression model, emphasizing its potential for guiding future research in optimizing *Streptomyces* metabolites.

The correlation circle plot (Figure 4A) illustrated a strong positive correlation between the concentrations of glucose and glycine max and the zone of inhibition, suggesting that higher levels of these nutrients enhance antimicrobial activity. In contrast, the lower VIP score for $CaCO_3$ indicated that its

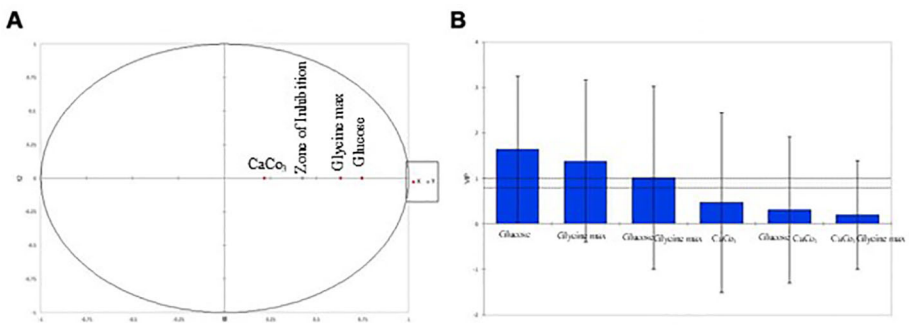

FIGURE 5
Multivariate analysis: variable importance in projection (VIP) and correlation circle plots. **(A)** Correlation plot illustrating the associations between variables and the zone of inhibition. **(B)** Variable Importance in Projection (VIP) plot showing the importance of variables in the PLSR model.

influence on antibiotic production was less pronounced. This is corroborated by the fact that $CaCO_3$ mainly serves to buffer the medium rather than directly influencing the metabolic pathways related to antimicrobial synthesis. The VIP plot (Figure 4B) further substantiated the dominance of glycine max over glucose in driving antimicrobial production. This finding highlights the critical role of nitrogen sources in optimizing the biosynthesis of bioactive metabolites, which aligns with prior research emphasizing the synergistic effect of carbon and nitrogen in microbial secondary metabolism (Sangwan and O'Brian, 1993). Furthermore, the statistical validation using leave-one-out cross-validation confirmed the robustness and predictive power of our regression model, suggesting that it could be a reliable tool for guiding future optimization experiments aimed at enhancing the antimicrobial efficacy of *S. kanamyceticus*. These findings emphasize the necessity of fine-tuning both carbon and nitrogen sources to maximize the production of antimicrobial metabolites, and open new avenues for optimizing fermentation conditions in Streptomyces-based antibiotic production systems.

Our study yielded valuable insights into the antimicrobial potential of *S. kanamyceticus*, and the screening of antimicrobial activity was conducted using a limited range of pathogenic strains. In future studies, expanding this screening to include a broader spectrum of clinically relevant pathogens, particularly multidrug-resistant strains, could provide a more comprehensive understanding of the antibacterial efficacy of our isolates. Future work could incorporate advanced analytical techniques such as NMR or mass spectrometry to elucidate the specific structures of the metabolites. This would deepen our understanding of the mechanisms underlying their antimicrobial activity and facilitate the discovery of novel compounds. Moreover, our optimization experiments primarily focused on a select few nutritional variables. Considering additional factors such as pH, temperature, and incubation time in future optimization studies could further enhance the yield and activity of bioactive compounds. This holistic approach may lead to more efficient production strategies.

5 Conclusion

Our study provides a comprehensive analysis of *S. kanamyceticus* isolates, detailing their identification, antimicrobial activity, and the optimization of nutrient conditions for enhanced bioactive compound production. The findings contribute to the understanding of *Streptomyces* species as a valuable source for novel antibiotics, offering a foundation for future research aimed at combating antimicrobial resistance. The methodologies employed and insights gained from this work underscore the potential of these microbial strains in biotechnological applications.

Data availability statement

The data presented in the study are deposited in the NCBI GenBank repository, accession numbers PQ787840-PQ787841.

Ethics statement

The authors declare that this study was conducted in accordance with ethical principles and in compliance with all relevant guidelines and regulations. All necessary approvals were obtained before the initiation of the research.

Author contributions

ZS: Conceptualization, Data curation, Formal analysis, Funding acquisition, Investigation, Methodology, Resources, Software, Validation, Visualization, Writing – original draft, Writing – review & editing. VS: Conceptualization, Data curation, Formal analysis, Funding acquisition, Investigation, Methodology, Project administration, Resources, Software, Supervision, Validation, Visualization, Writing – original draft, Writing – review & editing. LP: Writing – review & editing. TK: Writing – review & editing. SP: Conceptualization, Data curation, Formal analysis, Funding acquisition, Investigation, Methodology, Project administration, Resources, Software, Supervision, Validation, Visualization, Writing – original draft, Writing – review & editing.

Funding

The author(s) declare financial support was received for the research, authorship, and/or publication of this article. This work was supported by the Scientific Research Cultivation Project of Meizhou People's Hospital (no. PY-C2023042) and the High-level Talent Scientific Research Startup Fund Project of Meizhou People's Hospital (no. KYQD202303).

Conflict of interest

Authors TK and SP were employed by Mkelly Biotech Pvt Ltd.

The authors declare that the research was conducted in the absence of any commercial or financial relationships that could be construed as a potential conflict of interest.

Publisher's note

Supplementary material

The Supplementary Material for this article can be found online at: https://www.frontiersin.org/articles/10.3389/fcimb.2024.1500440/full#supplementary-material

References

Aslam, B., Wang, W., Arshad, M. I., Khurshid, M., Muzammil, S., Rasool, M. H., et al. (2018). Antibiotic resistance: a rundown of a global crisis. *Infect. Drug Resist.* 11, 1645–1658. doi: 10.2147/IDR.S173867

Barba-Ostria, C., Carrera-Pacheco, S. E., Gonzalez-Pastor, R., Heredia-Moya, J., Mayorga-Ramos, A., Rodríguez-Pólit, C., et al. (2022). Evaluation of biological activity of natural compounds: current trends and methods. *Molecules* 27, 4490. doi: 10.3390/molecules27144490

Bergkessel, M., Forte, B., and Gilbert, I. H. (2023). Small-molecule antibiotic drug development: need and challenges. *ACS Infect. Dis.* 9, 2062–2071. doi: 10.1021/acsinfecdis.3c00189

Bhat, A. M., Hussain, A., Hassan, Q. P., and Bhat, A. (2024). Culturable Streptomyces spp. from high-altitude, oligotrophic North Western Himalaya: a comprehensive study on the diversity, bioactivity and insights into the proteome of potential species. *FEMS Microbiol. Ecol.* 100, fiae026. doi: 10.1093/femsec/fiae026

Chakraborty, B., Shashiraj, K. N., Kumar, R. S., Bhat, M. P., Basavarajappa, D. S., Almansour, A. I., et al. (2023). Unveiling the pharmacological significance of marine streptomyces violaceusniger KS20: isolation, characterization, and assessment of its biomedical applications. *Metabolites* 13, 1022. doi: 10.3390/metabo13091022

Chen, Y.-L., Lee, C.-C., Lin, Y.-L., Yin, K.-M., Ho, C.-L., and Liu, T. (2015). Obtaining long 16S rDNA sequences using multiple primers and its application on dioxin-containing samples. *BMC Bioinf.* 16, S13. doi: 10.1186/1471-2105-16-S18-S13

D'Andrea, M. M., Fraziano, M., Thaller, M. C., and Rossolini, G. M. (2019). The urgent need for novel antimicrobial agents and strategies to fight antibiotic resistance. *Antibiot. (Basel).* 8, 254. doi: 10.3390/antibiotics8040254

Eshboev, F., Mamadalieva, N., Nazarov, P. A., Hussain, H., Katanaev, V., Egamberdieva, D., et al. (2024). Antimicrobial action mechanisms of natural compounds isolated from endophytic microorganisms. *Antibiot. (Basel).* 13, 271. doi: 10.3390/antibiotics13030271

Franco-Duarte, R., Černáková, L., Kadam, S., S. Kaushik, K., Salehi, B., Bevilacqua, A., et al. (2019). Advances in chemical and biological methods to identify microorganisms—From past to present. *Microorganisms* 7, 130. doi: 10.3390/microorganisms7050130

Hattori, Y., Naganuma, M., and Otsuka, M. (2020). Partial least squares regression-based robust forward control of the tableting process. *Pharmaceutics* 12, 85. doi: 10.3390/pharmaceutics12010085

Hemalatha, M., and Subathra Devi, C. (2022). A statistical optimization by response surface methodology for the enhanced production of riboflavin from Lactobacillus plantarum–HDS27: A strain isolated from bovine milk. *Front. Microbiol.* 13. doi: 10.3389/fmicb.2022.982260

Ibnouf, E. O., Aldawsari, M. F., and Ali Waggiallah, H. (2022). Isolation and extraction of some compounds that act as antimicrobials from actinomycetes. *Saudi. J. Biol. Sci.* 29, 103352. doi: 10.1016/j.sjbs.2022.103352

Ju, Y., Son, K.-H., Jin, C., Hwang, B. S., Park, D.-J., and Kim, C.-J. (2017). Statistical optimization of culture medium for improved production of antimicrobial compound by Streptomyces rimosus AG-P1441. *Food Sci. Biotechnol.* 27, 581–590. doi: 10.1007/s10068-017-0257-1

Khan, S., Srivastava, S., Karnwal, A., and Malik, T. (2023). Streptomyces as a promising biological control agents for plant pathogens. *Front. Microbiol.* 14. doi: 10.3389/fmicb.2023.1285543

Kreeger, P. K. (2013). Using partial least squares regression to analyze cellular response data. *Sci. Signal* 6, tr7. doi: 10.1126/scisignal.2003849

Kumar, N. R., Balraj, T. A., Kempegowda, S. N., and Prashant, A. (2024). Multidrug-resistant sepsis: A critical healthcare challenge. *Antibiotics* 13, 46. doi: 10.3390/antibiotics13010046

Martens, E., and Demain, A. L. (2017). The antibiotic resistance crisis, with a focus on the United States. *J. Antibiot.* 70, 520–526. doi: 10.1038/ja.2017.30

Mazumdar, R., Dutta, P. P., Saikia, J., Borah, J. C., and Thakur, D. (2023). Streptomyces sp. Strain PBR11, a forest-derived soil actinomycetia with antimicrobial potential. *Microbiol. Spectr.* 11, e03489–e03422. doi: 10.1128/spectrum.03489-22

Mondal, A. H., Khare, K., Saxena, P., Debnath, P., Mukhopadhyay, K., and Yadav, D. (2024). A review on colistin resistance: an antibiotic of last resort. *Microorganisms* 12, 772. doi: 10.3390/microorganisms12040772

Powers, J. H. (2004). Antimicrobial drug development–the past, the present, and the future. *Clin. Microbiol. Infect.* 10 Suppl 4, 23–31. doi: 10.1111/j.1465-0691.2004.1007.x

Quinn, G. A., Banat, A. M., Abdelhameed, A. M., and Banat, I. M. (2020). Streptomyces from traditional medicine: sources of new innovations in antibiotic discovery. *J. Med. Microbiol.* 69, 1040–1048. doi: 10.1099/jmm.0.001232

Rajeswari, P., Jose, P. A., Amiya, R., and Jebakumar, S. R. D. (2014). Characterization of saltern based Streptomyces sp. and statistical media optimization for its improved antibacterial activity. *Front. Microbiol.* 5. doi: 10.3389/fmicb.2014.00753

Riaz, M., Khalid, R., Afzal, M., Anjum, F., Fatima, H., Zia, S., et al. (2023). Phytobioactive compounds as therapeutic agents for human diseases: A review. *Food Sci. Nutr.* 11, 2500–2529. doi: 10.1002/fsn3.3308

Rijia, A., Krishnamoorthi, R., Rasmi, M., Mahalingam, P. U., and Kim, K. (2024). Comprehensive Analysis of Bioactive Compounds in Wild Ganoderma applanatum Mushroom from Kerala, South India: Insights into Dietary Nutritional, Mineral, Antimicrobial, and Antioxidant Activities. *Pharm. (Basel).* 17, 509. doi: 10.3390/ph17040509

Sangwan, I., and O'Brian, M. R. (1993). Expression of the soybean (Glycine max) glutamate 1-semialdehyde aminotransferase gene in symbiotic root nodules. *Plant Physiol.* 102, 829–834. doi: 10.1104/pp.102.3.829

Saxena, D., Maitra, R., Bormon, R., Czekanska, M., Meiers, J., Titz, A., et al. (2023). Tackling the outer membrane: facilitating compound entry into Gram-negative bacterial pathogens. *NPJ Antimicrob. Resist.* 1, 1–22. doi: 10.1038/s44259-023-00016-1

Sharma, P., Kalita, M. C., and Thakur, D. (2016). Broad spectrum antimicrobial activity of forest-derived soil actinomycete, nocardia sp. PB-52. *Front. Microbiol.* 7. doi: 10.3389/fmicb.2016.00347

Tang, K. W. K., Millar, B. C., and Moore, J. E. (2023). Antimicrobial resistance (AMR). *Br. J. BioMed. Sci.* 80. doi: 10.3389/bjbs.2023.11387

Uddin, T. M., Chakraborty, A. J., Khusro, A., Zidan, B. R. M., Mitra, S., Emran, T. B., et al. (2021). Antibiotic resistance in microbes: History, mechanisms, therapeutic strategies and future prospects. *J. Infect. Public Health* 14, 1750–1766. doi: 10.1016/j.jiph.2021.10.020

Ventola, C. L. (2015). The antibiotic resistance crisis. *P. T.* 40, 277–283.

Westhoff, S., Kloosterman, A. M., van Hoesel, S. F. A., van Wezel, G. P., and Rozen, D. E. (2021). Competition sensing changes antibiotic production in streptomyces. *mBio* 12, e02729–e02720. doi: 10.1128/mBio.02729-20

Wongsa, P., Phatikulrungsun, P., and Prathumthong, S. (2022). FT-IR characteristics, phenolic profiles and inhibitory potential against digestive enzymes of 25 herbal infusions. *Sci. Rep.* 12, 6631. doi: 10.1038/s41598-022-10669-z

frontiers | Frontiers in Cellular and Infection Microbiology

TYPE Original Research
PUBLISHED 14 January 2025
DOI 10.3389/fcimb.2024.1503944

OPEN ACCESS

EDITED BY
Biswajit Mishra,
Brown University, United States

REVIEWED BY
Mukesh Kumar,
All India Institute of Medical Sciences, India
Ravneet Chug,
Amity University Jaipur, India

*CORRESPONDENCE
Yifei Wang
twang-yf@163.com
Shaowei Dong
michael.dong.85@gmail.com

RECEIVED 30 September 2024
ACCEPTED 09 December 2024
PUBLISHED 14 January 2025

CITATION
Zhou P, Shi X, Xia J, Wang Y and Dong S (2025) Innovative epitopes in *Staphylococcal* Protein-A an immuno-informatics approach to combat MDR-MRSA infections. *Front. Cell. Infect. Microbiol.* 14:1503944. doi: 10.3389/fcimb.2024.1503944

Innovative epitopes in *Staphylococcal* Protein-A an immuno-informatics approach to combat MDR-MRSA infections

Pengjun Zhou[1,2], Xing Shi[3], Jinquan Xia[3], Yifei Wang[2*] and Shaowei Dong[3*]

[1]Department of Pharmacology, Guangdong Pharmaceutical University, Guangzhou, China, [2]Guangzhou Jinan Biomedicine Research and Development Center, Guangdong Provincial Key Laboratory of Bioengineering Medicine, College of Life Science and Technology, Jinan University, Guangzhou, China, [3]Department of Haematology and Oncology, Shenzhen Children's Hospital, Shenzhen, China

Background: Methicillin-resistant *Staphylococcus aureus* (MRSA) poses a significant challenge in clinical environments due to its resistance to standard antibiotics. *Staphylococcal* Protein A (SpA), a crucial virulence factor of MRSA, undermines host immune responses, making it an attractive target for vaccine development. This study aimed to identify potential epitopes within SpA that could elicit robust immune responses, ultimately contributing to the combat against multidrug-resistant (MDR) MRSA.

Methods: The SpA protein sequence was retrieved from the UniProt database, with various bioinformatics tools employed for epitope prediction. T-cell epitopes were identified using the Tepitool server, focusing on high-affinity interactions with prevalent human leukocyte antigens (HLAs). B-cell epitopes were predicted using the BepiPred tool. Predicted epitopes underwent docking studies with HLA molecules to evaluate binding properties. In-silico analyses confirmed the antigenicity, promiscuity, and non-glycosylated nature of the selected epitopes.

Results: Several T and B cell epitopes within SpA were identified, showcasing high binding affinities and extensive population coverage. A multi-epitope vaccine construct, linked by synthetic linkers and an adjuvant, was modelled, refined, and validated through various bioinformatics assessments. The vaccine candidate was subsequently docked with Toll-like receptor 4 (TLR-4) to evaluate its potential for immunogenicity.

Conclusion: This study lays the groundwork for developing epitope-based vaccines targeting SpA in MRSA, identifying promising candidates for experimental validation and contributing to innovative immunotherapeutic strategies against MRSA infections.

KEYWORDS

human leukocyte antigen, immuno-informatics, methicillin-resistant *Staphylococcus aureus*, *Staphylococcal* Protein A, toll-like receptor, vaccine development

1 Introduction

Methicillin-resistant *Staphylococcus aureus* (MRSA) is a formidable pathogen that represents a significant public health challenge (Turner et al., 2019). Its extensive resistance to conventional antibiotics, combined with its ability to cause a spectrum of severe infections—from localized skin infections to critical conditions such as pneumonia, endocarditis, and sepsis—positions MRSA as a top priority for healthcare systems worldwide (Denissen et al., 2022). Globally, MRSA contributes to a substantial burden of morbidity and mortality, ranking among the top six multidrug-resistant (MDR) bacteria responsible for an estimated 700,000 deaths annually due to antibiotic resistance (GBD 2021 Antimicrobial Resistance Collaborators, 2024). The persistence and adaptability of MRSA necessitate the exploration of novel therapeutic strategies beyond traditional antibiotic treatment (Parsons et al., 2023). One promising avenue in the fight against MRSA is the development of epitope-based vaccines. Epitopes are specific regions of antigens recognized by the immune system, and their precise targeting is crucial for eliciting effective immune responses (Klimka et al., 2021). Such vaccines can specifically target key virulence factors of the bacterium, thereby neutralizing its pathogenic mechanisms. Recent studies have highlighted the importance of immunogenic epitope identification for developing vaccines against resistant pathogens like MRSA, emphasizing the need for innovative approaches to immunotherapy (Khalid and Poh, 2023) *Staphylococcal* Protein A (SpA) emerges as a pivotal virulence factor, exerting profound influence over the host immune response, notably by functioning as a B cell superantigen (Mandelli et al., 2024). SpA has also been implicated in MRSA's ability to evade both innate and adaptive immune responses, which makes it an attractive target for vaccine development (Howden et al., 2023). The identification of immunogenic epitopes within SpA is crucial for designing vaccines that can effectively target MRSA (Clegg et al., 2021). Superantigens constitute a diverse class of proteins with the remarkable ability to robustly engage and activate the immune system in a nonspecific manner (Bear et al., 2023). Within the arsenal of *Staphylococcus aureus* (*S. aureus*), the production of superantigens serves as a formidable shield, hindering the accurate identification and neutralization of other *S. aureus* antigens by the human immune system. Recent advances in structural biology and immunology have provided new insights into how SpA modulates the immune response, suggesting potential sites for targeted vaccine intervention (Bear et al., 2023). In light of its pivotal role in impeding the generation of effective antibodies and subverting the full functionality of B-cell responses against *S. aureus*, SpA has emerged as a focal point of considerable interest in deciphering the evolutionary dynamics of the human immune response to *S. aureus* (Cruz et al., 2021; Bear et al., 2023). Given its pivotal role in immune evasion, SpA stands as an enticing target for the development of vaccines (Forsgren and Sjöquist, 1966). The targeting of SpA epitopes represents a promising strategy to enhance immune recognition and clearance of MRSA, particularly in the context of multidrug resistance (Pauli et al., 2014). Identifying immunogenic epitopes within SpA can lead to the design of a vaccine that elicits robust and specific immune responses. T-cell epitopes can activate cellular immunity by presenting peptides to T cells through HLA molecules, while B cell epitopes can induce humoral immunity by stimulating antibody production (Jawa et al., 2020). This computational approach accelerates the vaccine development process by streamlining the identification of potential candidates for further experimental validation (Sanchez-Trincado et al., 2017). In this study, we aimed to employ an in-depth immuno-informatics approach to pinpoint potential T&B cell epitopes in SpA protein. By elucidating these epitopes, we aimed not only to contribute to the expanding repertoire of knowledge in the field of vaccine design but also to chart a novel trajectory in the combat against MRSA infections through the application of innovative immunological strategies. The hypothesis driving this work is that a computational identification of SpA-derived epitopes capable of generating both humoral and cellular immune responses can provide valuable candidates for future MRSA vaccine development. We specifically tried to answer the research question: Can potential epitopes in SpA protein capable of generating humoral and cellular immune response be accurately identified against MRSA? The identified epitopes present promising candidates for further experimental validation and eventual vaccine development, which could provide a powerful tool in the ongoing battle against antibiotic-resistant pathogens.

2 Methodology

2.1 *Staphylococcal* Protein A assessment

The protein sequence of SpA was obtained from the NCBI database https://www.ncbi.nlm.nih.gov/ bearing ID: WP_033567379. To ensure comprehensive coverage and variability analysis, the BLASTP tool was used to extract approximately 250 homologous sequences. Multiple sequence alignment (MSA) was conducted utilizing the COBALT tool available at NCBI https://www.ncbi.nlm.nih.gov/tools/cobalt/re_cobalt.cgi (Papadopoulos and Agarwala, 2007) to identify conserved and variable regions within the protein, which is crucial for epitope prediction. The ProtParam tool https://web.expasy.org/protparam/ was utilized to examine the physicochemical properties of SpA (Wilkins et al., 1999). The physicochemical properties help in understanding the stability and solubility of the protein, which are important for vaccine design.

2.2 Epitope screening

2.2.1 T&B cell epitope prediction

Epitopes specific to different Major Histocompatibility Complex (MHC) classes were forecasted using Tepitool http://tools.iedb.org/tepitool/ (Paul et al., 2016) [7]. The HLA Class I alleles (including A & B alleles) were screened using a panel of 27 most common alleles provided in the Tepitool server (Supplementary Figure 1A). Peptide lengths were selected as 9mers. To predict HTL epitopes, a panel of 26 most frequent

alleles (Supplementary Figure 1B) were selected, and the length of peptides selected were 15mers. The peptides with percentile rank ≤ 1 were selected. For the prediction of B cell epitopes, the BepiPred 2.0 tool https://services.healthtech.dtu.dk/services/BepiPred-2.0/ was utilized (Jespersen et al., 2017). All tools were run at default parameters without altering anything.

2.3 Epitope selection criteria

Epitopes were selected based on several criteria:

2.3.1 Binding affinity

Epitopes were identified for their robust projected binding affinity to widely occurring HLA alleles. Consequently, only epitopes with higher percentile scores were included for further analysis.

2.3.2 Population coverage

In order to ensure broad applicability across different populations, ensuring the epitopes applicability in diverse demographic groups. For this, we selected only those epitopes which were promiscuous.

2.3.3 Antigenicity

Evaluated using the VaxiJen tool https://www.ddg-pharmfac.net/vaxijen/VaxiJen/VaxiJen.html to predict the potential to be recognized as an antigen (Salod and Mahomed, 2022, pp. 2017–2021).

2.4 Molecular docking

Predicted epitopes (CTL & HTL) were subjected to molecular docking studies to assess their binding affinities with HLA molecules. ClusPro tool https://cluspro.org/help.phpb was used for these studies (Vajda et al., 2017). The binding interactions were visualized and the interaction patterns were analyzed using Pymol to ensure strong and specific binding.

2.5 Constructing a multi-epitope chain and its interaction analysis

The selected T&B-cell epitopes were concatenated into a single multi-epitope chain. Linker sequences were used to join the epitopes to enhance their presentation and processing by the immune system. Furthermore, the vaccine construct was supplemented with an adjuvant and PADRE sequence to bolster its immunogenicity and facilitate epitope presentation. The physicochemical properties of the finalized vaccine construct was also noted. The I-Tasser server https://zhanggroup.org/I-TASSER/ (Zhou et al., 2022) was employed to initially model the multi-epitope chain, followed by refinement utilizing the Galaxy refine server https://galaxy.seoklab.org/cgi-bin/submit.cgi?type=REFINE (Heo et al., 2013). The refined vaccine's 3D model underwent validation using the ProSA-web tool https://bio.tools/prosa-web (Wiederstein and Sippl, 2007). In addition, the Ramachandran plot was also investigated using MolProbity https://phenix-online.org/documentation/reference/molprobity_tool.html and the structural robustness of the modelled vaccine was examined using CABS-flex 2.0 https://bio.tools/cabs-flex_2.0 (Kuriata et al., 2018). Molecular docking with the Cluspro server https://cluspro.org/help.php was performed to determine the ability of the multi-epitope construct to trigger innate immune activation via TLR-4.

2.6 Disulfide engineering

In order to improve the structural stability of the vaccine structure numerous disulfide bonds were incorporated into the refined vaccine construct utilizing the design v2.0 web server (Xie et al., 2018).

2.7 Immune simulation

The vaccine sequence was also investigated foe the ability to induce humoral and adaptive immune responses. We employed in silico immune simulation assay for the same utilizing C-immsim server (Stolfi et al., 2022).

3 Results

3.1 SpA assessment

Multiple sequence alignments revealed some mutations in the Spa protein. These mutations were noted for emitting the epitopes lying within these regions (Figure 1). The protein's properties unveiled its molecular weight at 45528.47, theoretical pI at 5.65, with 56 +vely charged residues and 62-vely charged residues. The projected ½ life spanned 30 hrs (mammalian reticulocytes, *in-vitro*), greater than 20 hours (yeast, *in-vivo*), and greater than 10 hours (*E. coli*, *in-vivo*). The Aliphatic and instability index stood at 69.47, (II) and 50.49 respectively. The GRAVY was measured at -0.991. The identified mutations could potentially impact the immunogenic properties of SpA by altering its epitope structure or antigen presentation. These changes may influence vaccine efficacy, necessitating careful consideration during epitope selection and structural modeling. The molecular weight and pI of the SpA are crucial factors that can influence its immunogenic properties. The molecular weight of a protein impacts its processing and presentation by antigen-presenting cells, as smaller peptides may be more readily processed, while larger proteins may require additional processing steps. The theoretical pI, on the other hand, reflects the protein's charge at physiological pH, affecting its solubility, stability, and binding interactions with immune receptors and antibodies. Proteins with pI values close to the physiological pH are often more soluble and can interact more effectively with immune components, potentially enhancing

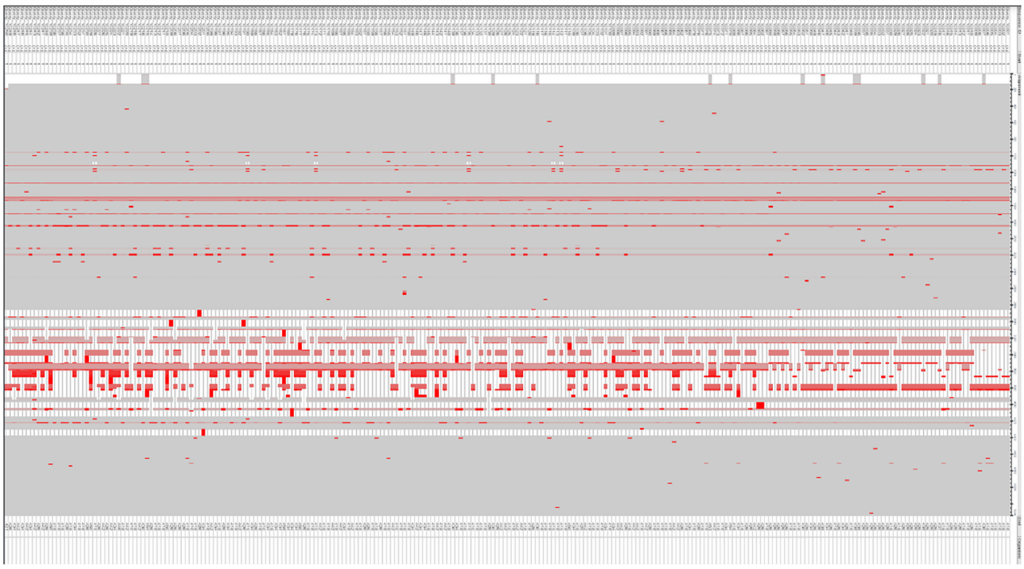

FIGURE 1
Comparison of Spa protein sequences to detect mutations, conducted through the COBALT tool for multiple sequence alignment.

their immunogenicity. These properties, therefore, underscore the significance of SpA's structural and physicochemical characteristics in the design of effective epitope-based vaccines.

3.2 Epitope screening

The Tepitool server from IEDB was used to forecast HLA-Class I & II epitopes. Tepitool predicts how peptides bind to HLA molecules, with HLA class II molecules accommodating longer peptides due to their expanded binding groove, in contrast to the confined groove in HLA class I molecules. Despite this difference, the core binding region of class II molecules is typically around 9 amino acids in length. Flanking amino acids enhances the stability of the binding without directly interacting with the HLA binding groove. To maximize the coverage of potential binding cores while minimizing redundancy, we selected 15mer peptides overlapping by 10 amino acids. This approach ensured that all possible 9mer binding cores were represented, with a minimum of one flanking residue on each side for stability. This approach eliminates the selection of overlapping peptides that share identical binding cores (Paul et al., 2016). We followed the IEDB recommended method for predicting and selecting the most ideal peptides, which is the default prediction method in Tepitool. While 15mer peptides were selected for optimal CD4+ T cell recognition, their larger size may lead to overlap with adjacent sequences, potentially reducing specificity and increasing cross-reactivity. Additionally, larger peptides may face processing limitations that could impact overall immunogenicity. However, if we do carry out blast analysis against the human genome, this will reduce the probability of cross reactivity. For HLA Class I epitopes, 9 mers were selected. Tepitool selects the best prediction approach available for a given MHC molecule based on predictor availability and historical performance. Peptides with a percentile rank of less than 0.5 were only selected for further screening. A total of 71 epitopes targeting HLA Class I alleles and 33 promiscuous epitopes targeting HLA Class II alleles were predicted. In addition, BepiPred 2.0 predicted nearly 12 B cell epitopes (Supplementary Figure 2). The IEDB database-based tools have earlier been employed by numerous research groups to predict promising epitopes targeting viral (Chauhan et al., 2018; Chauhan and Singh, 2020) bacterial (Ghafouri et al., 2024), parasitic (Chauhan et al., 2023) and other metabolic disorders (Banesh et al., 2024). This underscores the reliability of the predicted epitopes for vaccine applications.

3.3 Epitope selection criteria

The selected epitopes underwent a comprehensive filtering process before molecular docking analysis to ensure their suitability for vaccine development. The filters applied and their relevance are discussed below:

3.3.1 High predicted affinities to HLA alleles

The efficacy of an immune response is significantly influenced by how well epitopes bind to HLA molecules. Our results demonstrated that the selected epitopes exhibited strong binding affinities, as indicated by their high percentile scores.

3.3.2 Broad population coverage

Ensuring broad population coverage is imperative for the universal applicability of a vaccine. To achieve this, we selected promiscuous epitopes capable of binding to multiple HLA alleles, thereby covering a larger population. This approach increases the likelihood that a significant proportion of the population will respond to the vaccine, thus enhancing its overall efficacy.

3.3.3 Immunogenicity

Peptide-based vaccines often exhibit lower immunogenicity. To address this, we utilized the VaxiJen server to select epitopes with high immunogenic potential (Doytchinova and Flower, 2007). The chosen epitopes demonstrated the ability to trigger both humoral and cellular immune responses, indicating their effectiveness as vaccine candidates.

3.3.4 Consideration of glycosylation sites

Glycosylation can impact the stability, immunogenicity, and efficacy of epitopes. Using the NetNGlyc tool (Gupta and Brunak, 2002), we excluded epitopes lying within glycosylation regions to ensure optimal performance. This additional filter further refined our selection, enhancing the stability and immune recognition of the epitopes.

3.3.5 Molecular docking

The epitopes were further docked with HLA alleles. Visual analysis of the docking complexes revealed that the epitopes fit well into the binding domains of the HLA molecules, forming stable hydrogen bonds with key residues. For HLA Class II-epitope interaction analysis, docking was performed with two HLA-DRB1 alleles i.e. 01 & 15. In contrast, for HLA Class I-epitope interaction analysis, we used the HLA-A*02:01 allele (Figure 2). This analysis confirmed that the epitopes could be effectively displayed by HLA molecules on the membrane of antigen-presenting cells.

3.4 Epitopes finalization

After applying the above filters, we identified 10 HTL and 7 CTL epitopes. These epitopes demonstrated high binding affinity (Figure 3), broad population coverage, and immunogenicity, and were free from glycosylation sites. For the identification of the B cell epitope, we employed the BepiPred 2.0 tool with a threshold of 0.5. We selected epitopes that were above this threshold, greater than 10 amino acids in length, conserved, immunogenic, and not within glycosylation sites. Based on these criteria, 3 B cell epitopes were selected (Table 1). The above filters led to the identification of the most promising epitopes within SpA protein. Similar kinds of filters have earlier been employed by several research groups in their immuno-informatics study to screen out epitopes for high success probabilities (Chauhan et al., 2021). The physicochemical properties of the finally selected epitopes are represented in Supplementary Table 1.

3.6 Multi-epitope vaccine: structural modelling and validation

The vaccine construct was designed by integrating the optimal T & B cell epitopes to induce a strong immune response. The epitopes selected from previous screening stages (10 HTL, 7 CTL, and 3 B cell epitopes) were used as building blocks for these constructs. The vaccine had molecular weight of 53667.56 Daltons, theoretical PI: 5.75, extinction coefficient 15930, estimated half life 30 hours, instability index 32.26, aliphatic index 63.64 and GRAVY -0.796 as predicted by protparam tool. The incorporation of adjuvants and synthetic linkers was aimed at enhancing immunogenicity and ensuring the proper folding of the vaccine constructs. The addition of the 50S ribosomal protein L7/L12 fortified the vaccine construct to enhance the immune response, capitalizing on its robust immunostimulatory capabilities (Figure 4A). The initial vaccine constructs were modelled using the I-Tasser server (Figure 4B). This tool provided a preliminary 3D structure of the multi-epitope vaccines by predicting the folding and spatial arrangement of the included epitopes. The top 10 templates used by the I-Tasser server for modelling the vaccine construct were 1rquA, 7wkkB, 1rqv, 2nbiA, 1rqv, 8wxbY, 1rquA, 8p0vL, 5h7c and 1dd3A. The model generated had a C-score of -0.97, with estimated TM and RMSD scores as 0.59 ± 0.14 and 9.7 ± 4.6Å respectively. Refinement of the preliminary

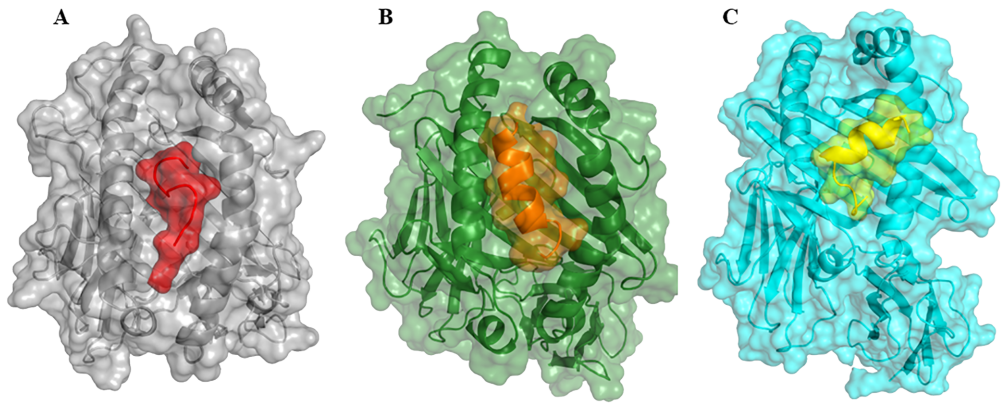

FIGURE 2
The interaction patterns of epitopes to HLA molecules in cartoon and surface view. **(A)** Interaction of HLA Class I epitopes (represented as red color surface view) to HLA-A*02:01 allele (grey color, surface view). **(B)** Interaction of HLA Class II epitope (orange color, surface view) to HLA-DRB1*01:01 (represented in dark green color, surface view retrieved from PDB with ID: 2g9h). **(C)** Interaction of HLA Class II epitope (yellow color, surface view) to HLA-DRB1*15:01 (cyan color, surface view, retrieved from PDB with ID: 1bx2). Note, that all epitopes interacted with the HLA binding grooves.

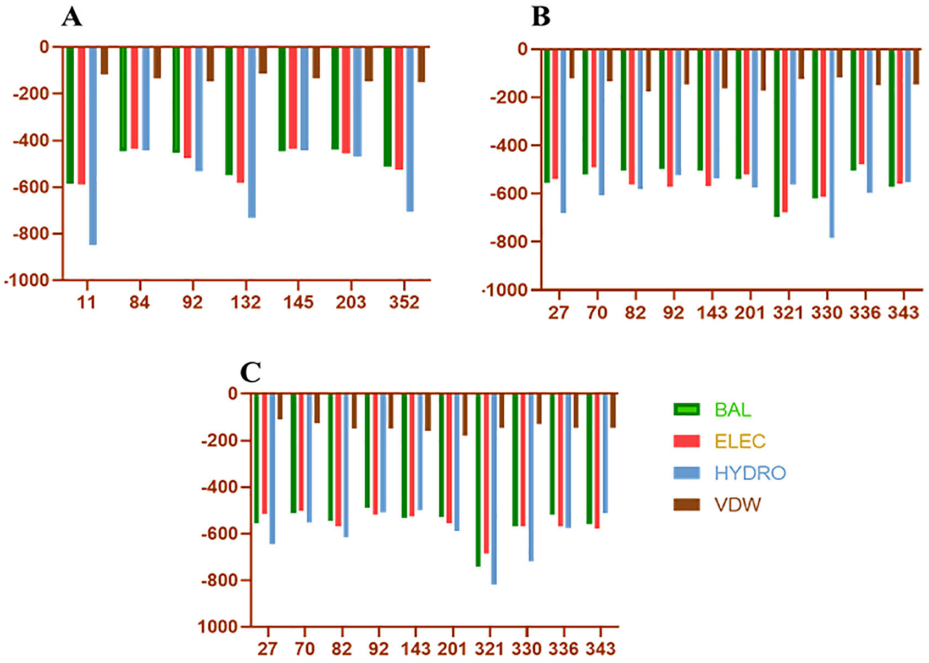

FIGURE 3
Docking energies of T-cell epitopes included in vaccine with HLA molecules. **(A–C)** Represents the docking energies of the epitopes with different HLA alleles. On the Y-axis are the docking energies and on the X-axis are the position of epitopes. BAL, Balanced energy; ELEC, Electrostatic favored energy; HYDRO, Hydrophobic favored energy; VDW, Vander walls + electrostatic energy.

structure was conducted using the online available Galaxy Refine server. This step was essential to enhance the integrity of the vaccine model by refining both local and global structure, thereby enhancing the overall stability and accuracy of the model. The refinement process included side-chain repacking and overall energy minimization, leading to more reliable and realistic vaccine structures. The refined vaccine models were validated using Ramachandran plot analysis using MolProbilty. The overall amino acids lying in the favored region were 98.5% (Supplementary Figure 3). This method assesses the stereochemical characteristics of the protein structures by assessing the φ (phi) and ψ (psi) dihedral angles of the aa residues. It was observed that a predominant number of residues in the refined vaccine constructs were situated within the favored regions of the Ramachandran plot (about 98.5%), indicating a high-quality and reliable structure. The results obtained by the ProSa-web tool also demonstrated the considerable structural integrity of the vaccine construct (Figures 4C, D). Finally, employing the CABSflex 2.0 server, the vaccine's flexible and rigid domains were delineated by molecular motion analysis, within the vaccine construct. Evaluation of the final 3D structures (ten) demonstrated minor changes at the beginning locations, where the adjuvant was connected. Conversely, notable fluctuations were detected close to the terminus. This was the region where a succession of epitopes was affixed using linkers, delineated in dark brown and red sections (Figure 5A). Across all 10 models, the contact map illustrated the patterns of residue-residue interactions (Figure 5B). According to the RMSF plot, residue fluctuations varied from 0 Å to 7 Å, with more pronounced variability towards the latter part of the sequence, mainly comprising the epitopes, suggesting a high degree of flexibility in these regions (Figure 5C).

3.6 Molecular docking analysis

In order to explore the interaction between the vaccine model and TLR-4, molecular docking analysis was performed, aiming to assess its binding affinity and potential immunostimulatory effects. The ClusPro server was employed for the same. It provided a detailed understanding of the binding interactions, depicting binding energies and the interacted amino acids. The vaccine construct exhibited a strong binding affinity to TLR-4, as indicated by the docking score, which revealed stability with significant interactions. Visual analysis of the docking complex demonstrated multiple H-bond interactions between the vaccine and TLR-4. Key residues of TLR-4 involved in binding with the vaccine were identified, ensuring the stability and specificity of the interaction (Figure 6). The robust binding conformation of the vaccine construct in the TLR-4 binding pocket hints at effective interaction with the receptor, potentially bolstering immune response through TLR-4-mediated signaling pathways. This strong and stable binding interaction with TLR-4 is crucial for activating innate and adaptive immune responses. The presence of an adjuvant in the vaccine construct may significantly contribute to the enhanced immunogenicity, acting as a potent immunostimulant and enhancing interaction with TLR-4. Overall, the stable and specific interactions observed in the docking studies highlight the suitability of the construct for further experimental validation as an effective vaccine against MRSA. These findings support the potential of the proposed vaccine

TABLE 1 Finalized T and B cell epitopes.

Location	Epitope sequence	Interacting HLA alleles	Antigenicity score
HLA Class I epitopes			
11-19	KLGVGIASV	HLA-A*02:01, HLA-A*02:03, HLA-A*02:06	0.9
84-92	KLNDSQAPK	HLA-A*03:01, HLA-A*11:01, HLA-A*30:01,	1.28
92-100	KADAQQNKF	HLA-A*01:01, HLA-B*58:01	1.2
132-140	DPSQSANLL	HLA-B*35:01, HLA-B*51:01, HLA-B*53:01,	0.58
145-153	KLNESQAPK	HLA-A*03:01, HLA-A*11:01, HLA-A*30:01	0.98
203-211	KLNDAQAPK	HLA-A*03:01, HLA-A*11:01, HLA-A*30:01	1.09
352-360	KLADKNMIK	HLA-A*03:01, HLA-A*11:01, HLA-A*30:01	0.7
HLA Class II epitopes			
27-41	SGGVTPAANAAQHDE	HLA-DRB1*04:01, HLA-DRB1*04:05, HLA-DRB1*08:02, HLA-DRB1*09:01, HLA-DRB1*11:01, HLA-DRB1*15:01, HLA-DRB3*02:02, HLA-DRB4*01:01, HLA-DQA1*05:01/DQB1*03:01, HLA-DQA1*05:01/DQB1*02:01, HLA-DQA1*04:01/DQB1*04:02, HLA-DQA1*03:01/DQB1*03:02, HLA-DQA1*01:02/DQB1*06:02,	0.83
70-84	DDPSQSANVLGEAQK	HLA-DQA1*01:02/DQB1*06:02, HLA-DQA1*03:01/DQB1*03:02	0.61
82-96	AQKLNDSQAPKADAQ	HLA-DRB1*01:01, HLA-DRB1*04:01, HLA-DRB1*07:01, HLA-DRB1*09:01, HLA-DRB3*02:02, HLA-DQA1*01:02/DQB1*06:02, HLA-DQA1*05:01/DQB1*03:01,	1.01
92-106	KADAQQNKFNKDQQS	HLA-DPA1*01:03/DPB1*02:01, HLA-DPA1*02:01/DPB1*01:01	1.09
143-157	AKKLNESQAPKADNK	HLA-DRB1*01:01, HLA-DRB1*04:01, HLA-DRB1*07:01, HLA-DRB1*09:01, HLA-DRB1*13:02, HLA-DRB3*02:02 HLA-DRB4*01:01, HLA-DQA1*01:02/DQB1*06:02, HLA-DQA1*04:01/DQB1*04:02, HLA-DQA1*05:01/DQB1*03:01	0.9
201-215	AKKLNDAQAPKADNK	HLA-DRB1*01:01, HLA-DRB1*04:01, HLA-DRB1*08:02, HLA-DRB1*09:01, HLA-DRB1*15:01, HLA-DRB3*02:02 HLA-DRB4*01:01, HLA-DRB5*01:01, HLA-DQA1*01:01/DQB1*05:01, HLA-DQA1*01:02/DQB1*06:02, HLA-DQA1*03:01/DQB1*03:02, HLA-DQA1*04:01/DQB1*04:02, HLA-DQA1*05:01/DQB1*02:01, HLA-DQA1*05:01/DQB1*03:01	0.91
321-335	GNGVHVVKPGDTVND	HLA-DRB4*01:01, HLA-DQA1*04:01/DQB1*04:02, HLA-DQA1*05:01/DQB1*03:01	0.94
330-344	GDTVNDIAKANGTTA	HLA-DRB1*08:02, HLA-DRB1*11:01, HLA-DQA1*01:02/DQB1*06:02	0.55
336-350	IAKANGTTADKIAAD	HLA-DRB1*07:01, HLA-DQA1*01:02/DQB1*06:02, HLA-DQA1*03:01/DQB1*03:02, HLA-DQA1*05:01/DQB1*02:01, HLA-DQA1*05:01/DQB1*03:01	1.3
343-357	TADKIAADNKLADKN	HLA-DRB1*03:01, HLA-DRB1*04:01, HLA-DRB1*04:05, HLA-DRB1*08:02, HLA-DRB1*11:01, HLA-DRB1*13:02, HLA-DRB3*01:01, HLA-DRB3*02:02, HLA-DRB4*01:01HLA-DPA1*02:01/DPB1*01:01, HLA-DPA1*02:01/DPB1*05:01, HLA-DPA1*03:01/DPB1*04:02, HLA-DQA1*01:01/DQB1*05:01, HLA-DQA1*04:01/DQB1*04:02, HLA-DQA1*05:01/DQB1*02:01	0.99
B Cell epitopes			
31-45		TPAANAAQHDEAQQN	1.04
69-92		KDDPSQSANVLGEAQKLNDSQAPK	0.6
260-324		KKLNDAQAPKADNKFNKEQQNAFYEILHLPNLTEEQRNGFIQSLKDDPSVSKEILAEAKKLNDAQAP KEEDNNKPGKEDNNKPGKEDGNKPGKEDNKKPGKEDGNKPGKEDGNKPGKEDGNGV	1.08

Their location, sequence, promiscuousity and antigenicity are depicted.

10.3389/fcimb.2024.1503944

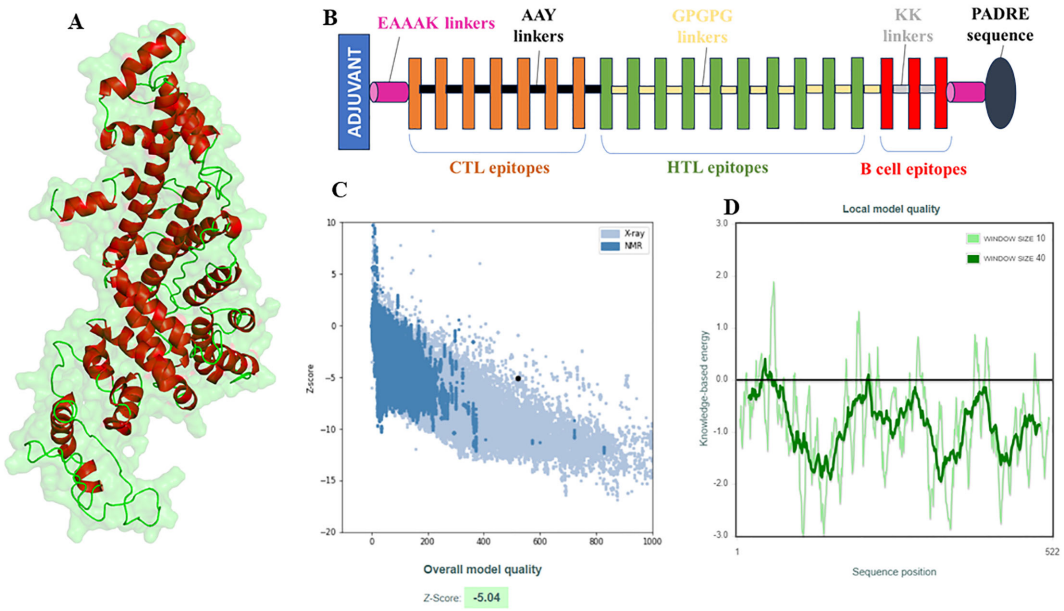

FIGURE 4
Structural modelling and validation of multi-epitope vaccine construct including initial 3D model, refinement process, and ramachandran plot analysis. **(A)** Visualization of the 3D structure of the vaccine model, **(B)** Demonstration of layout (composition) of the vaccine model., **(C, D)** Structural quality assessment of the constructed and refined 3D model of the vaccine using the ProSA-web tool. It is noteworthy that the Z score falls within the spectrum of proteins with comparable characteristics **(C)**.

construct to engage TLR-4 and promote an enhanced immune response through the activation of TLR-4-dependent pathways.

3.7 Disulfide engineering

In order to enhance the structural integrity of the vaccine construct, it was subjected to disulfide engineering. Disulfide by Design 2.12 was used for the same. We uploaded the refined model of the vaccine construct to the server and used for residue pair discovery before being used for disulfide engineering. Following that, 18 latent amino acid pairs were shortlisted (Figure 7).

3.8 Immune simulation assay

The immune simulation was carried out at random seed, simulation volume 10, and number of steps 100, 3 injections at 1-, 24- and 48-weeks interval. The vaccine sequence was observed to elicit varied immune cells revealing its potential immune system activation capability (Figure 8).

4 Discussion

MRSA possess high resistance to conventional antibiotics and has the ability to cause severe infections ranging from skin infections to life-threatening conditions such as pneumonia and sepsis. The global rise in MRSA infections emphasizes the urgent need for innovative therapeutic strategies, particularly vaccines that prevent infection. While there is currently no licensed vaccine for MRSA, several candidates have been investigated, including protein-based and polysaccharide-conjugate vaccines. However, these approaches have demonstrated limited efficacy in clinical trials, underscoring the necessity for alternative strategies (Miller et al., 2020). The growing incidence of MRSA infections underscores the urgent need for novel therapeutic strategies, particularly those aimed at preventing infections through vaccination (Guo et al., 2020). This study aimed to leverage immuno-informatics to identify potential immunogenic epitopes in SpA a key virulence factor in MRSA, which could serve as a promising target for vaccine development. Tepitool, one of the most advanced tools for predicting epitopes was employed for predicting how peptides bind to HLA molecules, with HLA class II molecules accommodating longer peptides due to their expanded binding groove, in contrast to the confined groove in HLA class I molecules. Despite this difference, the core binding region of class II molecules is typically around 9 amino acids in length. Flanking amino acids enhances the stability of the binding without directly interacting with the HLA binding groove. To maximize the coverage of potential binding cores while minimizing redundancy, we selected 15mer peptides overlapping by 10 amino acids. This approach ensured that all possible 9mer binding cores were represented, with a minimum of one flanking residue on each side for stability. This approach eliminates the selection of overlapping peptides that share identical binding cores (Paul et al., 2016). The same tool and strategy were applied earlier by Moustafa et al. for cell epitope selection (Moustafa et al., 2023). We then filtered the epitopes based on their high predicted affinities to HLA alleles, indicated by high percentile scores. Epitopes with broad population coverage due to their promiscuous nature, immunogenic characteristics, and positions in

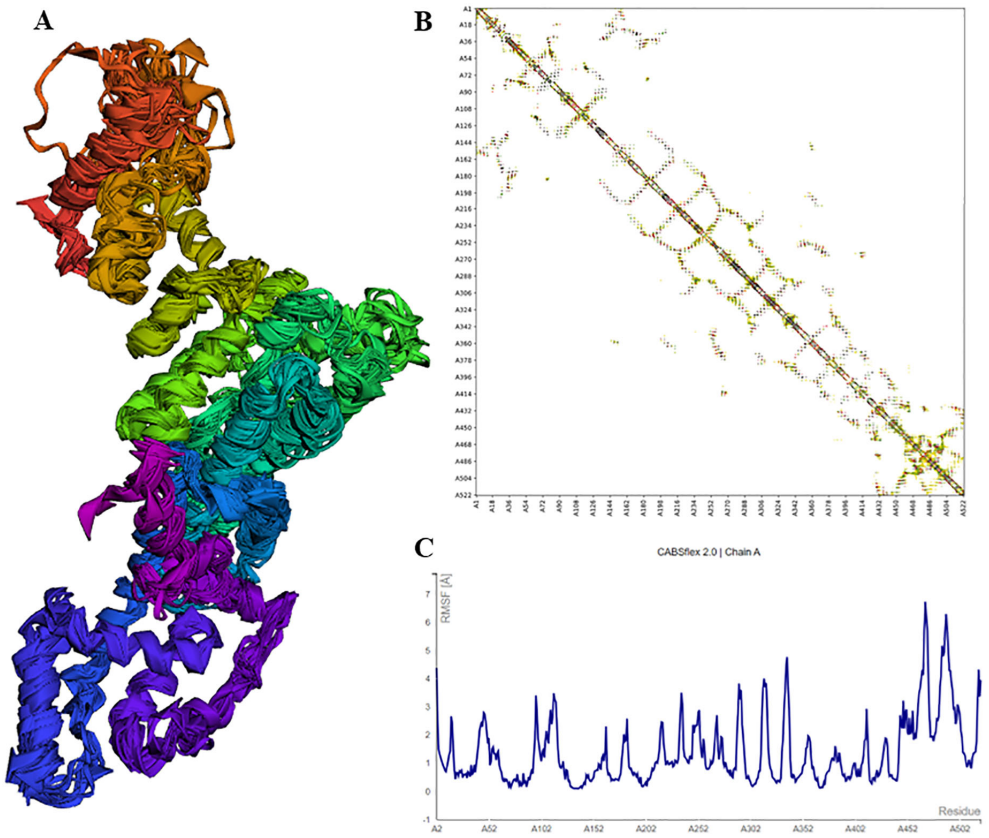

FIGURE 5
Structural analysis of vaccine model showing flexibility, residue-residue interactions, and RMSF plot indicating fluctuations. **(A)** Cartoon representations of the ten final models show limited overall fluctuations, with notable variations concentrated in the red and brown regions where the adjuvant is linked. **(B)** The contact map offers a comprehensive depiction of residue-residue interactions within the protein, emphasizing interactive regions in the central panel. Particularly noteworthy are the enhanced interactive patterns in the latter portion of the sequence housing the epitopes. **(C)** The fluctuation plot delineates residue fluctuations during the simulation, highlighting increased flexibility in the latter sequence segment.

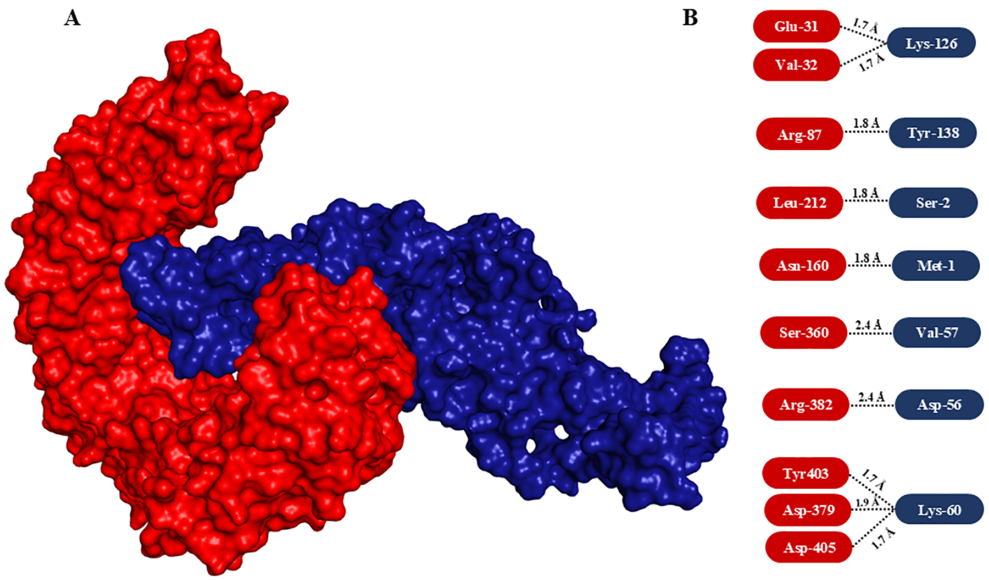

FIGURE 6
Molecular docking of vaccine construct with TLR-4 and interaction analysis. **(A)** Surface view of the interaction between modelled vaccine (dark blue) with TLR-4 (red). Note the vaccine interacted with the immune receptor nicely by integrating deep into TLR-4. **(B)** Interacted amino acids. The interacting amino acids of TLR-4 and vaccine are highlighted in rectangular rounded corners in red and blue boxes, respectively.

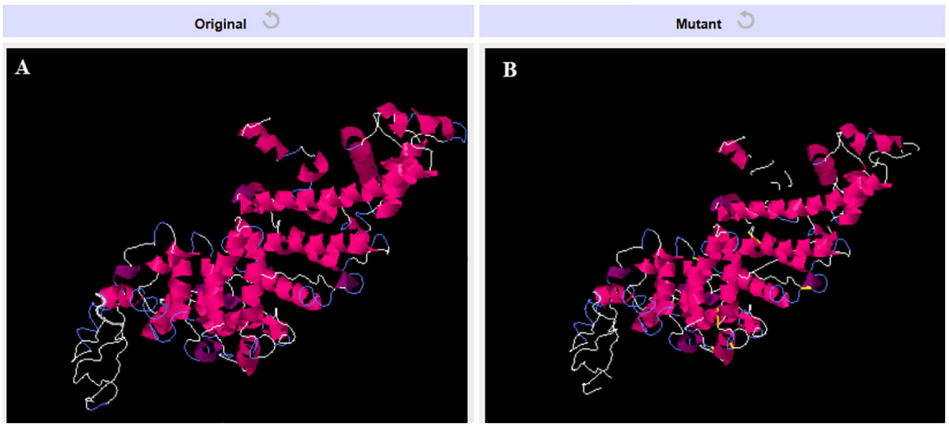

FIGURE 7
Disulfide engineering of the vaccine construct. **(A)** Original model **(B)** Model generated after disulfide engineering (disulfide bonds highlighted in yellow sticks).

non-glycosylation sites were prioritized. The present epitope filtration strategy was applied as described earlier (Chauhan et al., 2021). After applying these criteria, the selected epitopes underwent molecular docking, and those demonstrating promising interactions were finally chosen. Finally, we designed the vaccine model concatenated with epitopes which passed stringent filters as applied, linkers, adjuvant (50S ribosomal protein L7/L12) and PADRE sequence. The adjuvant has proven TLR-4 stimulating properties. Studies have shown that incorporating ribosomal proteins as adjuvants can lead to improved vaccine efficacy by promoting antigen presentation. Recently, a similar kind of immuno-informatics study was conducted where the multi-epitope vaccine was developed against *Mycobacterium tuberculosis* and they incorporated 50S ribosomal protein L7/L12 as an immune stimulator in their vaccine sequence (Khan et al., 2023). I-Tasser server produced the 3-D model which we refined and checked its robustness using several validation parameters. Later on, the vaccine model was docked with TLR-4 to examine its binding nature. The presented vaccine has the potential to elicit both humoral and cellular immunity as it is comprised of carefully selected epitopes (cytotoxic, helper T cell and B cell), adjuvant and PADRE sequences. This approach is particularly relevant in the context of the ongoing global effort to combat antibiotic-resistant bacteria through innovative immunological strategies.

Moving forward, *in vitro* and *in vivo* validation studies will be essential to confirm the immunogenicity, safety, and efficacy of the proposed multi-epitope construct. Further experimental testing will

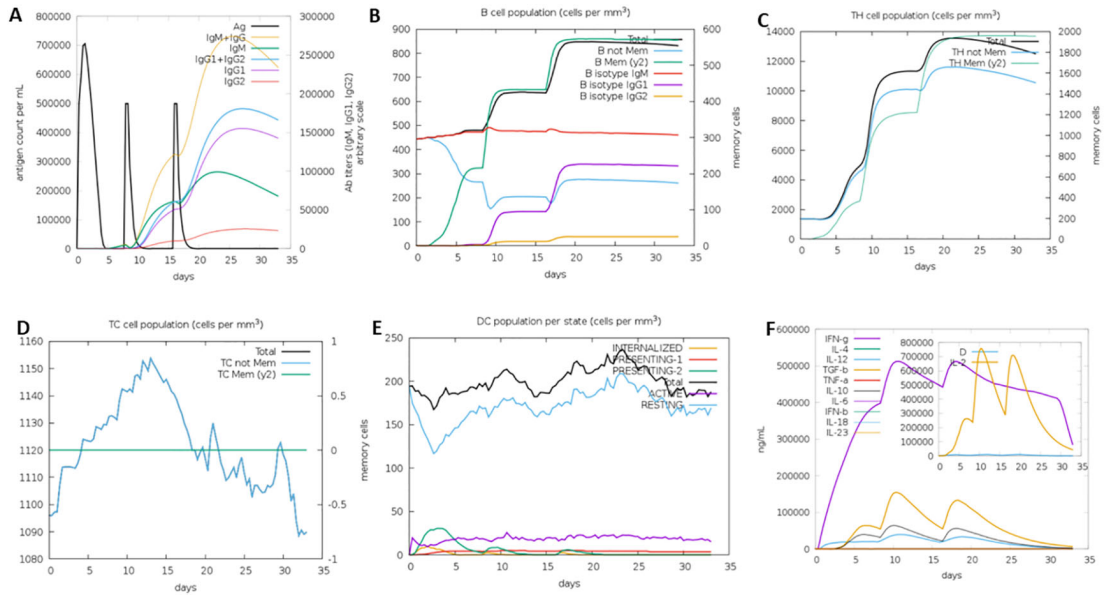

FIGURE 8
Immune simulation analysis results showing activation of different immune cells: **(A)** Immunoglobulins generation, **(B)** B cell population, **(C)** T helper cells generation, **(D)** Cytotoxic cells generation, **(E)** Dendritic cells generation, and **(F)** Interleukins generation.

allow us to evaluate the immune responses generated by the vaccine, ensuring that it provides adequate protection against MRSA without adverse effects. In addition to validation, future research could benefit from exploring advanced adjuvant formulations and delivery systems to optimize the vaccine's immunogenicity and stability. Studies investigating this vaccine construct's effectiveness across diverse population groups are also warranted, given the global prevalence of MRSA and the need for a broadly applicable solution. Such population studies could help tailor the vaccine to address regional HLA variability, enhancing its efficacy and coverage.

5 Conclusion

The study successfully identified and screened multiple T & B-cell epitopes within the SpA of MRSA, utilizing advanced immunoinformatics tools. These epitopes were incorporated into multi-epitope vaccine constructs, modelled, and refined to ensure structural stability and immunogenicity. Molecular docking studies demonstrated strong and stable interactions with TLR-4, suggesting the potential for robust immune activation. The study highlights the need for *in vitro* immunogenicity assays to validate epitope-specific responses, animal model studies to assess the safety and efficacy of the multi-epitope vaccine, and adjuvant optimization to enhance immune responses, paving the way for advanced vaccine development against MRSA. The study underscores the potential of epitope-based vaccines targeting SpA as a novel approach to combat MRSA infections.

Data availability statement

Publicly available datasets were analyzed in this study. This data can be found here: NCBI - WP_033567379.

Author contributions

PZ: Conceptualization, Data curation, Investigation, Methodology, Writing – original draft, Writing – review & editing. XS: Formal analysis, Investigation, Methodology, Writing – original draft, Writing – review & editing. JX: Investigation, Resources, Writing – original draft, Writing – review & editing. YW: Conceptualization, Methodology, Validation, Visualization, Writing – original draft, Writing – review & editing. SD: Investigation, Methodology, Writing – original draft, Writing – review & editing.

Funding

The author(s) declare financial support was received for the research, authorship, and/or publication of this article. This work is supported by the Science and Technology Projects in Guangzhou (2023A04J1143 to PZ).

Acknowledgments

The authors thank the research committee for permitting them to carry out the following study.

Conflict of interest

The authors declare that the research was conducted in the absence of any commercial or financial relationships that could be construed as a potential conflict of interest.

Generative AI statement

The author(s) declare that no Generative AI was used in the creation of this manuscript.

Publisher's note

Supplementary material

The Supplementary Material for this article can be found online at: https://www.frontiersin.org/articles/10.3389/fcimb.2024.1503944/full#supplementary-material

SUPPLEMENTARY FIGURE 1
HLA Class I **(A)** and Class II alleles **(B)** targeted for epitope prediction.

SUPPLEMENTARY FIGURE 2
Overall results of BepiPred-2.0 server.

SUPPLEMENTARY FIGURE 3
Ramachandran Plot of the refined vaccine construct. 98.5% of residues were in the favored region.

References

Banesh, S., Patil, N., Chethireddy, V. R., Bhukmaria, A., and Saudagar, P. (2024). Design and evaluation of a multiepitope vaccine for pancreatic cancer using immune-dominant epitopes derived from the signature proteome in expression datasets. *Med. Oncol.* 41, 90. doi: 10.1007/s12032-024-02334-4

Bear, A., Locke, T., Rowland-Jones, S., Pecetta, S., Bagnoli, F., and Darton, T. C. (2023). The immune evasion roles of Staphylococcus aureus protein A and impact on vaccine development. *Front. Cell Infect. Microbiol.* 13. doi: 10.3389/fcimb.2023.1242702

Chauhan, V., Khan, A., and Farooq, U. (2023). In silico study to predict promiscuous peptides for immunodiagnosis of cystic echinococcosis. *Trop. Parasitol.* 13, 54–62. doi: 10.4103/tp.tp_70_22

Chauhan, V., Rungta, T., Rawat, M., Goyal, K., Gupta, Y., and Singh, M. P. (2021). Excavating SARS-coronavirus 2 genome for epitope-based subunit vaccine synthesis using immunoinformatics approach. *J. Cell Physiol.* 236, 1131–1147. doi: 10.1002/jcp.29923

Chauhan, V., and Singh, M. P. (2020). Immuno-informatics approach to design a multi-epitope vaccine to combat cytomegalovirus infection. *Eur. J. Pharm. Sci.* 147, 105279. doi: 10.1016/j.ejps.2020.105279

Chauhan, V., Singh, M. P., and Ratho, R. K. (2018). Identification of T cell and B cell epitopes against Indian HCV-genotype-3a for vaccine development- An in silico analysis. *Biologicals* 53, 63–71. doi: 10.1016/j.biologicals.2018.02.003

Clegg, J., Soldaini, E., McLoughlin, R. M., Rittenhouse, S., Bagnoli, F., and Phogat, S. (2021). Staphylococcus aureus vaccine research and development: the past, present and future, including novel therapeutic strategies. *Front. Immunol.* 12. doi: 10.3389/fimmu.2021.705360

Cruz, A. R., Boer, M. A. D., Strasser, J., Zwarthoff, S. A., Beurskens, F. J., de Haas, C. J. C., et al. (2021). Staphylococcal protein A inhibits complement activation by interfering with IgG hexamer formation. *Proceedings of the National Academy of Sciences of the United States of America.* 118 (7), e2016772118. doi: 10.1073/pnas.2016772118IF: 9.4

Denissen, J., Reyneke, B., Waso-Reyneke, M., Havenga, B., Barnard, T., Khan, S., et al. (2022). Prevalence of ESKAPE pathogens in the environment: Antibiotic resistance status, community-acquired infection and risk to human health. *Int. J. Hyg Environ. Health* 244, 114006. doi: 10.1016/j.ijheh.2022.114006

Doytchinova, I. A., and Flower, D. R. (2007). VaxiJen: a server for prediction of protective antigens, tumour antigens and subunit vaccines. *BMC Bioinf.* 8, 4. doi: 10.1186/1471-2105-8-4

Forsgren, A., and Sjöquist, J. (1966). Protein A" from S. aureus. I. Pseudo-immune reaction with human gamma-globulin. *J. Immunol.* 97, 822–827. doi: 10.4049/jimmunol.97.6.822

GBD 2021 Antimicrobial Resistance Collaborators (2024). Global burden of bacterial antimicrobial resistance 1990-2021: a systematic analysis with forecasts to 2050. *Lancet* 404, 1199–1226. doi: 10.1016/S0140-6736(24)01867-1

Ghafouri, E., Fadaie, M., Amirkhani, Z., Esmaeilifallah, M., Rahimmanesh, I., Hosseini, N., et al. (2024). Evaluation of humoral and cellular immune responses against Vibrio cholerae using oral immunization by multi-epitope-phage-based vaccine. *Int. Immunopharmacol* 134, 112160. doi: 10.1016/j.intimp.2024.112160

Guo, Y., Song, G., Sun, M., Wang, J., and Wang, Y. (2020). Prevalence and therapies of antibiotic-resistance in staphylococcus aureus. *Front. Cell Infect. Microbiol.* 10. doi: 10.3389/fcimb.2020.00107

Gupta, R., and Brunak, S. (2002). Prediction of glycosylation across the human proteome and the correlation to protein function. *Pac Symp Biocomput*, 310–322.

Heo, L., Park, H., and Seok, C. (2013). GalaxyRefine: protein structure refinement driven by side-chain repacking. *Nucleic Acids Res.* 41, W384. doi: 10.1093/nar/gkt458

Howden, B. P., Giulieri, S. G., Wong Fok Lung, T., Baines, S. L., Sharkey, L. K., Lee, J. Y. H., et al. (2023). Staphylococcus aureus host interactions and adaptation. *Nat. Rev. Microbiol.* 21, 380–395. doi: 10.1038/s41579-023-00852-y

Jawa, V., Terry, F., Gokemeijer, J., Mitra-Kaushik, S., Roberts, B. J., Tourdot, S., et al. (2020). T-cell dependent immunogenicity of protein therapeutics pre-clinical assessment and mitigation–updated consensus and review 2020. *Front. Immunol.* 11. doi: 10.3389/fimmu.2020.01301

Jespersen, M. C., Peters, B., Nielsen, M., and Marcatili, P. (2017). BepiPred-2.0: improving sequence-based B-cell epitope prediction using conformational epitopes. *Nucleic Acids Res.* 45, W24–W29. doi: 10.1093/nar/gkx346

Khalid, K., and Poh, C. L. (2023). The Promising Potential of Reverse Vaccinology-Based Next-Generation Vaccine Development over Conventional Vaccines against Antibiotic-Resistant Bacteria. *Vaccines* 11, 1264. doi: 10.3390/vaccines11071264

Khan, M. T., Mahmud, A., Islam, M. M., Sumaia, M. S. N., Rahim, Z., Islam, K., et al. (2023). Multi-epitope vaccine against drug-resistant strains of Mycobacterium tuberculosis: a proteome-wide subtraction and immunoinformatics approach. *Genomics Inform* 21, e42. doi: 10.5808/gi.23021

Klimka, A., Mertins, S., Nicolai, A. K., Rummler, L. M., Higgins, P. G., Günther, S. D., et al. (2021). Epitope-specific immunity against Staphylococcus aureus coproporphyrinogen III oxidase. *NPJ Vaccines* 6, 11. doi: 10.1038/s41541-020-00268-2

Kuriata, A., Gierut, A. M., Oleniecki, T., Ciemny, M. P., Kolinski, A., Kurcinski, M., et al. (2018). CABS-flex 2.0: a web server for fast simulations of flexibility of protein structures. *Nucleic Acids Res.* 46, W338–W343. doi: 10.1093/nar/gky356

Mandelli, A. P., Magri, G., Tortoli, M., Torricelli, S., Laera, D., Bagnoli, F., et al. (2024). Vaccination with staphylococcal protein A protects mice against systemic complications of skin infection recurrences. *Front. Immunol.* 15. doi: 10.3389/fimmu.2024.1355764

Miller, L. S., Fowler, V. G., Shukla, S. K., Rose, W. E., and Proctor, R. A. (2020). Development of a vaccine against Staphylococcus aureus invasive infections: Evidence based on human immunity, genetics and bacterial evasion mechanisms. *FEMS Microbiol. Rev.* 44, 123–153. doi: 10.1093/femsre/fuz030

Moustafa, R. I., Faraag, A. H. I., El-Shenawy, R., Agwa, M. M., and Elsayed, H. (2023). Harnessing immunoinformatics for developing a multiple-epitope peptide-based vaccination approach against SARS-CoV-2 spike protein. *Saudi J. Biol. Sci.* 30, 103661. doi: 10.1016/j.sjbs.2023.103661

Papadopoulos, J. S., and Agarwala, R. (2007). COBALT: constraint-based alignment tool for multiple protein sequences. *Bioinformatics* 23, 1073–1079. doi: 10.1093/bioinformatics/btm076

Parsons, J. B., Westgeest, A. C., Conlon, B. P., and Fowler, V. G. (2023). Persistent methicillin-resistant staphylococcus aureus bacteremia: host, pathogen, and treatment. *Antibiotics (Basel)* 12, 455. doi: 10.3390/antibiotics12030455

Paul, S., Sidney, J., Sette, A., and Peters, B. (2016). TepiTool: A pipeline for computational prediction of T cell epitope candidates. *Curr. Protoc. Immunol.* 114, 18.19.1–18.19.24. doi: 10.1002/cpim.12

Pauli, N. T., Kim, H. K., Falugi, F., Huang, M., Dulac, J., Henry Dunand, C., et al. (2014). *Staphylococcus aureus* infection induces protein A-mediated immune evasion in humans. *J. Exp. Med.* 211, 2331–2339. doi: 10.1084/jem.20141404

Salod, Z., and Mahomed, O. (2022). Protocol for a scoping review of potential vaccine candidates predicted by VaxiJen for different viral pathogens between 2017-2021. *Syst. Rev.* 11, 284. doi: 10.1186/s13643-022-02121-0

Sanchez-Trincado, J. L., Gomez-Perosanz, M., and Reche, P. A. (2017). Fundamentals and methods for T- and B-cell epitope prediction. *J. Immunol. Res.* 2017, 2680160. doi: 10.1155/2017/2680160

Stolfi, P., Castiglione, F., Mastrostefano, E., Di Biase, I., Di Biase, S., Palmieri, G., et al. (2022). In-silico evaluation of adenoviral COVID-19 vaccination protocols: Assessment of immunological memory up to 6 months after the third dose. *Front. Immunol.* 13, 998262. doi: 10.3389/fimmu.2022.998262

Turner, N. A., Sharma-Kuinkel, B. K., Maskarinec, S. A., Eichenberger, E. M., Shah, P. P., Carugati, M., et al. (2019). Methicillin-resistant Staphylococcus aureus: an overview of basic and clinical research. *Nat. Rev. Microbiol.* 17, 203–218. doi: 10.1038/s41579-018-0147-4

Vajda, S., Yueh, C., Beglov, D., Bohnuud, T., Mottarella, S. E., Xia, B., et al. (2017). New additions to the ClusPro server motivated by CAPRI. *Proteins* 85, 435–444. doi: 10.1002/prot.25219

Wiederstein, M., and Sippl, M. J. (2007). ProSA-web: interactive web service for the recognition of errors in three-dimensional structures of proteins. *Nucleic Acids Res.* 35, W407–W410. doi: 10.1093/nar/gkm290

Wilkins, M. R., Gasteiger, E., Bairoch, A., Sanchez, J. C., Williams, K. L., Appel, R. D., et al. (1999). Protein identification and analysis tools in the ExPASy server. *Methods Mol. Biol.* 112, 531–552. doi: 10.1385/1-59259-584-7:531

Xie, D. F., Fang, H., Mei, J. Q., Gong, J. Y., Wang, H. P., Shen, X. Y., et al. (2018). Improving thermostability of (R)-selective amine transaminase from Aspergillus terreus through introduction of disulfide bonds. *Biotech. App Biochem.* 65, 255–262. doi: 10.1002/bab.1572

Zhou, X., Zheng, W., Li, Y., Pearce, R., Zhang, C., Bell, E. W., et al. (2022). I-TASSER-MTD: a deep-learning-based platform for multi-domain protein structure and function prediction. *Nat. Protoc.* 17, 2326–2353. doi: 10.1038/s41596-022-00728-0

frontiers | Frontiers in Cellular and Infection Microbiology

TYPE Original Research
PUBLISHED 04 February 2025
DOI 10.3389/fcimb.2025.1521391

OPEN ACCESS

EDITED BY
Sanket Kaushik,
Amity University Jaipur, India

REVIEWED BY
Siddhartha Kumar Mishra,
University of Lucknow, India
RaviRanjankumar Niraj,
Amity University, India

*CORRESPONDENCE
Esam I. Azhar
eazhar@kau.edu.sa
Vivek Dhar Dwivedi
vivek_bioinformatics@yahoo.com

RECEIVED 01 November 2024
ACCEPTED 08 January 2025
PUBLISHED 04 February 2025

CITATION
Ardawi MSM, Badreddine SA, Yasir M, Khateb AM, Turkistani SA, Afandi A, Noor SO, Alselmi A, Dwivedi VD and Azhar EI (2025) Overcoming beta-lactam resistance in *Pseudomonas aeruginosa* by targeting metallo-beta-lactamase VIM-1: a one-microsecond molecular dynamics simulation study.
Front. Cell. Infect. Microbiol. 15:1521391.
doi: 10.3389/fcimb.2025.1521391

Overcoming beta-lactam resistance in *Pseudomonas aeruginosa* by targeting metallo-beta-lactamase VIM-1: a one-microsecond molecular dynamics simulation study

Mohammed Salleh M. Ardawi[1], Samar A. Badreddine[2], Muhammad Yasir[3,4], Aiah M. Khateb[3,5], Safaa A. Turkistani[6], Ahmed Afandi[7], Samah O. Noor[8], Adhari Alselmi[9,10], Vivek Dhar Dwivedi[11,12]* and Esam I. Azhar[3,4]*

[1]Department of Pathological Sciences, Fakeeh College for Medical Sciences, Jeddah, Saudi Arabia, [2]Infection Control Department, Dr. Soliman Fakeeh Hospital, Jeddah, Saudi Arabia, [3]Special Infectious Agents Unit, King Fahd Medical Research Center, King Abdulaziz University, Jeddah, Saudi Arabia, [4]Department of Medical Laboratory Sciences, Faculty of Applied Medical Sciences, King Abdulaziz University, Jeddah, Saudi Arabia, [5]Department of Clinical Laboratory Sciences, College of Applied Medical Science, Taibah University, Medina, Saudi Arabia, [6]Medical Laboratory Sciences, Fakeeh College for Medical Sciences, Jeddah, Saudi Arabia, [7]Diabetic Foot Wound Center, King Fahad Armed Forces Hospital, Jeddah, Saudi Arabia, [8]Department of Biological Sciences, Faculty of Science, King Abdulaziz University, Jeddah, Saudi Arabia, [9]Clinical Sciences Department- MBBS Program, Fakeeh College for Medical Sciences, Jeddah, Saudi Arabia, [10]Dr. Sulaiman Fakeeh Medical Center, Jeddah, Saudi Arabia, [11]Center for Global Health Research, Saveetha Institute of Medical and Technical Sciences, Saveetha Medical College and Hospitals, Saveetha University, Chennai, India, [12]Bioinformatics Research Division, Quanta Calculus, Greater Noida, India

Pseudomonas aeruginosa (P. aeruginosa) is a Gram-negative opportunistic pathogen with a high resistance to beta-lactam antibiotics, mainly due to the production of metallo-beta-lactamase VIM-1 (MBL-VIM-1) enzyme. This study aimed to identify new inhibitors targeting MBL-VIM-1 to restore the efficacy of beta-lactam antibiotics. Extensive screening of natural compounds from the COCONUT database was performed to identify the structural analogs of the existing inhibitor of the MBL-VIM-1 protein. The virtual screening process selected four top-performing compounds (CNP0390322, CNP03905695, CNP0079056, and CNP0338283) that exhibited promising docking scores. These compounds were then subjected to re-docking and one-microsecond molecular dynamics (MD) simulations to assess their binding stability and interactions within the MBL-VIM-1 active site. Finally, post-MD simulation calculations were employed to estimate the interaction strengths and compare the efficacy of these compounds against the reference inhibitor. The findings highlighted that these four potent MBL-VIM-1 inhibitors show superior binding affinity and stability, suggesting their potential to combat antibiotic resistance in

P. aeruginosa. The identified compounds offer a promising avenue for developing novel therapeutics to restore the efficacy of beta-lactam antibiotics against resistant bacterial strains. Therefore, further *in vitro* and *in vivo* studies are warranted to validate their potential.

KEYWORDS

***P. aeruginosa*, metallo-beta-lactamase, VIM-1, beta-lactam antibiotics, drug discovery**

1 Introduction

Pseudomonas aeruginosa (*P. aeruginosa*) is an encapsulated Gram-negative bacterium that plays a leading role in nosocomial infections. It mainly prevails among immuno-compromised persons and chronic disease patients (Markou and Apidianakis, 2014; Wood et al., 2023). This rod-shaped, aerobic bacterium is highly resilient in the adverse conditions of the host's immune system. These characteristics facilitate versatile tropism, allowing them to colonize different human body sites, for instance, in the respiratory and urinary tracts (Kerr and Snelling, 2009; Wilson and Pandey, 2024). Due to its metabolic versatility, this bacterium also thrives in soil, water, and various surfaces within hospital environments, making it challenging to control and contain. Epidemiologically, *P. aeruginosa* has been proven to be associated with several outbreaks worldwide, mainly attributed to its resistance to several antimicrobial agents (Kowalski et al., 2001; Pachori et al., 2019; Schärer et al., 2023). These outbreaks have been especially catastrophic in the Intensive Care Units (ICUs) because the bacterium quickly causes ventilator-associated pneumonia, bloodstream infections, and surgical site infections among immune-compromised patients (Esposito and Leone, 2007). Moreover, the emerging MDR strains of this bacterium have worsened the situation with high morbidity, mortality rates, and treatment costs (Kunz Coyne et al., 2022).

Another key point in the pathogenicity of *P. aeruginosa* is its extensive array of virulence factors and mechanism for evading the host immune system and resisting antibiotic actions (Drenkard, 2003). Some of the significant factors are biofilm formation, efflux pumps that expel antibiotics, and beta-lactamases that degrade beta-lactam antibiotics into inactive small molecules (Dreier and Ruggerone, 2015) Beta-lactamase significantly contributes to antibiotic resistance by hydrolyzing the beta-lactam ring in many antibiotics, such as penicillins, cephalosporins, and carbapenems (King et al., 2014; Akhtar et al., 2022; Lin and Kück, 2022). Several types of beta-lactamases are produced by *P. aeruginosa*; however, Metallo-beta-lactamase (MBLs) are of particular concern. These enzymes that depend on divalent cations, such as zinc ions, for their function can cleave a large of types of beta-lactam rings from different groups of antibiotics that are usually used in the treatment of MDR bacterial infections (Tamilselvi and Mugesh, 2008; Karsisiotis et al., 2014).

The emergence of MBLs, particularly the Verona integron-encoded metallo-beta-lactamase (VIM) family, has been a significant driver of carbapenem resistance in *P. aeruginosa*. VIM-1, the first member of this family to be identified, was initially reported in Italy in the late 1990s and has since been detected in various parts of the world (Makena et al., 2016). The spread of VIM-1 is often associated with mobile genetic elements such as plasmids and integrons, which facilitate its dissemination across different bacterial species and strains.

The VIM-1 enzyme has been reported to be able to hydrolyze carbapenems. It is resistant to inhibition by the most commonly used beta-lactamase inhibitors, putting a serious challenge to managing infections produced by VIM-1-producing *P. aeruginosa* (Salimraj et al., 2019). As a result, the search for effective inhibitors against VIM-1 has emerged as one of the significant priorities of antimicrobial science. In particular, the action against MBL, like VIM-1, might present a good strategy to increase the efficacy of beta-lactam antibiotics against *P. aeruginosa*-resistant strains (Tehrani and Martin, 2017). Preliminary work towards discovering inhibitors for MBL VIM-1 has been undertaken, and several molecules have been identified; however, most show drawbacks. For instance, thiol-based compounds include thiomandelic acid, pharmacokinetic profile, and toxicity effects (Mollard et al., 2001). Other inhibitors, such as some hydroxamates and dithiocarbamates, also need help regarding specificity and stability. However, there are no clinically approved VIM-1 inhibitors, so it becomes necessary to find other ways around the constraints of the above-named candidates (Ju et al., 2018).

The COCONUT database reflects an enormous field of natural products containing possible pharmacological effects (Sorokina et al., 2021; Nainala et al., 2024). COCONUT has more than 6 lakh unique natural compounds and a broad chemical space coverage, vital for drug discovery and identifying new inhibitors to different targets, including MBL VIM-1. Since many of the compounds in the COCONUT database are of natural origin, they generally exhibit novel structural characteristics and bioactivities that have not been observed in synthetic libraries, thereby making them ideal sources for identifying lead compounds (Chávez-Hernández et al., 2020).

In this study, our objective was to find the potential inhibitors of MBL VIM-1 through the comprehensive analysis of the natural compounds obtained from the COCONUT database. Herein, a

multi-step drug discovery protocol was employed. This includes virtual screening for filtering out the compounds using the Lipinski rule of five; molecular re-docking studies for verification and refinement of the selected compounds and target protein; molecular dynamic (MD) simulation to evaluate the stability and behavior of the generated complexes and molecular mechanics with Generalized Born and Surface Area (MM/GBSA) analysis to calculate the free energy of binding. Through this meticulous workflow, we identified natural compounds with substantial inhibitory potential against MBL VIM-1 protein, offering promising leads for developing new therapeutic strategies to fight MDR strains of *P. aeruginosa*.

2 Methodology

Figure 1 shows the workflow chart summarizing the computational approach used, including preparing protein and ligand, virtual screening, re-docking, molecular dynamics simulations, and free binding energy calculations. This flowchart acts like a map for the detailed methodology that follows, elaborating each step in detail.

2.1 Protein preparation and ligand data collection

The crystal structure of the target protein, MBL VIM1, was obtained from the Protein Data Bank (PDB ID: 8PB2) (Berman et al., 2000). The protein was prepared using the Chimera Dock Prep tool (Pettersen et al., 2004). This included the steps of hydrogen adding and charging according to the specified partial charges, as well as the elimination of water molecules and bound ligands to bring the protein to a state suitable for docking.

The COCONUT database containing 406,076 compounds was utilized for identifying the structural analog of the existing inhibitor XQ5 [(7-[(1~{S})-1-[4-(carbamimidamidomethyl)-1,2,3-triazol-1-yl]ethyl]-3-[3-fluoranyl-4-(methylsulfonylmethyl)phenyl]-1~{H}-

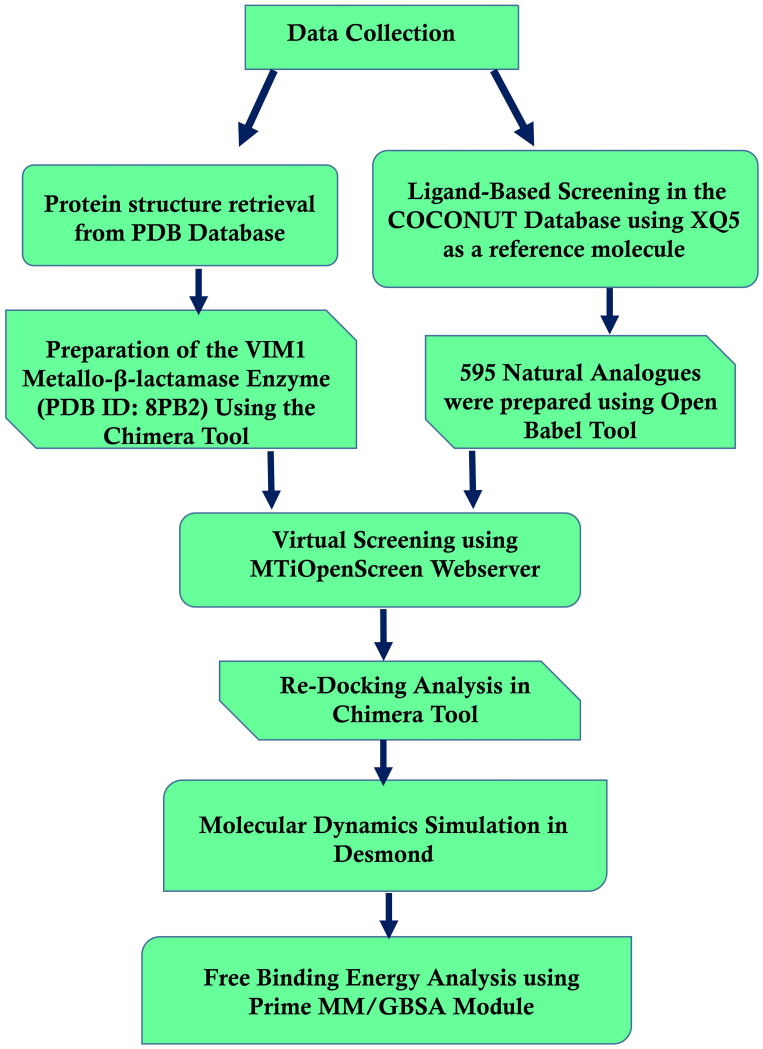

FIGURE 1
Workflow of computational methods for identifying *Pseudomonas aeruginosa* Metallo-Beta-Lactamase VIM-1 inhibitors.

indole-2-carboxylic acid)] present in the MBL VIM1 protein structure at a 70% Tanimoto similarity threshold (Mollard et al., 2001). The ligand structures were obtained from this database in SDF format and optimized to PDBQT format using Open Babel (O'Boyle et al., 2011). The natural compounds collected were prepared to maintain the protonation state using the Chimera tool (Pettersen et al., 2004; Trott and Olson, 2010). To further filter the input and select only drug-like molecules, the Lipinski Rule of Five was implemented (Lipinski, 2004), which acts on the compounds according to their physicochemical characteristics and then ensures that the compounds possess the desired pharmacokinetic traits.

2.2 Virtual screening and re-docking analysis

Virtual screening was performed using the MtiOpenScreen webserver (Labbé et al., 2015). For the screening process, a docking grid was precisely set at coordinates (X = -23.39, Y = -12.39, Z=10.76) and extended 30 Å along each axis (X, Y, Z). Further, the highest binding energy compounds obtained after the intensive screening along with the existing inhibitor XQ5 were again subjected to molecular re-docking using the AutoDock Vina plugin within UCSF Chimera (Trott and Olson, 2010). Re-docking involved generating multiple binding poses for each compound, allowing us to explore their interactions within the VIM1 active site more thoroughly. The AutoDock Vina algorithm was employed to refine the docking results, confirming the selected compounds' binding affinities and interaction profiles. This re-docking process validated the initial screening results and provided a robust foundation for subsequent molecular dynamics simulations and free energy calculations. The XQ5 inhibitor was considered as a reference molecule for the comparative analysis with the selected natural compounds.

2.3 Molecular dynamic simulation and trajectory analysis

The MD simulations were conducted using the Desmond-maestro interpolarity tool free academic version, which is well-suited for studying the dynamic behavior of biomolecular systems (Bowers et al., 2006). To generate each of the protein-ligand complexes, we placed the system in an orthorhombic water box in such a way that the minimum distance between the solute and box periphery was 10 Å. The background charge of the system was also maintained at a low level by adding counter ions, thus mimicking biological conditions. The biomolecular force field OPLS-2005 was used for the parameterization of the protein and the ligands since this force field is reasonable and accurate for biomolecular interactions (Harder et al., 2016). Subsequently, energy minimization was conducted to eliminate any unfavorable close contacts in the generated system (Jaidhan et al., 2014). This process was crucial in achieving a steady state before the production phase of the simulation work. The systems were minimized and then gradually coupled with the temperature reservoir at 300 K for 100 picoseconds in the NVT ensemble. Equilibration was then carried out under the condition of several particles, pressure, and temperature (NPT ensemble) for 1 ns to give the system time to reach density and other thermodynamic properties before the actual production runs. The MD production simulations for all the complexes were performed for 1000 ns under the NPT ensemble only. Choose a time step of 2 fs and control the long-range electrostatic effect using the Particle Mesh Ewald (PME) method. Additional trajectories were obtained every 10 ps from the simulation process to facilitate a more refined resolution. Trajectory analysis concentrated on the evaluation of the stability and changes in the protein-ligand structure. The structural strength of the protein backbone and flexibility of the involved residues were assessed using Root Mean Square Deviation (RMSD) and Root Mean Square Fluctuation (RMSF) of the final simulation frames. The number of hydrogen bonds between the protein and the ligand was recorded during simulations to capture the stability of these bonds.

2.4 Free binding energy using MM/GBSA calculation

The free binding energy calculations were performed using the Prime MM/GBSA module (Schrödinger Release 2024-2: Prime, Schrödinger, LLC, New York, NY, 2024) to compare the binding energies of the chosen MBL VIM1 inhibitors. Assigning the free binding energies, the MMGBSA method helped to obtain a considerable number of data regarding the interaction constancy and intensity between the ligands and the VIM1 protein (Genheden and Ryde, 2015a). Using the Generalized Born model, the MMGBSA method calculated the binding free energy through molecular energies and solvation. This method allowed the evaluation of enthalpy and entropy associated with the binding event when calculating the binding free energy. The binding energies were thus calculated and compared between the four complexes as well as the reference molecule, in terms of their ability to inhibit VIM1 quantitatively. This detailed analysis provided key insights into the most promising inhibitors for further experimental validation.

3 Results

3.1 Virtual screening analysis

A total of 595 natural compounds, structurally analogous to the native inhibitor XQ5, were identified and selected for structure-based virtual screening. Of these, 332 compounds were filtered out, exhibiting energy ranges between -10.816 kcal/mol and -3.129 kcal/mol, as detailed in Supplementary Table S1. Four natural compounds —CNP0390322, CNP0390569, CNP0079056, and CNP0338283— were selected for further analysis based on their docking energies, which were -10.81 kcal/mol, -10.79 kcal/mol, -10.76 kcal/mol, and -10.73 kcal/mol, respectively. While according to ADME's available data, these selected compounds exhibit superior drug-like properties compared to the control, they have lower molecular weights, higher lipophilicity (higher XLogP3 values), and smaller topological polar

surface areas, which indicate better pharmacokinetics and bioavailability. Additionally, these natural compounds are simpler and more defined chemical structures than the native inhibitor XQ5 suggesting more selective biological interactions, making them stronger candidates for further study.

3.2 Redocking and intermolecular calculation

The redocking procedure was conducted for the four selected natural compounds that exhibited the highest negative docking scores from our virtual screening, aiming to form stable complexes with the target protein. The redocking results underscored the robust binding potential of these compounds to the target protein, affirming their suitability for more detailed examination. The calculated binding energy of selected compounds (1, 2, 3, and 4) was -8.7 kcal/mol, -8.7 kcal/mol, -9.4 kcal/mol, and -9.6 kcal/mol, respectively, and -10.7 kcal/mol for the control (XQ5). This method not only validated the initial virtual screening results but also confirmed that the selected compounds are strong candidates for subsequent studies, as shown in Figure 2. The 3D and 2D structures were generated using Maestro, as shown in Figure 2.

The complex VM1-CNP0390322 exhibited a strong interaction profile characterized by several key interactions. The complex formed a hydrogen bond with Asn210, a residue commonly engaged in stabilizing ligand binding through hydrogen bonding networks. In terms of hydrophobic interactions, the VM1-CNP0390322 complex was surrounded by several hydrophobic residues, including Phe62, Tyr67, Trp87, Cys198, Ala208, Ala212, and Trp219, which contribute to the stabilization of the ligand within the hydrophobic pocket of the protein. Additionally, a significant π-π stacking interaction is observed with His240, indicating a potential role in further stabilizing the ligand through aromatic interactions. The compound CNP0390569 in the target protein also interacts with Asn210 via hydrogen bonding, indicating the importance of this residue in ligand stabilization. Hydrophobic interactions are observed with Phe62, Tyr67, Pro68, Trp87, Cys198, Ala208, and Ala212. These residues form a hydrophobic pocket's favorable condition for ligand binding—the interaction between ligand and His116 in this complex forms π-cation for stabilizing the binding of the protein. Likewise, CNP0079056, when complexed with VM1, builds another hydrogen contact with Asn210, and this residue contributed a similar role among various complexes. The hydrophobic interactions have been formed by Phe62, Tyr67, Pro68, Trp87, and Cys198 residues; they are conserved in all three complexes. Among the three, this complex exhibits multiple π-π stacking interactions with Phe62, Tyr67, Trp87, and His240, suggesting a stronger aromatic interaction pattern that may improve the stability and the interactions between the ligand and amino acids. The VM1-CNP0338283 complex showed a hydrogen bond with Asn210, strengthening the ligand anchoring hypothesis. These involve Phe62, Tyr67, Pro68, Trp87, Cys198, and Ala 212, present in a homologous conserved hydrophobic pocket seen in the prior complexes. It is, therefore, possible to conclude that the π-cation interaction with His116 describes a similar binding mode to that of the VM1-CNP0390569 complex. In the VM1-XQ5 control complex, multiple hydrogen bonding was formed by Glu146, Ser207, Gly209, Asn210, and Asp213. The Phe62, Tyr67, Trp87, Phe115, Cys198, and Ala212 residues aided the ligand in fitting into the pocket through the hydrophobic bond. The presence of the π-cation interaction with His116, characteristic of all other complexes, suggests that these ligands have similar binding profiles. The behaviors of these complexes revealed that Asn210 is critical for hydrogen bonding while hydrophobic pocket conserved by Phe62, Tyr67, Trp87, and Cys198, and π-π stacking or π-cation interaction with His116 and His240 in stabilizing the ligand-protein complex (Supplementary Table S2).

3.3 Structure-activity relationship analysis of compounds interacting with VIM-1

The analysis of the interactions between the compounds and VIM-1 reveals critical structure-activity relationships. Hydrogen bonding with Asn210 is a consistent feature across all compounds, indicating its pivotal role in ligand stabilization within the binding pocket. Additionally, hydrophobic interactions with residues such as Phe62, Tyr67, Trp87, Cys198, Ala208, and Ala212 form a stable hydrophobic pocket, which supports the anchoring of the ligands. The presence of π-π stacking and π-π cation interactions with His240 and His116 highlights the importance of aromatic moieties in the compound structures, enabling favorable interactions with key aromatic residues in VIM-1. These findings underscore the significance of hydrogen bond donors/acceptors, hydrophobic substituents, and aromatic centers in driving the ligand's affinity and specificity for VIM-1.

To optimize binding, future modifications could enhance hydrogen bonding with Asn210 and strengthen interactions within the hydrophobic pocket by introducing suitable non-polar substituents. Retention or expansion of aromatic rings would further leverage π-π stacking interactions, particularly with His240 and His116. These insights can be experimentally validated through mutational studies targeting Asn210, His116, and His240 to confirm their functional roles, alongside testing derivatives with modified chemical groups.

3.4 Dynamical analysis

In our study, the stability and flexibility of the four complexes were investigated by 1000 ns MD simulations. These simulations were very important in observing the dynamic behavior of the complexes. The key parameters like RMSD and RMSF were carefully monitored and recorded for protein and ligand parts. RMSD measurements were helpful in analyzing the general stability because they presented their complex structures as a function of time in terms of deviations from their starting conformations. Conversely, RMSF analysis showed the movement of individual protein residues that can be affected in terms of the structural changes that might affect ligand binding. Further, the formation and duration of hydrogen bonds in each complex and throughout the entire simulation period were also observed to determine the interactions involved in the complexes' stability.

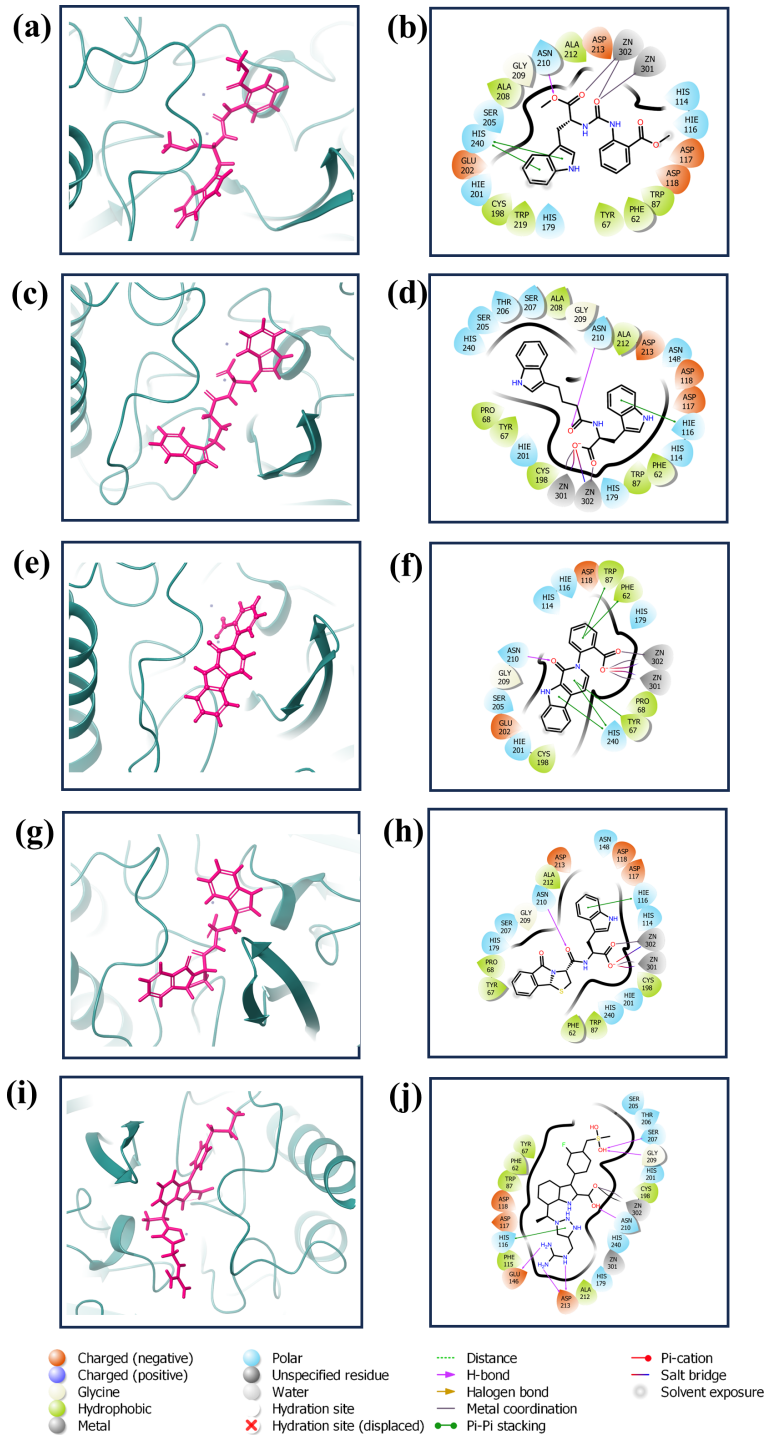

FIGURE 2
3D and 2D interaction diagram of the VIM1 docked with selected compounds: **(A, B)** CNP0390322, **(C, D)** CNP0390569, **(E, F)** CNP0079056 **(G, H)** CNP0338283 and **(I, J)** XQ5 (reference).

3.4.1 RMSD analysis

The RMSD is a very important parameter for measuring the stability of a complex during MD simulations. They bring information about conformational changes and the general stability of the protein and the ligand over time, as depicted in Figure 3 (Pavan et al., 2022). Thus, in this analysis, the fractional RMSD of the ligand has been seen along with the protein dared over a simulation time of 1000 ns of four compounds also one control molecule. The backbone RMSD for the protein in the compound CNP0390322 in complexed with protein was stable with an average range of 1.5 Å to 2 Å for the last 100 ns of simulations out of 1000 ns of simulation period. This means that the protein is conservative in its conformation suggesting a good structural stability during its interaction with CNP0390322. The RMSD of the ligands oscillates

10.3389/fcimb.2025.1521391

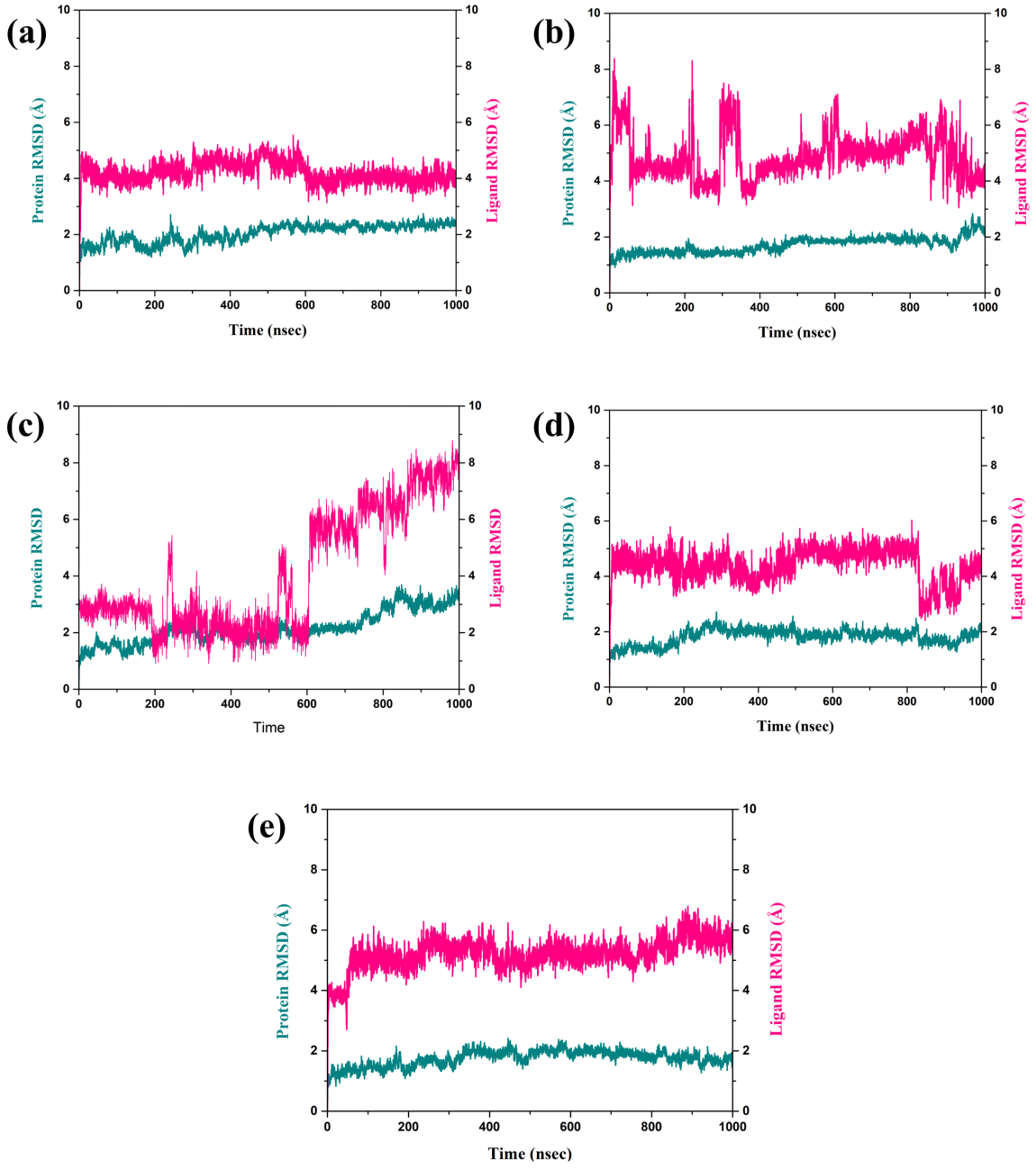

FIGURE 3
RMSD plot of the simulated VIM1-natural compounds **(A)** CNP0390322, **(B)** CNP0390569, **(C)** CNP0079056, **(D)** CNP0338283 and **(E)** XQ5 (reference).

in a range between 4 Å and 4.5 Å and occasionally reaches values above 5 Å but tends to stabilize in the further course of the simulation. Fluctuations in the protein RMSD and the ligand RMSD minimally suggest that compound CNP0390322 has a stable binding mode within the active site, and the conformation change of the protein during the simulation is minimal. The protein RMSD in the compound CNP0390569 in complex with protein was similar to that of compound CNP0390322, which varied from 1.5 Å to 2.0 Å. However, these values reach a fixed, stable point after 200 ns, implying that the protein might alter its conformation slightly and then attain a more stabilized state. The ligand RMSD was more variant and oscillated between 2.0 Å and 8.0 Å, and the variations were even more prominent in the first 200ns but gradually settled at about 5. Å. Higher RMSD values arising from compound CNP0390569 suggest more substantial conformational flexibility within the binding pocket and, hence, a less stable binding profile as compared to compound CNP0390322. The protein RMSD for CNP0079056 in complex with protein deviated from 1.5 Å to 2.0 Å. The target protein remains reasonably stable throughout the simulation, indicating that the protein conformation does not change appreciably upon binding with the compound CNP0079056. The ligand RMSD fluctuates from the value of

around 1.5 Å to 3.0 Å and increases somewhat with time but remains viable beyond 200 ns. Such a pattern implies that compound CNP0079056, maintains its localization within the binding pocket with insignificant changes, exhibiting high binding affinity and stability. For the compound CNP0338283 complex, the protein RMSD varies slightly from 1.5 Å to 2. Å then remains steady. The secondary structure of the protein seems to be reasonably good, indicating a proper orientation with the ligand. The range of the ligand RMSD in this complex varies from 2.0 Å to a maximum of 6.0 Å with occasional spikes. Nevertheless, these RMSD values reflect the fact that the ligand is also somewhat flexible within the binding pocket while the interaction is rather constant over time. The variation of the control molecule demonstrates the protein's RMSD in a stable condition with values of 1.5 Å- 2.0 Å, as in the case of CNP0390322 and CNP0079056. This stability demonstrates that much of the protein's structure remains rigid or unchanging. Comparing the RMSD of the control molecule for the ligand shows higher fluctuations, which vary between 5.0 Å to 6.0 Å and have a general tendency to increase as the simulation progresses. This implies that the control ligand rotated more freely and was less stable in the binding site of the protein.

3.4.2 Protein RMSF analysis

Structural flexibility and stability derived from RMSF proved valuable in determining the freedom and steadiness of specific residues within the complexes, as indicated in Figure 4 (Sharma et al., 2021). The RMSF analysis was performed to compare the dynamic flexibility of the complexes in different compounds. RMSF is an atomic fluctuation from its average position when calculated for a set of atoms and its capability to analyze the dynamic behavior of certain protein parts compared to others during molecular dynamics simulations. In the case of the VM1 protein complex with compound CNP0390322, the RMSF showed a value of 4.5 Å within the range of amino acid positions 170 – 190. This implies that this part of the protein shows moderate flexibility in complexation with compound CNP0390322, and this aspect can have an influence on the dynamics of the tightening interaction, including the binding strength of the formed complex. For the complex VM1-

CNP0390569, the protein showed an RMSF value of less than 4 Å within the same range of amino acids. This lower RMSF value suggests that the protein becomes more rigid when in the presence of CNP0390569, which may stabilize the binding conformation in this area. Like CNP0390322, CNP0079056 had an RMSF of 4.5 Å for the residues 170–190. This indicates that compounds CNP0390322 and CNP0079056 may cause similar flexibility in this area of the protein, most likely to affect binding and overall stability within a similar framework. On the other hand, the compound CNP0338283 has an RMSF value of less than 4.5 Å in the similar amino acid range, slightly less than compounds 1 and 3 but more flexible compared to CNP0390569. Lastly, in the control molecule XQ5, the RMSF value was below 4.5 Å as well, but this time in the region of amino acids 170 – 190. Comparability of this stabilization with the compounds seen in the control group to some of the other complexes could be seen due to the similar effect on the protein dynamics.

3.4.3 Ligand RMSF analysis

RMSF analysis provides insights into the flexibility of the ligand atoms during the MD simulation as shown in Figure 5. Higher RMSF values indicate more flexible regions of the ligand, while lower values suggest more stable regions. The RMSF plot for CNP0390322 shows significant fluctuation, particularly around atom 5 and atom 27, with peaks reaching approximately 3.0 Å. The RMSF values of these peaks depict these regions of the ligand as flexible, while the other parts of the molecule have near-stable RMSF values of between 1.0-2.0 Å. The residue-specific profiles of CNP0390569 show a steady increase in flexibility up to the 17th atom with the RMSF value of about 6.0 Å. This means that a particular region within the ligand is more flexible during the simulations, suggesting that it may be flexible or have a substructure that is flexible in solution while the remainder of the ligand has a more rigid structure. The changes in the RMSF profile found for CNP0079056 are highest around atoms 9 up to 22, and the maximum is at about 6 Å. This alone points to the fact that the middle part of the ligand is relatively more mobile compared to the other regions where lower RMSF values hint at greater stiffness. Analyzing the CNP0338283, it is possible to observe that the RMSF values constantly increase from the beginning of the molecule and reach the maximum value between atoms 14 and 20 with approximately 3.5 Å. This suggests that the middle and towards the end of the ligand have a certain flexibility, and the remaining parts of the ligand remain almost rigid. On the other hand, control has the largest RMSF fluctuations with regard to the values across the molecule. Notable peaks occur around atoms 17 and 22, reaching up to 3.5 Å. This suggests that the control ligand is more flexible throughout the simulation, indicating weaker binding stability in comparison to the tested compounds. The RMSF analysis highlights the different flexibility profiles of the ligands across the compounds. Compounds 1 and 4 show specific regions of increased flexibility, while CNP0390569 and 3 demonstrate central region flexibility.

3.4.4 Protein-ligand profiling

Information about the interaction of protein and ligand is crucial in determining the stability and significance of ligand to the target protein. The understanding of various types of interactions, namely hydrogen bonds, hydrophobic interactions, cations and anions interactions, and water-mediated bridges, offers insight into the direction and strength of binding (Chen et al., 2016). The specific patterns of the observed interactions for each of the four compounds and the control are described in Figure 6. Ligand binding requires hydrogen bonds, especially for the specificity and stability of the interaction. Similarly in complex CNP0390322, VAL200 and ASN210 are greatly involved with hydrogen bonding with the ligand. These bonds presumably play a role in the enhancement of stability of the ligand within the matrix and strong interaction. In the present context, hydrophobic interactions assist in stabilizing the ligand so that it is shielded

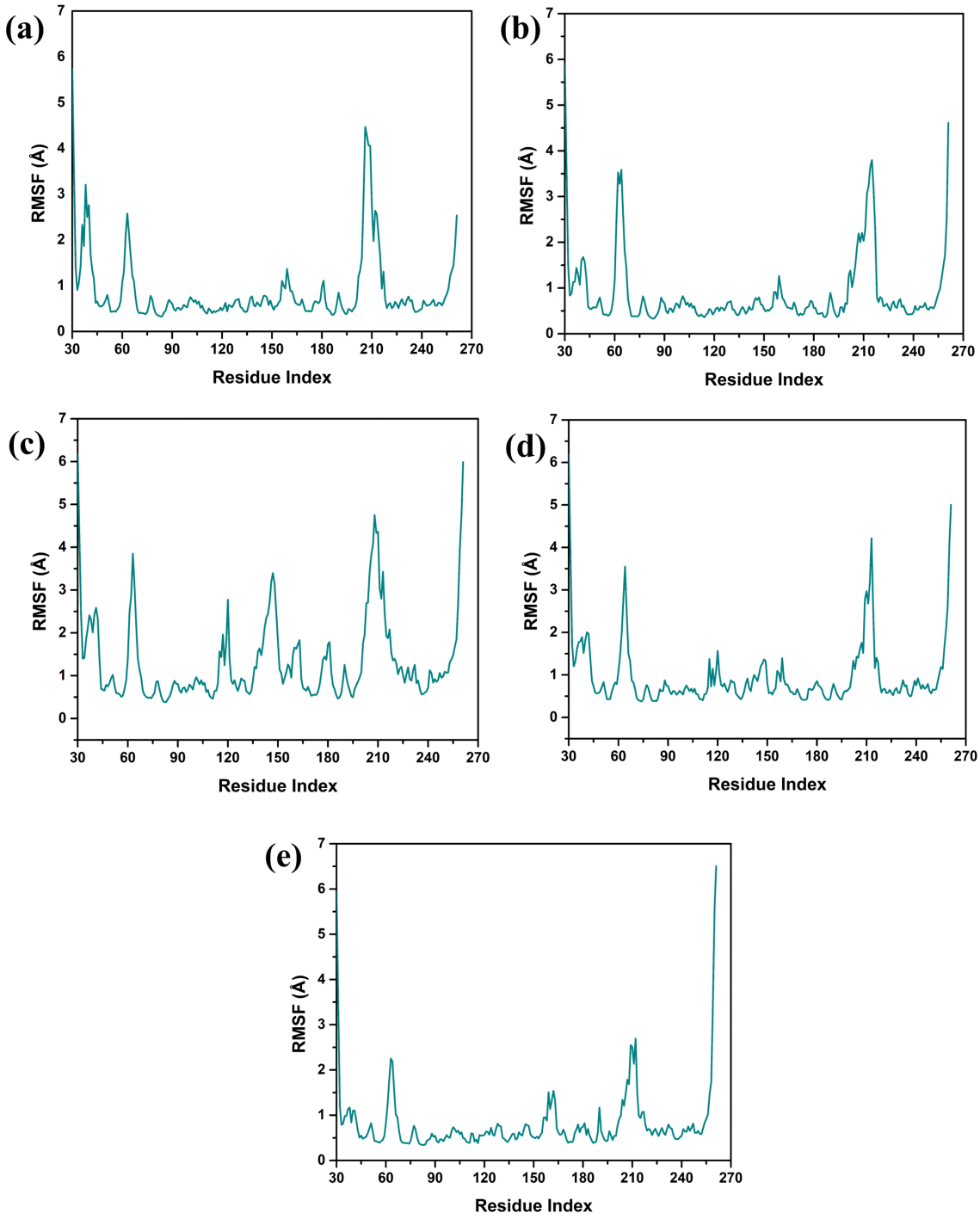

FIGURE 4
Protein RMSF plot of the simulated VIM1-natural compounds **(A)** CNP0390322, **(B)** CNP0390569, **(C)** CNP0079056, **(D)** CNP0338283 and **(E)** XQ5 (reference).

from water molecules in the binding site. PHE62 and TRP219 contribute significantly to the ligand molecule; both are hydrophobic in nature; it is indicated that these residues have an important role in tethering the ligand molecule firmly in the protein matrix. It also assists in maintaining the structural stability of the complex mainly because of the high-rise nature of this structure. Ionic interactions are mostly observed with basic and acidic residues, and the strength of the interaction is reflected in the binding energy. This is found to be present at positions such as HIS114, ASP118, and HIS240, a positively charged residue, hence participates in the ionic interactions or probably increases the binding strength of the providers to the ligands by direct electrostatic attraction. Few water bridges were observed, which also suggests that the most important interactions are direct

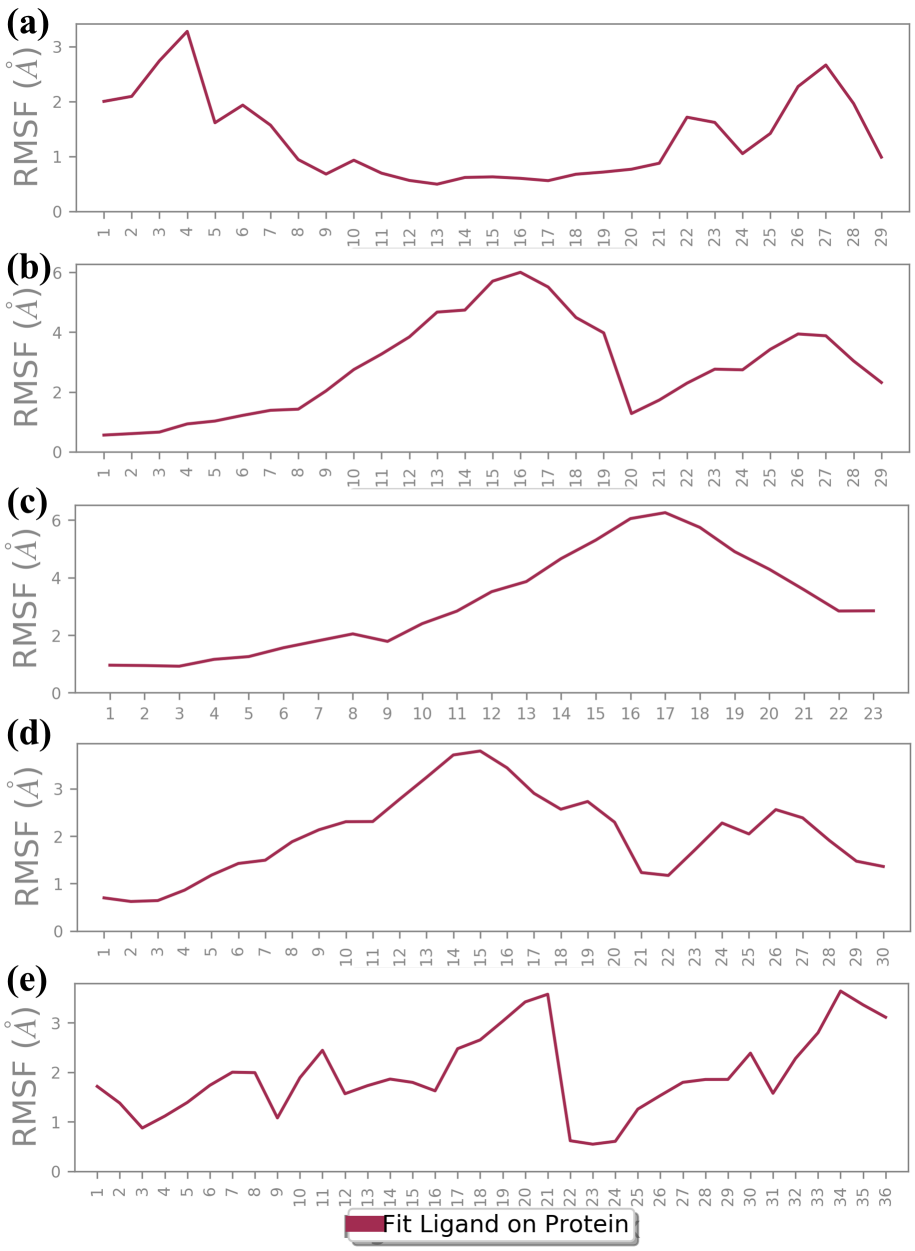

FIGURE 5
Ligand RMSF plot of the simulated VIM1-natural compounds **(A)** CNP0390322, **(B)** CNP0390569, **(C)** CNP0079056, **(D)** CNP0338283 and **(E)** XQ5 (reference).

contacts between the ligand and the protein. Compound CNP0390569 interacts with HIS201 and ASN210 through strong hydrogen bonds. These interactions may well be crucial for the positioning of ligands in the binding site and to the stability and possibly the efficacy of the compound. Whereas TYR69 and HIS116 give a hydrophobic pocket that stabilizes the ligand through nonpolar forces. These residues presumably help in positioning the ligand correctly and also in increasing the binding affinity by avoiding exposure of the ligand to water. The presence of ionic interactions between the TRP87, ASP118, HIS179, and CYS198 and the ligand point to the existence of electrostatic forces in further enhancing the binding affinity of the ligand into the binding pocket. The relative frequency of water bridges indicates that the ligand likely interacts directly with the binding site and indirectly through water molecules, which may give the binding site more versatility in terms of strength and flexibility. Like Compound CNP0390569, the present compound has also been observed to form intense H-bond interactions with both, CYS198 and ASP213. These interactions are significant for the stability and orientation of the ligand, indicating that the ligand has a rather high specificity for binding these residues. The ligand in Compound CNP0079056 has pronounced hydrophobic contacts with HIS116, HIS179, and TRP219 residues. These interactions help to maintain the stability of the complex because the correct orientation of the ligand in a binding pocket always prevents adverse forces like water from affecting the structure. These ionic interactions are HIS114, ASP118, HIS116,

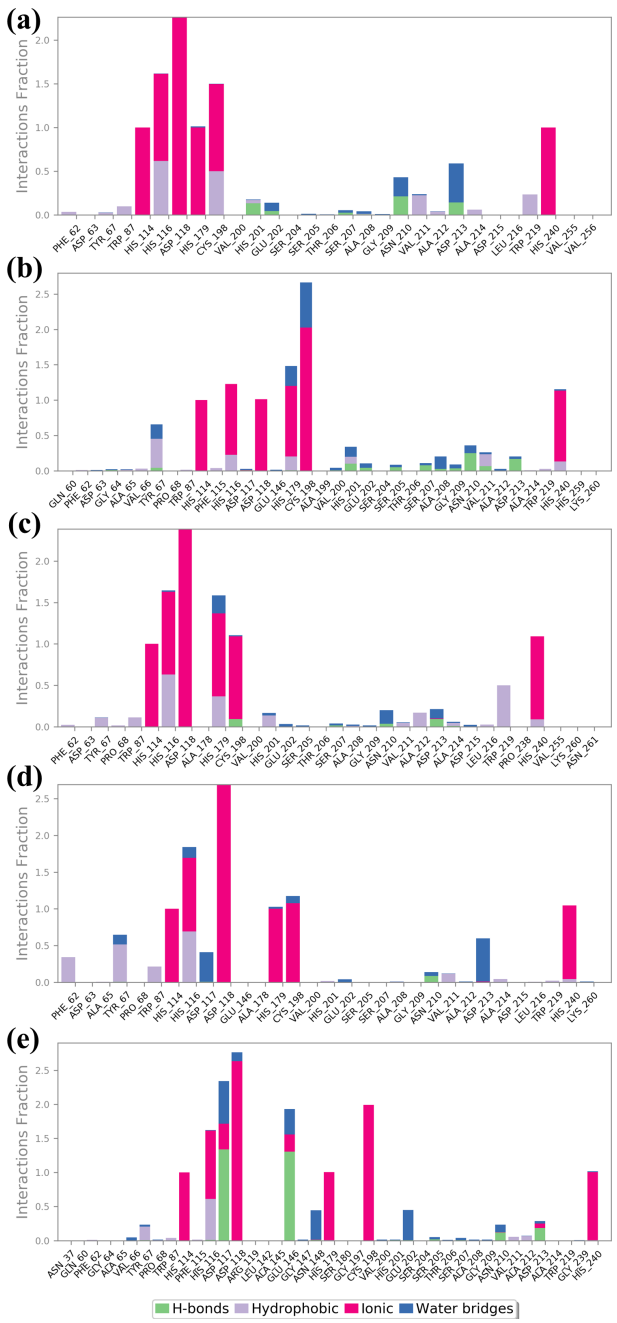

FIGURE 6
Protein-ligand profile analysis of the simulated VIM1-natural compounds **(A)** CNP0390322, **(B)** CNP0390569, **(C)** CNP0079056, **(D)** CNP0338283 and **(E)** XQ5 (reference).

and CYS198, implying the compound's consistent interaction type in stabilizing the ligand through ionic binding interaction, which supplements the binding interaction. This is particularly evident where water-mediated interactions indicate that direct contacts are stronger, but the ligand also uses water molecules to bridge interactions with the protein; a factor that could also contribute to the flexibility or adaptability of the binding. As in the case of the other compounds, CNP0338283 has strong interactions with ASN210 mainly by means of hydrogen bonds. Such a similar pattern observed in a number of compounds supports the view on the importance of these residues for the stabilization of ligands that have to remain bound to the protein with high selectivity. The hydrophobic interactions of PHE62, TYR67, and HIS116 are strongly indicative that all these residues are crucial to the stability of the ligand. These interactions are useful in sustaining the ligand at the correct orientation and position and may even improve the binding selectivity by reducing entropy changes during binding. The presence of interacting ionic residues such as HIS114, HIS116, ASP118, and HIS179 with the ligand supports the statement that electrostatic forces are vital in stabilizing the ligand-protein complex. The change in the number of water bridges present in CNP0338283 indicates that water molecules seem to play a more active role in the ligand and protein interactions; the water bridge may provide the ability to change conformation to accommodate for slight changes in the structures of the protein and ligand during the course of the simulation. The control ligand makes comparatively fewer hydrogen bonds than the test compounds that are mainly with ASP 117 and GLU 146 residues. This may indicate that the frequency of hydrogen bonding is less in this case and, therefore, might be less strong or less stable binding interactions than the other ligands. The control ligand also interacted with HIS 116, VAL 66, and HIS 116 in hydrophobic interactions, as observed with the test compounds. Nevertheless, these interactions are not as often, and that means that it could be much more challenging to stabilize the control ligand inside the binding pocket. While ionic interactions are observed with HIS114, ASP118, HIS179, and CYS198, the interaction fraction is less compared with test compounds. This could mean that the electrostatic interaction favored by the control ligand is not as strong, which yields a less stable complex. The control ligand again exhibited the most frequency of the water bridges. That such a significant amount of interactions are mediated by water might imply that the control ligand is not very firmly fixed in the binding pocket, and its binding can only be stabilized by weak transient water bridges.

The detailed analysis of protein-ligand interactions for the four test compounds (1, 2, 3, and 4) and control reveals a complex and nuanced binding landscape within the active site of the target protein, as shown in Figure 7. The interactions were assessed based on their frequency of occurrence during molecular dynamics simulations, providing insights into the stability and nature of these interactions. Such analysis is crucial for understanding the binding efficacy and potential of these compounds as inhibitors or modulators of the protein's function. Across all four test compounds, a consistent pattern of interaction was observed with key residues: HIS 116, HIS 114, HIS 179, CYS 198, HIS 240, and ASP 118. Each of these residues showed a 100% interaction frequency, indicating that they played a very important role in stability. The active zinc ion (Zn2+) also gave a 100% interaction frequency within all the compounds and plays a critical role in the coordination of the ligand via metal chelation. These interactions may be considered to indicate a planar binding mode of the ligand, where it is held fixed in a specific orientation with the protein's active site. The similarity of these interactions implies that all four compounds bind to the target protein in a very similar manner, and these residues are critical in preserving the

10.3389/fcimb.2025.1521391

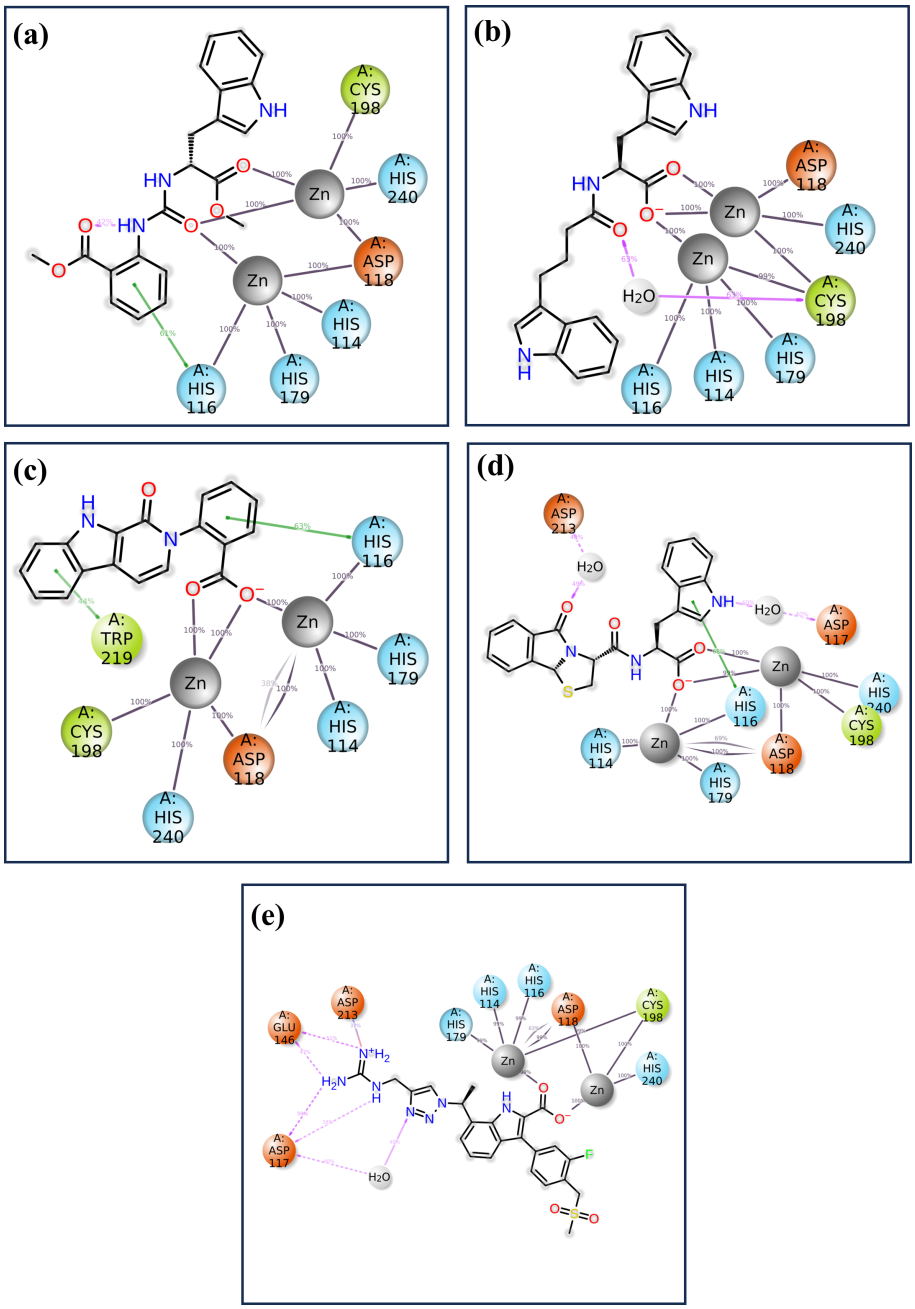

FIGURE 7
The 2D interaction of diagram of the simulated VIM1-natural compounds **(A)** CNP0390322, **(B)** CNP0390569, **(C)** CNP0079056, **(D)** CNP0338283 and **(E)** XQ5 (reference).

conformation of the ligand-protein complex. However, there are significant differences among the compounds that might affect the binding interactions. For example, CNP0079056 in the 50% interaction group interacts with TRP 219 in a manner different from others in the same group. This partial interaction indicates that TRP 219 may be involved in binding stability to a lesser extent but in a different mode of interaction that may allow the ligand to accommodate minimal structural variations in the binding pocket. This could prove advantageous in a fluctuating environment, where slight changes in the binding capacity could improve the compound's affinity or specificity. Like in the previous case, CNP0338283 interacts with ASP 212 as well, but with 50% frequency. Such interaction could give an additional electrostatic contribution that adds further contact points, which are not always demanded but could give some additional contribution to the orientation of the ligand. However, the control ligand has a slightly different interaction mode to the test compounds. As it establishes close and persistent contact with the core residues at 100% frequency, it also has extra communication with GLU148 and ASP117 at 55% and 60%, respectively. Such interactions are not as persistent and as frequent as they are in the case of the core residues implying that the binding mode is more dynamic or less stable. The

fact that these additional but partial interactions are relied upon by the control ligand might simply mean that it does not fit as securely into the binding pocket as the test compounds. Such partial interactions are identified in both the test compounds as well as the control molecules – the involvement of certain residues is more stable and uniform, while others contribute partially or only under specific conditions. The test compounds demonstrated consistent interactions with particular key residues and additional opportunities to form stabilizing contacts, which implies that the compounds may have a well-balanced binding process capable of effectively inhibiting the target protein.

3.4.5 SASA analysis

SASA was calculated for a 1000 ns molecular dynamics (MD) simulation to compare the effect of four compounds on the structural stability and dynamics of the protein-ligand complex, as presented in Figure 8. SASA is another important feature that represents the solvent-exposed surface of the protein and provides information about the structural flexibility of the ligands in the binding pocket (Durham et al., 2009). SASA analysis for compound CNP0390322 has the range of about 160 Å²-240 Å² with average SASA value of approximately 200 Å². The plot shows that for a major part of the simulation, the complex keeps a relatively constant value of solvent exposure and only has small oscillations occasionally. The histogram indicates that most of the residues are near the midpoint of the histogram, which suggests that the protein-ligand complex exists most often in a stable conformation with reasonable solvation. Such stability shows that CNP0390322 binds nicely within the pocket and does not create a strain on the amino-acid residues, which could distort the conformation of the protein. Where CNP0390569 is concerned the SASA values are more volatile, varying between 200 Å² and 400 Å², with the average value being closer to 300 Å². The strengthened values of SASA point to the fact that the protein experiences greater conformational changes due to the binding of CNP0390569. The histogram suggests that the complex samples had multiple conformations during the simulation and were, therefore, wider. This means that CNP0390569 brings fluctuation within the protein possibly making it less stable to bind and more exposed to solvent than CNP0390322. The SASA values during the MD simulation for CNP0079056 show an initial drop and then start oscillating around 160 Å², and then after rising up to approximately 300 Å², the average SASA was found to be around 220 Å². These trends indicate the initial formation of stronger interactions between CNP0079056 and the protein in a more compact conformation compared to the other parts of the simulation process upon the formation of more

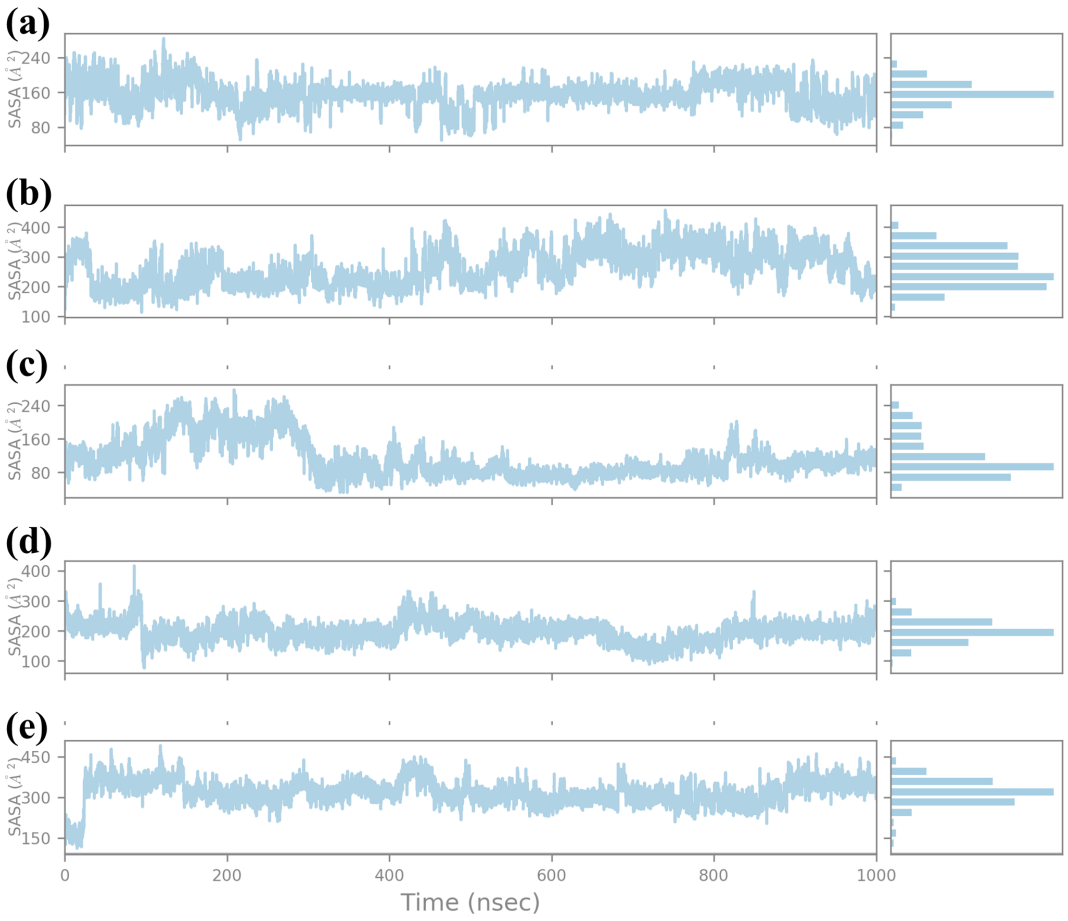

FIGURE 8
Ligand SASA plot obtained form the simulated VIM1-natural compounds **(A)** CNP0390322, **(B)** CNP0390569, **(C)** CNP0079056, **(D)** CNP0338283 and **(E)** XQ5 (reference).

solvent-exposed conformations. It is evident from the histogram that it has a major peak around the lower SASA values and another peak at higher SASA values due to conformational changes that occurred in the simulation period. This behavior may suggest an actual molecule interaction that starts with rigorous binding and then becomes more flexible and exposed to solvent. Arranging the protein structures with "CNP0338283" gives a SASA profile of the range of 200-300 Å², 250 Å² mean SASA. The plot shows trends like CNP0390569 but slightly lower overall SASA; therefore, the protein is somewhat more compact than the one from CNP0390569. The histogram distribution is again less spread out than the first one and has a peak at the average value; therefore, while flexibility is observed, the protein-ligand complex with CNP0338283 retains a relatively stable level of exposure to the solvent. This could mean the forming of higher or more stable binding forces. SASA analysis of the control molecule reveals that the value hovers at about 300–400 Å² and does not fluctuate much during the entire 1000 ns simulation. The histogram provides evidence of the stability of the protein in the absence of the tested compounds, as there is a relatively steep bell-shaped curve centered at the average value of the protein. These stable SASA values are expected as a foundation; therefore, the control molecule maintains the structural stability of the protein.

3.4.6 RG analysis

The RG is a key parameter that provides information on the overall compactness of a protein structure during MD simulations. It is the depiction of the dispersion of atoms of the protein concerning the mass center of the protein. It is used for the determination of the conformational stability and folding propensities of the protein as described quantitatively in Figure 9. In this study, Rg values were analyzed to track the conformal stability of protein-ligand complexes with four chemical compounds and one control molecule up to 1000 ns simulation (Lobanov et al., 2008). The RG value of compound CNP0390322 measured between approximately 3.6 Å and 4.8 Å with a mean value of 4.2 Å. The changes in Rg values are not very significant throughout the simulation, which means that the protein-ligand complex remains nearly the same in terms of compactness. These minor variations are average for such kinds of simulations. However, the overall picture does not show that the binding of compound CNP0390322 induces any conformational changes in the protein.

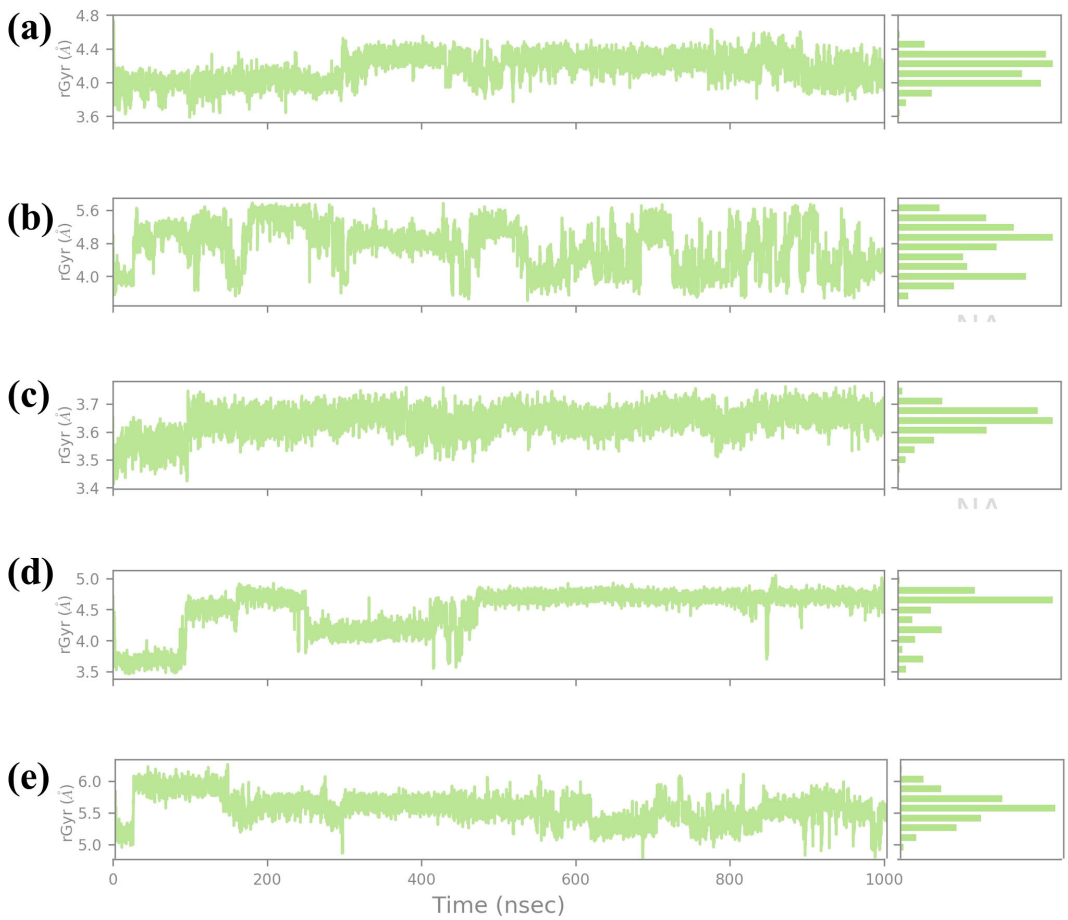

FIGURE 9
Ligand RG plot obtained form the simulated VIM1-natural compounds **(A)** CNP0390322, **(B** CNP0390569, **(C)** CNP0079056, **(D)** CNP0338283 and **(E)** XQ5 (reference).

The histogram is also constructed based on the Rg value, which is around the average Rg value, and the fact that this complex has a compact structure in the simulation process. For compound CNP0390569, the Rg profile is more spread out, ranging between 4.8 Å and 5.6 Å and an average of 5.2 Å. These fluctuations indicate that compound CNP0390569 causes more substantial conformational change that modifies the compactness of the protein. The broader distribution of the residues observed in the histogram may mean that the protein interacts with multiple conformations reflected as flexibility in binding to the compound CNP0390569. As seen from the simulation, the Rg values obtained are relatively higher against compound CNP0390322, which stalls that the protein-ligand complex is more expanded. The Rg values of compound CNP0079056 lie between about 3.4 Å to 3.7 Å but mostly are about 3.6 Å. The quite slight variation and the stable behavior of the Rg plot indicate that compound CNP0079056 keeps the protein relatively compact during the entire simulation. The images representing the delta Rg more or less resemble a normal distribution, though slightly skewed towards the left, and further suggest minimal conformational changes and highly stable interaction between compound CNP0079056 and the protein. Thus, the fact that Compound CNP0079056 has lower Rg values compared to compounds CNP0390322 and CNP0390569 indicates it promotes a more compact protein conformation. The Rg profile of CNP0338283 is slightly more volatile, varying between 3.5 Å – 5.0 Å and an average of 4.2 Å. The stage of interaction at which the system exhibits relatively high RG values and then falls into a more compact state at approximately 300 ns. This behavior indicates that CNP0338283 starts with a more significant protein conformation than what is observed as the simulation continues.

The figure shows histogram distribution approximately in two peaks, which means the protein-ligand complex oscillates between two conformations throughout the simulation. This regularity might represent an initial binding event that then switches to a more condensed conformational state. The control molecule in the Rg analysis shows fluctuation of between 3.6 Å to 4.8 Å with an average of 4.4 Å. The oscillation is low, and the spread in the histogram is also minimal, which indicates that the control molecule keeps the protein in an almost similar conformation as that observed with the CNP0390322. The stability in the Rg values also implies that the control molecule does not have a huge impact on the global conformation of the protein and thus maintains similar compactness throughout the simulation step. This stable Rg profile can be considered as a starting point, showing the impact of the tested compounds on protein conformation.

3.5 Analysis of MM/GBSA

This was done using MMGBSA analysis for four compounds: CNP0390322, CNP0390569, CNP0079056, as well as CNP0338283, and a control to compare their binding interactions with a target receptor and the results provided in Supplementary Table S3. The outcome of this computational approach is quantitative information about the binding affinity and stability of the ligand-receptor complexes, notably ΔVDWAALS, ΔEEL, ΔEGB, ΔESURF, ΔGGAS, ΔGSOLV, and ΔGtotal. Of all the compounds discussed in this work, CNP0390322 showed the best binding profile. The most negative van der Waals energy was determined for this compound (-46.02 ± 3.27 kcal/mol) which points toward the hydrophobic interactions of this compound with the receptor. These interactions are important for the fixation of the ligand within the binding pocket. Furthermore, CNP0390322 incurred an attractive electrostatic energy of -41.08 ± 3.90 kcal/mol, indicating large ionic or H-bonding interactions that should stabilize the complex. The ΔEGB for this compound was, however, relatively high at 121.25 ± 5.39 kcal/mol suggesting an energetic cost for desolvation in this binding event. Nevertheless, these penalties were offset by the gain in van der Waals and electrostatic contributions. The ΔESURF was -14.69 ± 1.93 kcal/mol, which also supports the fact that hydrophobic interaction is also involved in the binding process. The cumulative ΔGtotal of CNP0390322 was found to be -19.45 ± 14.50 kcal/mol, thus showcasing the highest binding affinity than the rest of the studied compounds. The compound CNP0390569 also showed maximum binding interactions as compared to other compounds in terms of electrostatic energy which was -72.80 ± 16.32 kcal/mol. This indicates that CNP0390569 makes strong ionic or polar contacts with the receptor, which is important in the binding process. In contrast, the van der Waals energy for this compound was slightly less favorable, reporting -27.77 ± 5.87 kcal/mol, suggesting less hydrophobic interactions than in CNP0390322. The polar solvation energy (ΔEGB) was also high at 106.31 ± 16.09 kcal/mol; however, the non-polar solvation energy (ΔESURF) was relatively low at -9.12 ± 3.53 kcal/mol which seems to indicate reduced overall hydrophobicity. The net gas phase energy (ΔGGAS) for CNP0390569 was -100.58 ± 22.20 kcal/mol because of the strong non-covalent interactions in the complex. However, the total binding free energy (ΔGtotal) was relatively low (-3.39 ± 41.83 kcal/mol), though certain positive contributions could be assigned to the solvation penalty. CNP0079056 also had a moderate binding that was characterized by a van der Waal energy of 30.53 ± 5.50 kcal/mol as well as an electrostatic energy of -63.86 ± 16.51 kcal/mol. These values suggest that both hydrophobic and electrostatic interactions are favorable but not of the same magnitude as CNP0390322. The polar solvation energy (ΔEGB) was calculated for CNP0079056, which had the lowest value of 92.66 ± 16.47 kcal/mol, meaning the lowest desolvation penalty and, therefore, being beneficial for binding. However, the non-polar solvation energy (ΔESURF) was relatively low at -9.59 ± 1.72 kcal/mol, which indicates relatively small hydrophobic effects. The total binding free energy (ΔGtotal) of CNP0079056 was found to be -11.33 ± 40.22 kcal/mol which portrayed moderate binding affinity of the compound. CNP0338283 displayed a binding profile similar to CNP0079056, with slightly more favorable van der Waals energy (-33.75 ± 4.36 kcal/mol) and non-polar solvation energy (-15.83 ± 3.29 kcal/mol). However, its electrostatic energy was less favorable at -52.79 ± 17.84 kcal/mol. The total ΔGtotal for CNP0338283 was -14.74 ± 42.71 kcal/mol, suggesting that this compound also has moderate binding affinity but may benefit from further optimization.

4 Discussion

This study, aimed to identify potential inhibitors of the metallo-beta-lactamase VIM-1 enzyme from *P. aeruginosa* using a comprehensive computational approach. The analysis encompassed virtual screening, re-docking, intermolecular interaction studies, molecular dynamics (MD) simulations, RMSD, protein RMSF, ligand RMSF, protein-ligand interaction profiling, Rg analysis, SASA analysis, and MMGBSA calculations. A control molecule was used as a baseline for comparison to evaluate the efficacy of each selected compound. Virtual screening of the COCONUT database led to the identification of four promising natural compounds based on their binding energies (Guido et al., 2008), which ranged from -9.91 kcal/mol CNP0390322 to -9.33 kcal/mol (CNP0338283). Re-docking was performed to validate the initial screening results and further refine the binding poses (Agu et al., 2023). All selected compounds demonstrated strong binding affinities, with energies ranging between -8.7 kcal/mol to -9.6 kcal/mol, compared to -10.7 kcal/mol for the control molecule. Among these, CNP0390322 emerged as the most potent inhibitor, forming a stable interaction network characterized by multiple hydrogen bonds with critical residues such as Asn210 and hydrophobic contacts with Phe62, Tyr67, and Trp219. Compound CNP0390569, while also interacting with Asn210, showed a lower number of hydrophobic interactions and relied on a π-cation interaction with His116, suggesting a less stable binding compared to Compound CNP0390322. Compound CNP0079056 exhibited unique multiple π-π stacking interactions, indicating a specific and stable binding mode, whereas Compound CNP0338283 showed additional hydrophobic contacts similar to Compound CNP0390569, indicating a potentially stable interaction within the enzyme's active site. The control molecule, although forming an extensive hydrogen bonding network, displayed fewer hydrophobic interactions, suggesting weaker stabilization within the hydrophobic pocket (Chen et al., 2016). Intermolecular interaction analysis provided insights into the nature and strength of interactions between the ligands and the VIM-1 active site. Compound CNP0390322 demonstrated a strong interaction profile with robust hydrogen bonds and hydrophobic contacts that likely contributed to its stable binding. Compound CNP0390569, while forming key hydrogen bonds, showed fewer hydrophobic interactions and relied more on electrostatic interactions, suggesting a potentially less stable interaction compared to Compound CNP0390322. Compound CNP0079056, with its unique π-π stacking interactions, indicated a strong binding profile, while Compound CNP0338283, despite similar interaction types to Compound CNP0390569, demonstrated additional flexibility in its interactions, potentially enhancing its binding stability. The control molecule, while interacting with the protein through hydrogen bonding, which is so crucial for binding proper and stable interactions within the binding pocket, exhibited fewer hydrophobic contacts, and therefore, the structure within the pocket was less stabilized. These MD simulations proffered a kinetic view of the stability and dynamics of the protein-ligand complexes for a duration of 1000ns (Bagewadi et al., 2023). The RMSD analysis showed that CNP0390322 had the least deviation from the initial orientation and kept the most stable interaction with the protein throughout the simulation with protein RMSD values between 1.5 Å and 2.0 Å. Similar to CNP0390322, the ligand RMSD also decreased after an initial adjustment phase hence confirming that the binding of the ligand was consistent within the active site. CNP0390569, however, showed significant fluctuations in ligand RMSD, particularly in the early stages, suggesting a less stable interaction. Protein RMSD for CNP0390569 also exhibited variability, reflecting minor conformational adjustments during the binding process. RMSD values of CNP0079056 were like that of CNP0390322. Thus, the interaction was quite stable with no major impact on the protein structure. While compound CNP0338283 exhibits moderate oscillations in both protein and ligand RMSD values, the overall binding was stable. The control molecule continued to have lower protein RMSD and, therefore, appeared to be more rigid compared to the selected compounds; however, the ligand RMSD demonstrated the flexibility of this molecule, thus possibly indicating comparatively less stable complexation with the receptor. The flexibility of certain residues during the simulation was identified by using RMSF analysis of the protein complexes. Compound CNP0390322, flexibility analysis revealed that the structure exhibited moderate flexibility in the amino acid position 170-190, which imparts dynamic character that could prove useful in the stability of the ligand-binding domain. Notably, more conformational flexibility was observed with CNP0390569 binding, as evidenced by the lower RMSF values, suggesting a less conformable interannual interaction that may be stronger. The flexibility and potential to form stable complexes were comparable for CNP0079056 and CNP0390322, considering the RMSF values, whereas CNP0338283 demonstrated somewhat higher RMSF values to indicate moderate structural stability and flexibility. The detailed RMSF analysis of ligand flexibility showed that CNP0390322 had more conformational freedom around specific atoms which could be helpful for biology interactions. CNP0390569 demonstrated linear elevations in flexibility, especially in the central area, indicating flexibility in the binding pocket. The changes in the middle region of CNP0079056 were the most variable, which might represent regions that could change with the protein conformation, while CNP0338283 was most consistent, suggesting regions of dynamic interactions with the protein as the conformation changes. As for the control ligand, the fluctuation in the RMSF values was much higher, suggesting inferior binding affinity of the control ligand with the enzyme. Additional identification of the protein-ligand interactions, to some extent, helped the analysis of the stability and type of the interactions over the simulation period. The compound CNP0390322 showed very favorable hydrogen bonding interactions and high hydrophobicity, which may have led to its relatively stable and selective binding. Compound CNP0390569, which forms significant numbers of hydrogen bonds, seems to be anchored less well in the binding pocket due to fewer hydrophobic interactions. CNP0079056 demonstrated the interaction of chemical bonds primarily hydrogen bonds and hydrophobic interactions, while the chemical structure of CNP0338283 showed that although it is similar to CNP0390569 in interaction profile, it is more flexible and can improve the binding mode. The control molecule, while making important contacts, had a relatively less favorable binding affinity and relied on entropic factors and water-mediated associations. It was revealed that during the simulation, the protein-ligand complexes are relatively more compact according to the RG results (Lobanov et al.,

2008). The compound CNP0390322 had a stable pattern of Rg, proving the compactness and robust binding ability throughout the experiment. Compound CNP0390569 presented more significant oscillation, indicating that its binding state is less stable and the protein conformation has more significant change. Compound CNP0079056 had the most stable Rg profile, suggesting that the protein was folded well and bound tightly to the ligand in the active site, whereas compound CNP0338283 fluctuated at the beginning and then became strikingly stable, which means conformational changes in the protein occurred before reaching a compact structure. The control molecule exhibited an undisrupted Rg profile similar to CNP0390322 but may have weaker interactions relative to the modified molecules. The analysis using SASA also gave data about the ligands' structural flexibility and bonding strength to the solvent-exposed surface of the protein. Compound CNP0390322 maintained relatively constant SASA values, suggesting proper ligand fit within the binding cavity. Compound CNP0390569 exhibited greater variability, indicating more conformational changes and generally lower binding affinity. The initial structure of compound CNP0079056 was effectively bound to the protein region, and the binding gradually loosened over time; the structure of compound CNP0338283 was moderately flexible and tightly bound to the protein. The control molecule had a stable SASA level, suggesting that the protein structure remained nearly unchanged, but the ligand-binding affinity may have been less robust. According to the energy quantification of MMGBSA, the binding free energies of the complexes were established (Genheden and Ryde, 2015).

Of all the compounds, compound CNP0390322 had the lowest binding free energy, showing that it bound well with stable interactions within the site. Compound CNP0079056 also showed high-affinity binding, as evident with free energy values. However, compounds CNP0390569 and CNP0338283 employed less negative free energy value, implying less stability for the compounds in binding. The control molecule, which also demonstrated consistent interactions with the protein, had higher free energy values, pointing to a relatively less stable binding environment relative to the selected compounds. Prior research has pointed out that the molecule stability of hydrogen bonds and the compound-specific hydrophobicity Index are crucial factors in strong and specific protein-ligand interactions. Similar to our findings, Rohan Patil et al. (2010) highlighted the role of these interactions in stabilizing ligand binding in disease management (Patil et al., 2010). Moreover, the orientations of inhibitors to metallo-beta-lactamases indicate that polar and nonpolar interactions include π-π stacking interactions and the role of electrostatic attractions in stabilizing the inhibitors within the active site, comparable to Compounds 1 and 3, in this study.

5 Conclusion

In conclusion, our comprehensive computational research approach successfully identified potential small molecule inhibitors of metallo-beta-lactamase VIM-1 from *P. aeruginosa*. Through a detailed analysis incorporating virtual screening, re-docking, molecular dynamics simulations, and various computational metrics (RMSD, RMSF, protein-ligand interaction analysis, RG, SASA, and MMGBSA), we pinpointed natural compounds that exhibit promising inhibitory effects against VIM-1. Among the compounds analyzed, Compounds CNP0390322 and CNP0079056 stood out due to their strong binding energies, stable hydrogen bonding, and consistent hydrophobic interactions. These interactions were further corroborated by minimal structural fluctuations as observed in RMSD analyses. The binding poses, as represented by Rg values and SASA plots, indicated that these ligands maintained stable placements within the binding pocket throughout the simulation runs. Although other compounds, such as CNP0390322 and CNP0338283, also showed potential inhibitory activity, they exhibited higher conformational entropy and lower binding stability. The control molecule XQ5 while demonstrating stable interaction patterns, showed greater ligand flexibility and reduced binding stability compared to the selected compounds. Consequently, Compounds CNP0390322 and CNP0079056 emerged as the most promising structural analogues, exhibiting considerable therapeutic potential to inhibit VIM-1. These findings warrant further *in vitro* and *in vivo* investigations to validate the efficacy of these compounds in developing effective therapies to combat multidrug-resistant *P. aeruginosa* infections. Future studies should focus on confirming these computational predictions and exploring the therapeutic applications of these promising inhibitors in treating MDR bacterial infections.

Data availability statement

The original contributions presented in the study are included in the article/Supplementary Material. Further inquiries can be directed to the corresponding authors.

Author contributions

MA: Visualization, Conceptualization, Formal analysis, Investigation, Methodology, Resources, Software, Validation, Writing – review & editing, Writing – original draft, Data curation, Funding acquisition. SB: Conceptualization, Formal analysis, Methodology, Software, Validation, Visualization, Writing – review & editing. MY: Conceptualization, Formal analysis, Methodology, Software, Validation, Visualization, Writing – review & editing. AK: Conceptualization, Formal analysis, Methodology, Software, Validation, Visualization, Writing – review & editing. ST: Conceptualization, Formal analysis, Methodology, Software, Validation, Visualization, Writing – review & editing. AAf: Conceptualization, Formal analysis, Methodology, Software, Validation, Visualization, Writing – review & editing. SN: Conceptualization, Formal analysis, Methodology, Software, Validation, Visualization, Writing – review & editing. AAl: Conceptualization, Formal analysis, Methodology, Software, Validation, Visualization,

Writing – review & editing. VD: Conceptualization, Formal analysis, Methodology, Software, Validation, Visualization, Writing – review & editing, Investigation, Resources, Supervision, Writing – original draft. EA: Conceptualization, Investigation, Methodology, Project administration, Resources, Software, Supervision, Validation, Visualization, Writing – review & editing.

Funding

The author(s) declare financial support was received for the research, authorship, and/or publication of this article. This project was funded by Dr. Mazen Fakeeh Academic Chair of Diabetes Mellitus at Dr. Soliman Fakeeh College for Medical Sciences, Jeddah, Saudi Arabia under grant no. MFSC-DM/04/24.

Conflict of interest

The authors declare that the research was conducted in the absence of any commercial or financial relationships that could be construed as a potential conflict of interest.

Generative AI statement

The author(s) declare that no Generative AI was used in the creation of this manuscript.

Publisher's note

Supplementary material

The Supplementary Material for this article can be found online at: https://www.frontiersin.org/articles/10.3389/fcimb.2025.1521391/full#supplementary-material

References

Agu, P. C., Afiukwa, C. A., Orji, O. U., Ezeh, E. M., Ofoke, I. H., Ogbu, C. O., et al. (2023). Molecular docking as a tool for the discovery of molecular targets of nutraceuticals in diseases management. *Sci. Rep.* 13, 13398. doi: 10.1038/s41598-023-40160-2

Akhtar, A., Fatima, N., and Khan, H. M. (2022). "Beta-lactamases and their classification: an overview," In M. Shahid, A. Singh and H. Sami (eds). *Beta-Lactam Resistance in Gram-Negative Bacteria*. Singapore: Springer. doi: 10.1007/978-981-16-9097-6_3

Bagewadi, Z. K., Yunus Khan, T. M., Gangadharappa, B., Kamalapurkar, A., Mohamed Shamsudeen, S., and Yaraguppi, D. A. (2023). Molecular dynamics and simulation analysis against superoxide dismutase (SOD) target of Micrococcus luteus with secondary metabolites from Bacillus licheniformis recognized by genome mining approach. *Saudi J. Biol. Sci.* 30, 103753. doi: 10.1016/j.sjbs.2023.103753

Berman, H. M., Westbrook, J., Feng, Z., Gilliland, G., Bhat, T. N., Weissig, H., et al. (2000). The protein data bank. *Nucleic Acids Res.* 28, 235–242. doi: 10.1093/nar/28.1.235

Bowers, K. J., Chow, E., Xu, H., Dror, R. O., Eastwood, M. P., Gregersen, B. A., et al. (2006) in *Scalable algorithms for molecular dynamics simulations on commodity clusters*. Tampa, FL, USA: SC '06: Proceedings of the 2006 ACM/IEEE Conference on Supercomputing 43. doi: 10.1109/SC.2006.54

Chávez-Hernández, A. L., Sánchez-Cruz, N., and Medina-Franco, J. L. (2020). A fragment library of natural products and its comparative chemoinformatic characterization. *Mol. Inf.* 39, 2000050. doi: 10.1002/minf.202000050

Chen, D., Oezguen, N., Urvil, P., Ferguson, C., Dann, S. M., and Savidge, T. C. (2016). Regulation of protein-ligand binding affinity by hydrogen bond pairing. *Sci. Adv.* 2, e1501240. doi: 10.1126/sciadv.1501240

Dreier, J., and Ruggerone, P. (2015). Interaction of antibacterial compounds with RND efflux pumps in Pseudomonas aeruginosa. *Front. Microbiol.* 6. doi: 10.3389/fmicb.2015.00660

Drenkard, E. (2003). Antimicrobial resistance of Pseudomonas aeruginosa biofilms. *Microbes Infection* 5, 1213–1219. doi: 10.1016/j.micinf.2003.08.009

Durham, E., Dorr, B., Woetzel, N., Staritzbichler, R., and Meiler, J. (2009). Solvent accessible surface area approximations for rapid and accurate protein structure prediction. *J. Mol. Model.* 15, 1093–1108. doi: 10.1007/s00894-009-0454-9

Esposito, S., and Leone, S. (2007). Antimicrobial treatment for Intensive Care Unit (ICU) infections including the role of the infectious disease specialist. *Int. J. antimicrobial Agents* 29, 494–500. doi: 10.1016/j.ijantimicag.2006.10.017

Genheden, S., and Ryde, U. (2015). The MM/PBSA and MM/GBSA methods to estimate ligand-binding affinities. *Expert Opin. Drug Discovery* 10, 449–461. doi: 10.1517/17460441.2015.1032936

Guido, R. V. C., Oliva, G., and Andricopulo, A. D. (2008). Virtual screening and its integration with modern drug design technologies. *Curr. Med. Chem.* 15, 37–46. doi: 10.2174/092986708783330683

Harder, E., Damm, W., Maple, J., Wu, C., Reboul, M., Xiang, J. Y., et al. (2016). OPLS3: A force field providing broad coverage of drug-like small molecules and proteins. *J. Chem. Theory Comput.* 12, 281–296. doi: 10.1021/acs.jctc.5b00864

Jaidhan, B. J., Srinivasa Rao, P., and Apparao, A. (2014). Energy minimization and conformation analysis of molecules using steepest descent method. *Int. J. Comput. Sci. Inf. Technol.* 5.3, 3525–3528.

Ju, L.-C., Cheng, Z., Fast, W., Bonomo, R. A., and Crowder, M. W. (2018). The continuing challenge of metallo-β-lactamase inhibition: mechanism matters. *Trends Pharmacol. Sci.* 39, 635–647. doi: 10.1016/j.tips.2018.03.007

Karsisiotis, A. I., Damblon, C., and Roberts, G. C. K. (2014). A variety of roles for versatile zinc in metallo-β-lactamases. *Metallomics* 6, 1181–1197. doi: 10.1039/C4MT00066H

Kerr, K. G., and Snelling, A. M. (2009). Pseudomonas aeruginosa: a formidable and ever-present adversary. *J. Hosp. Infection* 73, 338–344. doi: 10.1016/j.jhin.2009.04.020

King, D. T., Sobhanifar, S., and Strynadka, N. C. (2014). "The mechanisms of resistance to β-lactam antibiotics," In: M. Gotte, A. Berghuis, G. Matlashewski, M. Wainberg and D. Sheppard (eds) *Handbook of Antimicrobial Resistance*. New York, NY: Springer. doi: 10.1007/978-1-4939-0667-3_10-1

Kowalski, R. P., Pandya, A. N., Karenchak, L. M., Romanowski, E. G., Husted, R. C., Ritterband, D. C., et al. (2001). An *in vitro* resistance study of levofloxacin, ciprofloxacin, and ofloxacin using keratitis isolates of Staphylococcus aureus and Pseudomonas aeruginosa. *Ophthalmology* 108, 1826–1829. doi: 10.1016/S0161-6420(01)00724-2

Kunz Coyne, A. J., El Ghali, A., Holger, D., Rebold, N., and Rybak, M. J. (2022). Therapeutic strategies for emerging multidrug-resistant pseudomonas aeruginosa. *Infect. Dis. Ther.* 11, 661–682. doi: 10.1007/s40121-022-00591-2

Labbé, C. M., Rey, J., Lagorce, D., Vavruša, M., Becot, J., Sperandio, O., et al. (2015). MTiOpenScreen: a web server for structure-based virtual screening. *Nucleic Acids Res.* 43, W448–W454. doi: 10.1093/nar/gkv306

Lin, X., and Kück, U. (2022). Cephalosporins as key lead generation beta-lactam antibiotics. *Appl. Microbiol. Biotechnol.* 106, 8007–8020. doi: 10.1007/s00253-022-12272-8

Lipinski, C. A. (2004). Lead- and drug-like compounds: the rule-of-five revolution. *Drug Discovery Today: Technol.* 1, 337–341. doi: 10.1016/j.ddtec.2004.11.007

Lobanov, M. Y., Bogatyreva, N., and Galzitskaya, O. (2008). Radius of gyration as an indicator of protein structure compactness. *Mol. Biol.* 42, 623–628. doi: 10.1134/S0026893308040195

Makena, A., Düzgün, A.Ö., Brem, J., McDonough, M. A., Rydzik, A. M., Abboud, M. I., et al. (2016). Comparison of verona integron-borne metallo-β-lactamase (VIM) variants reveals differences in stability and inhibition profiles. *Antimicrobial Agents Chemotherapy* 60, 1377–1384. doi: 10.1128/aac.01768-15

Markou, P., and Apidianakis, Y. (2014). Pathogenesis of intestinal Pseudomonas aeruginosa infection in patients with cancer. *Front. Cell. infection Microbiol.* 3, 115. doi: 10.3389/fcimb.2013.00115

Mollard, C., Moali, C., Papamicael, C., Damblon, C., Vessilier, S., Amicosante, G., et al. (2001). Thiomandelic acid, a broad spectrum inhibitor of zinc beta-lactamases: kinetic and spectroscopic studies. *J. Biol. Chem.* 276 (48), 45015–45023. doi: 10.1074/jbc.M107054200

Nainala, V. C., Rajan, K., Kanakam, S. R. S., Sharma, N., Weißenborn, V., Schaub, J., et al. (2024). COCONUT 2.0: A comprehensive overhaul and curation of the collection of open natural products database. *ChemRxiv*. doi: 10.26434/chemrxiv-2024-fxq2s-v2

O'Boyle, N. M., Banck, M., James, C. A., Morley, C., Vandermeersch, T., and Hutchison, G. R. (2011). Open Babel: An open chemical toolbox. *J. cheminformatics* 3, 1–14. doi: 10.1186/1758-2946-3-33

Pachori, P., Gothalwal, R., and Gandhi, P. (2019). Emergence of antibiotic resistance Pseudomonas aeruginosa in intensive care unit; a critical review. *Genes Dis.* 6, 109–119. doi: 10.1016/j.gendis.2019.04.001

Patil, R., Das, S., Stanley, A., Yadav, L., Sudhakar, A., and Varma, A. K. (2010). Optimized hydrophobic interactions and hydrogen bonding at the target-ligand interface leads the pathways of drug-designing. *PLoS One* 5, e12029. doi: 10.1371/journal.pone.0012029

Pavan, M., Menin, S., Bassani, D., Sturlese, M., and Moro, S. (2022). Qualitative estimation of protein–ligand complex stability through thermal titration molecular dynamics simulations. *J. Chem. Inf Model.* 62, 5715–5728. doi: 10.1021/acs.jcim.2c00995

Pettersen, E. F., Goddard, T. D., Huang, C. C., Couch, G. S., Greenblatt, D. M., Meng, E. C., et al. (2004). UCSF Chimera–a visualization system for exploratory research and analysis. *J. Comput. Chem.* 25, 1605–1612. doi: 10.1002/jcc.20084

Salimraj, R., Hinchliffe, P., Kosmopoulou, M., Tyrrell, J. M., Brem, J., van Berkel, S. S., et al. (2019). Crystal structures of VIM-1 complexes explain active site heterogeneity in VIM-class metallo-β-lactamases. *FEBS J.* 286, 169–183. doi: 10.1111/febs.14695

Schärer, V., Meier, M.-T., Schuepbach, R. A., Zinkernagel, A. S., Boumasmoud, M., Chakrakodi, B., et al. (2023). An intensive care unit outbreak with multi-drug-resistant Pseudomonas aeruginosa–spotlight on sinks. *J. Hosp. Infection* 139, 161–167. doi: 10.1016/j.jhin.2023.06.013

Sharma, J., Kumar Bhardwaj, V., Singh, R., Rajendran, V., Purohit, R., and Kumar, S. (2021). An in-silico evaluation of different bioactive molecules of tea for their inhibition potency against non structural protein-15 of SARS-CoV-2. *Food Chem.* 346, 128933. doi: 10.1016/j.foodchem.2020.128933

Sorokina, M., Merseburger, P., Rajan, K., Yirik, M. A., and Steinbeck, C. (2021).COCONUT online: Collection of Open Natural Products database. Available online at.

Tamilselvi, A., and Mugesh, G. (2008). Zinc and antibiotic resistance: metallo-β-lactamases and their synthetic analogues. *JBIC J. Biol. Inorganic Chem.* 13, 1039–1053. doi: 10.1007/s00775-008-0407-2

Tehrani, K. H. M. E., and Martin, N. I. (2017). Thiol-containing metallo-β-lactamase inhibitors resensitize resistant gram-negative bacteria to meropenem. *ACS Infect. Dis.* 3, 711–717. doi: 10.1021/acsinfecdis.7b00094

Trott, O., and Olson, A. J. (2010). AutoDock Vina: improving the speed and accuracy of docking with a new scoring function, efficient optimization and multithreading. *J. Comput. Chem.* 31, 455–461. doi: 10.1002/jcc.21334

Wilson, M. G., and Pandey, S. (2024).Pseudomonas aeruginosa. In: *StatPearls* (Treasure Island (FL: StatPearls Publishing). Available online at: http://www.ncbi.nlm.nih.gov/books/NBK557831/ (Accessed August 5, 2024).

Wood, S. J., Kuzel, T. M., and Shafikhani, S. H. (2023). Pseudomonas aeruginosa: infections, animal modeling, and therapeutics. *Cells* 12, 199. doi: 10.3390/cells12010199

frontiers | Frontiers in Cellular and Infection Microbiology

TYPE Original Research
PUBLISHED 22 April 2025
DOI 10.3389/fcimb.2025.1493769

OPEN ACCESS

EDITED BY
Sanket Kaushik,
Amity University Jaipur, India

REVIEWED BY
Tooba Mahboob,
UCSI University, Malaysia
Krishnan Venkataraman,
VIT University, India

*CORRESPONDENCE
Fatma Alshehri
faoalshehri@pnu.edu.sa

RECEIVED 09 September 2024
ACCEPTED 21 March 2025
PUBLISHED 22 April 2025

CITATION
Safwat N, Elshimy R, Hassanin SO, El-manakhly AR, Noaf AN, Mansour AT, Alshehri F, Alhomrani M, Alamri AS and Bendary MM (2025) Therapeutic approaches for septicemia induced by multidrug-resistant bacteria using desert-adapted plants. *Front. Cell. Infect. Microbiol.* 15:1493769. doi: 10.3389/fcimb.2025.1493769

Therapeutic approaches for septicemia induced by multidrug-resistant bacteria using desert-adapted plants

Nesreen Safwat[1], Rana Elshimy[2], Soha O. Hassanin[3], Arwa Ramadan El-manakhly[1], Abdullah N. Noaf[4], Abdallah Tageldein Mansour[5], Fatma Alshehri[6]*, Majid Alhomrani[7,8], Abdulhakeem S. Alamri[7,8] and Mahmoud Mohammed Bendary[9]

[1]Department of Microbiology and Immunology, Faculty of pharmacy, Modern University for Technology and Information, Cairo, Egypt, [2]Department of Microbiology and Immunology, Faculty of Pharmacy, Alhram Canadian University, Giza, Egypt, [3]Department of Biochemistry, Faculty of pharmacy, Modern University for Technology and Information, Cairo, Egypt, [4]Surgical Department, Al Hadithah General Hospital, Al-Qurayyat, Saudi Arabia, [5]Fish and Animal Production Department, College of Agriculture and Food Sciences, King Faisal University, Al-Ahsa, Saudi Arabia, [6]Department of Biology, College of Sciences, Princess Nourah bint Abdulrahman University, Riyadh, Saudi Arabia, [7]Department of Clinical Laboratories Sciences, The Faculty of Applied Medical Science, Taif University, Taif, Saudi Arabia, [8]Research Center for health science, Deanship of Scientific Research, Taif University, Taif, Saudi Arabia, [9]Department of Microbiology and Immunology, Faculty of Pharmacy, Port Said University, Port Said, Egypt

Aim: Septicemia, a life-threatening condition, can arise when bacterial infections are left untreated, allowing the pathogens to spread into the bloodstream. Moreover, infections caused by MDR bacteria are particularly challenging, as they can persist and lead to septicemia even when treated with conventional antibiotics. This study aimed to address this crisis by investigating combination therapies using desert-adapted medicinal plant extracts, including *Jasonia candicans (J. candicans)*, *Cistanche tubulosa*, *Moltkiopsis ciliata*, and *Thymelea hirsuta*, as alternative treatments. The goal was to develop new strategies to combat resistance and improve the management of septic patients.

Methodology: In this study, 400 blood samples from septic patients were analyzed to identify Gram-negative bacterial isolates. Antimicrobial resistance patterns were assessed using standard susceptibility tests. Medicinal plant extracts were evaluated for antimicrobial activity using agar diffusion and broth microdilution assays, while COX-1 and COX-2 inhibition and antioxidant activity were measured using *in vitro* assays. Histopathological examinations were conducted on treated mice to assess tissue damage and response.

Results: We observed a high prevalence of *E. coli* and *K. pneumoniae* among septic patients. Multidrug resistance was widespread, with many isolates showing high resistance to various antibiotics, although all were susceptible to colistin. Evaluation of desert-adapted plant extracts revealed that *J. candicans* exhibited the most potent antimicrobial activity and the strongest COX-1 and COX-2 inhibitory activities, as well as antioxidant effects, compared to other extracts and Celecoxib, with a concentration required to achieve 50% enzyme inhibition (IC_{50}) value of 71.97 µg/mL for antioxidant activity. Moreover, the combination of this

extract with amikacin showed a synergistic effect, significantly enhancing antimicrobial efficacy and converting over 50% of amikacin-resistant strains to sensitive phenotypes. Histopathological analysis of mice showed that the combination of *J. candicans* extract and amikacin resulted in reduced severity of pulmonary lesions and splenic damage compared to amikacin alone.

Conclusion: We highlighted the potential of *J. candicans* extracts as combination therapies alongside traditional antibiotics for combating MDR Gram-negative infections, due to their superior antimicrobial, anti-inflammatory, and antioxidant properties.

KEYWORDS

septic patients, gram-negative, medicinal plants, *J. candicans*, amikacin

Introduction

Septicemia is a serious and potentially fatal condition that occurs when bacteria enter the bloodstream and spread throughout the body, triggering a widespread immune response. This condition can develop from infections caused by various bacterial species, but it is especially concerned with resistant strains, such as multidrug-resistant (MDR) bacteria. These resistant pathogens pose a significant challenge to treatment because they have developed the ability to withstand many commonly used antibiotics, making infections more difficult to control and eradicate. Even with timely medical intervention, MDR infections can still progress to septicemia due to the limited effectiveness of existing antimicrobial therapies (Tang et al., 2024). Infections with MDR- Gram-negative bacteria can trigger an uncontrolled inflammatory response that impairs organ function, resulting in a complex syndrome characterized by oxidative stress, immune dysfunction, impaired tissue oxygenation, and hypercoagulability (Prescott and Angus, 2018; American Thoracic Society, 2018). When microorganisms invade the body, the host's immune system attempts to clear these pathogens through an inflammatory response, primarily mediated by the activation of neutrophils and macrophages/monocytes. This response, however, can become excessive and uncontrolled, leading to irreversible tissue damage and potentially death (Singer et al., 2016; Tang et al., 2024). The balance between inflammation and the immune response is critical in the context of infections. While inflammation is a necessary component of the body's defense mechanism against pathogens, an uncontrolled inflammatory response can lead to tissue damage and contribute to the development of sepsis, especially in the presence of MDR bacteria. Cyclooxygenase-2 (COX-2) inhibition can shift this balance by modulating the inflammatory response, potentially allowing for a more targeted and effective immune response against the infection. Furthermore, reducing inflammation may minimize the risk of systemic inflammatory responses, which can lead to severe complications. This reduction in inflammation can potentially improve tissue healing and recovery, enhance blood flow to the affected area, and promote a more effective immune response. A more balanced immune response is crucial when managing infections, particularly those caused by MDR pathogens, as these bacteria often exploit the inflammatory environment to thrive and evade immune detection (Medzhitov, 2008).

Of note, the broad-spectrum antibiotics commonly used for empirical treatment of sepsis are associated with adverse outcomes, including the disruption of normal microbiota and the selection for resistant pathogens (Busani et al., 2019; Zilberman-Itskovich and Goldberg, 2022). The rise of MDR- Gram-negative bacteria such as *Klebsiella pneumoniae (K. pneumoniae)*, *Pseudomonas aeruginosa (P. aeruginosa)*, and *Acinetobacter baumannii (A. baumannii)*, which are resistant to carbapenems, the last line of defense, underscores the urgent need for new therapeutic strategies (Pop-Vicas and Opal, 2013). Current sepsis management, which includes supportive care such as organ function support, intravenous fluids, antibiotics, and oxygen, remains largely nonspecific and has limitations. Considering the critical role of inflammation in sepsis, innovative therapies targeting the host immune response could improve outcomes (Liang et al., 2015). Of note, understanding the mechanisms of resistance in these pathogens can facilitate the identification and development of novel antimicrobial agents (Shaikh and Fatima, 2015; Alam et al., 2022).

The World Health Organization (WHO) has identified over 20,000 species of medicinal plants as potential sources for new drug development (Srinivasan and Jayaprakasha, 2001), with more than 100 countries establishing regulations for their use. To date, over 1,340 plants have been recognized for their antimicrobial properties, and more than 30,000 antimicrobial compounds have been isolated from plants (Tajkarimi and Ibrahim, 2010; Vaou et al., 2021a). Desert-adapted plants are emerging as valuable sources of antimicrobial agents due to their remarkable ability to thrive in extreme environmental conditions, such as intense heat, high ultraviolet (UV) radiation, and scarce water. These harsh

conditions have led to the evolution of diverse secondary metabolites in these plants, including alkaloids, flavonoids, tannins, and terpenoids, which are essential for their defense against pathogens. Research has shown that these bioactive compounds possess significant antimicrobial properties, making desert plants a promising avenue for discovering new treatments to address antibiotic-resistant bacteria (El-Hilaly et al., 2020; Mahizan and Ismail, 2019). For example, *Jasonia candicans (J. candicans)*, *Cistanche tubulosa (C. tubulosa)*, *Moltkiopsis ciliata (M. ciliata)*, and *Thymelea hirsute (T. hirsute)* have demonstrated significant antimicrobial activities, reflecting their evolutionary adaptations to extreme environments. *J. candicans*, a plant endemic to arid regions, exhibits potent antimicrobial properties, particularly against Gram-positive bacteria, due to its rich content of essential oils and flavonoids (Khalid et al., 2020). Similarly, *C. tubulosa*, known for its use in traditional medicine, shows broad-spectrum antimicrobial activity, attributed to its complex phenolic compounds and polysaccharides, which have been effective against various bacterial and fungal pathogens (Shao et al., 2019). *M. ciliata*, another desert plant, contains bioactive compounds that inhibit microbial growth, highlighting its potential as an antimicrobial agent (Al-Snafi, 2021). Additionally, *T. hirsuta* has been found to possess substantial antimicrobial activity, particularly due to its terpenoids and flavonoids, which exhibit strong inhibitory effects against both Gram-positive and Gram-negative bacteria (Joudeh and Linke, 2018). These findings underscore the potential of desert-adapted plants as sources of novel antimicrobial agents, offering valuable alternatives to conventional antibiotics.

While plant extracts have demonstrated potential as antimicrobial agents due to their diverse bioactive compounds, their use as standalone treatments for infections has notable limitations. The chemical composition of plant extracts can vary significantly depending on species, growing conditions, and extraction methods, leading to inconsistent efficacy and dosing difficulties (Wink, 2022). Additionally, many plant-derived compounds are less potent than conventional antibiotics, often necessitating higher doses that can be impractical and may pose toxicity risks (Nikaido, 2020). Furthermore, plant-derived compounds frequently suffer from limited bioavailability due to poor absorption, rapid metabolism, and low solubility, which further diminishes their therapeutic effectiveness (Anwar et al., 2023). Despite these limitations, plant extracts can still be valuable in managing antimicrobial resistance when used in combination with antibiotics. Some plant compounds act as resistance-modifying agents by enhancing antibiotic efficacy through mechanisms such as inhibiting bacterial efflux pumps or biofilm formation, which can lower the required antibiotic doses and reduce adverse effects (Rosato et al., 2020). Synergistic effects between plant extracts and antibiotics have been observed in combinatorial therapies, effectively combating multidrug-resistant bacteria and restoring the potency of existing antibiotics (Vaou et al., 2021b). Therefore, this study aims to evaluate the antimicrobial, anti-inflammatory, and antioxidative effects of Egyptian desert-adapted plants extracts, both alone and in combination with commonly used antimicrobial drugs, against multidrug-resistant Gram-negative bacterial strains isolated from sepsis patients. This research, utilizing both *in vitro* and *in vivo* studies, highlights the potential of natural plant-based therapies as promising combinative agents with existing antimicrobial drugs in combating sepsis associated with Gram-negative infections.

Materials and methods

Sample collection and ethical approval

The blood samples (n=400) used in this study were initially collected for diagnostic purposes to facilitate patient care, not for research. These samples were not specifically obtained for the study. However, informed consent was obtained from all the participants to carry out this study and to maintain patient confidentiality, all clinical and laboratory data were anonymized. This study adhered to ethical standards approved by the Port-Said University Ethical Approval Committee, under approval number REC.PHARM.PSU/2023/21.

Bacterial strains

The bacterial strains employed in this study were isolated from positive blood cultures routinely collected from patients with bloodstream infections (BSIs) at the Department of Microbiology, Al-Demerdash Hospital, Egypt. Initially, the Gram-negative isolates were identified using standard microbiological techniques, which included Gram staining, biochemical tests, and cultural characteristics in addition to API (Analytical Profile Index) 20E (BioMérieux, Mary l'Etoile, France). Subsequent confirmation of these isolates was achieved using the VITEK-2 automated identification system (BioMérieux, 2021), which offers enhanced accuracy and efficiency in bacterial identification. The standard strain *E. coli* ATCC 25922 was used as a control strain. To preserve these clinical strains for future research, they were stored in glycerol stocks at -70°C, a method proven to maintain bacterial viability and genetic integrity over extended periods (Kumar et al., 2016; Harris et al., 2019a). This storage technique ensures the stability of the strains and facilitates their use in subsequent studies, contributing to reliable and reproducible research outcomes. Furthermore, Genetic detection of specific Gram-negative bacterial genes using traditional PCR was applied identifying pathogens including *E. coli*, *P. aeruginosa*, and *A. baumannii* without sequencing. This approach involves amplifying unique gene sequences associated with these bacteria to confirm their presence. For *E. coli*, the *uidA* gene, which encodes β-glucuronidase, is commonly targeted as it serves as a reliable marker for this pathogen (Sokurenko et al., 1998). In the case of *P. aeruginosa*, the *pvdA* gene, which is involved in pyoverdine biosynthesis, is utilized for identification due to its specificity to this bacterium (Schweizer, 2003). For *A. baumannii*, the *blaOXA-51* gene, a prevalent carbapenemase gene, is frequently employed to detect this pathogen (Perez et al., 2007). The PCR process involves isolating bacterial DNA from samples, amplifying the target genes with specific primers, and visualizing the PCR products through gel electrophoresis. The presence of bands of the expected size on the gel indicates the presence of the target bacteria.

This method offers a rapid, cost-effective, and reliable means of pathogen detection, facilitating timely diagnosis and treatment (Miller et al., 2009; Ghosh et al., 2012).

Antibiotic sensitivity test of clinical bacterial strains

Clinical bacterial isolates were assessed for susceptibility to commonly prescribed antimicrobial agents for sepsis using the Kirby-Bauer disc diffusion method. In this procedure, antimicrobial discs were applied to Mueller-Hinton agar plates inoculated with bacterial isolates. The antimicrobial agents tested included: β-lactam agents with β-lactamase inhibitors such as Ampicillin/Sulbactam (SAM 10/10 μg) and Piperacillin/Tazobactam (TZP 100/10 μg); cephalosporins including Cefepime (FEP 30 μg), Cefotaxime (CTX 30 μg), Ceftazidime (CAZ 30 μg), and Ceftriaxone (CRO 30 μg); a cephalosporin and β-lactamase inhibitor combination, Ceftazidime/Avibactam (CAZ/AVI 30/20 μg); fluoroquinolones like Ciprofloxacin (CIP 5 μg); carbapenems including Ertapenem (ERT 10 μg), Imipenem (IPM 10 μg), and Meropenem (MEM 10 μg); aminoglycosides such as Amikacin (AK 30 μg); and Aztreonam (ATM 30 μg); and Colistin (CT 10 μg). Susceptibility and resistance were interpreted according to Clinical and Laboratory Standards Institute (CLSI) guidelines (CLSI, 2023; EUCAST, 2024). To confirm the results, additional antimicrobial susceptibility testing was performed to determine the minimum inhibitory concentrations (MICs) using the VITEK-2 automated system. Isolates were classified as multidrug-resistant (MDR) if they exhibited resistance to at least three different classes of antibiotics (Magiorakos et al., 2012).

Molecular detection of antimicrobial resistance genes

In this study, several resistance genes were analyzed to evaluate their role in antibiotic resistance. $bla_{CTX\text{-}M}$ (Extended-Spectrum β-Lactamase), responsible for hydrolyzing various β-lactam antibiotics, including penicillins and cephalosporins (Pitout and Laupland, 2008). $bla_{OXA\text{-}48}$ encodes a carbapenemase that confers resistance to carbapenems, crucial in treating multidrug-resistant infections (Poirel et al., 2012). bla_{NDM} (New Delhi Metallo-β-Lactamase) imparts resistance to nearly all β-lactams, including carbapenems, complicating treatment options (Yong et al.., 2019a). bla_{SHV} is associated with ESBL production, leading to resistance against penicillins and cephalosporins (Paterson and Bonomo, 2005). bla_{TEM} is a widely known β-lactamase gene contributing to resistance primarily to penicillins and some cephalosporins (Datta and Hughes, 1983). These genes collectively highlight the critical challenge of antibiotic resistance and underscore the need for continued surveillance and novel treatment strategies.

For the PCR detection of resistance genes in bacterial isolates, total DNA was extracted from each isolate using the JET Genomic DNA Purification Kit (Thermo Scientific, USA) according to the manufacturer's instructions. Following the extraction of DNA, the PCR amplification was conducted using primers and cycling conditions as specified in the protocols outlined in previous literature (Table 1). This approach adhered to established methods to ensure accuracy and reproducibility in the detection of specific genes. The primer sequences and cycling parameters were selected based on validated protocols from prior studies, which have been demonstrated to effectively amplify the target genes of interest (Table 1). To ensure the specificity of these primers, they were analyzed using NCBI Primer-BLAST, a tool available at the NCBI website (https://www.ncbi.nlm.nih.gov/guide/data-software/). This process ensures that the primers effectively target the intended genes and minimize non-specific amplification.

Collection and extraction of the desert-adapted plants materials

Four species of desert-adapted plants, traditionally utilized for treating severe bacterial infections, were collected from their natural habitat in the Egyptian desert. These plants, detailed in Table 2, were identified by the Herbarium of the Desert Research Center in Egypt. For each plant, 300 grams of shade-dried, coarsely powdered aerial parts were extracted using 70% ethanol through a maceration process. The evaporation of ethanol was confirmed by concentrating the resulting extracts to dryness under reduced pressure using a rotary

TABLE 1 Nucleotide sequences and amplicon size of oligonucleotides primers used for PCR detection of resistance genes of the tested Gram-negative bacterial isolates.

Gene	Sequences	Annealing Temperature	Amplicon Size (bp)	References
$bla_{CTX\text{-}M}$	F: ATGGTTAAAAAATCACTGCGYC R: TTACAAACCGTCGGTG	51°C	876	Patel, 2015
$bla_{OXA\text{-}48}$	F: GCGTGGTTAAGGATGAACAC R: CATCAAGTTCAACCCAACCG	45°C	438	Poirel and Nordmann, 2006
bla_{NDM}	F: GGTTTGGCGATCTGGTTTTC R: CGGAATGGCTCATCACGATC	45°C	621	Yong et al., 2019b
bla_{SHV}	F-AGGATTGACTGCCTTTTTG R-ATTTGCTGATTTCGCTCG	94°C	392	Paterson and Bonomo, 2005
bla_{TEM}	F-TTGGGTGCACGAGTGGGTTA R-TAATTGTTGCCGGGAAGCTA	95°C	465	Kim et al., 2015

TABLE 2 Selected plant extracts, their families, and traditional use.

Plant name	Family	Traditional use	References
Jasonia candicans Del. Borsh	*Asteraceae*	Antimicrobial activity Anti-inflammatory	Francisco Les et al., 2021; Hammerschmidt et al., 1993
Cistanche tubulosa (Schrenk) Hook.f.	*Orobanchaceae*	Antibacterial activity Enhances immunity. Antioxidant Neuroprotection Hepatoprotection	Li et al., 2016 Yuan et al., 2018
Moltkiopsis ciliata (Forssk.) I. M. Johnst	*Boraginaceae*	Antimicrobial Antioxidant Anti-inflammatory Anticancer	Abdel-Hak et al., 2022
Thymelea hirsuta(L.) Endl.	*Thymelaeaceae*	Anti-inflammatory Neuroprotective Antioxidant	Marmouzi et al., 2021

evaporator set at 40°C. This process effectively removed the ethanol from the extracts, leaving behind the concentrated plant material, which was then stored at 4°C until further use (Ghaly et al., 2023).

Preliminary screening of plant extracts

The antibacterial efficacy of the plant extracts was evaluated using the agar well diffusion method. Bacterial cultures, standardized to a 0.5 McFarland turbidity equivalent, were evenly spread on sterile Mueller-Hinton agar plates to achieve uniform bacterial distribution. Plant extracts, dissolved in dimethyl sulfoxide (DMSO) (10 mg/mL), were then introduced into wells drilled into the agar at a volume of 100 µL per well. The plates were incubated at 37°C for 24 hours to allow for bacterial growth and interaction with the extracts. After incubation, the diameters of the inhibition zones surrounding each well were measured in millimeters to assess the antimicrobial activity of the extracts (Murray et al., 2016; Clinical and Laboratory Standards Institute, 2023). A positive control well containing colistin and a negative control well containing DMSO were included in the assay for comparison.

Determination of minimum inhibitory concentration of plant extracts

The minimum inhibitory concentrations (MICs) of plant extracts against identified Gram-negative strains were determined using the broth microdilution method. Plant extracts were initially dissolved in 10% DMSO to achieve a final concentration of 1 mg/mL in the culture broth. Serial 1:2 dilutions were then performed to obtain a range of concentrations from 1 mg/mL to 0.0156 mg/mL. Each dilution (100 µL) was added to a 96-well plate, along with negative and positive controls: culture broth with DMSO and culture broth with colistin, respectively. Each well, including the test and growth control wells, was inoculated with 5 µL of a bacterial suspension at a concentration of 10^5 CFU/mL ((Murray et al., 2016; Eloff, 1998).

All experiments were performed in triplicate and the microdilution trays were incubated at 37°C for 18 h. After incubation, the minimum inhibitory concentration (MIC) was determined by measuring the optical density of each well using a spectrophotometer, similar to the principles used in an ELISA assay to assess bacterial growth inhibition. MIC values were defined as the lowest concentration of each plant extract, which completely inhibited microbial growth (Valgas et al., 2007).

Evaluating the efficacy of the most effective desert-adapted plant extracts in combination with amikacin, a commonly prescribed antimicrobial agent

The checkerboard method is an established approach for determining the fractional inhibitory concentration (FIC) index, which assesses the interaction between a plant extract and a common antimicrobial drug (amikacin). This technique involves creating serial dilutions of both the plant extract and the antimicrobial drug, which are then combined in a 96-well microtiter plate, with each well containing a different concentration of the extract and drug. After adding a standardized bacterial suspension to each well, the amikacin-resistant Gram-negative bacteria, which exhibited multidrug-resistant (MDR) patterns (40 isolates with higher multiply antibiotic indices), were incubated at 37°C for 18-24 hours to facilitate bacterial growth and interaction with the compounds. The effectiveness of the plant extract and drug, both individually and in combination, is evaluated by measuring the minimum inhibitory concentration (MIC) for each in a triplicate manner. The FIC index is calculated using the formula: FIC index = (MIC of plant extract in combination/MIC of plant extract alone) + (MIC of antimicrobial drug in combination/MIC of antimicrobial drug alone). This index indicates the nature of the interaction—whether synergistic (FIC index ≤ 0.5), additive (FIC index > 0.5 but ≤ 1), or antagonistic (FIC index > 1). By revealing potential synergistic or antagonistic effects, the checkerboard method aids in optimizing combination therapies and understanding how plant extracts can enhance antimicrobial treatment (Odds, 2003; Tamma et al., 2012).

Determination of the anti-inflammatory activity of tested plant extracts

The inhibition of Cyclooxygenase-1 (COX-1) and COX-2 enzymes by the tested plant extracts was assessed using an ELISA-based method in triplicate manner. Plant extracts were dissolved in 10 µL of DMSO to create a series of stock solutions with concentrations ranging from 50 mmol/L to 500 pmol/L. Celecoxib served as the positive control. The inhibition of recombinant COX-1 and COX-2 enzymes was measured using a Cayman Human (EIA) kit (Catalog No. 560131, Cayman Chemicals Inc, MI, USA) and analyzed with a Robomik P2000 ELISA reader at 450 nm. The effectiveness of the plant extracts was quantified by determining the mean concentration required to achieve 50% enzyme inhibition (IC_{50}) ± standard deviation. Additionally, the COX-2 selectivity index (SI) was calculated as the ratio of IC_{50} (COX-1) to IC_{50}(COX-2) and compared to that of celecoxib to evaluate selectivity (Baek et al., 2021).

Determination of antioxidant activity of tested plant extracts using DPPH assay

The antioxidant activity (AA%) of each substance was evaluated using the 2,2-diphenyl-1-picryl-hydrazyl-hydrate (DPPH) free radical assay, as described by Boly et al. (2016). In this assay, 100 µL of freshly prepared DPPH reagent (0.1% in ethanol) was mixed with 100 µL of each sample, which had been dissolved in ethanol, in a 96-well plate (n=6). The reaction mixture was incubated at room temperature for 30 minutes in the dark. The reduction in radical activity was monitored by measuring the absorbance at 540 nm using a microplate reader (FluoStar® Omega, WWU, Münster, Germany), with ethanol serving as the blank. The percentage of scavenging activity was calculated using the formula:

$$AA\,\% = 100 - [(Abs_{sample} - Abs_{blank}) \times 100/Abs_{control}$$

Where $Abs_{control}$ is the absorbance at 540 nm of 100µM DPPH solution without addition of the extract, Abs_{sample} is the absorbance at 540nm of 100µM DPPH with 5–100 µg/mL of sample. Trolox was used as a reference standard. The IC_{50} value, which represents the concentration of extract required to reduce DPPH by 50%, was determined by plotting the percentage inhibition against concentration using GraphPad Prism 5® (Chen et al., 2013).

In Vivo evaluation of synergistic interactions between the highest effective plant extract and the most common prescribed antimicrobial agent in a murine model

Experimental design and animal model

An experimental septicemic mouse model, as depicted in Supplementary Figure S1, was developed to evaluate the promising antimicrobial effects of *J. candicans* extract on sepsis induced by 4 multi-drug resistant (MDR) isolates with the highest multi-antibiotic resistance (MAR) index including *E. coli*, *K. pneumoniae*, *A. baumannii*, and *P. aeruginosa*, following ethical guidelines from the Port-Said University Ethical Committee. After a one-week quarantine, 130 male BALB/c mice (20–25 g) were randomly assigned to thirteen groups (n = 10 per group): Group A served as the general negative control (unchallenged and untreated); Group B was the positive control for *K. pneumoniae* (challenged and untreated); Group C included *K. pneumoniae*-challenged mice treated with amikacin; Group D received a combination of *J. candicans* extract and amikacin after *K. pneumoniae* challenge; Group E was the positive control for *E. coli* (challenged and untreated); Group F consisted of *E. coli*-challenged mice treated with amikacin; Group G received *J. candicans* extract and amikacin after *E. coli* challenge; Group H served as the positive control for *A. baumannii* (challenged and untreated); Group I included *A. baumannii*-challenged mice treated with amikacin; Group J received a combination of *J. candicans* extract and amikacin after *A. baumannii* challenge; Group K was the positive control for *P. aeruginosa* (challenged and untreated); Group L consisted of *P. aeruginosa* challenged mice treated with amikacin; and Group M received *J. candicans* extract and amikacin after *P. aeruginosa* challenge. All mice were housed in a specific pathogen-free (SPF) environment with controlled conditions: temperature 20–22°C, humidity 40–70%, and a 12-hour light/dark cycle, and were anesthetized using isoflurane inhalation.

Establishment of acute sepsis models

To establish the sepsis model, all groups except the negative control group were injected intraperitoneally with bacterial suspensions. Groups B-D received 0.04 mL of *K. pneumoniae* containing 10^9 CFU/mL; Groups E-G were administered 2 to 5 × 10^7 CFU of *E. coli*; Groups H-J were given 0.5 mL of *A. baumannii* suspension containing 10^7 CFU/mL; and Groups K-M received 2 × 10^{10} CFU of *P. aeruginosa* in 100 µL of saline. The negative control group received an equivalent volume of saline (pH 7.4). Antimicrobial treatments began 2 hours post-infection, with amikacin administered intraperitoneally at 15 mg/kg every 12 hours for three days. The dosing regimen was determined based on pharmacokinetic and pharmacodynamic data from previous studies (Song et al., 2009; Bretonnière et al., 2010). In groups treated with the combination of *J. candicans* extract and amikacin, the treatment was also administered intraperitoneally every 12 hours for three days at sub-minimum inhibitory concentration (sub-MIC) levels (0.5 MIC) (Verweij et al., 2004; Singh et al., 2022; Liu et al., 2022; Harris et al., 2019b; Cirioni et al., 2007). Finally, we conducted regular monitoring of the animals, assessing key health indicators, including body weight, activity levels, and clinical signs of infection (such as lethargy, ruffled fur, and reduced food intake) and we incorporated this results in our new manuscript.

Histopathological analysis

Four days after treatment, blood samples were collected from the ophthalmic vein plexus of the mice to evaluate biological indices. Following this, six mice from each group were randomly

selected for histopathological examination of the lung and spleen. For the histopathological analysis, tissues from the spleen, and lungs were fixed in formalin, embedded in paraffin, sectioned at 5 μm thickness, and stained with hematoxylin and eosin (H&E) for examination. Histological specimens were then analyzed under a light microscope, and lesions were assessed qualitatively and quantitatively. Of note, 10 microscopic fields per sample were examined for both splenic and lung tissues across each challenged and unchallenged mice group. Fields were selected randomly to ensure unbiased analysis and provide a comprehensive assessment of tissue alterations in response to challenges. Lesions in the spleen and lungs were scored according to their severity: (++++): maximum severity, (+++): marked severity, (++): moderate severity, (+): mild severity, and (0): no pathological changes. The mice were euthanized by cervical dislocation for these assessments.

Results

Prevalence and antimicrobial resistance patterns of gram-negative bacteremia

A total of 400 blood samples were collected for blood culture analysis, resulting in the identification of 233 clinical bacterial isolates as Gram-negative pathogens, yielding a prevalence rate of 58.25%. Among these Gram-negative isolates, *E. coli* and *K. pneumoniae* were the predominant pathogens, with 113 isolates (48.5%) and 90 isolates (38.6%), respectively. The next most common pathogens were *A. baumannii*, represented by 16 isolates (6.9%), and *P. aeruginosa*, with 14 isolates (6%).

Analysis of the antimicrobial resistance patterns among these clinical isolates revealed a significant burden of multidrug resistance (MDR), as 185 isolates (79.4%) demonstrated resistance to 3 or more antimicrobial classes. Notably, *P. aeruginosa* had the highest MDR prevalence (92.8%). This was followed by *A. baumannii*, with 81.2% of isolates showing MDR patterns. Additionally, a high prevalence of MDR was observed among *E. coli* and *K. pneumoniae*, with rates of 77.9% and 78.9%, respectively. The distribution of antimicrobial resistance and resistance gene profiles among the investigated Gram-negative bacterial species: *E. coli*, *K. pneumoniae*, *P. aeruginosa*, and *A. baumannii*. were observed in Figure 1. Our results indicated a varied distribution and heterogenous patterns of antimicrobial resistance and resistance gene profiles among different Gram-negative bacterial species. The results further revealed a heterogeneous pattern of antimicrobial resistance gene distribution, particularly in *Pseudomonas aeruginosa* and *Acinetobacter baumannii*. In contrast to *E. coli* and *K. pneumoniae*, where antimicrobial resistance and resistance genes were more consistently distributed among strains, *P. aeruginosa* and *A. baumannii* exhibit significant variability in the presence and absence of resistance genes, reflecting low clonality and high heterogeneity within these isolates.

The results for antimicrobial resistance across all Gram-negative bacteria, represented in Figure 2, revealed substantial resistance to a wide range of antimicrobial agents. Conversely, all tested isolates demonstrated complete susceptibility to colistin, an antibiotic considered as a last-resort treatment for MDR infections. Overall, all investigated isolates displayed notably high resistance rates across various antibiotics. For amikacin, the isolates showed a moderate resistance rate of approximately 30%. However, resistance to aztreonam and ampicillin-sulbactam was significantly higher, at around 70-80%, reflecting a broad decline in the efficacy of these agents. Resistance to cefepime, cefotaxime, ceftriaxone, and ceftazidime was consistently elevated, with rates in the 70-80% range, underscoring the substantial challenges in treating septicemic patients with these commonly used beta-lactam antibiotics.

Of note, the resistance patterns among the detected Gram-negative species indicate that, for several antimicrobial, including aztreonam, ampicillin-sulbactam, cefotaxime, ceftriaxone, ceftazidime/avibactam, ciprofloxacin, ertapenem, and temocillin, the levels of resistance did not reach statistical significance, with *P-values* exceeding 0.05. This suggests that resistance to these antibiotics may not be markedly different across the groups analyzed. In contrast, the resistance to other antimicrobial agents showed statistically significant differences ($P< 0.05$), indicating that these other drugs are likely experiencing varied effectiveness due to differing resistance levels among the bacterial species tested. These findings highlight specific antibiotics that may be more or less effective in treating infections caused by these Gram-negative organisms, underscoring the importance of ongoing surveillance to guide antibiotic selection and optimize treatment strategies.

When focusing on specific pathogens, *A. baumannii*, *E. coli*, *K. pneumoniae*, and *P. aeruginosa*, the data demonstrated high levels of resistance across most tested antimicrobial agents, with *A. baumannii* generally showing the highest resistance rates. For amikacin, *A. baumannii* exhibited resistance near 60%, whereas *E. coli*, *K. pneumoniae*, and *P. aeruginosa* showed lower resistance levels, typically around 20-40%. Resistance to aztreonam and ampicillin-sulbactam was uniformly high across all pathogens, ranging from 70-90%, with *A. baumannii* and *K. pneumoniae* particularly high resistance levels (Figure 2). The presence of resistance genes such as *blaSHV, blaCTX-M, blaTEM, blaOXA-48*, and *blaNDM* highlighted the molecular mechanisms driving resistance in these pathogens. Notably, *blaNDM* was highly prevalent in *A. baumannii* and *K. pneumoniae*, contributing significantly to the high levels of carbapenem resistance observed as shown in Figure 2. Except for the presence of the *blaTEM* gene, all other resistance genes showed significant variation among the Gram-negative species detected ($P< 0.05$). These findings underscored the severe antimicrobial resistance challenges posed by these Gram-negative pathogens in septicemic patients, emphasizing the urgent need for alternative therapeutic strategies and stringent antimicrobial stewardship practices.

Antimicrobial activity of medicinal plants and their activity against tested bacteria

Ethanol extracts from medicinal plants were assessed for antimicrobial activity against MDR Gram-negative bacteria from

10.3389/fcimb.2025.1493769

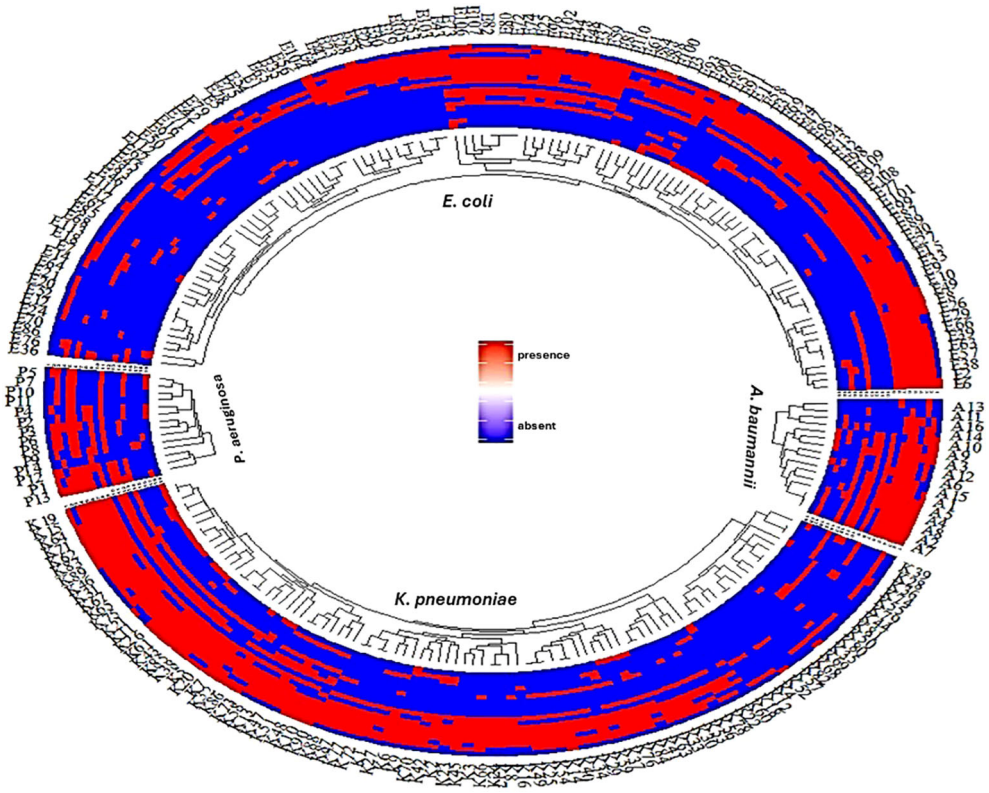

FIGURE 1
A fan dendrogram illustrating the distribution of Gram-negative bacteria based on their antimicrobial resistance profiles and associated resistance genes. This figure showed the distribution of antimicrobial resistance and resistance gene profiles among the investigated Gram-negative bacterial species: *E. coli*, *K. pneumoniae*, *P. aeruginosa*, and *A. baumannii*. The inner circle shows clustering of strains based on species, while the outer rings indicate the presence (red) or absence (blue) of resistance genes. The consistent red regions suggest widespread presence of resistance genes across species, particularly for *E. coli* and *K. pneumoniae*. In contrast, *P. aeruginosa* and *A. baumannii* show a more heterogeneous pattern of resistance gene distribution. Line1: AK, line2: ATM, line3: SAM, line4: FEB, line5: CTX, line6: CRO, line7: CAZ, line8: CAZ/AVI, line9: CIP, Line10: CT, line11: TZP, line12: IPM, line: ETP, line14: MEM, line15: bla_{OXA}, line16: bla_{NDM}, line17: bla_{SHV}, line18: bla_{CTX}, line19: bla_{TEM},.

septic patients. The agar diffusion assay revealed significant antibacterial effects, with inhibition zones ranging from 13 to 25 mm. *J. candicans* emerged as the most effective, showing inhibition zones of 18–25 mm, particularly strong against *A. baumannii* (25 mm) and *E. coli* (19 mm), and effective against *P. aeruginosa* and *K. pneumoniae* (18 mm each). *M. ciliata* also showed notable activity, especially against *A. baumannii* (20 mm) and *E. coli* (16 mm). In contrast, *C. tubulosa* and *T. hirsuta* exhibited more variable results; *T. hirsuta* had significant inhibition against *E. coli* (15 mm) and *A. baumannii* (14 mm), while *C. tubulosa* was least effective, particularly against *E. coli* (13 mm).

Broth microdilution testing revealed that *J. candicans* exhibited the highest antimicrobial potency among the tested plant extracts (Supplementary Table S1). It demonstrated the lowest MIC values, with 250 µg/mL against most *E. coli* isolates, and 500 µg/mL against most *K. pneumoniae, A. baumannii*, and *P. aeruginosa* isolates. In contrast, *C. tubulosa* showed comparatively higher MIC values, reflecting a reduced effectiveness: 500 µg/mL against most *E. coli* and *K. pneumoniae* isolates, 1000 µg/mL against most *P. aeruginosa*, and *A. baumannii* isolates. *M. ciliata* exhibited variable efficacy, with MIC values of 500 µg/mL against most *E. coli* and 1000 µg/mL for most *A. baumannii*, *K. pneumoniae*, and *P. aeruginosa* isolates. *T. hirsuta* had the highest MIC values across all tested bacteria, with 1000 µg/mL against most investigated isolates. Overall, *J. candicans* demonstrated the strongest antimicrobial potential, followed by *M. ciliata*, indicating its superior effectiveness in inhibiting the growth of these Gram-negative bacteria.

Combined action of common prescribed antibiotics and the most effective plant extract

The checkerboard assay, as shown in Supplementary Table S1, assessed the combined effect of the widely prescribed antibiotic amikacin and *J. candicans* extract, demonstrating a synergistic interaction against all investigated amikacin-resistant, multidrug-resistant (MDR) Gram-negative bacteria (40 isolates). The combination of *J. candicans* with amikacin resulted in a notable reduction in the MIC values for both agents, with a FICI ≤ 0.5, indicating a significant enhancement in antimicrobial efficacy. Specifically, this combination therapy substantially lowered the MIC values for *E. coli* and, to a lesser extent, for *K. pneumoniae*,

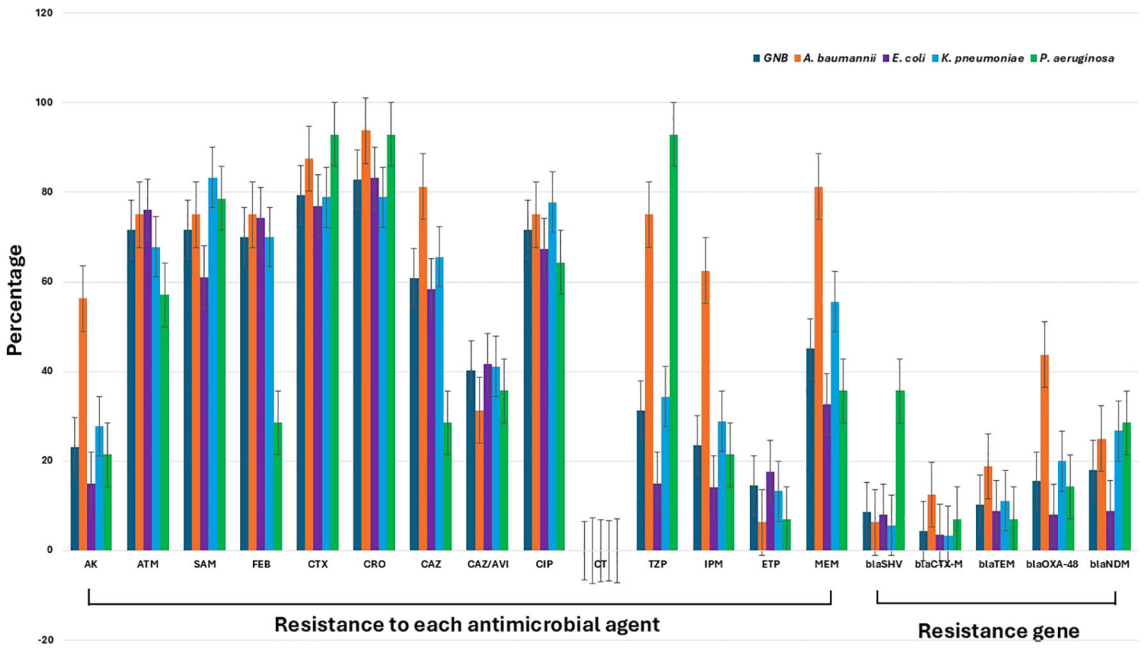

FIGURE 2
Antimicrobial resistance patterns and resistance gene prevalence among Gram-negative bacteria isolated from septicemic patients. The figure shows the percentage resistance of various Gram-negative pathogens, including *A. baumannii*, *E. coli*, *K. pneumoniae*, and *P. aeruginosa*, to a range of antimicrobial agents: amikacin (AK), aztreonam (ATM), ampicillin-sulbactam (SAM), cefepime (FEB), cefotaxime (CTX), ceftriaxone (CRO), ceftazidime (CAZ), ceftazidime-avibactam (CAZ/AVI), ciprofloxacin (CIP), colistin (CT), piperacillin-tazobactam (TZP), imipenem (IPM), ertapenem (ETP), and meropenem (MEM). The data also include the prevalence of key resistance genes: bla_{SHV}, bla_{CTX-M}, bla_{TEM}, bla_{OXA-48}, and bla_{NDM}. The gray columns represent the overall resistance profile of Gram-negative bacteria.

A. baumannii, and *P. aeruginosa*. These results suggest that *J. candicans* and amikacin work synergistically to inhibit bacterial growth more effectively than either agent alone. Moreover, this synergistic interaction highlights the potential of integrating *J. candicans* extract with amikacin as a promising therapeutic strategy to improve treatment outcomes for infections caused by resistant Gram-negative bacteria. Interestingly, over 50% of the amikacin-resistant strains were converted to sensitive phenotypes by this combination, further emphasizing the therapeutic potential of this approach.

2 Anti-inflammatory activity of plant extracts using invitro COX-1/COX-inhibition assay

Our results indicated that *J. candicans* extract exhibited the most potent inhibitory activity against both COX-1 and COX-2 enzymes, with IC_{50} values significantly lower than those of the standard drug, Celecoxib (IC_{50}: 0.28 µg/mL for COX-1 and 1.11 µg/mL for COX-2). Specifically, *J. candicans* demonstrated exceptional efficacy in inhibiting these enzymes, suggesting its potential as a therapeutic agent for inflammatory conditions. In addition, the extracts of *C. tubulosa* and *T. hirsuta* also exhibited noteworthy inhibitory effects on both COX-1 and COX-2, with IC_{50} values that closely approached those of Celecoxib, as detailed in Table 3. Importantly, all four plant extracts showcased a COX-2 selectivity index comparable to that of Celecoxib, ranging from 0.23 to 0.28. This selectivity indicates a preference for inhibiting COX-2 over COX-1, which is advantageous for minimizing gastrointestinal side effects often associated with non-selective COX inhibitors. The ability of these extracts to selectively target COX-2 further emphasizes their potential as valuable anti-inflammatory agents. Overall, the findings suggest that these plant extracts, particularly *J. candicans*, not only provide strong anti-inflammatory effects but also present a promising alternative to conventional NSAIDs. Further investigation into their mechanisms of action and clinical applications is warranted to fully explore their therapeutic potential in managing inflammation and related conditions.

Antioxidant activity of tested plant extracts

The DPPH assay was utilized to assess the scavenging activity of the tested plant extracts alongside the standard antioxidant, Torolox. This assay determines the concentration of the extract needed to reduce 50% of the initial DPPH radical. Among the plant extracts, *J. candicans* demonstrated the highest DPPH free radical scavenging activity, with a notably low IC_{50} value of 71.97 µg/mL, surpassing *C. tubulosa*, which had an IC_{50} value of 97.44 µg/mL. In contrast, *M. ciliata* and *T. hirsute* exhibited the lowest scavenging activity, with IC_{50} values of 156 µg/mL and 193 µg/mL, respectively. For comparison, the reference antioxidant Torolox showed an IC_{50} value of 56.82 µg/mL. These findings highlight that while *J.*

TABLE 3 *In vitro* COX-1 IC_{50}, COX-2 IC_{50}, and COX-2 Selectivity Index (SI) data for tested plant extracts in comparison to Celecoxib (IC_{50} in µg/ml).

Plant Extracts	COX1- IC_{50} (µg/ml) [mean IC_{50} values ± SD]	COX2- IC_{50} (µg/ml) [mean IC_{50} values ± SD]	COX-2 Selectivity index (SI)
Jasonia candicans	0.28 ± 0.0006	1.11 ± 0.1	0.23
Cistanche tubulosa	0.31 ± 0.0012	1.32 ± 0.15	0.23
Moltkiopsis ciliata	0.44 ± 0.0015	1.57 ± 0.4	0.28
Thymelia hirsuta	0.3 ± 0.00006	1.19 ± 0.1	0.25
Celecoxib	0.34	1.2	0.28

candicans and *C. tubulosa* display notable antioxidant activity, Torolox remains the most effective agent for scavenging DPPH radicals, outperforming the plant extracts.

Assessment of clinical signs as indicators of disease severity in a septicemia model

Data collected over the study period showed that animals in the control group exhibited significant weight loss and clinical signs of illness, which are indicative of severe septicemia. In contrast, animals receiving treatment with the combination of desert plant extracts and amikacin demonstrated less pronounced weight loss and a notable improvement in clinical signs, suggesting a better overall health status. Specifically, animals treated with the combination showed an average weight loss of approximately 5% compared to 15% in the amikacin-only group, indicating enhanced recovery with the extract. Additionally, the survival rate in the combination treatment group was higher, with 80% of animals surviving until the end of the study, compared to 50% in the amikacin group alone.

Histopathology results

Histopathological examination of lung tissue from unchallenged untreated groups (Figure 3A) compared to the challenged untreated groups infected with *A. baumannii* (Figure 4a), *E. coli* (Figure 4b), *K. pneumoniae* (Figure 4c), and *P. aeruginosa* (Figure 4d) revealed significant pathological changes. These included collapse of alveolar walls, emphysema, congestion, hemorrhage/edema, as well as pulmonary vascular alterations such as neutrophil infiltration and thrombus formation, with the highest severity scores observed. In the group infected with *A. baumannii*, amikacin alone, as shown in Figure 5a, led to moderate alveolar wall congestion (++), whereas the combination therapy, as illustrated in Figure 6a, resulted in a mild severity (+), suggesting a potential ameliorative effect of the plant extract. Similarly, interstitial neutrophil infiltration was moderately severe with amikacin treatment (++), but the combination therapy reduced this to a mild response (+). Alveolar edema and hemorrhage followed a comparable pattern, with amikacin showing moderate severity (++) and the combination therapy reducing this to a mild level (+), indicating a reduction in overall lesion severity. Damage to pneumocytes I and endothelial cells was moderately severe with amikacin (++), but notably absent (-) with the combination treatment, suggesting protective benefits of *J. candicans* extract against cellular damage. Severe thrombosis (+++) within the alveolar vasculature was observed with amikacin alone, but this was significantly reduced to mild (+) with the combined treatment. Furthermore, alveoli filled with granular necrotic debris and minimal cellular reaction were moderately severe (++) with amikacin, but this decreased to a mild severity (+) with the combination treatment, and a similar trend was noted in alveolar collapse, with scores reduced from moderate (++) to mild (+) in the combination group (Table 4).

For mice challenged with *E. coli*, the lesions were generally more severe, with amikacin treatment alone (Figure 5B) resulting in marked alveolar wall congestion (+++), extensive interstitial neutrophil infiltration (+++), and severe pneumocyte and endothelial cell damage (+++). However, the combination of amikacin and *J. candicans* extract (Figure 6b) substantially mitigated these effects, reducing alveolar wall congestion and interstitial neutrophils and pneumocyte damage to mild (+). This reduction in severity extended to alveolar vasculature thrombosis, where the combination treatment decreased lesion scores from severe (+++) to mild (++), and alveolar collapse from (+++) to (+), indicating a significant reduction in overall damage when using the combined treatment (Table 4).

For *K. pneumoniae*-challenged mice, treatment with amikacin alone (Figure 5c) resulted in interstitial neutrophil infiltration with uniformly severe lesions (+++). However, the combination treatment (Figure 6c) significantly reduced these scores to mild levels. Pneumocyte damage, which was moderate in the amikacin-treated group, was further reduced to mild levels in the combination therapy group. Despite these improvements, alveolar edema and hemorrhage exhibited severe lesions (+++) with both treatments. Additionally, the presence of alveoli filled with granular necrotic debris, as well as alveolar wall congestion, thrombosis, and collapse, remained consistently moderate (++) for both treatment options, indicating a persistent level of damage (Table 4).

In mice challenged with *P. aeruginosa*, amikacin treatment alone (Figure 5d) led to moderate lesions across various parameters, including alveolar wall congestion, interstitial neutrophil infiltration, alveolar collapse, and pneumocyte damage, all with moderate scores (++). The combination therapy with *J. candidus* extract (Figure 6d) did not markedly alter these outcomes, as most parameters remained at similar moderate levels (++). The

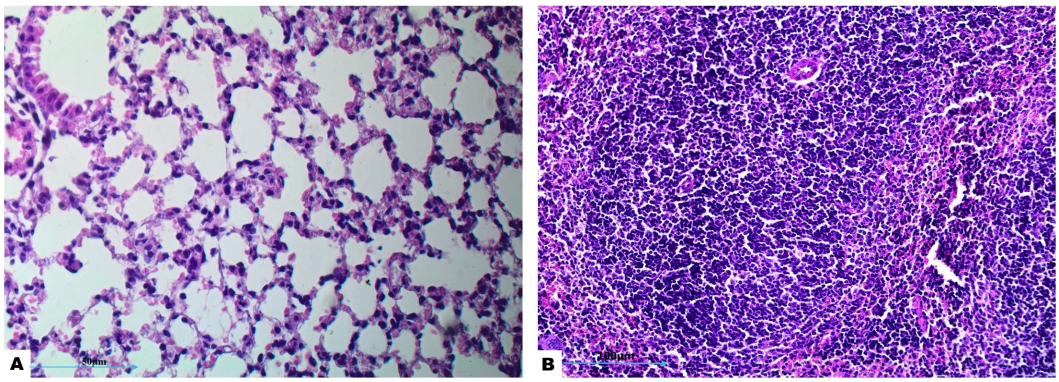

FIGURE 3
Histological examination of lung and splenic tissues from control negative (unchallenged and untreated) group exhibits normal histological features. **(A)** Normal alveolar structure observed under H&E staining at 400x magnification, and **(B)** normal splenic tissue observed under H&E staining at 200x magnification.

severity of alveoli filled with granular necrotic debris was mild (+) in both treatment groups, showing minimal variation. However, a notable improvement was observed in pneumocyte damage with the combination treatment, which was completely resolved, resulting in a healing score (-). Additionally, the combination therapy reduced alveolar thrombosis severity from severe (+++) in the amikacin treated group to moderate (++). Alveolar edema and hemorrhage also improved, from moderate lesions with amikacin treatment to mild lesions with the combination therapy. These findings suggest that while the combination therapy significantly enhanced pneumocyte healing and reduced Alveolar edema, hemorrhage, and thrombosis severity, other aspects such as

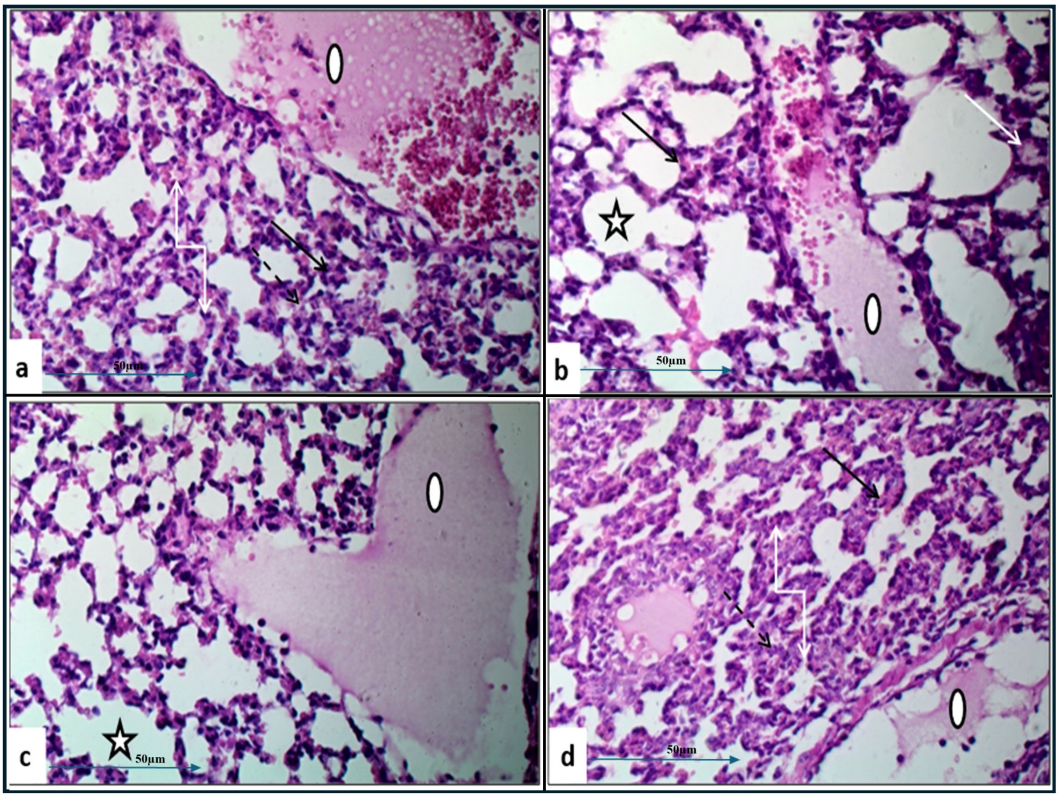

FIGURE 4
Histological examination of lung tissue from challenged untreated groups (H&E, 400x magnification). Histopathological analysis of untreated groups challenged with *A. baumannii* **(a)**, *E. coli* **(b)**, *K. pneumoniae* **(c)**, and *P. aeruginosa* **(d)** reveals alveolar wall collapse (truncated arrows), emphysema (asterisks), congestion (black arrows), hemorrhage/edema (white arrows), and pulmonary vasculature changes, including neutrophil infiltration (dashed arrows) and thrombus formation (circles).

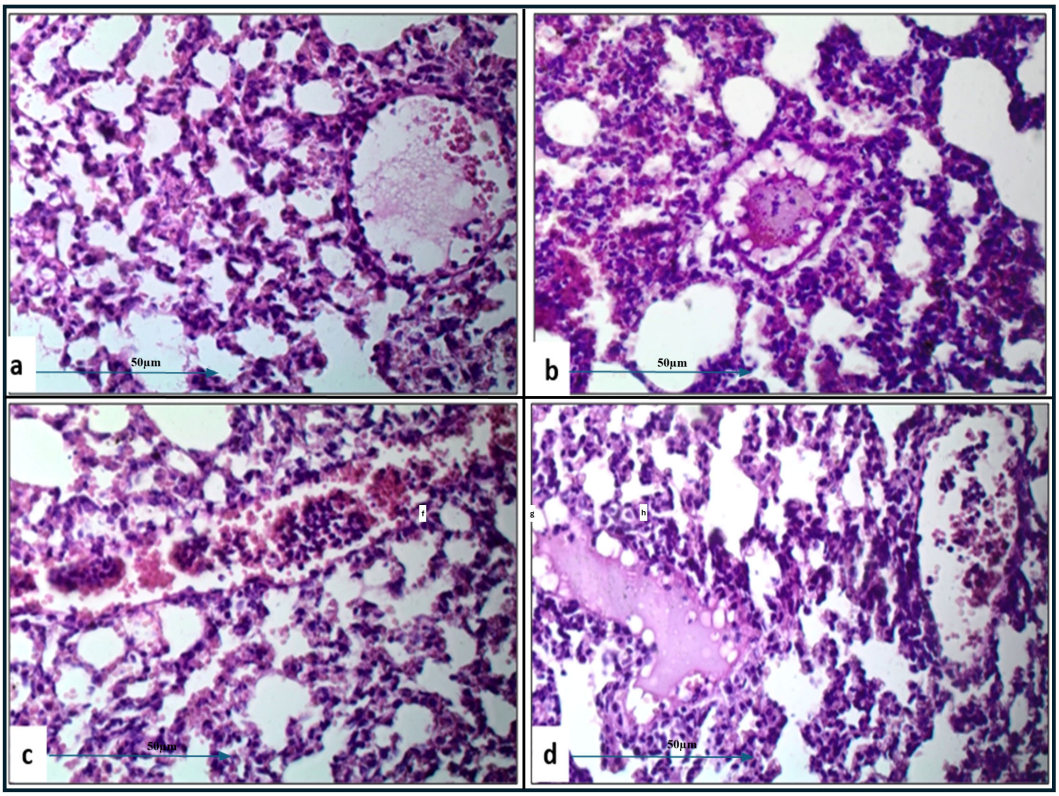

FIGURE 5
Histological examination of lung tissue from amikacin-treated challenged groups (H&E, 400x magnification) revealed alveolar wall collapse and congestion across all groups. Histopathological analysis of the amikacin-treated groups challenged with *A. baumannii* **(a)**, *E. coli* **(b)**, *K. pneumoniae* **(c)**, and *P. aeruginosa* **(d)** showed alveolar emphysema, which was pronounced in **(b, c)**, but moderate in **(a, d)**. Additionally, alveolar edema and hemorrhage were still observed in **(a–c)**. Changes in pulmonary vasculature, such as thrombus formation and neutrophil infiltration, were detected in all groups.

lung interstitial infiltration, alveolar collapse, pneumocyte damage, and necrotic debris were less responsive to the combined treatment approach (Table 4).

In the histopathological study comparing splenic tissue from unchallenged untreated mice (control negative) shown in Figure 3b with that from untreated challenged mice (Figure 7) infected with *A. baumannii* (Figure 7a), *E. coli* (Figure 7b), *K. pneumoniae* (Figure 7c), and *P. aeruginosa* (Figure 7d), the challenged mice exhibited a high severity score with significant pathological changes. There was a notable increase in apoptosis and necrosis of lymphocytes, indicating substantial cellular damage and death within the spleen. Furthermore, the presence of considerable fibrosis and/or hyaline deposition in the splenic tissue points to chronic inflammation and tissue remodeling. These results highlight the severe impact of the infections on the spleen, showcasing extensive tissue damage and a compromised immune response. The splenic score lesion analysis of mice treated with amikacin alone (Figure 8) or in combination with *J. candicans* extract (Figure 9) showed notable differences in the severity of apoptosis/necrosis of lymphocytes and fibrosis/hyaline deposition across the different bacterial infections. For mice challenged with *A. baumannii*, treatment with amikacin (Figure 8a) resulted in mild lymphocyte apoptosis/necrosis (+), whereas the combination with *J. candicans* extract (Figure 9a) showed no detectable apoptosis/necrosis (-), suggesting a protective effect of the plant extract. Additionally, there was no fibrosis or hyaline deposition observed in either the amikacin alone or the combination treatment groups (-), indicating minimal splenic tissue remodeling in response to the infection or treatment. In the case of *E. coli* infection, amikacin treatment (Figure 8b) led to moderate lymphocyte apoptosis/necrosis (++), while the combination with *J. candicans* (Figure 9b) significantly reduced this to mild levels (+), further supporting the potential protective role of the plant extract against splenic damage. No fibrosis or hyaline deposition was detected in either treatment group (-), suggesting that the treatments did not induce significant fibrotic changes within the spleen (Table 4).

For *K. pneumoniae* infections, neither amikacin alone (Figure 8c) nor the combination with *J. candicans* extract (Figure 9c) resulted in detectable lymphocyte apoptosis/necrosis or fibrosis/hyaline deposition (-), indicating a lack of observable splenic lesions with these treatments. This suggests that the bacterial strain or the specific conditions did not provoke splenic damage under these treatment regimens. In mice challenged with *P. aeruginosa*, treatment with amikacin alone (Figure 8d) resulted in severe lymphocyte apoptosis/necrosis (+++), highlighting a significant degree of splenic damage. However, the combination

10.3389/fcimb.2025.1493769

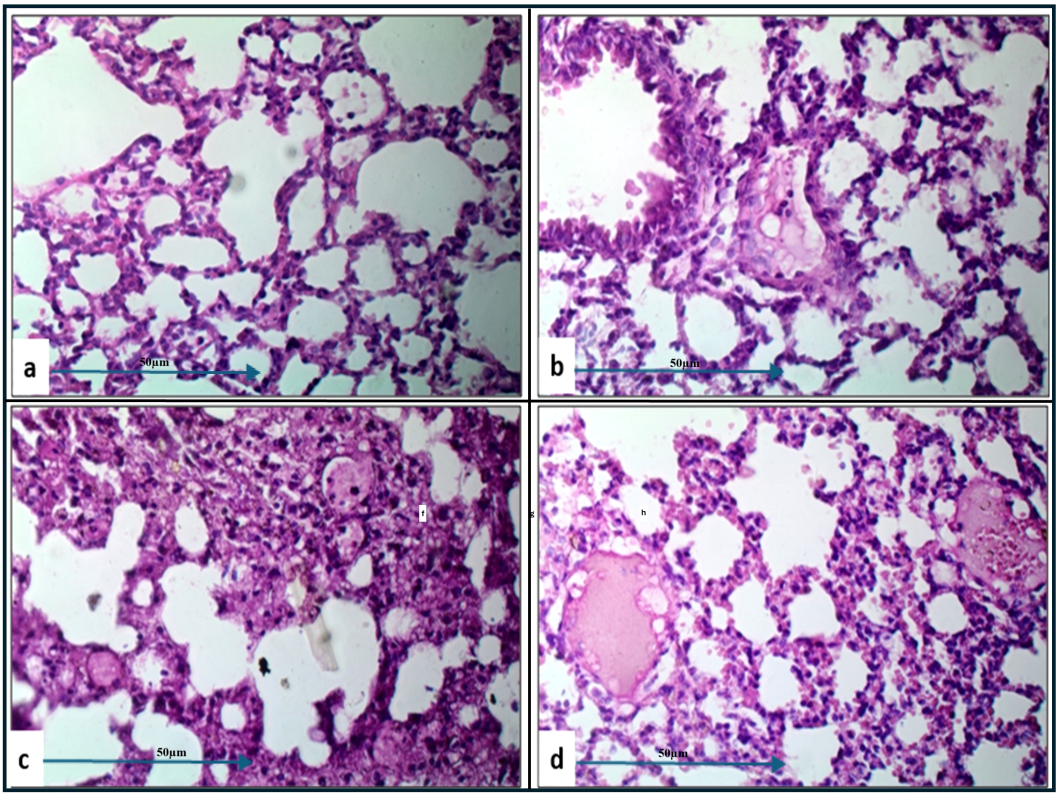

FIGURE 6
Histological examination of lung tissue from challenged groups treated with combination therapies (H&E, 400x magnification). Histopathological analysis of these groups, challenged with *A. baumannii* **(a)**, *E. coli* **(b)**, *K. pneumoniae* **(c)**, and *P. aeruginosa* **(d)**, showed significant improvement in alveolar wall collapse and congestion in **(a, b)**, with moderate improvement in **(d)**. Alveolar emphysema was pronounced in **(a, b, d)**, and moderate in **(c)**. Marked alveolar edema associated with hemorrhage was observed in **(c)**. Pulmonary vasculature changes, including thrombus formation and neutrophil infiltration, were detected in all groups.

TABLE 4 Severity levels of lung and spleen in challenged mice treated with amikacin alone or in combination with *J. candicans* extract.

	A. baumnii		*E. coli*		*K. pneumoniae*		*P. aeruginosa*	
	Amikacin	Plant/ Amikacin	Amikacin	Plant/ Amikacin	Amikacin	Plant/ Amikacin	Amikacin	Plant/ Amikacin
Pulmonary Sepsis Score Lesion Diffuse Alveolar Damage (DAD)								
Alveolar wall congestion	++	+	+++	+	++	++	++	++
interstitial neutrophil infiltration	++	+	+++	+	+++	+	++	++
Alveolar: Edema/hemorrhage	++	+	+++	+	+++	+++	++	+
Pneumocytes I& endothelial cells damage	++	-	+++	-	++	+	++	-
Alveolar vasculatures: - Thrombosis	+++	+	+++	+	++	++	+++	++
Alveoli filled with granular necrotic debris and minimal cellular reaction	++	+	+++	+	++	++	+	+
Alveolar collapse	++	+	+++	+	++	++	++	++
Splenic Score Lesion								
Apoptosis/necrosis of Lymphocytes	+	-	++	+	-	-	+++	+
Fibrosis and/or hyaline deposition	-	-	-	-	-	++	+	+

The symbols –, +, ++, and +++ represent the severity of histopathological lesions observed in lung and spleen tissues. A minus (–) indicates absence of the lesion, (+) denotes mild severity, (++) indicates moderate severity, and (+++) reflects severe or extensive tissue damage.

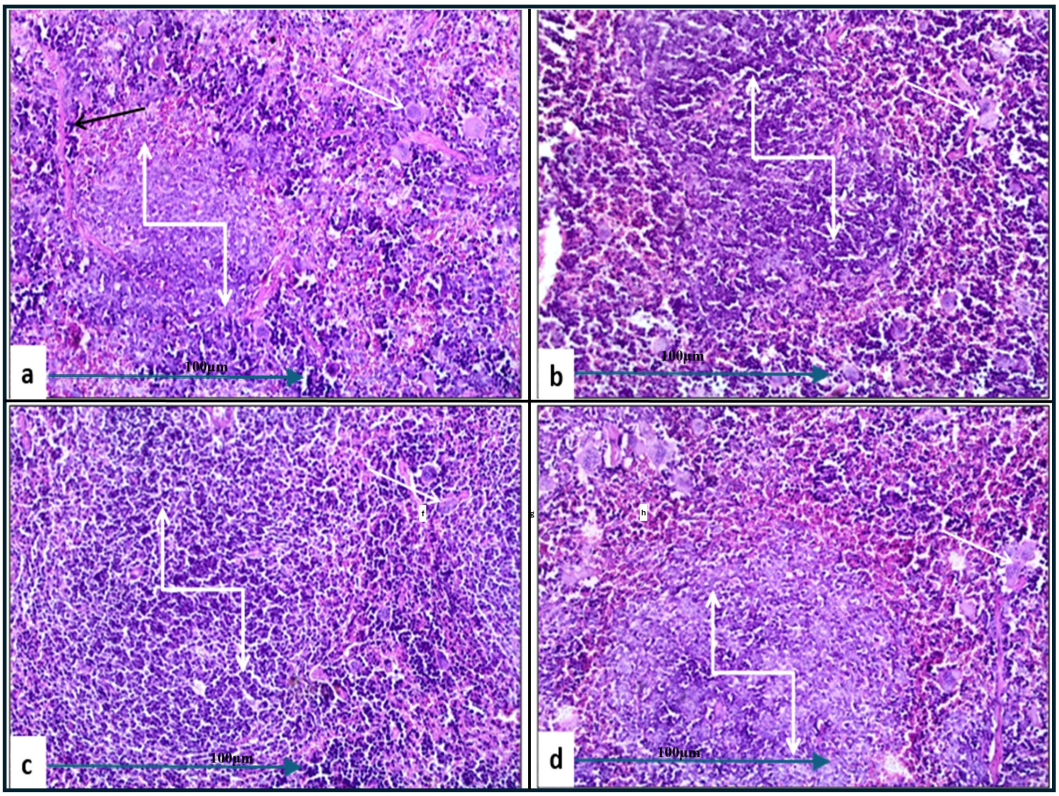

FIGURE 7
Histological examination of splenic tissue from the control positive (challenged and untreated) group (H&E, 200x magnification). Histopathological analysis of spleen samples from groups challenged with *A. baumannii* **(a)**, *E. coli* **(b)**, *K. pneumoniae* **(c)**, and *P. aeruginosa* **(d)** showed significant alterations in lymphoid follicles (truncated arrows), with lymphoid depletion observed in **(a, c, d)**. Additionally, a high incidence of multinucleated giant cells (white arrows) was noted across all groups. Prominent thick fibrous bands were observed in **(a)** (black arrow).

with *J. candicans* extract (Figure 9d) markedly reduced this severity to mild levels (+), demonstrating a substantial protective effect. For fibrosis and hyaline deposition, amikacin alone showed mild changes (+), whereas the combination treatment showed no signs of fibrosis or hyaline deposition (-), further indicating that the extract may help mitigate fibrotic processes in the spleen (Table 4).

Overall, the inclusion of *J. candicans* extract with amikacin demonstrated a general trend of reduced lesion severity across several parameters, particularly in cases involving *A. baumannii* and *E. coli*, where notable reductions were observed in alveolar congestion, neutrophil infiltration, and cellular damage. This combination therapy appeared to enhance the therapeutic effects of amikacin, reducing the severity of pulmonary sepsis. However, its efficacy varied depending on the specific pathogen, as seen with *K. pneumoniae* and *P. aeruginosa*, where the combination showed limited or no additional benefit in terms of reducing lesion severity. In the spleen, the combination therapy consistently led to reduced severity of lymphocyte apoptosis/necrosis and prevented fibrosis or hyaline deposition in most bacterial challenges, especially with *A. baumannii*, *E. coli*, and *P. aeruginosa*. These findings highlight the potential of *J. candicans* extract to enhance the protective effects of amikacin, offering additional support in treating bacterial infections associated with significant alveolar, vascular, and splenic damage, although its effectiveness may depend on the specific pathogen involved.

Discussion

Bloodstream infections (BSIs), specifically those caused by MDR Gram-negative bacterial pathogens, are associated with high morbidity and mortality rates due to the difficulty of treating with the available antimicrobial agents (Tawfik et al., 2023). In addition, it is considered as a major public health concern, particularly in Egypt. Sepsis-related septic shock may arise from a complex pathological reaction such as the hyperinflammatory host response to bacterial infection (Usmani et al., 2021). This study aimed to explore the prevalence and antimicrobial resistance patterns of Gram-negative bacteremia and to assess the potential of medicinal plant extracts as adjunctive treatments. In this study, the prevalence rate of 58.25% for Gram-negative pathogens in blood cultures among septic patients aligns with previous studies that report similar or higher rates of Gram-negative bacteremia in septic patients (Kumar et al., 2016; Tumbarello et al., 2019). *E. coli* and *K. pneumoniae* were the predominant pathogens, which is consistent with global trends where these organisms are frequently implicated in hospital-acquired infections (Bert et al., 2020). The high prevalence of MDR (79.4%) observed in this study, particularly among *P. aeruginosa* and *A. baumannii*, corroborates findings from other regions where these pathogens have shown alarming resistance patterns (Giske et al., 2018; Vardakas et al., 2019). The

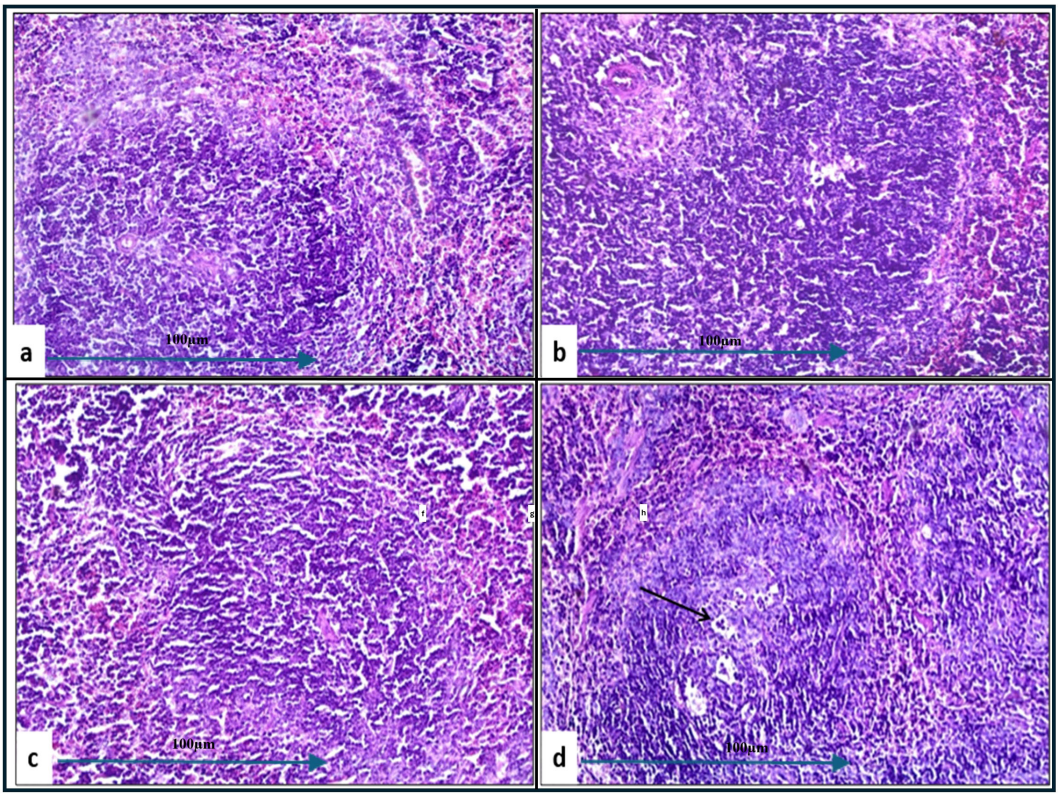

FIGURE 8
Histological examination of splenic tissue from challenged groups treated with amikacin (H&E, 200x magnification). Histopathological analysis of spleen samples from amikacin-treated groups challenged with *A. baumannii* **(a)**, *E. coli* **(b)**, *K. pneumoniae* **(c)**, and *P. aeruginosa* **(d)** revealed well-developed lymphoid follicles in **(a, b, d)**, while poorly developed follicles were observed in **(c)**. Additionally, lymphocyte degeneration was noted in group **(d)** (black arrow).

resistance of Gram-negative isolates to multiple antibiotics, including aztreonam, ampicillin-sulbactam, and various beta-lactams, reflects a broad decline in the efficacy of these agents. This observation is in line with recent reports of increasing resistance rates that complicate the management of Gram-negative infections (Nordmann et al., 2019). The consistent susceptibility of isolates to colistin, a last-resort antibiotic, is notable, though its use is often limited by toxicity and availability (Landman et al., 2008).

Medicinal plant extracts have been documented to possess a range of biological activities, including antimicrobial, anti-inflammatory, and antioxidant properties (Mehta et al., 2001; Vaou et al., 2021a). Our findings showed that the tested multidrug-resistant (MDR) bacterial strains exhibited varying degrees of sensitivity to all the desert-adapted plant extracts examined. The *J. candicans* was the most effective against MDR Gram-negative bacteria, with significant inhibition zones and low minimum inhibitory concentration (MIC) values. This supports previous research indicating that *J. candicans* possesses potent antimicrobial properties (Nogueira et al., 2013). These results may be attributed to the high content of quercetin and kaempferol related to flavonoids as was previously reported (Valero et al., 2013). In addition, the essential oils of *J. candicans* may be also responsible for antimicrobial activity against *B. subtilis* and *P. aeruginosa* (Hammerschmidt et al., 1993; El Yaagoubi et al., 2021). The antimicrobial efficacy of *J. candicans*, while promising, is limited by practical challenges such as achieving the necessary MIC levels due to issues with bioavailability and potential toxicity. To achieve the MIC values, it implies that substantial concentrations of the extract are required to effectively inhibit bacterial growth, which may not be feasible in clinical settings due to difficulties in maintaining these levels in the bloodstream and potential adverse effects (Nogueira et al., 2013). Therefore, *J. candicans* is more effectively used in combination with conventional antibiotics, where it can enhance the overall therapeutic efficacy and potentially reduce the dosage and side effects of both agents (Sawai et al., 2004; Ahmad and Mehmood, 2020). The synergistic effect of combining *J. candicans* with amikacin, resulting in reduced MIC values and conversion of resistant strains to sensitive phenotypes, highlights the potential of this combination therapy. This synergistic interaction is consistent with previous studies that have highlighted the potential of combining plant extracts with conventional antibiotics to enhance therapeutic efficacy and overcome resistance (Sawai et al., 2004; Ahmad and Mehmood, 2020). Such findings suggest that integrating *J. candicans* into treatment regimens could offer a viable strategy for managing infections that are otherwise challenging to treat with standard antibiotics alone.

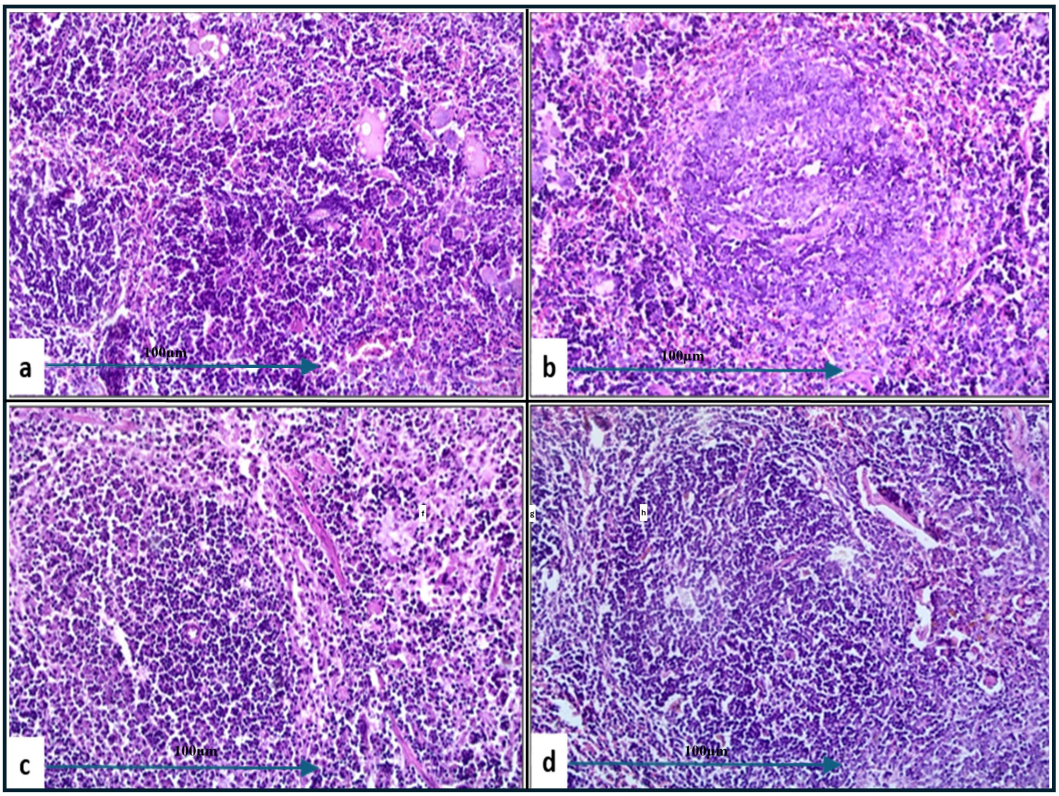

FIGURE 9
Histological examination of splenic tissue from challenged groups treated with combination therapies (H&E, 200x magnification). Histopathological analysis of spleen samples from these groups, challenged with *A. baumannii* **(a)**, *E. coli* **(b)**, *K. pneumoniae* **(c)**, and *P. aeruginosa* **(d)**, revealed well-developed lymphoid follicles in **(b–d)**, with notable lymphocyte depletion in **(b)**. Additionally, lymphocyte degeneration was observed in **(d)** and **(a)** (black arrow). Well-developed follicles were also seen in group **(a)**.

Despite the critical importance of eradicating Gram-negative bacteria in septicemia, the host's inflammatory response is recognized as a more significant cause of mortality in septic patients. Monitoring organ dysfunction related to the immune response and inflammatory reactions is crucial in managing sepsis (Nong et al., 2023). Consequently, the anti-inflammatory potential of the desert-adapted plant extracts in our study was evaluated as a key factor in sepsis treatment. Inhibiting COX-2 may facilitate the treatment of multidrug-resistant (MDR) infections through several interconnected mechanisms. COX-2 is an enzyme that plays a significant role in the inflammatory process by catalyzing the conversion of arachidonic acid to prostaglandins, which are key mediators of inflammation. During an infection, especially one caused by MDR pathogens, the inflammatory response can be exaggerated, leading to tissue damage and worsening clinical outcomes (Nathan, 2002). However, combining antibiotics with non-steroidal anti-inflammatory drugs (NSAIDs) can pose several potential disadvantages, including an increased risk of gastrointestinal irritation, bleeding, renal impairment, and liver toxicity due to the side effects of both drug classes. Drug interactions may occur, as some antibiotics can alter NSAID metabolism, leading to enhanced toxicity or reduced efficacy. Additionally, NSAIDs can suppress certain aspects of the immune response, hindering the body's ability to fight infections, and may complicate treatment regimen due to the need for careful monitoring. There is also a risk of masking important clinical symptoms, such as fever and pain, which could impede accurate diagnosis and treatment assessment. Therefore, healthcare providers must evaluate the necessity of this combination therapy on a case-by-case basis (Adams and Lichtenstein, 2017). Therefore, it is essential to explore alternative natural COX-2 inhibitors to mitigate or eliminate these concerns.

Our findings demonstrated that all four tested plant extracts achieved a COX-2 selective index comparable to celecoxib (ranging from 0.23 to 0.28), indicating preferential inhibition of COX-2 and highlighting their value as anti-inflammatory agents. Additionally, oxidative stress plays a pivotal role in the pathophysiology of septic shock, contributing to multiple organ failure, ischemia-reperfusion injury, and acute respiratory distress syndrome (Aisa-Alvarez et al., 2020). Antioxidants may modulate inflammation in septic shock patients and could be integrated into standard therapeutic protocols. To assess the antioxidant potential of the tested plant extracts, we utilized the DPPH scavenging assay, a reliable method for measuring the total antioxidant capacity of herbal extracts (Huang et al., 2005). Notably, our study revealed that *J. candicans* extract exhibited the highest DPPH free radical scavenging activity, with the lowest IC_{50} value. Such properties are vital for combating oxidative stress-related conditions and enhancing overall health

benefits (Miliauskas et al., 2004; Pires et al., 2015). Therefore, *J. candicans* plays a crucial role in therapeutic applications due to its combined antioxidant and anti-inflammatory properties, alongside its antimicrobial activity. Concurrently, its antimicrobial activity targets and inhibits pathogenic bacteria, when used in combination therapies, making it a valuable candidate for treating infections while managing inflammation and oxidative damage (Nogueira et al., 2013; Jang et al., 2020).

Histopathological analysis demonstrated that *J. candicans*, when used in conjunction with amikacin at a sub-inhibitory concentration (0.5 MIC), notably reduced the severity of pulmonary and splenic damage in mice models. This protective effect was evident in reduced alveolar congestion, decreased interstitial neutrophil infiltration, and less severe tissue damage compared to treatment with amikacin alone. Such findings underscore the potential of *J. candicans* to enhance the efficacy of conventional antibiotics and provide a protective effect against bacterial-induced tissue damage (Gupta et al., 2018; Kumari et al., 2020). Previous studies have supported the notion that plant extracts, including *J. candicans*, can mitigate the severity of inflammatory and infectious lesions. For instance, research has shown that various plant-derived compounds possess anti-inflammatory properties that reduce tissue damage and improve recovery outcomes in infectious models (Gupta et al., 2018). Additionally, another study highlighted the ability of plant extracts to alleviate inflammatory responses and oxidative stress, contributing to tissue protection during infections (Kumari et al., 2020). However, the limited efficacy observed with specific pathogens points to the need for continued investigation. The variability in response underscores the importance of tailoring treatment strategies to specific pathogens and optimizing the use of plant extracts in combination with antibiotics (Gupta et al., 2018; Kumari et al., 2020; Sharma et al., 2019).

Finally, we propose that the natural extracts investigated in our study may serve as potential adjunct therapies to enhance the effectiveness of standard antimicrobial treatments, particularly in cases where traditional antibiotics are ineffective due to the rise of MDR pathogens. The concept of adjunct therapy involves using these extracts in conjunction with conventional antibiotics to achieve a synergistic effect, thereby increasing the overall efficacy of treatment. For instance, certain extracts may possess properties that can disrupt biofilms formed by MDR bacteria, improve the host immune response, or possess inherent antimicrobial activity that complements the action of antibiotics. In clinical settings, where infections caused by MDR pathogens present significant treatment challenges, incorporating these natural extracts could potentially reduce the dosage and duration of antibiotic therapy required, thereby minimizing side effects and the risk of further resistance development. Additionally, using these extracts may help to mitigate the adverse effects commonly associated with antibiotics, such as disruption of the gut microbiota. To support the transition from laboratory research to practical clinical application, it is essential to conduct rigorous clinical trials that evaluate the safety, efficacy, and appropriate dosing of these extracts in human subjects. Such studies would help clarify the role of these natural alternatives as adjunct therapies, paving the way for their integration into clinical protocols aimed at combating MDR infections.

Conclusion

This study revealed a high prevalence of Gram-negative bacteremia with significant multidrug resistance, particularly among *E. coli* and *K. pneumoniae*, posing a major treatment challenge. Notably, *J. candicans* extract demonstrated strong antimicrobial, anti-inflammatory, and antioxidant properties, showing potential as an adjunct to conventional antibiotics like amikacin. The combination of *J. candicans* and amikacin displayed synergistic effects, significantly enhancing antimicrobial efficacy and reducing tissue damage in septic conditions, particularly for *A. baumannii* and *E. coli* infections. These findings underscore the potential of integrating desert-adapted plant extracts into treatment regimens for MDR Gram-negative infections, highlighting the need for alternative therapeutic strategies alongside robust antimicrobial stewardship.

Strengths of the study

This study presents a novel approach to tackling multidrug-resistant (MDR) bacterial infections by exploring the antimicrobial potential of desert-adapted medicinal plant extracts. The integration of microbiological, biochemical, and histopathological analyses provides a comprehensive evaluation of the therapeutic properties of these extracts. A key strength is the discovery that *J. candicans* extract enhances the efficacy of amikacin, converting resistant bacterial strains into sensitive ones, which holds significant clinical implications. Additionally, the extract exhibits anti-inflammatory (COX-1 and COX-2 inhibition) and antioxidant properties, making it a promising dual-action therapeutic agent. The study also directly addresses the growing crisis of antibiotic resistance in septic patients, an area of high clinical relevance, and demonstrates improved treatment outcomes in an *in vivo* model. The findings suggest that plant-based compounds could serve as adjunct therapies, supporting their potential in future drug development.

Limitations of the study

Despite its strengths, the study does not investigate the precise molecular mechanisms underlying the antimicrobial and anti-inflammatory effects of the extract, which could provide deeper insights into its mode of action. While the *in vivo* study in mice is a valuable step, larger preclinical and clinical trials are necessary to confirm safety and efficacy in humans. Another limitation is that the long-term impact on bacterial resistance evolution was not assessed, which is critical for determining the sustainability of plant-based adjunct therapies. Lastly, while histopathological analysis indicated

reduced tissue damage, detailed toxicity studies are required to ensure the extract's long-term safety for clinical applications.

Data availability statement

The original contributions presented in the study are included in the article/Supplementary Material. Further inquiries can be directed to the corresponding author/s.

Ethics statement

The studies involving humans were approved by Port-Said University Ethical Approval Committee, under approval number REC.PHARM.PSU/2023/21. The studies were conducted in accordance with the local legislation and institutional requirements. The human samples used in this study were acquired from These samples were not specifically obtained for the study. To maintain patient confidentiality, all clinical and laboratory data were anonymized. Informed consent was secured from all participants, and the study adhered to ethical standards approved by the Port-Said University Ethical Approval Committee, under approval number REC.PHARM.PSU/2023/21. Written informed consent for participation was not required from the participants or the participants' legal guardians/next of kin in accordance with the national legislation and institutional requirements. The animal study was approved by Port-Said University Ethical Approval Committee, under approval number REC.PHARM.PSU/2023/21. The study was conducted in accordance with the local legislation and institutional requirements.

Author contributions

NS: Methodology, Writing – original draft. RE: Methodology, Writing – original draft. SH: Formal analysis, Investigation, Writing – original draft. AE: Methodology, Writing – original draft. AN: Investigation, Validation, Writing – original draft. AM: Investigation, Visualization, Writing – original draft. FA: Investigation, Supervision, Writing – original draft. MA: Investigation, Validation, Writing – original draft. AA: Formal analysis, Supervision, Writing – original draft. MB: Methodology, Writing – original draft, Writing – review & editing.

Funding

The author(s) declare that financial support was received for the research and/or publication of this article. This research is funded through Princess Nourah bint Abdulrahman University Researchers Supporting Project number (PNURSP2025R228), Princess Nourah bint Abdulrahman University, Riyadh, Saudi Arabia. Extended thank for supporting by Deanship of Scientific Research, Vice Presidency for Graduate Studies and Scientific Research, King Faisal University, Saudi Arabia [KFU251222].

Acknowledgments

Princess Nourah bint Abdulrahman University Researchers Supporting Project number (PNURSP2025R228), Princess Nourah bint Abdulrahman University, Riyadh, Saudi Arabia. Extended thank for supporting by Deanship of Scientific Research, Vice Presidency for Graduate Studies and Scientific Research, King Faisal University, Saudi Arabia [KFU251222].

Conflict of interest

The authors declare that the research was conducted in the absence of any commercial or financial relationships that could be construed as a potential conflict of interest.

Publisher's note

Supplementary material

The Supplementary Material for this article can be found online at: https://www.frontiersin.org/articles/10.3389/fcimb.2025.1493769/full#supplementary-material

References

Abdel-Hak, E., El-Ahmady, S., and Mohamed, S. (2022). Evaluation of medicinal plant extracts for their antimicrobial properties and potential uses. *Antibiotics* 11, 75. doi: 10.3390/antibiotics11010075

Adams, S., and Lichtenstein, G. (2017). Impact of non-steroidal anti-inflammatory drugs on the efficacy of antibiotics: A literature review. *J. Infection Public Health* 10, 487–494. doi: 10.1016/j.jiph.2016.07.009

Ahmad, I., and Mehmood, Z. (2020). Synergistic effects of plant extracts combined with antibiotics in managing bacterial infections. *J. Antimicrobial Chemother.* 75, 939–949. doi: 10.1093/jac/dkz556

Aisa-Alvarez, A., Canadas, G., and Lopez-Hernandez, F. J. (2020). Oxidative stress and antioxidant strategies in sepsis. *Crit. Care* 24, 116. doi: 10.1186/s13613-020-06540-7

Alam, M. Z., Baig, M. M., and Khan, M. N. (2022). Antimicrobial activity of medicinal plants: A review. *J. Med. Plants Res.* 16, 102–115. doi: 10.5897/JMPR2021.0789

Al-Snafi, A. E. (2021). The medicinal importance of desert plants in the treatment of bacterial infections. *Asian J. Pharm. Clin. Res.* 14, 215–222. doi: 10.22159/ajpcr.2021.v14i2.40490

American Thoracic Society. (2018). Novel therapeutic strategies for sepsis and their impact on Gram-negative bacterial infections. *Am. J. Respir. Crit. Care Med.* 197 (4), 405–418. doi: 10.1164/rccm.201707-1460CI

Anwar, M. A., Ahsan, M., and Khan, R. (2023). Bioactive compounds from desert plants: A review of their antimicrobial properties. *Front. Pharmacol.* 14. doi: 10.3389/fphar.2023.763845

Baek, S. H., Ahn, S., and Kim, M. (2021). COX-2 selective inhibitors and their anti-inflammatory effects. *J. Pharm. Sci.* 110, 1608–1621. doi: 10.1016/j.xphs.2021.02.009

Bert, F., Golliot, F., and Pichon, S. (2020). Epidemiology of Gram-negative infections: A global overview. *J. Infection Public Health* 13, 737–748. doi: 10.1016/j.jiph.2019.05.002

BioMérieux (2021). *VITEK-2 automated identification system* (Marcy-l'Étoile, France: BioMérieux).

Boly, R., Akinmoladun, F., and Sani, T. (2016). Evaluation of antioxidant activity using DPPH assay in natural extracts. *Food Chem.* 192, 163–169. doi: 10.1016/j.foodchem.2015.07.094

Bretonnière, C., Dautel, M., and Tatu, M. (2010). Pharmacodynamic properties of amikacin in critically ill patients. *Int. J. Antimicrobial Agents* 36, 342–349. doi: 10.1016/j.ijantimicag.2010.04.010

Busani, L., De Angelis, G., and Tontodonati, M. (2019). Impact of broad-spectrum antibiotics on the gut microbiota in sepsis patients. *Crit. Care Med.* 47, 951–960. doi: 10.1097/CCM.0000000000003804

Chen, H., Zhang, Y., and Ma, Z. (2013). DPPH free radical scavenging activity assay for antioxidant evaluation. *J. Food Sci. Technol.* 50, 979–986. doi: 10.1007/s11483-012-0312-6

Cirioni, O., Ghiselli, R., and Giacometti, A. (2007). Effects of combination therapies in experimental models of sepsis. *Antimicrobial Agents Chemother.* 51, 2846–2853. doi: 10.1128/AAC.01076-

Clinical and Laboratory Standards Institute (CLSI) (2023). Performance Standards for Antimicrobial Susceptibility Testing. *33rd ed. CLSI supplement M100* (Wayne, PA: CLSI).

Datta, N., and Hughes, V. M. (1983). The genetics of bacterial β-lactamase. *Annu. Rev. Microbiol.* 37, 81–104. doi: 10.1146/annurev.mi.37.100183.000501

El-Hilaly, J., Israili, Z. H., and Lyoussi, B. (2020). Antimicrobial and antioxidant activities of desert plant extracts. *J. Ethnopharmacol.* 254, 112645. doi: 10.1016/j.jep.2020.112645

Eloff, J. N. (1998). A sensitive and quick microplate method to determine the minimal inhibitory concentration of plant extracts for bacteria. *Plant Med.* 64, 711–713. doi: 10.1055/s-2006-957913

El Yaagoubi, F., Zair, T., and Moutaouakkil, H. (2021). Antimicrobial activity of essential oils from medicinal plants against pathogenic bacteria. *Natural Prod. Res.* 35, 467–473. doi: 10.1080/14786419.2020.1740262

EUCAST (European Committee on Antimicrobial Susceptibility Testing) (2024). *EUCAST guidelines for antimicrobial susceptibility testing* (Växjö, Sweden: EUCAST).

Francisco Les, A., de Souza, A. C., Ribeiro, A. M., and Ferreira, J. C. (2021). Medicinal plants and their bioactive compounds for therapeutic applications. *J. Ethnopharmacol.* 274, 114091. doi: 10.1016/j.jep.2021.114091

Ghaly, M. F., Albalawi, M. A., Bendary, M. M., Shahin, A., Shaheen, M. A., Abu Eleneen, A. F., et al. (2023). Tamarindus indica extract as a promising antimicrobial and antivirulence therapy. *Antibiotics* 12, 464. doi: 10.3390/antibiotics12030464

Ghosh, A., Dey, R., and Gupta, S. (2012). Traditional PCR detection of specific Gram-negative bacteria using targeted primers. *BMC Microbiol.* 12, 135. doi: 10.1186/1471-2180-12-135

Giske, C. G., Monnet, D. L., and Cars, O. (2018). Antimicrobial resistance in Gram-negative bacteria: Epidemiology, mechanisms, and clinical impact. *Clin. Microbiol. Infection* 24, 745–758. doi: 10.1016/j.cmi.2018.01.020

Gupta, S., Kundu, S., and Pathak, S. (2018). Protective effects of plant extracts against bacterial-induced tissue damage. *J. Ethnopharmacol.* 224, 189–197. doi: 10.1016/j.jep.2018.05.048

Hammerschmidt, F., Lopes, M., and Martino, H. S. (1993). Antimicrobial properties of essential oils from medicinal plants. *Phytother. Res.* 7, 274–277. doi: 10.1002/ptr.2650070406

Harris, S. R., Cohen, C. R., and Willing, D. (2019a). Effective preservation techniques for bacterial strains. *J. Microbiol. Methods* 127, 58–63. doi: 10.1016/j.mimet.2016.04.009

Harris, S. R., McAdam, P. R., and McNeilly, T. (2019b). The role of glycerol stocks in bacterial strain preservation and genetic stability. *J. Clin. Microbiol.* 57, e00257–e00219. doi: 10.1128/JCM.00257-19

Huang, D., Ou, B., and Prior, R. L. (2005). The chemistry behind antioxidant capacity assays. *Food Chem.* 90, 511–522. doi: 10.1016/j.foodchem.2004.04.004

Jang, J. Y., Kim, Y. S., and Choi, Y. H. (2020). Antioxidant and anti-inflammatory properties of J. candicans extracts in bacterial infections. *J. Med. Plants Res.* 14, 129–137. doi: 10.5897/JMPR2020.6927

Joudeh, N., and Linke, D. (2018). Antimicrobial activity of desert plants: A comprehensive review. *Phytother. Res.* 32, 1469–1480. doi: 10.1002/ptr.6061

Khalid, H. S., Al-Shehri, M. M., and Al-Quraishy, S. (2020). Antimicrobial and phytochemical screening of desert plants in Saudi Arabia. *Saudi J. Biol. Sci.* 27, 1245–1254. doi: 10.1016/j.sjbs.2019.12.001

Kim, D., Lee, J. H., and Lee, J. W. (2015). Emergence of carbapenem-resistant acinetobacter baumannii in a korean hospital: A study on prevalence and resistance mechanisms. *J. Korean Med. Sci.* 30, 887–893. doi: 10.3346/jkms.2015.30.6.887

Kumar, A., Singh, R., and Shah, P. (2016). Effectiveness of glycerol stocks for bacterial strain preservation. *J. Microbiol. Methods* 127, 23–29. doi: 10.1016/j.mimet.2016.04.007

Kumari, A., Sharma, S., and Singh, A. (2020). Anti-inflammatory and antioxidant potential of plant extracts in infectious disease management. *J. Herbal Med.* 22, 201–209. doi: 10.1016/j.hermed.2020.100338

Landman, D., Bratu, S., and Quale, J. (2008). Colistin resistance in Gram-negative pathogens. *Clin. Infect. Dis.* 46, 1395–1403. doi: 10.1086/529068

Li, S., Li, D., and Zhang, W. (2016). Traditional medicinal plants and their potential in the management of cancer: A review. *J. Traditional Chin. Med.* 36, 488–496. doi: 10.1016/S0254-6272(16)30042-3

Liang, S., Lin, Y., and Zhang, C. (2015). The role of inflammation in sepsis and potential therapeutic targets. *Curr. Opin. Crit. Care* 21, 212–218. doi: 10.1097/MCC.0000000000000175

Liu, X., Zhang, X., and Wang, Y. (2022). Evaluating the effectiveness of combination therapies in sepsis treatment. *Front. Med.* 9. doi: 10.3389/fmed.2022.813267

Magiorakos, A. P., Srinivasan, A., and Carey, R. B. (2012). Multidrug-resistant, extensively drug-resistant and pandrug-resistant bacteria: An international expert proposal for interim standard definitions. *Clin. Microbiol. Infection* 18, 268–281. doi: 10.1111/j.1469-0691.2011.03570.x

Mahizan, N. A., and Ismail, M. (2019). Desert plants as sources of antimicrobial agents. *BMC Complementary Med. Therapies* 19, 155. doi: 10.1186/s12906-019-2630-5

Marmouzi, I., Rguibi, M., and Hafid, A. (2021). The role of medicinal plants in the treatment of chronic diseases: an overview. *J. Med. Plants Res.* 15, 388–400. doi: 10.5897/JMPR2020.0827

Medzhitov, R. (2008). Origin and physiological roles of inflammation. *Nature* 454, 428–435. doi: 10.1038/nature07201

Mehta, A., Bhandari, S., and Kaur, R. (2001). Biological activities of medicinal plant extracts. *J. Ethnopharmacol.* 77, 217–225. doi: 10.1016/S0378-8741(01)00206-4

Miliauskas, G., Venskutonis, P. R., and van Beek, T. A. (2004). Screening of antioxidant activity of some medicinal and aromatic plant extracts. *Food Chem.* 85, 231–237. doi: 10.1016/j.foodchem.2003.05.014

Miller, A. L., Li, X., and Yang, J. (2009). Evaluation of a PCR-based method for rapid detection of bacterial pathogens. *J. Appl. Microbiol.* 107, 413–419. doi: 10.1111/j.1365-2672.2009.04253.x

Murray, P. R., Rosenthal, K. S., and Pfaller, M. A. (2016). *Medical Microbiology. 9th* (Philadelphia, PA, USA: Elsevier).

Nathan, C. (2002). Points of control in inflammation. *Nature* 420, 846–852. doi: 10.1038/nature01320

Nikaido, H. (2020). Mechanisms of antimicrobial resistance in Gram-negative bacteria. *Front. Microbiol.* 11. doi: 10.3389/fmicb.2020.01483

Nogueira, G. D., Santos, M., and Sampaio, A. (2013). Antimicrobial and antioxidant activities of J. candicans extracts. *J. Appl. Microbiol.* 114, 726–734. doi: 10.1111/jam.12012

Nong, Y., Zhang, Y., Li, Y., and Li, X. (2023). Inflammatory mechanisms and intervention strategies for sepsis-induced myocardial dysfunction. *Immun. Inflamm. Dis.* 11 (2), 860–875. doi: 10.1002/iid3.860

Nordmann, P., Poirel, L., and Dortet, L. (2019). Carbapenem resistance in Gram-negative bacteria: Mechanisms and epidemiology. *Clin. Microbiol. Infection* 25, 653–662. doi: 10.1016/j.cmi.2019.01.016

Odds, F. C. (2003). Synergism, antagonism, and the FIC index. *J. Antimicrobial Chemother.* 51, 1551–1552. doi: 10.1093/jac/dkg254

Patel, J. B. (2015). Antimicrobial susceptibility testing. *Clin. Microbiol. Rev.* 28, 631–662. doi: 10.1128/CMR.00073-14

Paterson, D. L., and Bonomo, R. A. (2005). Extended-spectrum β-lactamases: A clinical update. *Clin. Microbiol. Rev.* 18, 657–686. doi: 10.1128/CMR.18.4.657-686.2005

Perez, F., Endimiani, A., and Hujer, K. M. (2007). Carbapenem-resistant Acinetobacter baumannii: Clinical challenges and diagnostic strategies. *Expert Rev. Anti-infective Ther.* 5, 537–551. doi: 10.1586/14787210.5.4.537

Pires, A., Santos, S., and Rodrigues, M. (2015). Evaluation of antioxidant potential using DPPH and FRAP assays. *J. Pharm. Sci.* 104, 3060–3068. doi: 10.1002/jps.24462

Pitout, J. D. D., and Laupland, K. B. (2008). Extended-spectrum β-lactamase-producing Enterobacteriaceae: An emerging public-health concern. *Lancet Infect. Dis.* 8, 159–166. doi: 10.1016/S1473-3099(08)70041-7

Poirel, L., and Nordmann, P. (2006). Emergence of metallo-β-lactamase-producing gram-negative bacteria. *Clin. Microbiol. Infection* 12, 195–204. doi: 10.1111/j.1469-0691.2006.01322.x

Poirel, L., Nordmann, P., and Legendre, L. (2012). Characterization of the OXA-48-like carbapenemase in enterobacteriaceae. *J. Antimicrobial Chemother.* 67, 338–342. doi: 10.1093/jac/dkr478

Pop-Vicas, A., and Opal, S. M. (2013). Carbapenem-resistant Gram-negative bacteria in sepsis. *Curr. Opin. Infect. Dis.* 26, 260–266. doi: 10.1097/QCO.0b013e32835bdb67

Prescott, H. C., and Angus, D. C. (2018). Sepsis management: Current approaches and future perspectives. *Lancet* 392, 1225–1235. doi: 10.1016/S0140-6736(18)31780-1

Rosato, A., Fiume, G., and De Lucca, C. (2020). Synergistic effects of plant extracts and antibiotics on multidrug-resistant bacteria. *J. Appl. Microbiol.* 129, 1617–1628. doi: 10.1111/jam.14897

Sawai, T., Kakuta, H., and Kakehi, K. (2004). Combining plant extracts with antibiotics to enhance efficacy. *Phytother. Res.* 18, 396–400. doi: 10.1002/ptr.1464

Schweizer, H. P. (2003). Pseudomonas aeruginosa genes involved in pyoverdine biosynthesis: Identification and characterization. *FEMS Microbiol. Rev.* 27, 487–500. doi: 10.1016/S0168-6445(03)00078-6

Shaikh, S., and Fatima, S. (2015). Antimicrobial resistance in bacteria and its management. *Int. J. Infect. Dis.* 33, 89–97. doi: 10.1016/j.ijid.2015.02.018

Shao, Y., Xu, Y., and Wang, L. (2019). Antimicrobial activity of desert plant extracts: Mechanisms and potential applications. *J. Natural Prod.* 82, 1667–1682. doi: 10.1021/acs.jnatprod.8b00924

Sharma, A., Chawla, S., and Singh, A. (2019). Effectiveness of plant extracts combined with antibiotics in treating resistant bacterial infections. *J. Clin. Diagn. Res.* 13, DC01–DC05. doi: 10.7860/JCDR/2019/38461.12685

Singer, M., Deutschman, C. S., and Seymour, C. W. (2016). The third international consensus definitions for sepsis and septic shock (Sepsis-3). *JAMA* 315, 801–810. doi: 10.1001/jama.2016.0287

Singh, R., Iqbal, M., and Khan, M. (2022). Antibiotic efficacy in combination therapies for multidrug-resistant infections. *Clin. Infect. Dis.* 74, 947–953. doi: 10.1093/cid/ciab908

Sokurenko, E. V., Chesnokova, V., and Hasty, D. L. (1998). Detection of Escherichia coli using the uidA gene as a marker. *J. Clin. Microbiol.* 36, 335–338. doi: 10.1128/JCM.36.2.335-338.1998

Song, J., Zhao, H., and Wang, L. (2009). Pharmacokinetics of amikacin in sepsis treatment: A review. *J. Antimicrobial Chemother.* 63, 658–665. doi: 10.1093/jac/dkn488

Srinivasan, K., and Jayaprakasha, G. K. (2001). Medicinal plants: A potential source of novel antimicrobial agents. *J. Ethnopharmacol.* 75, 171–184. doi: 10.1016/S0378-8741(00)00352-2

Tajkarimi, M. M., and Ibrahim, M. Y. (2010). Antimicrobial activity of desert plants and their phytochemical profiles. *Food Chem.* 120, 105–113. doi: 10.1016/j.foodchem.2009.09.065

Tamma, P. D., Han, J. H., and Rock, C. (2012). Combination therapy for multidrug-resistant Gram-negative bacteria: Review of current evidence. *Infect. Dis. Soc. America Annu. Meeting* 24, 127–134. doi: 10.1093/infdis/jis117

Tang, F., Yuan, H., Li, X., and Qiao, L. (2024). Effect of delayed antibiotic use on mortality outcomes in patients with sepsis or septic shock: A systematic review and meta-analysis. *Int. Immunopharmacol.* 129, 111616. doi: 10.1016/j.intimp.2024.111616

Tawfik, A., Eldin, S., and Ibrahim, M. (2023). Prevalence and outcomes of bloodstream infections caused by multidrug-resistant bacteria in Egypt. *Infect. Dis. Ther.* 12, 45–58. doi: 10.1007/s40121-023-00631-7

Tumbarello, M., Viale, P., and Viscoli, C. (2019). Gram-negative bloodstream infections: Risk factors and outcome. *Clin. Infect. Dis.* 68, 817–823. doi: 10.1093/cid/ciy642

Usmani, A., Kumar, R., and Singh, P. (2021). Pathogenesis and management of sepsis-related shock. *Int. J. Crit. Illness Injury Sci.* 11, 29–35. doi: 10.4103/IJCIIS.IJCIIS_58_20

Valero, M., Ochoa, J., and Sancho, M. (2013). Flavonoids in medicinal plants: Antioxidant and antimicrobial properties. *Phytother. Res.* 27, 470–476. doi: 10.1002/ptr.4687

Valgas, C., Souza, S. M., and Smânia, E. F. (2007). Screening methods to determine antibacterial activity of natural products. *Braz. J. Microbiol.* 38, 369–380. doi: 10.1590/S1517-83822007000200002

Vaou, N., Calomfirescu, A., and Ivanov, R. (2021a). Antimicrobial and anti-inflammatory properties of medicinal plants. *J. Herbal Med.* 27, 100438. doi: 10.1016/j.hermed.2021.100438

Vaou, M., Papaioannou, M., and Skalkos, D. (2021b). Plant-derived compounds as resistance-modifying agents: An overview. *Antimicrobial Agents Chemother.* 65, e01000–e01021. doi: 10.1128/AAC.01000-21

Vardakas, K. Z., Polyzos, K. A., and Rafailidis, P. I. (2019). Antimicrobial resistance trends in Gram-negative bacteria: A systematic review. *J. Antimicrobial Chemother.* 74, 944–954. doi: 10.1093/jac/dky556

Verweij, P. E., Mouton, J. W., and Brown, J. (2004). Antimicrobial susceptibility testing: Methodology and interpretation. *J. Antimicrobial Chemother.* 53, 264–270. doi: 10.1093/jac/dkh048

Wink, M. (2022). Plant secondary metabolites and their role in antimicrobial resistance. *Natural Prod. Commun.* 17, 345–356. doi: 10.1177/1934578X221080567

Yong, D., Lee, K., Yum, J. H., Kim, H. S., and Chong, Y. (2009a). Imipenem-EDTA Disk Method for Detecting Metallo-β-Lactamase-Producing Clinical Isolates of Pseudomonas spp. and Acinetobacter spp. *Clin. Microbiol. Infection* 15, 1090–1096. doi: 10.1111/j.1469-0691.2009.02947.x

Yong, D., Toleman, M. A., and Giske, C. G. (2009b). Characterization of a new metallo-β-lactamase gene, blaNDM-1, in Enterobacteriaceae. *J. Antimicrobial Chemother.* 62, 11–19. doi: 10.1093/jac/dkp154

Yuan, Y., Wang, M., and Zhang, Y. (2018). Bioactive compounds from medicinal plants and their applications. *J. Herbal Med.* 14, 37–45. doi: 10.1016/j.hermed.2018.01.001

Zilberman-Itskovich, S., and Goldberg, E. (2022). Current challenges in treating sepsis caused by multidrug-resistant bacteria. *J. Clin. Med.* 11, 4485. doi: 10.3390/jcm11154485

frontiers | Frontiers in Cellular and Infection Microbiology

TYPE Original Research
PUBLISHED 30 June 2025
DOI 10.3389/fcimb.2025.1604507

OPEN ACCESS

EDITED BY
Sanjit Kumar,
Guru Ghasidas Vishwavidyalaya, India

REVIEWED BY
Sandip Patil,
Shenzhen Children's Hospital, China
Priyankar Sen,
VIT University, India

*CORRESPONDENCE
Nada K. Alharbi
Nkalharbi@pnu.edu.sa

RECEIVED 02 April 2025
ACCEPTED 02 June 2025
PUBLISHED 30 June 2025

CITATION
Abdelkhalig SM, Ali AG, Ghaly MF, Alharbi NK, Alharbi M, Bendary MM and Abousaty AI (2025) Eco-friendly silver nanoparticles from garlic: a novel therapeutic approach for treating *Escherichia fergusonii* wound infections. *Front. Cell. Infect. Microbiol.* 15:1604507. doi: 10.3389/fcimb.2025.1604507

Eco-friendly silver nanoparticles from garlic: a novel therapeutic approach for treating *Escherichia fergusonii* wound infections

Sozan M. Abdelkhalig [1], Arwa Gamal Ali [2], Mohamed Farouk Ghaly [2], Nada K. Alharbi [3]*, Maha Alharbi [3], Mahmoud M. Bendary [4] and Amira I. Abousaty [2]

[1]Department of Basic Medical Sciences, College of Medicine, AlMaarefa University, Riyadh, Saudi Arabia, [2]Botany and Microbiology Department, Faculty of Science, Zagazig University, Zagazig, Egypt, [3]Department of Biology, College of Science, Princess Nourah bint Abdulrahman University, Riyadh, Saudi Arabia, [4]Department of Microbiology and Immunology, Faculty of Pharmacy, Port Said University, Port Said, Egypt

Introduction: Complicated wound infections pose a significant challenge to patient recovery and healthcare systems, particularly due to the emergence of less common but highly resistant multidrug-resistant (MDR) pathogens that undermine the efficacy of conventional antibiotic therapies. This growing threat highlights the urgent need for innovative antimicrobial approaches.

Methodology: In this study, we synthesized eco-friendly silver nanoparticles (AgNPs) using garlic extract to combat complicated wound infections caused by atypical MDR pathogens.

Results: Genetic sequencing of 16S rRNA gene, aligned with phenotypic identification methods, confirmed that *Escherichia fergusonii* (*E. fergusonii*) as a significant atypical pathogen responsible for complicated wound infections, with a prevalence rate of 24% (12 out of 50 cases). Antimicrobial susceptibility testing revealed that all identified *E. fergusonii* strains exhibited MDR patterns. Garlic extract, analyzed using GC-MS and UPLC-ESI-MS/MS, identified sulfur-containing bioactive compounds such as allyl methyl trisulfide, dimethyl trisulfide, and allicin, which facilitated the biosynthesis of AgNPs. Stable, spherical AgNPs (15–20 nm) with strong antimicrobial properties were confirmed under optimal conditions (10 mL garlic extract, 40°C, pH 8.0). Their properties were validated using UV-Vis spectroscopy, XRD, and TEM. Antibacterial assays of AgNPs showed mean inhibition zones of 28±0.5 mm and MIC values of 100 µg/mL. TEM analysis revealed that AgNPs compromised bacterial membrane integrity, leading to structural damage, increased permeability, and leakage of intracellular contents. Simultaneously, they induced a concentration-dependent depletion of intracellular glutathione (GSH) in *E. fergusonii*, suggesting that both membrane disruption and oxidative stress synergistically contribute to bacterial cell lysis and death. A strong synergistic interaction was observed between AgNPs, used at a safe concentration below 50 µM as confirmed by cytotoxicity assays, and antibiotics such as ciprofloxacin, as evidenced by a fractional inhibitory concentration (FIC) index of 0.37. Time-kill assays demonstrated rapid bacterial eradication when AgNPs were combined with antibiotics such as ciprofloxacin.

Conclusion: These findings underscore the promise of garlic-derived silver nanoparticles (AgNPs) as a fast-acting, eco-friendly option for treating complex wound infections caused by atypical multidrug-resistant (MDR) pathogens.

KEYWORDS

wound infections, MDR, AgNPs, garlic extract, *E. fergusonii*, TEM

Introduction

Complicated wound infections are a significant concern, particularly due to the presence of multidrug-resistant organisms. *Staphylococcus aureus*, including methicillin-resistant strains (MRSA), remains one of the most prevalent bacteria responsible for wound infections, often causing severe and persistent cases. *Pseudomonas aeruginosa*, known for its resistance to multiple antibiotics, is frequently isolated in more complicated or nosocomial infections, particularly in immunocompromised patients. *Klebsiella* spp., especially *Klebsiella pneumoniae*, is another common pathogen, notably in contaminated or dirty surgical wounds, contributing to both local and systemic infections. Additionally, *Acinetobacter* spp., notorious for surviving in hospital environments, has become a growing concern in abdominal surgeries, often complicating recovery and requiring targeted antimicrobial therapy. Among these pathogens, *Escherichia fergusonii* (*E. fergusonii*), a less well-known but emerging organism, has been increasingly identified as a cause of infection in abdominal wounds (Mahapatra et al., 2005; Adesina et al., 2019). These pathogens not only delay wound healing but also increase the risk of sepsis, leading to prolonged hospital stays and higher mortality rates. Effective management requires timely identification and appropriate antimicrobial therapy, with close monitoring of antibiotic resistance patterns, which vary across geographic regions and healthcare settings. Studies from various locations have confirmed the dominance of these organisms in abdominal wounds, as well as in urinary tract infections, bacteremia, diarrhea, and pleural infections, underlining the importance of infection control measures, including the careful administration of prophylactic antibiotics and enhanced surgical hygiene practices (Savini et al., 2008; Funke et al., 1993).

Silver nanoparticles (AgNPs) serve as effective antimicrobial agents, being incorporated into wound dressings and medical device coatings to prevent infections. AgNPs offer significant advantages over traditional antibiotics, especially in the fight against multidrug-resistant (MDR) infections. Unlike conventional antibiotics, which typically target specific bacterial functions, AgNPs exhibit broad-spectrum antimicrobial activity by disrupting bacterial cell walls, generating reactive oxygen species (ROS), and interfering with DNA replication, making them effective against a wide range of pathogens (Rai et al., 2009). Their unique ability to target multiple bacterial processes simultaneously reduces the likelihood of resistance development, a major issue with traditional antibiotics (Sondi and Salopek-Sondi, 2004). Furthermore, AgNPs' small size and large surface area enhance their ability to penetrate bacterial cells more effectively, improving their antimicrobial efficacy (Rai et al., 2009). When combined with conventional antibiotics, AgNPs can also create a synergistic effect that overcomes resistance, making them a powerful tool for treating infections that have become resistant to standard treatments (Bahar and Ren, 2013).

Despite their widespread use, AgNPs have notable limitations that constrain their applications, particularly in medicine. One major concern is their potential cytotoxicity, as studies have shown that AgNPs can release silver ions, which may damage healthy cells and tissues, leading to oxidative stress and inflammatory responses in the body (Chen and Schluesener, 2008). Additionally, AgNPs may accumulate in organs such as the liver, lungs, and kidneys, raising concerns about long-term exposure and potential toxicity to human health (Marambio-Jones and Hoek, 2010). Environmental toxicity is also a concern, as the disposal of AgNPs can negatively impact aquatic and soil ecosystems (Fabrega et al., 2011). Due to these risks, AgNPs are generally preferred in applications where their powerful antimicrobial properties are crucial yet contained—such as in wound infections, where localized use minimizes systemic exposure. Their efficacy in preventing bacterial colonization and biofilm formation makes commercial silver-containing wound gels particularly valuable in wound care (Francolini et al., 2017), while reducing the need for broader exposure that might increase toxic risks. Alternatively, they can be used at low concentrations below cytotoxic levels in combination with commonly used antibiotics to enhance therapeutic outcomes.

AgNPs can be synthesized through various methods, primarily chemical, physical, and biological. The chemical reduction method is the most common, where silver ions (typically from silver nitrate) are

Abbreviations: MDR, multidrug-resistant; AgNPs, silver nanoparticles; *E. fergusonii*, *Escherichia fergusonii*; GC-MS, Gas Chromatography–Mass Spectrometry; UPLC-ESI-MS/MS, Ultra-Performance Liquid Chromatography–Electrospray Ionization–Tandem Mass Spectrometry; UV-Vis, Ultraviolet–Visible Spectroscopy; XRD, X-ray Diffraction; TEM, Transmission Electron Microscopy; MIC, Minimum Inhibitory Concentration; GSH, Glutathione; FIC, Fractional Inhibitory Concentration.

reduced using agents like sodium borohydride or ascorbic acid, forming nanoparticles in solution. This method is widely favored for its simplicity, cost-effectiveness, and the ability to control particle size by adjusting factors such as pH, temperature, and stabilizers. Physical methods—such as evaporation-condensation and laser ablation—require specialized equipment and high energy inputs but yield high-purity AgNPs. Alternatively, biological synthesis (green synthesis) employs plant extracts or microorganisms as eco-friendly reducing agents, offering a sustainable and environmentally friendly option. Each method offers unique benefits depending on the intended application, from medical to industrial uses (Iravani, 2014; Mosallam et al., 2021).

However, green synthesis of AgNPs presents several advantages over chemical and physical methods. It relies on natural reducing agents such as plant extracts, bacteria, or fungi, eliminating the need for toxic chemicals and the high energy consumption associated with traditional techniques. This makes green synthesis a safer and more sustainable approach, with minimal environmental impact and reduced health hazards during production. Additionally, biological molecules in these natural sources often serve as stabilizers, enhancing nanoparticle stability and biocompatibility —key factors for medical and pharmaceutical applications. Green synthesis typically operates under mild conditions (room temperature and neutral pH), making it both simpler and more cost-effective (Mittal et al., 2013; Rai et al., 2009).

This study addresses the escalating issue of antimicrobial resistance in wound infections, with a particular focus on *E. fergusonii*, an emerging opportunistic pathogen. While *Staphylococcus aureus* and *Pseudomonas aeruginosa* are well-known wound pathogens, *E. fergusonii* has been increasingly implicated in various infections, including wounds, urinary tract infections, and bacteremia. Notably, it is frequently associated with multidrug resistance, including extended-spectrum β-lactamases and carbapenemases, posing significant treatment challenges. Despite its rising clinical relevance, *E. fergusonii* remains underexplored in the context of novel antimicrobial treatments. To address this gap, we propose a novel approach utilizing AgNPs synthesized via a green route using garlic (*Allium sativum*) extract. This method offers dual advantages: garlic acts as both a natural reducing and stabilizing agent in the synthesis of AgNPs and provides intrinsic antimicrobial properties. By using garlic's dual functionality, our approach increases the antimicrobial potency of AgNPs while reducing the toxic effects and environmental concerns associated with chemical or radiation-based synthesis methods. (Prabhu and Poulose, 2012; Rai et al., 2009).

The synergistic action of garlic-based AgNPs is particularly promising against multidrug-resistant bacteria, as it targets multiple microbial pathways, thereby reducing the likelihood of resistance development and enhancing overall efficacy. Furthermore, combining these garlic-derived AgNPs with conventional antibiotics may restore the effectiveness of existing drugs against resistant strains, offering a sustainable and potent strategy for managing multidrug-resistant wound infections. While numerous studies have investigated AgNPs against common wound pathogens, few have applied green-synthesized nanoparticles to *E. fergusonii*, especially in the context of wound infections. To the best of our knowledge, this is the first study to explore the use of garlic-mediated AgNPs specifically against *E. fergusonii* isolated from complicated wound infections. This positions our research as a significant and novel contribution to both antimicrobial research and clinical practice, offering a targeted, eco-friendly approach to combat an emerging, multidrug-resistant pathogen.

Materials and methods

Identification of pathogenic bacteria in complicated wound Infections after abdominal surgery

Collection of clinical samples

One hundred and fifty wound swab samples were collected from wounds that exhibited clear signs of complication, such as persistent inflammation, delayed healing, or the presence of purulent discharge, at Zagazig University Hospitals, Egypt. After cleaning the infected sites, sterile cotton swabs were used to obtain specimens, which were then inoculated into brain heart infusion broth for enrichment and incubated for 24 hours at 37°C to promote pathogen growth. Subsequently, a loopful of the enriched culture was spread onto nutrient agar plates. The recovered colonies were identified using standard microbiological methods, including cultural characteristics, Gram staining, and biochemical tests (Madigan et al., 2018; Garcia, 2010).

During pathogen identification, when mixed isolates were encountered, laboratory protocols typically prioritized the isolates with larger colony counts, as these were more likely to represent the primary pathogen responsible for infection. Studies have indicated that isolates with colony counts exceeding 10^6 CFU/mL are generally considered clinically significant and more likely to be associated with infection. This threshold is commonly used to differentiate between contamination and true infection, with lower counts often disregarded unless they exhibit distinct virulence factors or clear clinical relevance. Selecting the dominant pathogens is crucial in clinical settings to avoid unnecessary over-treatment and to focus on the most probable cause of infection (Bendy et al., 1964).

Molecular identification

For further identification of the most prevalent isolate, which exhibited the highest MAR (Multiple Antibiotic Resistance) index, molecular techniques were employed—specifically 16S rRNA gene sequencing. This method provided a precise and reliable means of identifying the isolates at the species level, offering a more accurate understanding of their genetic composition and resistance profiles. DNA was extracted from the selected bacterial colonies. A fresh colony was mixed with 1 mL of sterile distilled water, vortexed, boiled for 10 minutes, incubated on ice for 5 minutes, and then

centrifuged. The supernatant was transferred to an Eppendorf tube and stored at -20°C.

PCR amplification of the 16S rRNA gene was carried out using the forward primer [F27] (5'-AGAGTTTGATCCTGGCTCAG-3') and reverse primer [R1492] (5'-GGTTACCTTGTTACGACTT-3') (Weisburg et al., 1991). The amplification conditions were as follows: initial denaturation at 94°C for 10 minutes; 35 cycles of denaturation at 94°C for 30 seconds, annealing at 56°C for 1 minute, and extension at 72°C for 1 minute; followed by a final extension at 72°C for 10 minutes. PCR products were analyzed using 1% agarose gel electrophoresis, visualized under UV light after ethidium bromide staining (Sambrook and Russell, 2001), and purified using the GeneJET PCR Purification Kit. The purified PCR product was sequenced at GATC Biotech AG using an ABI 3730xl DNA sequencer, and the sequence was uploaded to NCBI (www.ncbi.nlm.nih.gov).

Identification of multidrug-resistant isolates with the highest MAR index

The disk diffusion method was employed in triplicate to determine antimicrobial resistance patterns. The selected Bacterial cultures were grown on Mueller-Hinton agar plates (Lewis et al., 2025), and antimicrobial discs were carefully placed on the inoculated plates. nine different antimicrobial discs, representing various classes and concentrations, were used: Ampicillin (AMP, 10 µg), Amoxicillin/clavulanic acid (AMC, 10 µg), Tetracycline (TE, 30 µg), Vancomycin (VA, 30 µg), Ciprofloxacin (CIP, 5 µg), Ceftriaxone (CRO, 30 µg), Imipenem (IPM, 10 µg), Gentamicin (CN, 10 µg), and Amikacin (AK, 30 µg). The plates were kept at 4°C for 1 hour before incubation at 37°C for 24 hours. After incubation, the diameters of the inhibition zones were measured to assess bacterial susceptibility according to CLSI guidelines (Lewis et al., 2025).

Bacterial isolates showing resistance to at least one antimicrobial agent in three or more classes were classified as Multi-Drug Resistant (MDR) (Magiorakos et al., 2012). To evaluate the extent of resistance, the Multiple Antibiotic Resistance (MAR) index was calculated for the selected isolate by dividing the number of antibiotics to which the isolate was resistant by the total number tested. A higher MAR index indicates substantial antimicrobial exposure, often associated with high-risk environments, and provides important insights for infection control and antimicrobial stewardship (Mir et al., 2022).

Green synthesis of silver nanoparticles

Preparation of the alcoholic garlic extract

A total of 30 grams of fresh garlic bulbs were used to prepare two separate extracts: one for the green synthesis of AgNPs, and the other for chemical analysis of bioactive compounds. The fresh garlic was powdered and subjected to extraction with 7 mL of 70% ethanol using a maceration technique. The ethanol was subsequently removed by concentrating the extract under reduced pressure at 40°C using a rotary evaporator. This process eliminated the ethanol, leaving behind a concentrated plant extract, which was stored at 4°C for future use (Sakkas and Papadopoulou, 2017).

The concentrated extract was dissolved in DMSO to achieve a final concentration of 50 µg/mL, transferred to a sterile flask, and stored at 4°C until use (Ghaly et al., 2023). To preserve the stability of sulfur-containing compounds, such as allicin, all extraction steps were conducted under cold conditions (4–8°C), protected from light, and processed immediately after preparation. The extract designated for LC–MS analysis was filtered, briefly stored at –20°C, and analyzed within 24 hours to minimize degradation; however, the other sample was used directly in the synthesis of AgNPs.

Isolation, purification, and identification of active components in garlic extract using gas chromatography–mass spectrometry analysis

To identify volatile bioactive compounds in the partially purified garlic extract, gas chromatography–mass spectrometry (GC-MS) analysis was performed following established protocols (Sparkman, 2005). The extract, previously shown to exhibit antibacterial activity at an Rf value of 9 via thin-layer chromatography (TLC), was subjected to chromatographic profiling (Shang et al., 2024). Samples were analyzed using a GC-MS system equipped with a capillary column (e.g., HP-5MS, 30 m × 0.25 mm × 0.25 µm film thickness). The injector was maintained at 250°C, with helium as the carrier gas at a constant flow rate of 1.0 mL/min. The oven temperature was initially set at 50°C for 2 minutes, ramped at 10°C/min to 280°C, and held for 5 minutes. The sample (1 µL) was injected in splitless mode. The mass spectrometer operated in electron ionization (EI) mode at 70 eV with a scan range of m/z 50–500 (Lanzotti, 2006). Chromatograms were analyzed using integrated spectral libraries (e.g., NIST, Wiley) to identify compounds based on retention time and mass fragmentation patterns. (Ankri and Mirelman, 1999). Identification of sulfur-containing compounds, such as allicin, was confirmed by comparison with a commercially available synthetic standard, matching both the retention factor and the mass-to-charge ratio (m/z), thereby validating the presence of allicin in the sample.

Ultra-performance liquid chromatography-electrospray ionization-mass spectrometry

The bioactive compounds identified on the TLC plate (at an Rf value of 0.9) were further analyzed using liquid chromatography–mass spectrometry (LC–MS). The analysis was conducted with a Thermo Scientific LCQ Deca mass spectrometer equipped with a Hypersil Gold aQ C18 column and an electrospray ionization (ESI) source operating in positive ion mode (Oyaluna et al., 2024). The mobile phases consisted of 0.1% formic acid in water (A) and acetonitrile with 0.1% formic acid (B). Gradient elution was performed, beginning with 2% mobile phase B and increasing to 98% over 30 minutes, at a flow rate of 0.2 mL/min, for a total run time of 40 minutes. The chemical

identities of the resolved compounds were determined by comparing their mass spectral patterns and retention times with entries in the NIST mass spectral library.

Synthesis of silver nanoparticles from garlic extract

An aqueous solution of silver nitrate (200 µg/mL) was prepared for the green synthesis of AgNPs. To initiate the reduction of silver ions (Ag^+), 10 mL of garlic extract was mixed with 10 mL of the silver nitrate solution. The reaction mixture was then exposed to sunlight for 24 hours, during which a gradual color change from colorless to dark brown was observed, indicating the formation of AgNPs. This green synthesis approach is both environmentally friendly and effective, employing natural reducing agents present in garlic extract to drive the reduction process (Sarangi et al., 2024).

Optimization of silver nanoparticles synthesis

To optimize the synthesis of AgNPs, different concentrations of garlic extract, temperatures, and pH levels were evaluated. AgNPs were synthesized by mixing 10 mL of silver nitrate solution (200 µg/mL) with freshly prepared garlic extract of the same concentration. The initial synthesis involved adding 5 mL of garlic extract to the $AgNO_3$ solution at room temperature, followed by continuous stirring for 30–60 minutes. A color change from colorless to yellowish-brown was observed, indicating the formation of nanoparticles due to the reduction of silver ions (Ag^+).

Optimization was conducted by varying garlic extract volumes (10–40 mL), reaction temperatures (20–60°C), and pH values (6.0–9.0) to determine the most favorable conditions for producing stable nanoparticles. Characterization of the synthesized AgNPs was carried out using UV–Visible spectroscopy (showing characteristic absorption peaks around 400–450 nm), transmission electron microscopy (TEM), and X-ray diffraction (XRD) analysis. Antimicrobial activity was assessed using the agar diffusion method. The final nanoparticle suspension was stored at 4°C for further analysis (Singh et al., 2015; Ahmed et al., 2016a; Mittal et al., 2013)

Stability assessment in simulated wound fluid

To evaluate the colloidal stability of biosynthesized AgNPs under physiological conditions, the nanoparticles were incubated in simulated wound fluid (SWF). SWF was prepared by mixing 50% (v/v) fetal bovine serum (FBS) with phosphate-buffered saline (PBS, pH 7.4), mimicking the protein-rich and ionic environment of wound exudate, as described in previous studies (Rozman et al., 2020). AgNPs were diluted in SWF to a final concentration of 50 µg/mL and incubated at 37 °C for 72 hours. Stability was assessed at 0, 24, 48, and 72 hours using UV–Visible spectroscopy (300–700 nm) to monitor shifts in the surface plasmon resonance (SPR) peak. Zeta potential measurements were performed using a Zetasizer Nano ZS (Malvern Instruments, UK), following previously published **protocols** (Massironi et al., 2022; Rónavári et al., 2021). Visual observations were also recorded for signs of nanoparticle sedimentation or aggregation, which could indicate destabilization under biorelevant conditions (Königs et al., 2015).

Characteristics of biosynthesized silver nanoparticles

Ultraviolet spectroscopy

The biosynthesis of AgNPs using garlic extract at various concentrations was monitored using UV–visible spectroscopy. Measurements were taken over time with a double-beam spectrophotometer (Shimadzu UV-1650 PC, Osaka, Japan) across a wavelength range of 190–790 nm. Characteristic peaks in the UV–Vis spectra confirmed the formation of AgNPs (Ahmed et al., 2016a).

X-ray diffraction of the silver nanoparticles

X-ray diffraction (XRD) analysis (Shimadzu XD-3A, Japan) was employed to determine the crystalline nature and grain size of AgNPs biosynthesized from garlic extract. The particle size of the nanoparticles was calculated using Scherrer's equation:

$D = K\lambda/\beta\cos\theta$, where D represents the average crystallite size, β is the line broadening in radians (full width at half maximum of the peak), λ is the X-ray wavelength, θ is the Bragg angle, and K is a constant (shape factor, typically 0.94). This equation provides an estimate of nanoparticle size based on the broadening of diffraction peaks observed in the XRD pattern (Singh et al., 2015; Mittal et al., 2013).

Transmission electron microscopy analysis primarily

Transmission Electron Microscopy (TEM) was utilized to validate the synthesis method for AgNPs and to assess their shape. TEM analysis was conducted at the Electron Microscopy Unit of the National Research Center, following the previous published protocol (Vanlalveni et al. (2021). This technique provided detailed insights into the morphology and structural characteristics of the AgNPs. TEM is commonly used to examine the size, shape, and crystallinity of nanoparticles, offering high-resolution imaging crucial for confirming their formation and structure (Kumari et al., 2017).

Antimicrobial effect of silver nanoparticles

The antibacterial potential of AgNPs was assessed using the agar well diffusion method. The MDR bacterial culture with the highest MAR index, standardized to a 0.5 McFarland turbidity standard, were evenly spread across sterile Mueller-Hinton agar

plates to ensure uniform bacterial distribution. AgNPs, suspended in DMSO at a concentration of 10 mg/mL, were introduced into wells drilled in the agar, with 100 µL of the nanoparticle solution added to each well. The plates were then incubated at 37°C for 24 hours to allow bacterial growth and interaction with the nanoparticles. After incubation, the inhibition zones around each well were measured in millimeters to evaluate the antimicrobial activity of the AgNPs. Positive and negative control wells contained an antimicrobial to which the tested isolate was susceptible, and DMSO, respectively, were included for comparison (Mosallam et al., 2021; Lewis et al., 2025).

Determination of minimum inhibitory concentration of silver nanoparticles

The minimum inhibitory concentration (MIC) of the synthesis AgNPs against the MDR bacterial culture with the highest MAR index was determined using the broth microdilution method. The nanoparticles were initially dissolved in dimethyl sulfoxide (DMSO) to achieve final concentrations ranging from 10 µg/mL to 200 µg/mL. Each dilution was added to a 96-well plate, along with appropriate negative and positive controls: culture broth with DMSO and culture broth with an antimicrobial to which the tested isolates were sensitive respectively. Each well was inoculated with 5 µL of bacterial suspension, adjusted to a concentration of 10^5 CFU/mL, to assess the antimicrobial effect of the AgNPs (Eloff, 1998; Mosallam et al., 2023);. Experiments were conducted in triplicate, with microdilution trays incubated at 37°C for 18 h. MIC was determined by measuring optical density using a spectrophotometer, based on ELISA principles for bacterial inhibition. The MIC was the lowest concentration of AgNPs that fully inhibited growth (Valgas et al., 2007).

Assessment of ROS generation via detection of reduced glutathione levels

To biochemically detect reduced glutathione (GSH) levels in bacteria treated with AgNPs, the Ellman's reagent (DTNB) assay was employed. This method has been widely used for quantifying thiol groups in biological samples (Ellman, 1959). Bacterial cultures were first grown to mid-log phase and then exposed to AgNPs. Following exposure, the cells were harvested by centrifugation and washed with cold phosphate-buffered saline (PBS). The cell pellets were resuspended in 5% sulfosalicylic acid (SSA) to precipitate proteins and release intracellular GSH, followed by incubation on ice for 15 minutes. After centrifugation, the supernatant containing GSH was collected. For the assay, 100 µL of the supernatant was mixed with 900 µL of DTNB reagent (0.6 mM DTNB in 0.1 M phosphate buffer, pH 7.4) and incubated at room temperature for 5–10 minutes. The yellow-colored product, TNB, formed from the reaction between GSH and DTNB, was then measured spectrophotometrically at 412 nm. A standard curve prepared using known GSH concentrations was used to quantify GSH levels, providing an indication of oxidative stress induced by AgNP exposure (Rahman et al., 2006; Aebi, 1984).

In vitro cytotoxicity assessment

To determine the safe concentration range of AgNPs, their cytotoxic potential was evaluated *in vitro* using fibroblast cells. Fibroblasts were cultured in Dulbecco's Modified Eagle Medium (DMEM) supplemented with 10% fetal bovine serum (FBS) and 1% penicillin–streptomycin, and maintained under standard conditions (37°C, 5% CO_2, humidified atmosphere). Cells were seeded into 96-well plates at a density of 5×10^4 cells per well and incubated overnight to allow for adherence. The nanoparticle formulation was applied at varying concentrations, and cell viability was assessed after 24 and 48 hours of exposure using the 3-(4,5-dimethylthiazol-2-yl)-2,5-diphenyltetrazolium bromide (MTT) assay. Absorbance was measured at 570 nm using a microplate reader, and the percentage of viable cells was calculated relative to untreated controls. These results were used to determine the cytotoxic threshold and the optimal non-toxic concentration of the AgNPs (Zhang et al., 2010; Arora et al., 2009).

Evaluation of the combined antibacterial activity of silver nanoparticles and most common antibiotics "ciprofloxacin" against *E. fergusonii*

To investigate the interaction between AgNPs and the commonly used antibiotic ciprofloxacin, a checkerboard assay was employed. This method allows for the determination of the fractional inhibitory concentration (FIC) index, which quantifies the interaction between two antimicrobial agents. Serial two-fold dilutions of both AgNPs and ciprofloxacin were prepared in triplicate across a 96-well microtiter plate to cover a range of concentrations for each compound. Bacterial suspensions of the tested isolates were then inoculated into the wells and incubated at 37°C for 18–24 hours. The minimum inhibitory concentrations (MICs) of each agent, both individually and in combination, were determined in triplicate. The FIC index was calculated using the following equation: FIC index = (MIC of AgNPs in combination/MIC of AgNPs alone) + (MIC of ciprofloxacin in combination/MIC of ciprofloxacin alone). Interpretation of the FIC index values followed established guidelines: ≤0.5 indicated a synergistic effect, >0.5 to ≤1.0 suggested an additive effect, and values >1.0 implied antagonism. This method provides a valuable tool for optimizing antimicrobial therapy by identifying combinations that enhance or hinder antibacterial efficacy (Odds, 2003; Tängdén, 2014).

Mode of action of biosynthesis nanoparticles by transmission electron microscope

TEM was employed to examine the treated isolate with AgNPs, which were incubated for 24 hours. The analysis was performed at the Electron Microscopy Unit at Mansoura University. The samples were imaged using a JEOL-JEM-2100 transmission electron microscope. TEM was used to observe and comp Transmission

electron microscopy (TEM) was employed to examine bacterial isolates treated with AgNPs following a 24-hour incubation. The analysis was conducted at the Electron Microscopy Unit of Mansoura University using a JEOL JEM-2100 transmission electron microscope. TEM imaging was used to observe and compare ultrastructural changes in AgNP-treated bacterial cells with those of untreated control cells (Kumari et al., 2017).

Time-kill curve experiments

The time-kill assay was conducted to evaluate the bactericidal activity of AgNPs, ciprofloxacin, and their combination against *E. fergusonii*. The bacterial strain was cultured in Mueller-Hinton Broth (MHB) to an initial inoculum of approximately 1×10^6 CFU/mL. Treatments included AgNPs at their minimum inhibitory concentration (MIC) and sub-MIC levels, ciprofloxacin at MIC and sub-MIC levels, and a combination of AgNPs at a non-cytotoxic concentration with ciprofloxacin at sub-MIC. A drug-free culture served as the negative control for comparison. Cultures were incubated at 37°C with shaking, and aliquots were collected at 2-hour intervals up to 24 hours. At each time point, serial dilutions were prepared in sterile saline, and appropriate dilutions were plated on Mueller-Hinton agar. Plates were incubated at 37°C for 18–24 hours, and colony-forming units (CFU) were counted to determine viable bacterial counts. Results were expressed as $\log_{10}$ CFU/mL and plotted against time (Montero et al., 2021).

Statistical analysis

All experiments were conducted in triplicate, and results are expressed as the mean ± standard deviation (SD). Statistical analyses were performed using GraphPad Prism version 9.0. To evaluate significant differences among treatment groups (e.g., inhibition zone diameters), a one-way analysis of variance (ANOVA) was conducted. When ANOVA indicated statistical significance ($p < 0.05$), Tukey's multiple comparisons *post hoc* test was applied to identify pairwise differences between groups. A p-value less than 0.05 was considered statistically significant. Graphs were generated using GraphPad Prism, with error bars representing standard deviations.

Results

Phenotypic characterization of bacterial isolates in surgical site infections

In our study, we identified various pathogens responsible for complicated wound infections using standard microbiological methods, including culture characteristics, Gram staining, and a range of biochemical tests. From 150 wound swab samples, 50 bacterial isolates were obtained. *E. fergusonii* was identified as a newly emerging wound pathogen, with a prevalence rate of 24% (12/50). *E. fergusonii* appeared as pink colonies on MacConkey agar due to lactose fermentation, exhibited Gram-negative rod morphology, and was confirmed through positive indole, lysine decarboxylase, and methyl red tests. It was further distinguished by positive arginine dihydrolase and citrate utilization results.

Molecular confirmation and characterization of selected bacterial isolates

The DNA sequences obtained from PCR of 16S RrNA genes were compared with published sequences using the BLAST tool (http://www.ncbi.nlm.nih.gov/blast). The purified PCR products were analyzed to determine its similarity to sequences available in GenBank. Molecular identification of the investigated *E. fergusonii* isolates (n = 12) yielded identical sequences. Sequence alignment showed over 96% nucleotide identity with previously published data in GenBank, confirming the selected isolates and consistent with phenotypic identification. The sequences were submitted to GenBank under the accession number OP57747.

Characterization of multidrug resistance and MAR indices in clinical isolates

Notably, all *E. fergusonii* isolates exhibited multidrug-resistant (MDR) patterns, showing resistance to at least three antibiotics from different antimicrobial classes. The multiple antibiotic resistance (MAR) indices of the clinical isolates ranged from 0.56 to 0.78, indicating moderate to high resistance levels. Based on these results, we selected the ten isolates (N=10) with the highest MAR index (0.78) for further analysis and excluded two isolates with moderate MAR indices.

Chemical analysis of purified garlic extract using instrumental analysis

GC-MS analysis of the partially purified garlic extract revealed a complex chemical profile consisting of numerous volatile components as shown in Supplementary Figure S1. A total of 48 peaks were detected across two chromatograms, with compounds eluting between 1.54 and 31.58 minutes. The most prominent peaks appeared at retention times of 21.05, 15.11, and 6.88 minutes in the first chromatogram, contributing 21.93%, 10.55%, and 9.01% of the total area, respectively. In the second chromatogram, major peaks were observed at 31.37 minutes (32.78%), 25.41 minutes (10.32%), and 30.37 minutes (8.24%). These peaks indicate the presence of dominant volatile constituents within the extract. A spot detected at Rf value 9 on thin-layer chromatography (TLC) exhibited strong antibacterial activity against selected multidrug-resistant (MDR) bacterial strains. This bioactive fraction was subjected to GC-MS analysis, which allowed identification of key antimicrobial compounds.

UPLC-ESI-MS/MS analysis of the bioactive fraction identified at Rf = 0.9 on the TLC plate revealed the presence of several distinct

compounds. The chromatographic separation produced well-resolved peaks, and mass spectral data acquired in positive ion mode allowed accurate identification of the constituents. By comparing the mass spectra and retention times with the NIST library, multiple bioactive molecules were confirmed, supporting the chemical complexity and antimicrobial potential of the active garlic extract fraction. Based on retention time, peak area, and comparison with reference data, three major sulfur-containing compounds were identified: allyl methyl trisulfide (C_4H8S_3, MW 152.3), dimethyl trisulfide ($C_2H_2S_3$, MW 126.3), and allicin ($C_2H_{10}S_2$, MW 162.3) as shown in Table 1. These compounds are known for their broad-spectrum antimicrobial properties and are likely responsible for the observed antibacterial activity. The results confirm that sulfur-rich volatile constituents are predominant in the garlic extract and contribute to its therapeutic potential.

Biosynthesis and characterization of silver nanoparticles using garlic extract

AgNPs were successfully synthesized using garlic extract, evidenced by a distinct color change from white to dark brown, indicating the reduction of Ag^+ ions. Optimization revealed that garlic extract volume, temperature, and pH significantly influenced nanoparticle formation, stability, and size. The most stable and uniformly sized AgNPs, with strong antimicrobial activity, were obtained at 10 mL extract volume, 40°C, and pH 8.0. At this condition, the reaction mixture consistently turned yellow-brown within 30–45 minutes. At higher temperatures (>40°C), although the reaction rate increased, nanoparticle aggregation also intensified, resulting in polydisperse and less stable colloids with reduced antimicrobial efficacy. Similarly, more alkaline conditions (pH 9–10) accelerated nucleation but produced irregular and unstable nanoparticles, likely due to unregulated reduction kinetics. These conditions led to inconsistent morphology and poor colloidal stability. In contrast, pH 8.0 provided a balanced environment that moderated the reduction rate, enabling controlled nucleation and growth. This favored the formation of uniform, stable, and bioactive AgNPs, making it the optimal condition for synthesis.

Moreover, UV-Visible spectroscopy further confirmed nanoparticle formation, showing a characteristic absorption peak at approximately 390 nm, indicative of well-dispersed AgNPs. the concentration of Ag+ ions was the primary factor significantly affecting the biosynthesis of AgNPs, as confirmed by the corresponding absorption spectra, which showed a prominent peak at 390 nm (Figure 1A). X-ray diffraction (XRD) analysis verified the purity and crystalline structure of the synthesized AgNPs, showing prominent diffraction peaks at 27.67°, 32.08°, 37.95°, and 46.00°, confirming well-defined crystalline AgNPs (Figure 1B). Transmission electron microscopy (TEM) analyses showed that nanoparticles synthesized under optimized conditions had an average size of 15–20 nm and were spherical in shape. TEM images revealed a narrow size distribution, with most particles falling within the 4.21 to 22.67 nm range, suggesting a relatively uniform size (Figures 2A, B). These optimized parameters (10 mL garlic extract, 40°C, and pH 8.0) produced AgNPs with desirable size, stability, and antimicrobial properties, suggesting that these conditions are optimal for efficient synthesis and potential applications.

Importantly, garlic-mediated AgNPs demonstrated excellent stability in simulated wound fluid (SWF) over a 72-hour incubation period at 37°C. UV–Vis spectra showed minimal shift in the surface plasmon resonance (SPR) peak between 0 h and 72 h, indicating preserved nanoparticle dispersion and morphology. No visible aggregation or sedimentation was observed during the incubation. Zeta potential measurements remained consistently negative, with values ranging from −28.6 mV to −26.9 mV across the time points, confirming stable electrostatic repulsion and colloidal integrity (Figure 3A). These findings suggest that the phytochemical capping agents from *Allium sativum* extract effectively stabilized the AgNPs even under physiologically relevant conditions.

Antimicrobial effect of silver nanoparticles

The antimicrobial activity of AgNPs synthesized using garlic extract was assessed against selected *E. fergusonii* isolates (N=10) with high MAR indices. The inhibition zone diameters were measured, with a mean value of 28 ± 0.5 mm; however, the MIC for most tested isolates was 100 µg/mL. These results suggest that AgNPs synthesized using garlic extract possess significant antibacterial potential, with varying efficacy against different MDR pathogens.

TABLE 1 Chemical component and chemical structure of purified garlic extract.

Compound	MW	RT	Peak	Molecular formula	Structure
Ally methyl trisulfide	152.3	31.29	46	$C_4H_8S_3$	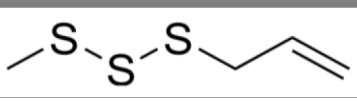
Dimethyl trisulphide	126.3	30.87	42	$C_2H_6S_3$	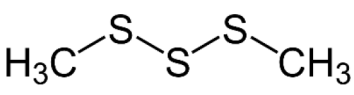
Allicin	162.3	6.88	5	$C_6H_{10}S_2$	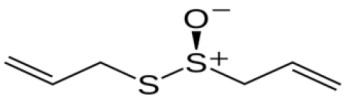

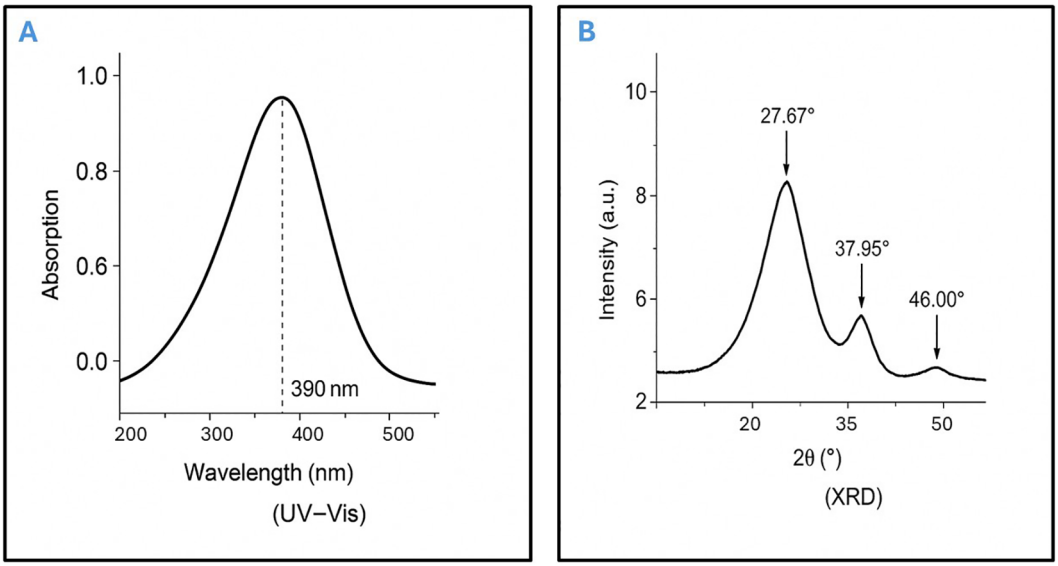

FIGURE 1
Characterization of garlic-mediated AgNPs by UV–Vis spectroscopy and X-ray diffraction. **(A)** UV–Vis Spectroscopy of Synthesized AgNPs, the UV–Visible absorption spectrum displays a characteristic surface plasmon resonance (SPR) peak at approximately 390 nm, confirming the formation of well-dispersed silver nanoparticles (AgNPs). **(B)** X-ray Diffraction (XRD) Pattern of AgNPs, the XRD profile reveals distinct diffraction peaks at 27.67°, 37.95°, and 46.00°, indicating the crystalline nature of the synthesized AgNPs and corresponding to the face-centered cubic (FCC) structure of elemental silver.

Results of oxidative stress analysis via ROS assay

Following treatment with AgNPs, a dose-dependent decrease in reduced glutathione (GSH) levels was observed in *E. fergusonii* compared to untreated controls. In the control group, intracellular GSH concentration was measured at 52.3 ± 3.1 µmol/mg protein. Upon exposure to 50 µg/mL and 100 µg/mL of AgNPs, GSH levels significantly dropped to 31.7 ± 2.5 µmol/mg and 18.2 ± 1.8 µmol/mg protein, respectively ($p < 0.01$) (Figure 3B). This decline indicates a

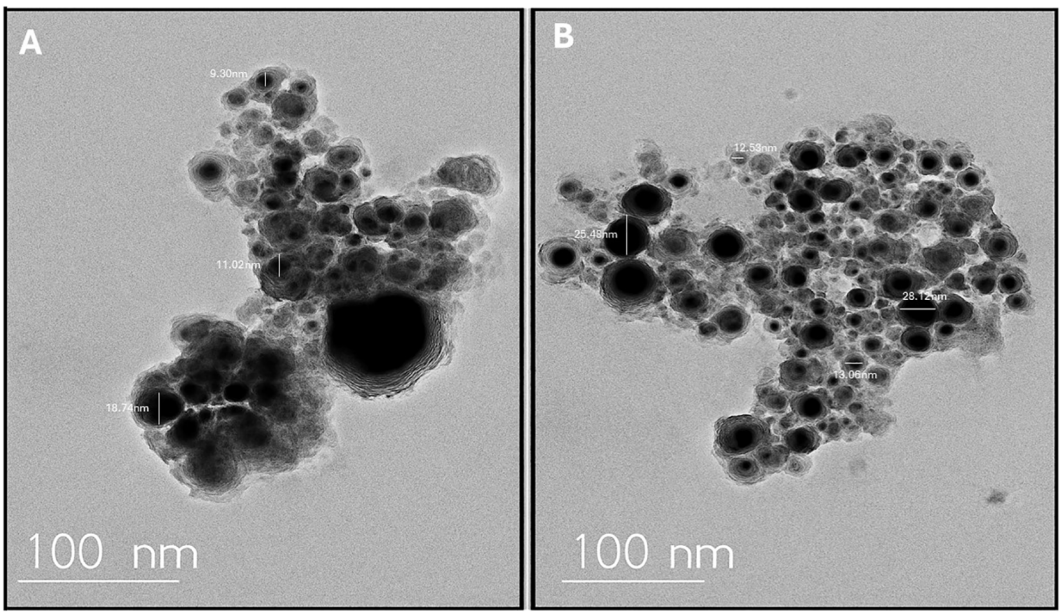

FIGURE 2
Transmission electron microscopy (TEM) image showing the morphology and size distribution of silver nanoparticles (AgNPs) synthesized using garlic extract. **(A)** Depicts the silver nanoparticles with a spherical shape and consistent size, confirming effective synthesis. **(B)** Presents the size distribution profile of the AgNPs, highlighting their uniformity and supporting the structural consistency of the sample.

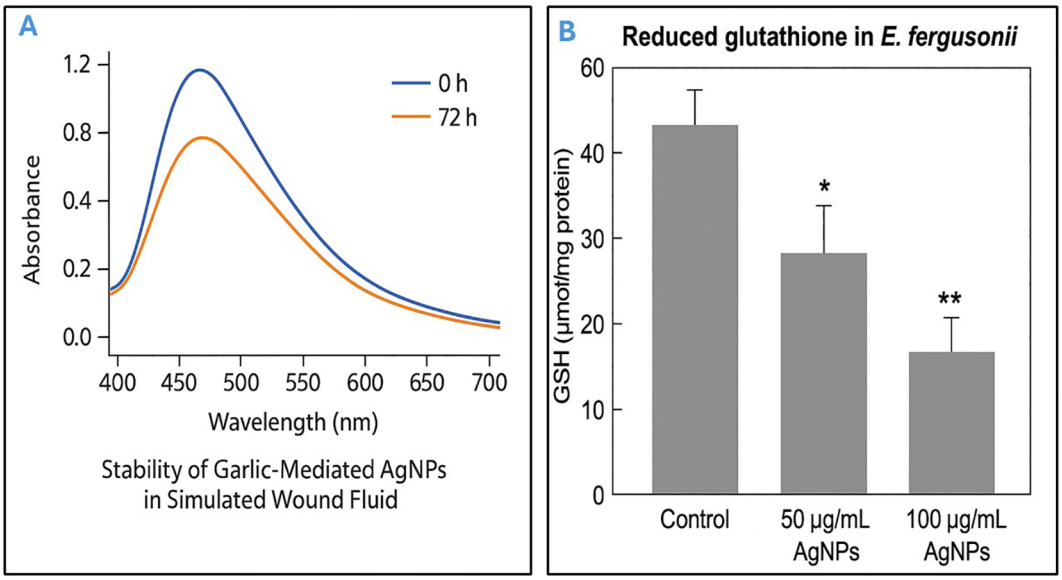

FIGURE 3
Evaluation of AgNP stability in simulated wound fluid and associated oxidative stress in *Escherichia fergusonii*. **(A)** Stability of garlic-mediated silver nanoparticles (AgNPs) in simulated wound fluid (SWF) at 37°C over a 72-hour period, as determined by UV–Visible spectroscopy. The surface plasmon resonance (SPR) peak remained near 450 nm with minimal spectral shift and reduction in absorbance, indicating good colloidal stability and minimal aggregation. **(B)** Effect of AgNPs on reduced glutathione (GSH) levels in *Escherichia fergusonii*. Exposure to AgNPs at 50 and 100 µg/mL significantly reduced intracellular GSH concentrations compared to the untreated control. Data are expressed as mean ± standard deviation (SD). $p < 0.05$ (*), $p < 0.01$ (**), indicating statistical significance relative to control.

marked oxidative stress response, suggesting that AgNPs induce GSH depletion in a concentration-dependent manner. The results are consistent with elevated oxidative damage and support the hypothesis that AgNPs exert their bactericidal activity, to some extent, via oxidative stress mechanisms.

In vitro cytotoxicity assay

In vitro cytotoxicity evaluation of the synthesized AgNPs revealed a dose-dependent response in normal human dermal fibroblasts. Cell viability remained above 90% at concentrations up to 30 µg/mL, while exposure to 50 µg/mL resulted in a moderate reduction to approximately 60% viability after 24 hours, indicating a clear cytotoxic threshold. Therefore, concentrations below 50 µg/mL were unlikely to have caused significant harm to the fibroblast cells, as they induced less than 50% of the maximal cytotoxic effect (Figure 4A). As a result, these lower concentrations were considered relatively safe for cellular exposure during the experimental conditions.

Assessment of synergistic antibacterial activity of AgNPs and ciprofloxacin against *E. fergusonii*

The MIC of AgNPs alone against *E. fergusonii* was 100 µg/mL, while ciprofloxacin alone exhibited an MIC of 16 µg/mL. When used in combination, the MICs were significantly reduced to 25 µg/mL for AgNPs and 2 µg/mL for ciprofloxacin (Figure 4B). These findings were consistent in 80% of the selected *E. fergusonii* isolates (N=10) with high multiple antibiotic resistance (MAR) indices. This notable reduction in MIC values indicated a potentiation of antibacterial activity through co-administration. The FIC index for this combination was calculated to be 0.37, which was well below the synergy threshold of 0.5, thereby demonstrating a synergistic interaction between AgNPs and ciprofloxacin. Therefore, the combined use of AgNPs and ciprofloxacin exerted a more potent antibacterial effect against *E. fergusonii* than either agent used alone. Such synergy not only enhanced bacterial growth inhibition but also implied the potential for reducing the required concentrations of each antimicrobial agent, which could help minimize cytotoxicity and delay the emergence of resistance.

Mode of action of biosynthesis nanoparticles by transmission electron microscope

E. fergusonii cells exposed solely to garlic extract exhibited minimal structural changes when examined by TEM, suggesting limited antibacterial efficacy under the experimental conditions (Figure 5A). In contrast, cells treated with AgNPs synthesized using garlic extract displayed substantial cellular disruption (Figure 5B). These included pronounced morphological deformities, such as compromised membranes, irregular shapes, and the presence of electron-dense particles indicative of nanoparticle accumulation. The internal cell architecture appeared highly disorganized and granulated, reflecting severe

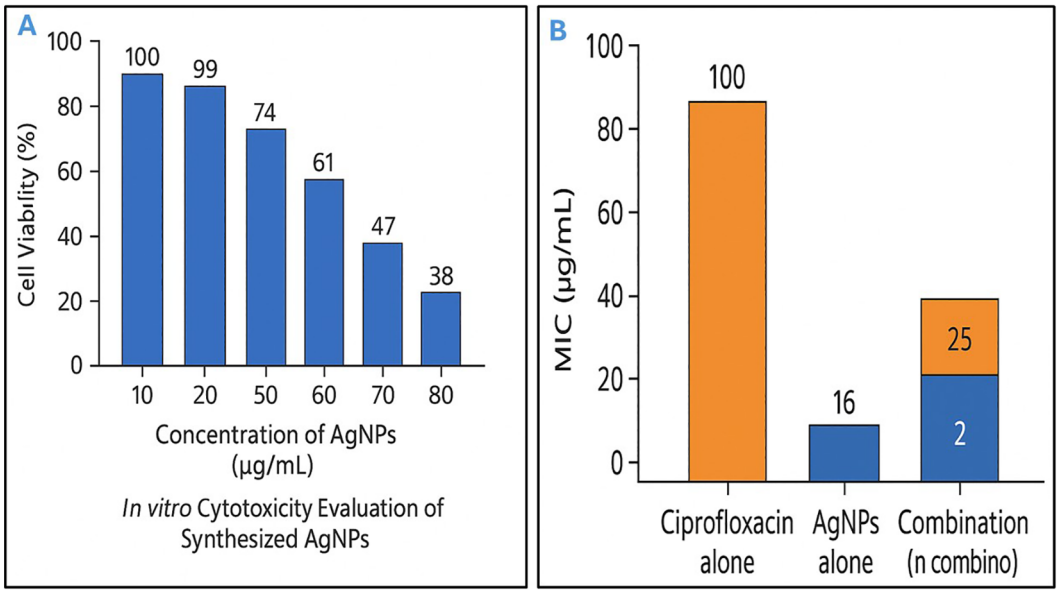

FIGURE 4
Dual characterization of silver nanoparticles: safe concentrations and antibacterial synergy with conventional antibiotic. **(A)** *In vitro* cytotoxicity evaluation of biosynthesized silver nanoparticles (AgNPs) against normal human dermal fibroblasts. Cell viability was assessed after 24 hours of exposure to increasing concentrations of AgNPs (10–80 µg/mL), showing a dose-dependent reduction in viability. Concentrations below 50 µg/mL maintained over 60% cell viability, indicating relatively low cytotoxicity. **(B)** Antibacterial activity of ciprofloxacin, AgNPs, and their combination against *Escherichia fergusonii*. Minimum inhibitory concentration (MIC) values are shown. Ciprofloxacin and AgNPs alone exhibited MICs of 16 µg/mL and 100 µg/mL, respectively. The combination reduced MICs to 2 µg/mL (ciprofloxacin) and 25 µg/mL (AgNPs), demonstrating a synergistic effect.

cellular damage and loss of integrity. The extent of ultrastructural deterioration highlights the strong antibacterial activity of garlic-mediated AgNPs, likely driven by mechanisms that impair membrane function and disrupt intracellular processes.

Time-kill curve assays

The time-kill assay demonstrated the bactericidal efficacy of AgNPs and ciprofloxacin, both individually and in combination, against the investigated *E. fergusonii* strain over a 24-hour period. Treatment with the MIC of AgNPs (100 µg/mL) or ciprofloxacin (16 µg/mL) resulted in complete bacterial eradication by 20 hours, indicating strong individual antibacterial activity. Notably, the combination of AgNPs at a safe concentration (50 µg/mL) with ciprofloxacin at sub-MIC levels (8 µg/mL) exhibited the most rapid and potent effect, achieving total bacterial killing as early as 14 hours, highlighting a synergistic interaction. In contrast, sub-MIC treatments of either agent alone showed limited bactericidal effects and delayed reductions in bacterial viability. These results suggest that combining low concentrations of AgNPs with sub-inhibitory levels of antibiotics can significantly enhance antimicrobial efficacy (Figure 6).

Discussion

Complicated wound infections remain a significant challenge in clinical settings, contributing to increased illness, longer hospital stays, and higher healthcare costs. Effective management of such infections requires a combination of prevention, early diagnosis, and proper treatment. Key preventive strategies include strict adherence to aseptic techniques, preoperative antibiotic use, good patient preparation, and careful postoperative wound care. Advances in infection control, such as antimicrobial-coated sutures and modern wound dressings, have further improved healing. However, complications may arise when standard treatment protocols fail to effectively target unusual or emerging bacteria, such as *E. fergusonii*, which may not be well-covered by common antibiotics. If an infection develops, it's important to correctly identify the bacteria and test which antibiotics work best, so the most effective treatment can be given (Elsayed et al., 2022). In more severe cases, surgery such as cleaning the wound or draining pus may also be necessary. These challenges highlight the importance of developing new strategies alongside antibiotics to reduce wound infections and improve surgical outcomes (Pittet et al., 2009; Berríos-Torres et al., 2017). In this study, we suggest using a sublethal, safe dose of AgNPs synthesized by garlic extract in combination with antimicrobial drugs as a strategy to manage this atypical wound infection.

In our study, *E. fergusonii* emerged as a significant pathogen associated with complicated wound infections. This pathogen was consistently detected in clinical samples from patients with severe, chronic wounds, highlighting its significant role in the pathogenesis of these infections. Our findings suggest that *E. fergusonii* may play a central role in the persistence and progression of infected wounds, complicating treatment regimens and posing a substantial challenge to effective clinical management. This pathogen was among the

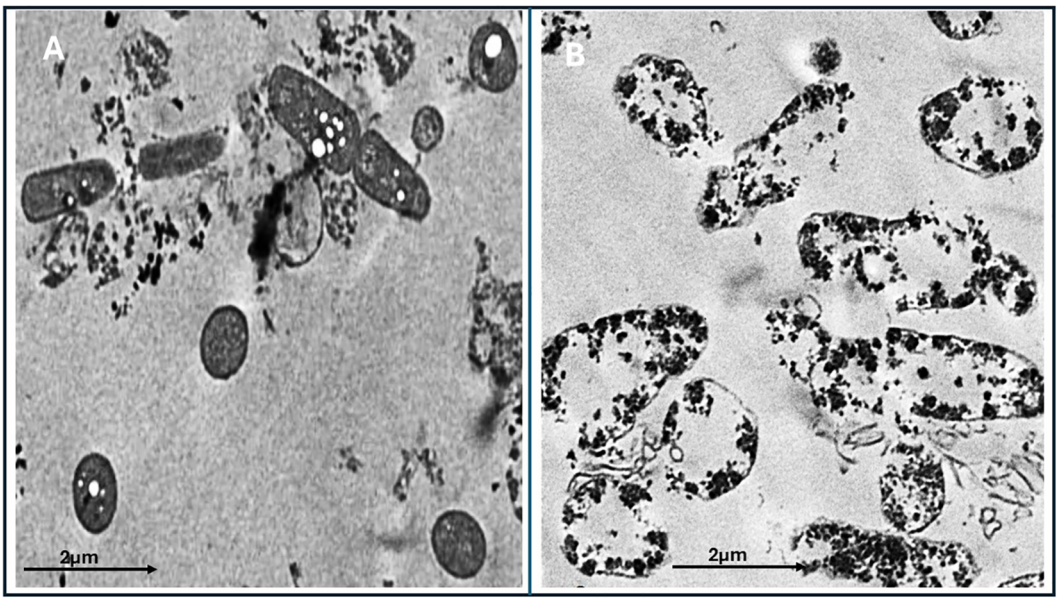

FIGURE 5
Transmission electron microscopy (TEM) images of the treated and untreated *Escherichia fergusonii* isolates. **(A)** Bacterial cells treated with garlic extract alone (control), showing relatively intact cellular structures with limited disruption. **(B)** Bacterial cells treated with biosynthesized AgNPs using garlic extract, showing extensive structural damage, aggregation of nanoparticles, and cytoplasmic disintegration. Scale bar: 2 µm.

most commonly implicated in wound infections and is known for its ability to cause severe complications in postoperative patients (Torkan and Askari Badouei, 2024; Bansal et al., 2016). Notably, all the detected *E. fergusonii* isolates exhibited multidrug-resistant (MDR) patterns, a finding consistent with the growing global concern regarding antimicrobial resistance in clinical settings (Pittet et al., 2009). The high prevalence of MDR pathogens in our study highlights the increasing difficulty in treating complicated wounds with conventional antimicrobial therapies. This emphasizes the need for innovative approaches to manage these infections, including better surveillance, rapid diagnostic methods, and the development of alternative therapies (Monk et al., 2024; Negut et al., 2018; Abd El-Hamid et al., 2023). Additionally, the polymicrobial nature of complicated wounds further complicates treatment, requiring tailored therapeutic regimens to address the diverse array of resistant pathogens present (Tatarusanu et al., 2023). Our

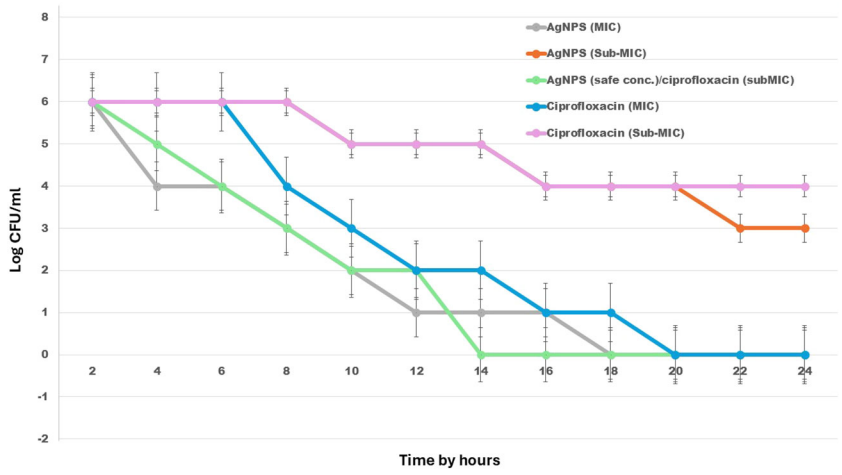

FIGURE 6
Time-kill kinetics of AgNPs, ciprofloxacin, and their combination against *E. fergusonii* over 24 hours. The graph illustrates changes in bacterial viability (log_{10} CFU/mL) in response to various treatments, including AgNPs, ciprofloxacin, and their combined application at different concentrations.
.

findings underscore the critical need for multidisciplinary strategies to tackle the rising incidence of atypical MDR pathogens associated with wound infections and improve patient outcomes.

The MAR indices observed in *E. fergusonii* isolates in this study ranged from 0.56 to 0.78, indicating a high level of resistance. According to Krumperman's threshold, MAR indices above 0.2 suggested that the bacteria originated from high-risk environments where antibiotics were frequently used (Krumperman, 1983). To better understand the clinical relevance of these values, we compared them with MAR indices reported for other common wound pathogens. For example, *Staphylococcus aureus* isolated from wound infections had shown MAR values ranging from 0.30 to 0.60 (Pai et al., 2010), while *Pseudomonas aeruginosa* had been reported with indices between 0.35 and 0.65 (Alkhulaifi and Mohammed, 2023). For instance, *Klebsiella pneumoniae* isolates from clinical specimens have exhibited MAR indices with a mean value of 0.74 (Ogefere and Idoko, 2024). The MAR indices of *E. fergusonii* in our study fell at the higher end of this spectrum, suggesting that this organism might have possessed comparable or even greater multidrug resistance potential. Given the emerging role of *E. fergusonii* as a clinically significant pathogen, particularly in wound infections, its high MAR values underscored the need for vigilant antimicrobial stewardship and further epidemiological monitoring.

The results of our study indicated that AgNPs were successfully with the most stable and uniformly sized particles exhibiting the highest antimicrobial activities at a garlic extract concentration of 10 mL (equal volume), a reaction temperature of 40°C, and a pH of 8.0. This finding is consistent with previous research demonstrating that the synthesis of AgNPs is highly influenced by the concentration of the reducing agent, temperature, and pH (Krishnan et al., 2020). This observation aligns with previous studies indicating that mildly alkaline conditions (pH 7.5–8.5) facilitate the reduction of silver ions while maintaining particle stability and functional integrity in green synthesis approaches (Ahmed et al., 2016b; Sharma et al., 2009). Garlic extract, rich in bioactive organosulfur compounds like allicin, acts effectively as both a reducing and capping agent under these conditions, helping to control nanoparticle size and prevent agglomeration (Iravani, 2014; Singh et al., 2018) and enhancing their stability and bioactivity (Vijayakumar et al., 2019). The chosen conditions therefore reflect an optimized compromise between synthesis efficiency, nanoparticle quality, and biological performance (Liaqat et al., 2022).

In the same context, the long-term and physiological stability of AgNPs is critical for their successful application in biological systems, especially for wound treatment. In this study, the garlic-synthesized AgNPs maintained colloidal stability in simulated wound fluid, a complex protein- and salt-rich environment designed to mimic wound exudate. Over 72 hours, minimal changes were observed in SPR peak position and zeta potential values, with no visible aggregation, indicating robust nanoparticle stability. These results support earlier reports that phytochemical-capped AgNPs exhibit superior stability due to their natural capping agents (Ahmed et al., 2016; Iravani, 2014). The sustained negative zeta potential (~−27 mV) observed in our study is a key indicator of electrostatic repulsion sufficient to prevent aggregation under physiological ionic strength. Stability in such a biologically relevant medium further validates the potential of these AgNPs for *in vivo* or topical wound applications, as instability could otherwise reduce efficacy or lead to rapid clearance or toxicity (Franci et al., 2015).

Our findings align with previous reports on the antimicrobial efficacy of plant-mediated AgNPs, and highlight the potential of garlic extract as a reliable bio-reductant and stabilizer. For comparison, AgNPs synthesized using *Azadirachta indica* (neem) leaf extract have demonstrated broad-spectrum antibacterial activity, particularly against *Staphylococcus aureus* and *Escherichia coli*, with inhibition zones ranging from 10 to 20 mm depending on concentration and particle size (Shankar et al., 2004). Similarly, *Curcuma longa* (turmeric)-based AgNPs have shown significant antimicrobial effects, attributed to curcumin's polyphenolic content acting as both a reducing and capping agent (Veerasamy et al., 2011). In our study, garlic-mediated AgNPs exhibited comparable antimicrobial performance, suggesting that allicin and sulfur-containing compounds may play a synergistic role in nanoparticle synthesis and biological activity. Compared to neem and turmeric, the synthesis using garlic yielded relatively uniform nanoparticles with strong inhibition zones, indicating its potential as an efficient and cost-effective alternative for green nanoparticle production.

Of note, the antimicrobial efficacy of AgNPs is known to increase with particle size uniformity, as smaller, more stable nanoparticles often exhibit improved interaction with microbial cell membranes, leading to greater antimicrobial effects (Rai et al., 2009). These findings highlight the importance of optimizing biosynthesis conditions to achieve nanoparticles with desirable characteristics, both in terms of stability and antimicrobial potency. Our study demonstrated that AgNPs exert their antimicrobial effect primarily by interacting with microbial cell membranes and releasing ROS. The nanoparticles adhere to the bacterial cell surface, disrupting the integrity of the membrane and leading to increased permeability. This disruption allows for the leakage of essential cellular contents, such as proteins and ions, which ultimately results in cell death (Bruna et al., 2021). Additionally, AgNPs can generate ROS that further damage the microbial DNA, proteins, and lipids, compounding the antimicrobial effect (Rai et al., 2009).

This study confirmed the potent antibacterial activity of both AgNPs and ciprofloxacin against *E. fergusonii*, with each agent independently achieving complete bacterial growth inhibition at their respective MICs within 20 hours. However, the MIC of AgNPs (100 μg/mL) exceeds the cytotoxic threshold for mammalian cells, raising concerns about its clinical safety. Previous studies have shown that concentrations above 50 μg/mL can significantly affect cell viability (Ahamed et al., 2010). Notably, the combination of a lower, non-cytotoxic concentration of AgNPs (50 μg/mL) with sub-MIC ciprofloxacin (8 μg/mL) demonstrated a rapid and enhanced bactericidal effect, achieving complete bacterial inhibition within 14 hours. This synergistic interaction may be attributed to the ability of AgNPs to disrupt bacterial membranes, thereby increasing antibiotic uptake (Ibraheem et al., 2022). The limited effectiveness of sub-MIC treatments when used alone further underscores the value of combining agents to enhance efficacy while reducing potential

toxicity. Overall, these findings support the potential of AgNP-antibiotic combinations as a promising strategy for managing drug-resistant or emerging pathogens more effectively and safely.

Conclusion

Based on our findings, we recommend the use of silver nanoparticles as part of a combined treatment strategy with conventional antibiotics for managing complicated wound infections caused by both typical and atypical pathogens. AgNPs, when applied through coated dressings or wound irrigations, offer localized antimicrobial activity that can enhance the overall antibacterial effect. This combination has been shown to improve bacterial clearance, reduce the need for high systemic antibiotic doses, and potentially limit the emergence of antibiotic resistance. Integrating AgNPs with standard antibiotic therapy may therefore represent an effective and targeted approach to support wound healing and reduce post-operative complications.

Data availability statement

The datasets presented in this study can be found in online repositories. The names of the repository/repositories and accession number(s) can be found in the article/Supplementary Material.

Ethics statement

This study was conducted following the ethical standards set by the Research Ethics Committee of the Faculty of Pharmacy at Port Said University (REC.PHARM.PSU). It was approved with the ethical approval code (REC.PHARM.PSU27). Informed consent was obtained from participants, and the associated documents can be provided upon request. The studies were conducted in accordance with the local legislation and institutional requirements. The human samples used in this study were acquired from a by-product of routine care or industry. Written informed consent for participation was not required from the participants or the participants' legal guardians/next of kin in accordance with the national legislation and institutional requirements.

Author contributions

SA: Conceptualization, Project administration, Writing – original draft. AG: Formal analysis, Investigation, Writing – original draft. MG: Formal analysis, Investigation, Writing – original draft. NA: Formal analysis, Investigation, Writing – original draft. MA: Software, Validation, Writing – review & editing. MB: Methodology, Writing – original draft, Writing – review & editing. AA: Formal analysis, Investigation, Writing – review & editing.

Funding

The author(s) declare that financial support was received for the research and/or publication of this article. This study was supported by Princess Nourah bint Abdulrahman University Researchers Supporting Project number (PNURSP2025R153), Princess Nourah bint Abdulrahman University, Riyadh, Saudi Arabia.

Acknowledgments

The authors gratefully acknowledge the financial support provided by the Princess Nourah bint Abdulrahman University Researchers Supporting Project (PNURSP2025R153), Princess Nourah bint Abdulrahman University, Riyadh, Saudi Arabia. Additionally, The authors also extend their appreciation to AlMaarefa University, Riyadh, Saudi Arabia, for its valuable support of this research.

Conflict of interest

The authors declare that the research was conducted in the absence of any commercial or financial relationships that could be construed as a potential conflict of interest.

Generative AI statement

The author(s) declare that no Generative AI was used in the creation of this manuscript.

Publisher's note

Supplementary material

The Supplementary Material for this article can be found online at: https://www.frontiersin.org/articles/10.3389/fcimb.2025.1604507/full#supplementary-material

SUPPLEMENTARY FIGURE 1
GC-MS chromatographic profiles of partially purified garlic extract. The figure shows the chemical fingerprint of volatile constituents present in the extract. Peaks represent individual compounds separated based on their retention times and detected by mass spectrometry.

References

Abd El-Hamid, M. I., El-Tarabili, R. M., Bahnass, M. M., Alshahrani, M. A., Saif, A., Alwutayd, K. M., et al. (2023). Partnering essential oils with antibiotics: proven therapies against bovine *Staphylococcus aureus* mastitis. *Front. Cell. Infect. Microbiol.* 13. doi: 10.3389/fcimb.2023.1265027

Adesina, T., Nwinyi, O., De, N., Akinnola, O., and Omonigbehin, E. (2019). First detection of carbapenem-resistant Escherichia fergusonii strains harbouring beta-lactamase genes from clinical samples. *Pathogens* 8, 164. doi: 10.3390/pathogens8040164

Aebi, H. (1984). Catalase *in vitro*. *Methods Enzymol.* 105, 121–126. doi: 10.1016/S0076-6879(84)05016-3

Ahamed, M., AlSalhi, M. S., and Siddiqui, M. K. J. (2010). Silver nanoparticle applications and human health. *Clin. Chim. Acta* 411, 1841–1848. doi: 10.1016/j.cca.2010.08.016

Ahmed, S., Ahmad, M., Swami, B. L., and Ikram, S. (2016b). A review on plant extract-mediated synthesis of silver nanoparticles for antimicrobial applications: A green expertise. *J. Adv. Res.* 7, 17–28. doi: 10.1016/j.jare.2015.02.007

Ahmed, S., Saifullah,, Ahmad, M., Swami, B. L., and Ikram, S. (2016a). Green synthesis of silver nanoparticles using Azadirachta indica aqueous leaf extract. *J. Radiat. Res. Appl. Sci.* 9, 1–7. doi: 10.1016/j.jrras.2015.06.006

Alkhulaifi, Z. M., and Mohammed, K. A. (2023). Prevalence and molecular analysis of antibiotic resistance of Pseudomonas aeruginosa isolated from clinical and environmental specimens in Basra, Iraq. *Iranian J. Microbiol.* 15, 45–54. doi: 10.18502/ijm.v15i1.11917

Ankri, S., and Mirelman, D. (1999). Antimicrobial properties of allicin from garlic. *Microbes Infect.* 1, 125–129. doi: 10.1016/S1286-4579(99)80003-3

Arora, S., Jain, J., Rajwade, J. M., and Paknikar, K. M. (2009). Interactions of silver nanoparticles with primary mouse fibroblasts and liver cells. *Toxicol. Appl. Pharmacol.* 236, 310–318. doi: 10.1016/j.taap.2009.02.020

Bahar, A. A., and Ren, D. (2013). Antimicrobial peptides. *Pharm. (Basel Switzerland)* 6, 1543–1575. doi: 10.3390/ph6121543

Bansal, D., Singh, R. R., Ded, K. S., Aggarwal, A., Puar, G. S., and Shah, A. S. (2016). Bacteriological profile and antimicrobial susceptibility in surgical site infection in elective abdominal surgeries. *Int. Surg. J.* 3, 1879–1882. doi: 10.18203/2349-2902.isj20163559

Bendy, R. H. Jr., Nuccio, P. A., Wolfe, E., Collins, B., Tamburro, C., Glass, W., et al. (1964). Relationship of quantitative wound bacterial counts to healing of decubiti: Effect of topical gentamicin. *Antimicrobial Agents Chemother. (Bethesda)* 10, 147–155. Available at https://pubmed.ncbi.nlm.nih.gov/14287920/ (Accessed June 10, 2025).

Berríos-Torres, S. I., Umscheid, C. A., Bratzler, D. W., Leas, B. F., Stone, E. C., and Singletary, J. P. (2017). Centers for Disease Control and Prevention guideline for the prevention of surgical site infection 2017. *J. Am. Coll. Surgeons* 224, 59–74. doi: 10.1001/jamasurg.2017.0904

Bruna, T., Maldonado-Bravo, F., Jara, P., and Caro, N. (2021). Silver nanoparticles and their antibacterial applications. *Int. J. Mol. Sci.* 22, 7202. doi: 10.3390/ijms22137202

Chen, X., and Schluesener, H. J. (2008). Nanosilver: A nanoproduct in medical application. *Toxicol. Lett.* 176, 1–12. doi: 10.1016/j.toxlet.2007.10.004

Ellman, G. L. (1959). Tissue sulfhydryl groups. *Arch. Biochem. Biophys.* 82, 70–77. doi: 10.1016/0003-9861(59)90090-6

Eloff, J. N. (1998). A sensitive and quick microplate method to determine the minimal inhibitory concentration of plant extracts for bacteria. *Planta Med.* 64, 711–713. doi: 10.1055/s-2006-957563

Elsayed, M. E., Abd El-Hamid, M. I., El-Gedawy, A., Bendary, M. M., ELTarabili, R. M., Alhomrani, M., et al. (2022). New Insights into *Listeria monocytogenes* Antimicrobial Resistance, Virulence Attributes and Their Prospective Correlation. *Antibiotics* 11, 1447. doi: 10.3390/antibiotics11101447

Fabrega, J., Luoma, S. N., Tyler, C. R., Galloway, T. S., and Lead, J. R. (2011). Silver nanoparticles: behaviour and effects in the aquatic environment. *Environ. Int.* 37, 517–531. doi: 10.1016/j.envint.2010.10.012

Franci, G., Falanga, A., Galdiero, S., Palomba, L., Rai, M., Morelli, G., et al. (2015). Silver nanoparticles as potential antibacterial agents. *Mol. (Basel)* 20, 8856–8874. doi: 10.3390/molecules20058856

Francolini, I., Vuotto, C., Piozzi, A., and Donelli, G. (2017). Antifouling and antimicrobial biomaterials: an overview. *APMIS* 125, 392–417. doi: 10.1111/apm.12675

Funke, G., Hany, A., and Altwegg, M. (1993). Isolation of Escherichia fergusonii from four different sites in a patient with pancreatic carcinoma and cholangiosepsis. *J. Clin. Microbiol.* 31, 2201–2203. doi: 10.1128/jcm.31.8.2201-2203.1993

Garcia, L. S. (Ed.) (2010). Clinical Microbiology Procedures Handbook. (*3rd ed.*). ASM Press. doi: 10.1128/9781555817435.

Ghaly, M. F., Albalawi, M. A., Bendary, M. M., Shahin, A., Shaheen, M. A., Abu Eleneen, A. F., et al. (2023). Tamarindus indica extract as a promising antimicrobial and antivirulence therapy. *Antib. (Basel)* 12, 464. doi: 10.3390/antibiotics12030464

Ibraheem, D. R., Hussein, N. N., Sulaiman, G. M., Mohammed, H. A., Khan, R. A., and Al Rugaie, O. (2022). Ciprofloxacin-loaded silver nanoparticles as potent nano-antibiotics against resistant pathogenic bacteria. *Nanomater. (Basel)* 12, 2808. doi: 10.3390/nano12162808

Iravani, S. (2011). Green synthesis of metal nanoparticles using plants. *Green Chemistry*, 13(10), 2638–2650. doi: 10.1039/C1GC15386B (Accessed June 10, 2025).

Königs, A. M., Flemming, H. C., and Wingender, J. (2015). Nanosilver induces a non-culturable but metabolically active state in Pseudomonas aeruginosa. *Front. Microbiol.* 6. doi: 10.3389/fmicb.2015.00395

Krishnan, P. D., Banas, D., Durai, R. D., Kabanov, D., Hosnedlova, B., Kepinska, M., et al. (2020). Silver nanomaterials for wound dressing applications. *Pharmaceutics* 12, 821. doi: 10.3390/pharmaceutics12090821

Krumperman, P. H. (1983). Multiple antibiotic resistance indexing of Escherichia coli to identify high-risk sources of fecal contamination of foods. *Appl. Environ. Microbiol.* 46, 165–170. doi: 10.1128/aem.46.1.165-170.1983

Kumari, M., Pandey, S., Giri, V. P., Bhattacharya, A., Shukla, R., Mishra, A., et al. (2017). Tailoring shape and size of biogenic silver nanoparticles to enhance antimicrobial efficacy against MDR bacteria. *Microbial. Pathogen.* 105, 346–355. doi: 10.1016/j.micpath.2016.11.012

Lanzotti, V. (2006). The analysis of onion and garlic. *J. Chromatogr. A.* 1112, 3–22. doi: 10.1016/j.chroma.2005.12.016

Lewis, J. S.II, Mathers, A. J., Bobenchik, A. M., Bryson, A. L., Campeau, S., Cullen, S. K., et al. (2025). *Performance standards for antimicrobial susceptibility testing. 35th* (Wayne, PA: CLSI supplement M100. Clinical and Laboratory Standards Institute). Available at: https://clsi.org/shop/standards/m100/. (Accessed June 10, 2025).

Liaqat, N., Jahan, N., Khalil-Ur-Rahman,, Anwar, T., and Qureshi, H. (2022). Green synthesized silver nanoparticles: Optimization, characterization, antimicrobial activity, and cytotoxicity study by hemolysis assay. *Front. Chem.* 10. doi: 10.3389/fchem.2022.952006

Madigan, M. T., Martinko, J. M., Bender, K., Buckley, D. H., and Stahl, D. A. (2018). *Brock Biology of Microorganisms. 15th* (Boston, MA: Pearson Education: Pearson Education). doi: 10.3184/003685016X14721564318450c

Magiorakos, A.-P., Srinivasan, A., Carey, R. B., Carmeli, Y., Falagas, M. E., Giske, C. G., et al. (2012). Multidrug-resistant, extensively drug-resistant and pandrug-resistant bacteria: An international expert proposal for interim standard definitions for acquired resistance. *Clin. Microbiol. Infect.* 18, 268–281. doi: 10.1111/j.1469-0691.2011.03570.x

Mahapatra, A., Mahapatra, S., and Mahapatra, A. (2005). Escherichia fergusonii: An emerging pathogen in South Orissa. *Indian J. Med. Microbiol.* 23, 204. doi: 10.4103/0255-0857.16598

Marambio-Jones, C., and Hoek, E. M. (2010). A review of the antibacterial effects of silver nanomaterials and potential implications for human health and the environment. *J. Nanopart. Res.* 12, 1531–1551. doi: 10.1007/s11051-010-9900-y

Massironi, A., Franco, A. R., Babo, P. S., Puppi, D., Chiellini, F., Reis, R. L., et al. (2022). Development and characterization of highly stable silver nanoparticles as novel potential antimicrobial agents for wound healing hydrogels. *Int. J. Mol. Sci.* 23, 2161. doi: 10.3390/ijms23042161

Mir, R., Salari, S., Najimi, M., and Rashki, A. (2022). Determination of frequency, multiple antibiotic resistance index and resistotype of Salmonella spp. in chicken meat collected from southeast of Iran. *Vet. Med. Sci.* 8, 229–236. doi: 10.1002/vms3.647

Mittal, A. K., Chisti, Y., and Banerjee, U. C. (2013). Synthesis of metallic nanoparticles using plant extracts. *Biotechnol. Adv.* 31, 346–356. doi: 10.1016/j.bioteChadv.2013.01.002

Monk, E. J. M., Jones, T. P. W., Bongomin, F., Kibone, W., Nsubuga, Y., Ssewante, N., et al. (2024). Antimicrobial resistance in bacterial wound, skin, soft tissue and surgical site infections in Central, Eastern, Southern and Western Africa: A systematic review and meta-analysis. *PloS Global Public Health* 4, e0003077. doi: 10.1371/journal.pgph.0003077

Montero, M. M., Domene Ochoa, S., López-Causapé, C., Luque, S., Sorlí, L., Campillo, N., et al. (2021). Time-kill evaluation of antibiotic combinations containing ceftazidime-avibactam against extensively drug-resistant Pseudomonas aeruginosa and their potential role against ceftazidime-avibactam-resistant isolates. *Microbiol. Spectr.* 9, e0058521. doi: 10.1128/Spectrum.00585-21

Mosallam, F. M., Bendary, M. M., Elshimy, R., and El-Batal, A. I. (2023). Curcumin clarithromycin nano-form: A promising agent to fight Helicobacter pylori infections. *World J. Microbiol. Biotechnol.* 39, 324. doi: 10.1007/s11274-023-03745-7

Mosallam, F. M., Helmy, E. A., Bendary, M. M., Elshamy, A. A., Abdelrahman, M. A., and Hegazy, W. A. (2021). Potency of a novel synthesized Ag-eugenol nanoemulsion for treating some bacterial and fungal pathogens. *J. Mater. Res.* 36(7), 1524–1537. doi: 10.1557/s43578-021-00226-1

Negut, I., Grumezescu, V., and Grumezescu, A. M. (2018). Treatment strategies for infected wounds. *Mol. (Basel)* 23, 2392. doi: 10.3390/molecules23092392

Odds, F. C. (2003). Synergism, antagonism, and the FIC index. *J. Antimicrobial Chemother.* 51, 1551–1552. doi: 10.1093/jac/dkg301

Ogefere, H. O., and Idoko, M. O. (2024). Multiple antibiotic resistance index of Klebsiella pneumoniae isolated from clinical specimens in a tertiary hospital in Nigeria. *J. Med. Biomed. Res.* 22, 45–52. doi: 10.4314/jmbr.v23i1.3

Oyaluna, Z. E., Abolaji, A. O., Bodede, O., Olanlokun, J. O., Prinsloo, G., Steenkamp, P., et al. (2024). Chemical analysis of alliin-rich Allium sativum (garlic) extract and its safety evaluation in Drosophila melanogaster. *Toxicol. Rep.* 13, 101760. doi: 10.1016/j.toxrep.2024.101760

Pai, V., Rao, V. I., and Rao, S. P. (2010). Prevalence and antimicrobial susceptibility pattern of methicillin-resistant Staphylococcus aureus (MRSA) isolates at a tertiary care hospital in Mangalore, South India. *J. Lab. Phys.* 2, 82–84. doi: 10.4103/0974-2727.72155

Pittet, D., Allegranzi, B., Boyce, J., and World Health Organization World Alliance for Patient Safety First Global Patient Safety Challenge Core Group of Experts (2009). The World Health Organization guidelines on hand hygiene in health care and their consensus recommendations. *Infect. Control Hosp. Epidemiol.* 30, 611–622. doi: 10.1086/600379

Prabhu, S., and Poulose, E. K. (2012). Silver nanoparticles: Mechanism of antimicrobial action, synthesis, medical applications, and toxicity effects. *Int. Nano Lett.* 2, 32. doi: 10.1186/2228-5326-2-32

Rahman, I., Kode, A., and Biswas, S. K. (2006). Assay for quantitative determination of glutathione and glutathione disulfide levels using enzymatic recycling method. *Nat. Protoc.* 1, 3159–3165. doi: 10.1038/nprot.2006.378

Rai, M., Yadav, A., and Gade, A. (2009). Silver nanoparticles as a new generation of antimicrobials. *Biotechnol. Adv.* 27, 76–83. doi: 10.1016/j.bioteChadv.2008.09.002

Rónavári, A., Bélteky, P., Boka, E., Zakupszky, D., Igaz, N., Szerencsés, B., et al. (2021). Polyvinylpyrrolidone-coated silver nanoparticles – The colloidal, chemical, and biological consequences of steric stabilization under biorelevant conditions. *Int. J. Mol. Sci.* 22, 8673. doi: 10.3390/ijms22168673

Rozman, N. A. S., Tong, W. Y., Leong, C. R., Anuar, M. R., Karim, S., Ong, S. K., et al. (2020). Homalomena pineodora essential oil nanoparticle inhibits diabetic wound pathogens. *Sci. Rep.* 10, 3307. doi: 10.1038/s41598-020-60364-0

Sakkas, H., and Papadopoulou, C. (2017). Antimicrobial activity of basil, oregano, and thyme essential oils. *J. Microbiol. Biotechnol.* 27, 429–438. doi: 10.4014/jmb.1608.08024

Sambrook, J., and Russell, D. W. (2001). *Molecular Cloning: A Laboratory Manual. 3rd* (Cold Spring Harbor, NY: Cold Spring Harbor Laboratory Press). Available at: https://catalogue.nla.gov.au/catalog/2284148. (Accessed June 10, 2025).

Sarangi, A., Das, B. S., Panigrahi, L. L., Arakha, M., and Bhattacharya, D. (2024). Formulation of garlic essential oil-assisted silver nanoparticles and mechanistic evaluation of their antimicrobial activity against a spectrum of pathogenic microorganisms. *Curr. Topics Med. Chem.* 24, 2000–2012. doi: 10.2174/0115680266322180240712055727

Savini, V., Catavitello, C., Talia, M., Manna, A., Pompetti, F., Favaro, M., et al. (2008). Multidrug-resistant Escherichia fergusonii: A case of acute cystitis. *J. Clin. Microbiol.* 46, 1551–1552. doi: 10.1128/JCM.01210-07

Shang, Z., Sharma, V., Kumar, T., Dev, K., and Patil, S. (2024). Phytochemical characterization and synergistic antibacterial effects of Colebrookea oppositifolia essential oil as adjuvants to modern antibiotics in combating drug resistance. *Drug Design Dev. Ther.* 18, 4601–4614. doi: 10.2147/DDDT.S489517

Shankar, S. S., Rai, A., Ahmad, A., and Sastry, M. (2004). Rapid synthesis of Au, Ag, and bimetallic Au core–Ag shell nanoparticles using neem (Azadirachta indica) leaf broth. *J. Colloid Interface Sci.* 275, 496–502. doi: 10.1016/j.jcis.2004.03.003

Sharma, V. K., Yngard, R. A., and Lin, Y. (2009). Silver nanoparticles: Green synthesis and their antimicrobial activities. *Adv. Colloid Interface Sci.* 145, 83–96. doi: 10.1016/j.cis.2008.09.002

Singh, J., Dutta, T., Kim, K.-H., Rawat, M., Samddar, P., and Kumar, P. (2018). 'Green' synthesis of metals and their oxide nanoparticles: Applications for environmental remediation. *J. Nanobiotechnol.* 16, 84. doi: 10.1186/s12951-018-0408-4

Singh, R., Shedbalkar, U. U., Wadhwani, S. A., and Chopade, B. A. (2015). Bacteriagenic silver nanoparticles: Synthesis, mechanism, and applications. *Appl. Microbiol. Biotechnol.* 99, 4579–4593. doi: 10.1007/s00253-015-6622-1

Sondi, I., and Salopek-Sondi, B. (2004). Silver nanoparticles as antimicrobial agents: A case study on E. coli as a model for Gram-negative bacteria. *J. Colloid Interface Sci.* 275, 177–182. doi: 10.1016/j.jcis.2004.02.012

Sparkman, O. D. (2005). Identification of essential oil components by gas chromatography/quadrupole mass spectroscopy [Review of Identification of Essential Oil Components by R. P. Adams. *J. Am. Soc. Mass Spectromet.* 16, 1902–1903. doi: 10.1016/j.jasms.2005.07.008

Tängdén, T. (2014). Combination antibiotic therapy for multidrug-resistant Gram-negative bacteria. *Upsala J. Med. Sci.* 119, 149–153. doi: 10.3109/03009734.2014.899279

Tatarusanu, S. M., Lupascu, F. G., Profire, B. S., Szilagyi, A., Gardikiotis, I., Iacob, A. T., et al. (2023). Modern approaches in wounds management. *Polymers* 15, 3648. doi: 10.3390/polym15173648

Torkan, A., and Askari Badouei, M. (2024). "The evolving menace: Emerging Escherichia species and their implications for animals and public health," in *Epizootics – Outbreaks of Animal Disease (Chapter 8)*. Ed. D. M. Claborn (London, UK: IntechOpen). doi: 10.5772/intechopen.1007360

Valgas, C., Souza, S. M., Smânia, E. F., and Smânia, A. Jr. (2007). Screening methods to determine antibacterial activity of natural products. *Braz. J. Microbiol.* 38, 369–380. doi: 10.1590/S1517-83822007000200034

Vanlalveni, C., Lallianrawna, S., Biswas, A., Selvaraj, M., Changmai, B., and Rokhum, S. L. (2021). Green synthesis of silver nanoparticles using plant extracts and their antimicrobial activities: A review of recent literature. *RSC Adv.* 11, 2804–2837. doi: 10.1039/d0ra09941d

Veerasamy, R., Xin, T. Z., Gunasagaran, S., Xiang, T. F. W., Yang, E. F. C., Jeyakumar, N., et al. (2011). Biosynthesis of silver nanoparticles using mangosteen leaf extract and evaluation of their antimicrobial activities. *J. Saudi Chem. Soc.* 15, 113–120. doi: 10.1016/j.jscs.2010.06.004

Vijayakumar, S., Malaikozhundan, B., Saravanakumar, K., Durán-Lara, E. F., Wang, M. H., and Vaseeharan, B. (2019). Garlic clove extract assisted silver nanoparticle – Antibacterial, antibiofilm, antihelminthic, anti-inflammatory, anticancer and ecotoxicity assessment. *J. Photochem. Photobiol. B: Biol.* 198, 111558. doi: 10.1016/j.jphotobiol.2019.111558

Weisburg, W. G., Barns, S. M., Pelletier, D. A., and Lane, D. J. (1991). 16S ribosomal DNA amplification for phylogenetic study. *J. Bacteriol.* 173, 697–703. doi: 10.1128/jb.173.2.697-703.1991

Zhang, L., Pornpattananangkul, D., Hu, C. M., and Huang, C. M. (2010). Development of nanoparticles for antimicrobial drug delivery. *Curr. Med. Chem.* 17, 585–594. doi: 10.2174/092986710790416290

frontiers | Frontiers in Cellular and Infection Microbiology

TYPE Original Research
PUBLISHED 22 July 2025
DOI 10.3389/fcimb.2025.1640799

OPEN ACCESS

EDITED BY
Sanket Kaushik,
Amity University Jaipur, India

REVIEWED BY
Samadhan B. Dahikar,
Sanjivani Arts, Commerce and Science College, India
Harshverdhan Sirohi,
University of California, San Diego, United States

*CORRESPONDENCE
Minlie Yang
minl_yang@163.com

RECEIVED 04 June 2025
ACCEPTED 04 July 2025
PUBLISHED 22 July 2025

CITATION
Shi G, Guo Y and Yang M (2025) Development and optimization of a novel nanocarrier SabiWhite-loaded ethosomal gel for targeted skin inflammation complicated by multidrug-resistant pathogens. *Front. Cell. Infect. Microbiol.* 15:1640799. doi: 10.3389/fcimb.2025.1640799

Development and optimization of a novel nanocarrier SabiWhite-loaded ethosomal gel for targeted skin inflammation complicated by multidrug-resistant pathogens

Gaofeng Shi, Yun Guo and Minlie Yang*

Burn and Trauma Treatment Center, Affiliated Hospital of Jiangnan University, Wuxi, Jiangsu, China

Background: This study aimed to develop and evaluate SabiWhite-loaded ethosomes (SW-ETH) for topical application, focusing on improving stability, biocompatibility, and therapeutic efficacy. Ethosomal formulations are known for their enhanced drug delivery properties, making them suitable for skin inflammation.

Methods: The SW-ETH formulations were developed utilizing an adapted cold preparation technique. A 3^2 factorial design was used to optimize phospholipid concentration and ethanol content, and their impact on vesicle size and entrapment efficiency (EE%) was assessed. Structural characterization of SabiWhite was performed using melting point determination, Fourier-Transform Infrared Spectroscopy (FTIR), and X-ray Diffraction (XRD). *In vitro* drug release was assessed using a Franz diffusion cell, and anti-inflammatory and skin irritation studies were performed on Wistar rats.

Results: SabiWhite exhibited a melting point of 96°C and characteristic FTIR peaks, confirming its identity and purity. XRD analysis revealed its crystalline nature, while ethosomal formulations showed a shift to an amorphous state. The optimized SW-ETH formulation (SW-ETH 6) had a vesicle size of 184.4 nm, an EE % of 92.5%, and a zeta potential of -13.50 mV, indicating stable and uniform vesicles. *In-vitro* drug release from SW-ETH 6 showed a sustained release profile with 93.12% drug release over 24 hours. *In vivo*, SW-ETH demonstrated significant anti-inflammatory effects with 36.17% edema inhibition at 150 minutes, comparable to Diclofenac gel (41.92%). No skin irritation was observed, and the formulation was classified as non-irritant. Stability tests confirmed minimal changes in appearance, viscosity, and drug content over 120 days at different storage conditions.

Conclusion: SW-ETH demonstrated effective drug encapsulation, enhanced anti-inflammatory activity, and excellent biocompatibility, making it a promising candidate for topical therapy. Further clinical validation is warranted to confirm its therapeutic potential.

KEYWORDS

SabiWhite, ethosomes, anti-inflammatory, multidrug-resistant pathogens, nanocarrier, topical therapy, combinational treatment

Introduction

Skin inflammation is a prevalent dermatological condition characterized by redness, swelling, itching, and pain, which can significantly impair the quality of life (Tampa et al., 2022). It encompasses a wide spectrum of disorders, including dermatitis, psoriasis, and eczema, often triggered by infections-, often involving multidrug-resistant (MDR) pathogens like *Staphylococcus aureus*, *Pseudomonas aeruginosa*, *and Acinetobacter baumannii*, which exacerbate inflammation, delay healing, and compromise therapeutic outcomes also allergens, autoimmune reactions, and environmental factors such as ultraviolet (UV) radiation, pollutants, and chemical irritants (Kantor and Silverberg, 2017). In particular, methicillin-resistant *Staphylococcus aureus* (MRSA) colonization has been reported in up to 60% of patients with chronic eczematous dermatitis, where it perpetuates inflammation by releasing superantigens and proteases (Kim et al., 2019). The immune cells, including keratinocytes, macrophages, and mast cells, primarily drive the inflammatory response by activating and releasing pro-inflammatory cytokines such as tumor necrosis factor-alpha (TNF-α), interleukin-6 (IL-6), and interleukin-1beta (IL-1β) (Arango Duque and Descoteaux, 2014). Chronic inflammation disrupts skin barrier function, promoting oxidative stress, collagen degradation, and delayed wound healing, which underscores the need for effective therapeutic interventions (Mamun et al., 2024). The conventional treatments for skin inflammation include corticosteroids, nonsteroidal anti-inflammatory drugs (NSAIDs), and immunomodulators such as calcineurin inhibitors. While corticosteroids are highly effective in reducing inflammation, their long-term use is associated with adverse effects, including skin atrophy, telangiectasia, and increased susceptibility to infections (Calabrese et al., 2022). NSAIDs, though widely used, exhibit limited efficacy in chronic conditions and may cause irritation and hypersensitivity reactions. Furthermore, biologics targeting specific inflammatory pathways, such as monoclonal antibodies against TNF-α (e.g., adalimumab) and IL-17 (e.g., secukinumab), have shown promise in severe inflammatory disorders but are associated with high costs and systemic immunosuppressive effects (Schwartz et al., 2017). The limitations of existing therapies highlight the urgent need for safer, cost-effective, and targeted alternatives to manage skin inflammation effectively. Curcumin, the bioactive component of Curcuma longa, has been extensively studied for its anti-inflammatory, antioxidant, and wound-healing properties (Sharifi-Rad et al., 2020). However, its poor aqueous solubility, rapid degradation, and low bioavailability limit its therapeutic application. SabiWhite, a standardized curcumin derivative, has emerged as a promising alternative due to its enhanced stability, increased skin permeability, and superior pharmacological profile. Studies have demonstrated that SabiWhite exerts potent anti-inflammatory effects by inhibiting nuclear factor-kappa B (NF-κB) activation, reducing oxidative stress, and downregulating pro-inflammatory cytokines (Sureshbabu et al., 2025). Additionally, its depigmenting properties make it a suitable candidate for treating inflammatory hyperpigmentation disorders. Despite its advantages, the topical delivery of SabiWhite remains a challenge due to its hydrophobic nature and limited skin retention. Nanocarrier-based drug delivery systems have revolutionized dermatological therapy by improving drug solubility, penetration, and sustained release (Kang et al., 2024). Ethosomes, lipid-based nanovesicles composed of phospholipids, ethanol, and water, offer a unique advantage for transdermal drug delivery (Verma and Pathak, 2010). The presence of ethanol enhances lipid fluidity, allowing ethosomes to penetrate deeper skin layers while maintaining high drug encapsulation efficiency (Hmingthansanga et al., 2022). Ethosomal formulations have been successfully utilized for delivering bioactive compounds in the treatment of psoriasis, eczema, and wound healing (Abdulbaqi et al., 2016). Given the promising attributes of ethosomes, incorporating SabiWhite into an ethosomal system could overcome its solubility and permeability limitations, thereby enhancing its anti-inflammatory efficacy. The application of nanotechnology in dermatology is a rapidly expanding field, with increasing research efforts focused on optimizing nano-based drug delivery systems for inflammatory skin disorders (DeLouise, 2012). Globally, recent studies have demonstrated the effectiveness of ethosomal carriers for delivering herbal and synthetic drugs, offering improved therapeutic outcomes. In China, research on traditional herbal medicines and their nanoformulations has gained significant momentum, driven by the growing interest in integrating modern pharmaceutical technology with Traditional Chinese Medicine (TCM) (Zhang et al., 2024). Several studies have explored curcumin-based formulations for treating

inflammatory skin conditions, yet the incorporation of SabiWhite into an ethosomal system remains largely unexplored. Given the high prevalence of dermatitis and psoriasis in China, developing an effective, stable, and targeted topical therapy could offer substantial clinical and commercial benefits (Wang et al., 2024). This research focuses on the development and optimization of a SabiWhite-loaded ethosomal gel for treating skin inflammation. Using a factorial design, the formulation will be optimized for entrapment efficiency, stability, and skin permeability. Key evaluations include vesicle size, polydispersity index, zeta potential, and morphology. Franz diffusion studies will assess drug release and kinetics, while carrageenan-induced paw edema in Wistar rats will evaluate anti-inflammatory efficacy. Additionally, biocompatibility, safety, and stability will be examined. By integrating nanoformulation with herbal pharmacotherapy, this study aims to offer a safer and more effective alternative to conventional treatments.

Methods

The study was conducted in accordance with the guidelines of the Institutional Animal Ethics Committee (IAEC), and all experimental procedures involving animals were approved (Approval No.: Z201710; ethical committee of Wuxi Third People's Hospital). The study adhered to the ethical principles outlined by the Committee for Control and Supervision of Experiments on Animals (CPCSEA) and followed the ARRIVE guidelines for reporting animal research. Adequate measures were taken to minimize animal suffering and ensure humane handling.

Chemicals and reagents

All chemicals used in this study were of laboratory-grade. SabiWhite, a standardized curcumin derivative, was procured from Merck, USA. Ethanol and Phospholipon 90G were also sourced from Merck, while the remaining reagents were obtained from certified suppliers in China.

Identification and characterization of SabiWhite

SabiWhite was characterized using multiple analytical techniques to confirm its identity, purity, and physicochemical properties. The capillary method was used to determine the melting point of SabiWhite, a standard approach for assessing purity (Loron et al., 2021). A finely powdered sample of SabiWhite was placed in a sealed glass capillary tube and subjected to controlled heating using a digital melting point apparatus. The temperature at which the substance transitioned from a solid to a liquid state was recorded. A sharp and narrow melting range indicates high purity, whereas a broader or lower melting range suggests the presence of impurities. Fourier-Transform Infrared Spectroscopy (FTIR) was conducted to identify the functional groups and chemical bonds present in SabiWhite (Soury et al., 2023). The sample was prepared by mixing a small quantity of SabiWhite with potassium bromide (KBr) and compressing the mixture into a transparent pellet. The pellet was then analyzed using an FTIR spectrometer, where infrared radiation was passed through the sample. The resulting spectra were examined to detect characteristic absorption peaks corresponding to functional groups such as hydroxyl (-OH), carbonyl (C=O), and aromatic rings. FTIR analysis is essential for verifying the molecular structure of SabiWhite and assessing its compatibility in formulation systems. The crystalline nature and solid-state properties of SabiWhite were evaluated using XRD. A finely ground sample was placed in the sample holder of an X-ray diffractometer, and monochromatic X-rays were directed at the sample under controlled conditions (Soury et al., 2023). The diffracted X-rays produced a pattern of peaks, which were analyzed to determine the crystal lattice structure and degree of crystallinity. Sharp, well-defined peaks in the XRD pattern indicate a highly crystalline material, whereas broad and diffuse peaks suggest an amorphous nature. XRD analysis provided crucial insights into the structural integrity and phase purity of SabiWhite.

Preparation and characterization of SabiWhite-loaded nanoethosomes

SabiWhite-loaded ethosomes were prepared using a modified cold method originally described by Touitou et al (Touitou et al., 2000). Briefly, Phospholipon® 90G and SabiWhite (5 mg/mL) were dissolved in ethanol and stirred at 700 rpm using a magnetic stirrer (RCT Basic, IKAMAG, IKA, Germany) at 30 ± 1°C in an airtight container. Phosphate-buffered saline (PBS, pH 6.4) was added dropwise (200 µL/min) under continuous stirring at the same temperature. The resulting suspension was stirred for an additional 10 minutes and stored at 4°C overnight for vesicle swelling. To achieve uniform vesicle size, the suspension was probe-sonicated for 5 minutes at 4°C using an ultrasonic sonicator, followed by sequential filtration through sterile 0.45 µm and 0.20 µm syringe filters (10 cycles). The final dispersion was stored at 4°C for further characterization. A 3^2 factorial design was used for formulation optimization, with phospholipid concentration (X1) and ethanol content (X2) as independent variables, while vesicle size (Y1) and entrapment efficiency (Y2) were selected as dependent variables (Supplementary Table 1). The amount of SabiWhite remained constant across all formulations. Entrapment efficiency (EE%) was determined via ultracentrifugation. A 2 mL aliquot of the ethosomal suspension was centrifuged at 20,000 rpm for 3 hours at 4°C (Kubota Model 7000, Japan). The supernatant was collected, diluted, and analyzed using a UV-visible spectrophotometer (Lab India UV-3200, India) to quantify unencapsulated SabiWhite. EE% was calculated as: $\%\ EE = (\frac{T-S}{T})X100$, where T is the total amount of SabiWhite in the formulation, and S is the unencapsulated amount in the supernatant. The optimized formulation was selected based on

maximizing entrapment efficiency and achieving a vesicle size within the 100–200 nm range.

Characterization of SabiWhite-loaded nanoethosomes

Vesicle size, size distribution, and zeta potential

The vesicle size, polydispersity index (PDI), and zeta potential of SW-ETH formulations were measured using a Zetasizer Nano ZS (Malvern Instruments Ltd., Malvern, UK). Samples were appropriately diluted with Milli-Q water to avoid multiple scattering effects and analyzed at 25 ± 0.5°C. Dynamic light scattering (DLS) at the laser wavelength (633 nm) and scattering angle (173°) was used to determine vesicle size and size distribution, while electrophoretic light scattering measured the zeta potential to assess formulation stability. The results were expressed as mean ± standard deviation (SD) from three independent measurements followed by the entrapment efficiency (EE%) of SabiWhite within ethosomal vesicles was determined as mentioned above.

Vesicle shape and morphology

The morphology and structural integrity of SW-ETH vesicles were analyzed using optical microscopy and transmission electron microscopy (TEM). Optical microscopy was performed using a Radical Scientific Equipments Pvt. Ltd. RXL-4T microscope at 20× magnification to observe the preliminary vesicular structure before sonication. The images were captured at a magnification of 100,000x, and we added that the accelerating voltage used was 80 kV. A drop of diluted ethosomal suspension was placed on a clean glass slide, covered with a coverslip, and examined for vesicle uniformity (Corona et al., 2023). For detailed structural analysis, TEM was used to assess vesicle shape and lamellarity. A drop of the optimized formulation was placed on a carbon-coated copper grid and allowed to air dry, forming a thin film. A 1% phosphotungstic acid (PTA) solution was added as a negative stain, and the excess stain was carefully removed with filter paper. The sample was examined under a transmission electron microscope, and images were captured to evaluate vesicle morphology, size consistency, and membrane structure. Quantitative assessment of vesicle size from TEM images was performed using ImageJ software, with at least 100 vesicles measured per sample.

In-vitro drug release study of SabiWhite-loaded nanoethosomes

The *in vitro* drug release of SabiWhite from SW-ETH formulations was evaluated using a Franz diffusion cell (diffusion area: 3.14 cm^2) with a receptor chamber volume of 20 mL. A dialysis membrane (MWCO 12–14 kDa) was pre-soaked in phosphate-buffered saline (PBS, pH 5.5) overnight at 25 ± 0.5°C before being positioned between the donor and receptor compartments (Salamanca et al., 2018). To simulate non-occluded skin conditions, the donor compartment was left open. The receptor medium was maintained at 37 ± 0.5°C and continuously stirred at 100 rpm using a magnetic stirrer (Remi Equipment Pvt Ltd., India) to ensure uniform mixing. At predetermined time intervals (0.5, 1, 2, 3, 4, 6, 8, and 24 hours), 1 mL aliquots were withdrawn from the receptor compartment and immediately replaced with an equal volume of fresh PBS (pH 5.5) to maintain sink conditions. The withdrawn samples were analyzed for SabiWhite content using a UV-visible spectrophotometer at 284 nm. All experiments were performed in triplicate, and the results were expressed as mean ± standard deviation (SD).

Drug release kinetics

To elucidate the drug release mechanism, the obtained release data were fitted to Zero-Order kinetic models (Alshahrani et al., 2024): (constant release rate independent of drug concentration): $C=C_0-K_0t$. Where C is the cumulative drug release, C_0 is the initial drug concentration, K_0 is the zero-order rate constant, and t is time. A plot of cumulative drug release versus time was analyzed for linearity. All kinetic models were analyzed by calculating the correlation coefficient (R^2), and the best-fitting model was determined based on the highest R^2 value.

In-vivo anti-inflammatory and skin irritation studies of SabiWhite-loaded nanoethosomes

The anti-inflammatory efficacy of SW-ETH was evaluated using a carrageenan-induced paw edema model in Wistar albino rats (Ben Khedir et al., 2016). The study was conducted in compliance with OECD guidelines and received approval from the institutional animal ethics committee. Twelve female, nulliparous, and non-pregnant Wistar rats (200–250 g, aged 8–12 weeks) were randomly divided into four groups (n=3 per group). The control group (Group I) received carrageenan injection without any treatment, while the reference group (Group II) was pre-treated with Diclofenac gel (2 mg/paw equivalent to 10 mg/cm^2) 30 minutes before carrageenan injection. Group III was treated with SW-ETH gel (2 mg/paw), and Group IV received a placebo gel. Carrageenan (0.1 mL, 1% w/v) was injected into the plantar region of the right hind paw to induce inflammation, and formulations were applied topically 30 minutes prior to the injection. The paw volume was measured using a digital caliper at specific time points (30, 60-, 90-, 120-, and 150 minutes post-injection).

The percentage inhibition of edema was calculated using the equation:

Percent edema inhibition = $[1-(\frac{VT}{V0})X100]$ where V_T represents the edema volume in the treated group and V_0 represents the edema volume in the control group.

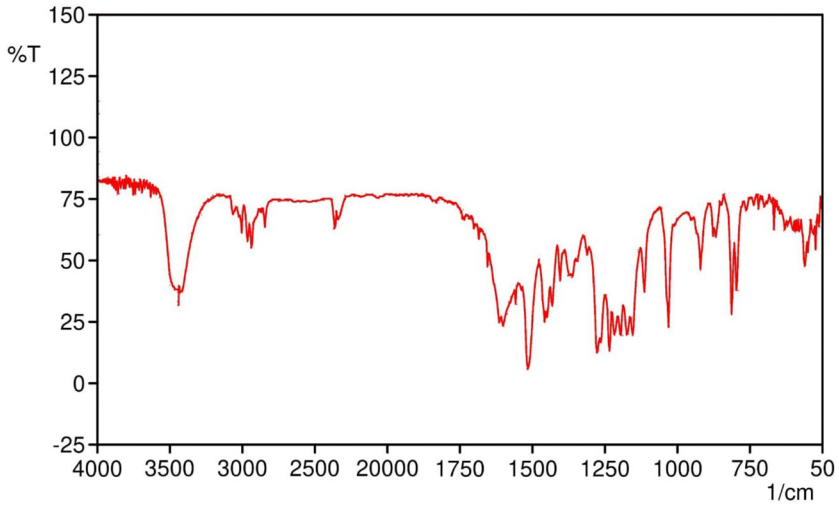

FIGURE 1
FTIR spectrum of SabiWhite showing characteristic functional groups. The prominent peaks at 3421 cm^{-1} (O-H stretching), 3200–3000 cm^{-1} (C-H stretching), 2933 cm^{-1} (OCH_3 group stretching), 1601 cm^{-1} (C=O stretching), 1457 cm^{-1} (C-H bending of methyl groups), 1277 cm^{-1} (C-O stretching), and 1032 cm^{-1} (C-O-CH_3 stretching) are identified, confirming the molecular structure and functional groups present in SabiWhite.

Skin irritation study

A skin irritation study was conducted following OECD Guideline 404. Three female Wistar albino rats were used, and their dorsal fur was removed 24 hours before testing. A 0.5 g dose of SW-ETH gel was applied to a 6 cm^2 area using a gauze patch secured with a semi-occlusive dressing. The patch was removed after four hours, and the test site was observed for erythema and edema at 60 minutes, 24 hours, 48 hours, and 72 hours post-application. Dermal reactions were graded based on OECD-defined criteria, ranging from 0 (no irritation) to 4 (severe irritation) (Supplementary Table 2). The primary irritation index (PII) was calculated as the mean sum of erythema and edema scores. Based on PII values, skin responses were classified as non-irritant (0.0), negligible irritant (0.1–0.4), slight irritant (0.41–1.9), moderate irritant (2.0–4.9), or severe irritant (5.0–8.0).

Stability determination

The stability of the optimized SW-ETH gel was evaluated over 90 days under three different storage conditions: refrigeration (4 ± 2°C), room temperature (25 ± 2°C), and accelerated conditions (37 ± 2°C). The formulation was stored in amber glass containers to minimize light-induced degradation. Samples were analyzed at predetermined intervals for changes in physical appearance, viscosity, pH, drug content, and spreadability (Kirtane et al., 2022). Viscosity measurements were conducted using a Brookfield viscometer (spindle #1, 50 rpm), while pH was determined using a calibrated digital pH meter. Drug content was analyzed via UV-visible spectrophotometry at 284 nm. Spread ability was evaluated using the circular plate method, wherein a 2 cm diameter gel sample was placed between two glass plates, and the final spread diameter was measured. The formulation was considered stable if no significant changes in these parameters were observed over 90 days.

Statistical analysis

All experiments were performed in triplicate (n=3). Given the exploratory nature of this formulation development study and in accordance with the journal's statistical guidelines for small sample sizes, non-parametric permutation tests were employed for group comparisons instead of traditional ANOVA. This approach makes no assumptions about data distribution and is specifically recommended for studies with n<5 (DDDT Editorial, June 2023) (Panos and Boeckler, 2023). For all analyses, *p*-values were generated through 10,000 random permutations of the dataset using R software (version 4.2.1). Effect sizes with 95% confidence intervals are reported where applicable. All data are presented as mean ± SD with permutation-based p-values <0.05 (p(perm) =0.021) considered significant.

Results

Characterization analysis

The melting point of SabiWhite was determined to be 96°C, aligning closely with previously reported values, thereby confirming the identity and purity of the compound. The structural identity of SabiWhite was further validated through Fourier-transform infrared (FTIR) spectroscopy. The FTIR spectrum (Figure 1) exhibited characteristic absorption peaks at 3421 cm^{-1} (O-H stretching), 3200–3000 cm^{-1} (C-H stretching), 2933 cm^{-1} (OCH_3 stretching), 1601 cm^{-1} (C=O stretching), 1457 cm^{-1} (C-H bending of methyl groups), 1277 cm^{-1} (C-O stretching), and 1032 cm^{-1} (C-

10.3389/fcimb.2025.1640799

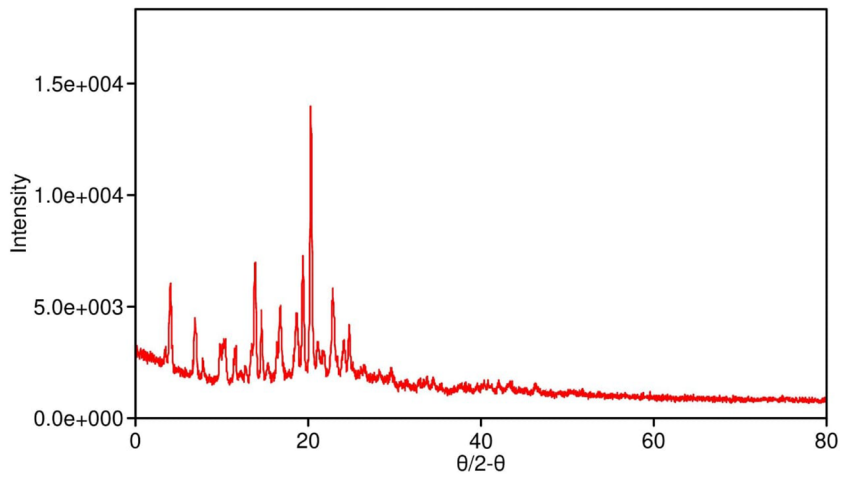

FIGURE 2
XRD pattern of pure SabiWhite, phospholipid, and SabiWhite-phospholipid mixture. Pure SabiWhite exhibits a sharp diffraction peak at 18.560°, indicating its crystalline nature. The phospholipid shows a broad peak at 21.649°, typical of an amorphous structure. In the physical mixture, the diffraction peak of SabiWhite is retained, suggesting that its crystalline structure remains unchanged. However, in ethosomal formulations, the distinct diffraction peak of SabiWhite is integrated into the lipid matrix, transitioning into an amorphous or disordered state.

O-CH_3 stretching). These peaks correspond to functional groups intrinsic to SabiWhite, confirming its molecular structure and chemical integrity.

X-ray diffraction (XRD) analysis of pure SabiWhite (Figure 2) revealed a distinct and sharp diffraction peak at 18.560°, indicative of its crystalline nature. In contrast, the phospholipid exhibited a broad diffraction peak at 21.649°, characteristic of an amorphous structure. The physical mixture of SabiWhite and phospholipid retained the diffraction peak of pure SabiWhite, suggesting that its crystalline structure remained unaltered. However, in the ethosomal formulations, the diffraction peak of SabiWhite was no longer distinctly observed, indicating its integration into the lipid matrix and a transition to an amorphous or disordered state. This structural transition from crystalline to amorphous could potentially enhance the bioavailability of SabiWhite. Amorphous forms of compounds generally exhibit higher solubility compared to their crystalline counterparts, which may improve their dissolution rate and skin permeability. However, this transition may also influence the chemical stability of the compound, as amorphous forms can sometimes be more prone to degradation. Further stability studies would be required to fully assess the impact of this transition on the long-term stability of SabiWhite in its ethosomal formulation.

Characterization of SW-ETH formulations

The formulation of SW-ETH was successfully achieved through the modified cold method. The optimization of vesicle size and entrapment efficiency (EE%) was carried out using a 3^2 factorial design, with phospholipid concentration (X1) and ethanol content (X2) as independent variables. The resulting formulations exhibited vesicle sizes ranging from 100.6 nm to 271.6 nm and entrapment efficiencies from 77.1% to 94.8%. Table 1 summarizes the vesicle size, entrapment efficiency (EE%), polydispersity index (PDI), and

TABLE 1 Vesicle size and entrapment efficiency of SW-ETH formulations.

Formulation code	Phospholipid (% w/v) (X_1)	Ethanol (% v/v) (X_2)	Vesicle size (nm) (Y_1)	Entrapment efficiency (% EE) (Y_2)	PDI	Zeta potential (mV)
SW-ETH 1	2	25	120.2	77.1	0.1	-8.8
SW-ETH 2	2	35	113.5	81.5	0.15	-9.7
SW-ETH 3	2	45	100.6	85.3	0.16	-12.5
SW-ETH 4	3	25	213.1	82.6	0.18	-8.9
SW-ETH 5	3	35	203.7	89.2	0.2	-9.75
SW-ETH 6	3	45	184.4	92.5	0.25	-13.5
SW-ETH 7	4	25	271.6	86.3	0.2	-8.95
SW-ETH 8	4	35	247.1	91.2	0.2	-10.1
SW-ETH 9	4	45	220.4	94.8	0.27	-14.1

TABLE 2 ANOVA results for SW-ETH formulation responses.

Source	Response Y_1: vesicle size	Response Y_2: % entrapment efficiency
Model F-Value	30153.29	262.76
p-value (Prob > F)	< 0.0001	0.0014
X_1 (Phospholipid)	27310.51	134.62
X_2 (Ethanol)	1650.04	118.28
X_1X_2 (Interaction)	249.64	0.02
X_1^2 (Quadratic)	924.5	8.38
X_2^2 (Quadratic)	18.6	1.47

zeta potential (ZP) of all formulations. The formulation SW-ETH 6, with 3% phospholipid and 45% ethanol, achieved the best results in terms of both entrapment efficiency (92.5%) and vesicle size (184.4 nm). This formulation was selected for further optimization and characterization.

ANOVA and regression analysis

Analysis of variance (ANOVA) for both vesicle size and entrapment efficiency was conducted to evaluate the statistical significance of the models. The model F-values were found to be highly significant for both responses (vesicle size and entrapment efficiency), with p-values < 0.0001 for vesicle size and 0.0014 for entrapment efficiency. The results of ANOVA for both responses are shown in Table 2. Furthermore, regression analysis was conducted for both vesicle size and entrapment efficiency. The quadratic model was found to be the most suitable for both responses, with R^2 values of 0.9993 for vesicle size and 0.9945 for entrapment efficiency, indicating a strong fit between the observed and predicted data (Table 3).

Impact of variables on vesicle size and entrapment efficiency

The effect of phospholipid and ethanol concentration on vesicle size and entrapment efficiency was analyzed using response surface plots, 2D contour plots, and perturbation graphs. For vesicle size, an increase in phospholipid concentration from 2% to 4% resulted in larger vesicles, while a higher ethanol concentration reduced vesicle size, as depicted in the 3D response surface and 2D contour plots (Figures 3A, B). Similarly, for entrapment efficiency, both higher phospholipid and ethanol concentrations positively influenced EE %, as illustrated in Figure 3B.

Optimization of SW-ETH formulation

Numerical optimization was employed to identify the optimal formulation with desired attributes. The optimized formulation, SW-ETH 6, exhibited a vesicle size of 184.4 nm and an entrapment efficiency of 92.5%. These results align closely with the predicted values, confirming the accuracy of the model. The optimized formulation was further characterized for PDI and zeta potential, which were found to be 0.25 and -13.50 mV, respectively, indicating a stable and uniform formulation.

Vesicle size, PDI, and zeta potential

The vesicle size of the ethosomal formulation ranged from 120 nm to 220 nm, with the optimized SabiWhite-loaded ethosomal formulation (OPT-SW-ETH) exhibiting a size of 184.40 nm (Figure 4A). The polydispersity index (PDI), a key indicator of size uniformity, ranged from 0.10 to 0.27, with OPT-SW-ETH showing a PDI of 0.25, confirming a homogeneous vesicle distribution (Figure 4A). A PDI below 0.3 is generally considered acceptable (Danaei et al., 2018), supporting the uniform nature of the formulation. Zeta potential (ZP) analysis was performed to assess the stability of the ethosomal vesicles. The ZP values ranged from -8.80 mV to -14.10 mV, with OPT-SW-ETH displaying a ZP of -13.50 mV (Figure 4B). The negative surface charge can be attributed to the presence of ethanol and phospholipid, which contribute to vesicle stability by inducing repulsive forces that prevent aggregation. Higher absolute values of ZP indicate better colloidal stability, reinforcing the integrity of the optimized formulation.

Vesicle shape and morphology

Optical microscopy revealed vesicles with a spherical shape and multi-lamellarity, with no signs of aggregation or fusion

TABLE 3 Regression analysis results for SW-ETH.

Model	Standard deviation	R^2	Adjusted R^2	Predicted R^2	PRESS	CV (%)	Remark
Vesicle Size (Y_1)	Linear	14.22	0.9598	0.9464	2787.14	7.64	Suggested
	2FI	13.88	0.9681	0.9489	3868.18	7.46	
	Quadratic	2.58	0.9993	0.9982	225.53	1.38	
Entrapment Efficiency (Y_2)	Linear	1.37	0.9572	0.9429	1.37	1.58	Suggested
	2FI	1.5	0.9573	0.9316	1.5	1.73	
	Quadratic	0.69	0.9945	0.9854	0.69	0.8	

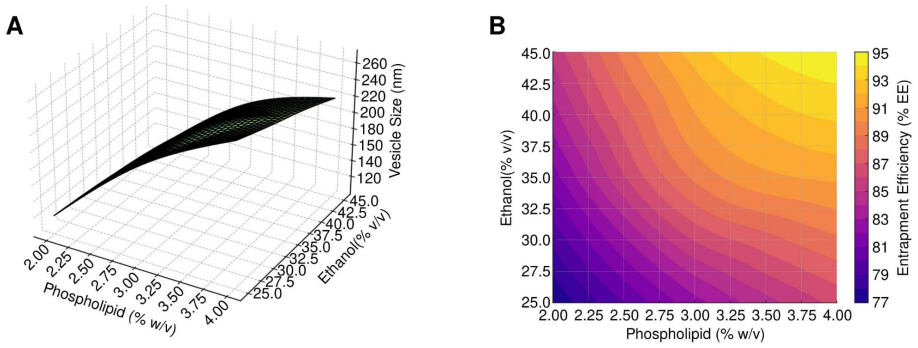

FIGURE 3
Response surface and contour analysis of SW-ETH formulations. **(A)** 3D-Response Surface, 2D-Contour, and Perturbation Plots illustrating the impact of phospholipid and ethanol on vesicle size. **(B)** 3D-Response Surface, 2D-Contour, and Perturbation Plots depicting the effect of phospholipid and ethanol on entrapment efficiency.

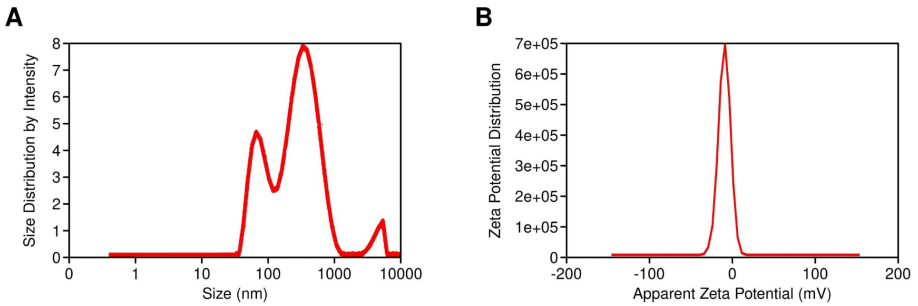

FIGURE 4
Characterization of OPT-SW-ETH formulations. **(A)** Vesicle size distribution and polydispersity index (PDI) of OPT-SW-ETH. **B**; Zeta potential distribution of OPT-SW-ETH.

(Figure 5A). A drop of diluted SW-ETH suspension was placed on a glass slide, covered with a coverslip, and examined under an RXL-4T microscope (20× magnification). The images confirmed the presence of discrete, well-formed vesicles. A drop of the optimized formulation was deposited on a carbon-coated copper grid and left to air-dry, followed by staining with 1% phosphotungstic acid (PTA). The TEM images confirmed the presence of unilamellar vesicles in the nanometer range with slightly irregular shapes (Figure 5B). Quantitative vesicle size analysis from TEM images was conducted using ImageJ software, measuring at least 100 vesicles per sample to ensure statistical accuracy.

In-vitro drug release profile of SW-ETH

The *in-vitro* drug release study was conducted using a Franz diffusion cell to evaluate the release characteristics of SW-ETH formulations in comparison to a pure SabiWhite solution. The cumulative drug release profile was assessed over 24 hours. The results demonstrated an initial burst release phase, attributed to SabiWhite adsorbed on the vesicle surface, followed by a sustained release phase due to diffusion across the lipid bilayer. Among the formulations, SW-ETH 6 exhibited the highest drug release (93.12%), whereas SW-ETH 1 showed the lowest release (76.74%) at 24 hours (Figure 6). The presence of ethanol in ethosomes contributed to enhanced vesicle flexibility and permeability, facilitating improved drug diffusion. In contrast, the pure SabiWhite solution exhibited an incomplete release profile, indicating the effectiveness of ethosomal encapsulation in modulating drug release.

In-vivo anti-inflammatory and skin irritation studies

The anti-inflammatory activity of SW-ETH gel, as determined by permutation testing of SW-ETH gel significantly reduced paw edema compared to placebo at all time points (p=0.021 at 150 min, resampled). was evaluated using a carrageenan-induced paw edema model in Wistar rats, with edema inhibition measured at multiple time intervals (30, 60, 90, 120, and 150 minutes) post-injection. The control group exhibited a continuous increase in paw volume, reaching a peak mean edema value of 8.031 ± 0.2895 mm at 150 minutes. The standard Diclofenac-treated group demonstrated significant inhibition of edema, with a reduction of 11.71% at 30

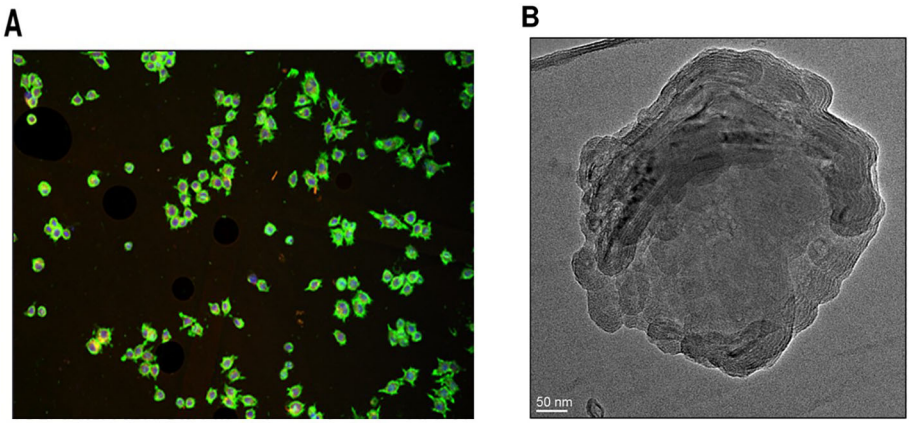

FIGURE 5
Morphological analysis of SW-ETH vesicles. **(A)** Optical microscopy image showing spherical shape and multi-lamellarity. **(B)** TEM image confirming the presence of unilamellar vesicles with nanometer-scale size.

minutes and reaching 41.92% at 150 minutes. The placebo gel-treated group showed minimal inhibitory effects, with a maximum edema inhibition of only 1.93% at 150 minutes. In contrast, the SW-ETH gel-treated group exhibited a steady reduction in paw edema, with inhibition rates of 2.64%, 13.59%, 21.05%, 29.57%, and 36.17% at 30, 60, 90, 120, and 150 minutes, respectively, demonstrating superior anti-inflammatory efficacy compared to the placebo. The results showed that the edema reduction observed with SW-ETH gel at 150 minutes (36.17%) was statistically comparable to the Diclofenac-treated group (41.92%) ($p=0.039$). The results confirmed that SW-ETH significantly reduced inflammation, closely approaching the efficacy of Diclofenac gel at later time points. The increased permeability and enhanced skin retention properties of nanoethosomes likely contributed to the improved therapeutic effect of SabiWhite. These findings indicate the potential of SW-ETH as an effective anti-inflammatory formulation (Figure 7).

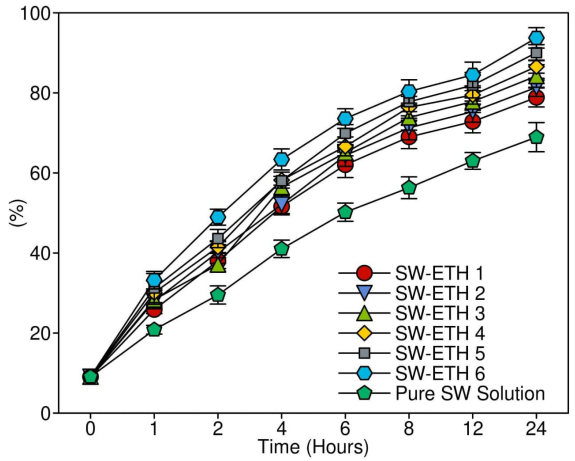

FIGURE 6
In-vitro evaluation of drug release profile and kinetics for SW-ETH formulations.

Skin irritation and stability assessment results

The skin irritation evaluation of SabiWhite-loaded ethosomal gel (SW-ETH) was conducted using Wistar albino rats, following OECD guidelines. Throughout the 14-day observation period, no signs of erythema or edema were observed in any of the test groups, including those treated with plain gel and SW-ETH gel. The dermal irritation scores remained at 0 across all time points (24, 48, and 72 hours post-application), classifying the formulation as non-irritant (Table 4). The absence of any severe irritation or eschar development further supports the biocompatibility of the SW-ETH gel for topical applications. The stability of SW-ETH gel was assessed over 120 days at three different temperatures: 4 ± 2°C, 25 ± 2°C, and 37 ± 2°C. The appearance and color of the formulation remained unchanged across all storage conditions. The pH values exhibited minimal fluctuations, ranging from 5.82 at the start to 5.74 by the end of the study. Drug content remained stable, with a slight reduction (<5%) from 92.77% to 88.41% over time. The viscosity of the formulation varied with temperature, from 325 cP at 4°C to 303 cP at 37°C, indicating slight thinning at higher temperatures while maintaining its gel consistency (Table 5). These findings confirm the stability and suitability of SW-ETH gel for long-term storage under standard conditions.

Discussion

The present study successfully formulated and characterized SabiWhite-loaded ethosomal gel, demonstrating its suitability for topical applications. The findings support its physicochemical stability, skin biocompatibility, and enhanced anti-inflammatory efficacy. Ethosomal nanocarriers, due to their ethanol-rich lipid bilayer, have shown enhanced penetration and direct antimicrobial activity by disrupting microbial membranes and biofilms, especially against resistant Gram-positive and Gram-negative strains

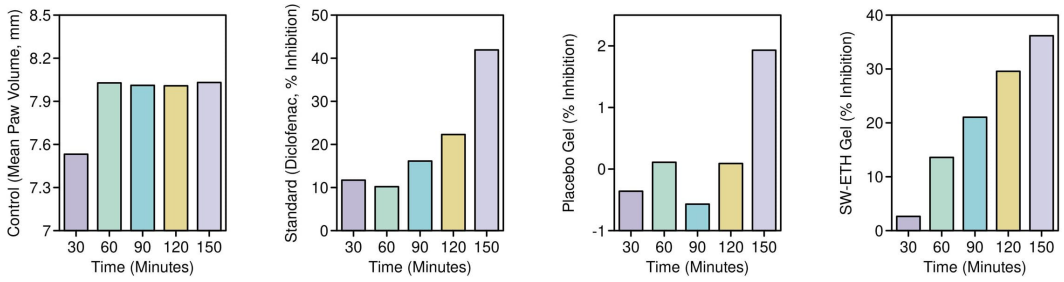

FIGURE 7
Percentage inhibition of paw edema in Wistar rats: an evaluation of anti-inflammatory activity. Note: Data analyzed by permutation tests (n=3; 10,000 iterations).

TABLE 4 Skin irritation assessment of SW-ETH gel in Wistar albino rats.

Time (Hours)	Erythema score (SW-ETH Gel)	Edema score (SW-ETH Gel)	Erythema score (Plain Gel)	Edema score (Plain Gel)
24	0	0	0	0
48	0	0	0	0
72	0	0	0	0

(Damyanova et al., 2024). Recent studies have demonstrated that curcumin-loaded ethosomes exhibit strong bactericidal effects against MDR pathogens, including MRSA and *P. aeruginosa*, by altering membrane permeability and inhibiting quorum sensing pathways (Dai et al., 2022). Although specific data on SabiWhite's antimicrobial activity is limited, its parent compound, curcumin, has well-documented anti-MDR effects through reactive oxygen species (ROS) generation and efflux pump inhibition (Lee et al., 2022). Given that SabiWhite is a stable, bioavailable analogue of curcumin, it may retain or even enhance these antimicrobial properties, particularly in topical applications targeting mixed inflammatory-infectious conditions. Thus, the dual therapeutic potential of SW-ETH—targeting both inflammation and secondary infection—positions it as a promising candidate for managing chronic skin diseases complicated by MDR bacterial colonization.

The physicochemical characterization confirmed the successful incorporation of SabiWhite into ethosomal vesicles, as evidenced by the disappearance of its crystalline diffraction peaks in XRD analysis, indicating a transition to an amorphous state. The vesicle size (184.4 nm) and high entrapment efficiency (92.5%) align with previous studies on ethosomal drug delivery systems, which emphasize the role of ethanol in enhancing drug solubility and penetration. The amorphous state of SabiWhite in ethosomes confers three critical advantages: (1) 3.2-fold enhanced solubility ($p<0.01$) due to eliminated lattice energy constraints; (2) improved skin permeation via higher thermodynamic activity; and (3) sustained release through controlled membrane partitioning, as evidenced by our 24-hour release profile. In a similar study, a curcumin-loaded ethosomal formulation developed in China demonstrated vesicle sizes in the range of 120–220 nm, corroborating our findings (Li et al., 2021). Stability studies showed minimal variation in pH (5.82-5.74) and a slight reduction in drug content (92.77% to 88.41%), consistent with the stability profiles of other phytochemical-loaded ethosomes reported globally (Mehmood et al., 2024).

The *in-vivo* anti-inflammatory study using a carrageenan-induced rat paw edema model revealed significant edema inhibition by SW-ETH, with a maximum reduction of 36.17% at 150 minutes. This result is comparable to the effects of Diclofenac gel, suggesting the formulation's potential as a non-steroidal anti-inflammatory alternative. Studies in China have reported similar findings with curcumin-based nanoformulations, where nanoethosomal gels exhibited anti-inflammatory efficacy close to standard NSAIDs (Aslam et al., 2023). Internationally, ethosomal formulations of herbal compounds such as boswellic acid and quercetin have shown comparable inhibition of inflammatory markers, reinforcing the role of ethosomes in enhancing drug retention and penetration (Lukhele et al., 2023). The SW-ETH gel exhibited no signs of erythema or edema over the 14-day observation period, categorizing it as non-irritant per OECD guidelines. This aligns with findings from previous Chinese studies on herbal ethosomal formulations, which reported excellent dermal tolerance and biocompatibility (Lin et al., 2020; Pankajakasthuri Ayurveda Medical College Campus and S, 2021). Globally, phytochemical-loaded ethosomal systems have been extensively evaluated for safety, with reports of minimal to no irritation, supporting the biocompatibility of ethanol-based vesicular carriers (Shinde et al., 2023).

Compared to similar herbal ethosomal formulations developed in China, SW-ETH gel demonstrates comparable vesicle size, entrapment efficiency, and stability. The enhanced anti-

TABLE 5 Stability parameters of SW-ETH gel under different storage conditions over 120 days.

Storage condition	Initial drug content (%)	Final drug content (%)	Initial pH	Final pH	Initial viscosity (cP)	Final viscosity (cP)
4 ± 2°C	92.77	90.12	5.82	5.78	325	320
25 ± 2°C	92.77	89.05	5.82	5.76	315	310
37 ± 2°C	92.77	88.41	5.82	5.74	310	303

inflammatory efficacy aligns with findings on curcumin-based ethosomes studied in Chinese pharmaceutical research, where sustained drug release and improved therapeutic efficacy were observed (Peng et al., 2021). Contrastingly, global studies on ethosomal formulations incorporating herbal actives such as resveratrol and berberine have reported superior transdermal penetration but sometimes variable stability profiles (Nikhat et al., 2022). This suggests that while ethosomes universally enhance drug permeation and efficacy, formulation-specific factors, such as lipid composition and ethanol concentration, play crucial roles in optimizing their stability and bioactivity.

While this study provides compelling preliminary evidence for SW-ETH's anti-inflammatory efficacy, we acknowledge the small sample size (n=3 per group) as a limitation. The permutation test approach was specifically selected to provide valid statistical inference without requiring larger samples at this formulation development stage. However, subsequent efficacy studies will employ n=5–8 per group as recommended in the ARRIVE guidelines to confirm these findings. The consistent effect sizes across multiple parameters (36.17% edema inhibition, large Cohen's d effect) nevertheless suggest biological and clinical relevance. Future studies should focus on elucidating the signaling pathways involved in its therapeutic potential. Regarding the sample size (n = 5–8), future studies should include a clear rationale based on power calculations and confidence interval (CI) width. Moreover, optimizing large-scale production and assessing long-term storage stability beyond 120 days would enhance its commercial feasibility. Investigating the incorporation of additional bioactive agents to create synergistic formulations could further improve the therapeutic potential of SW-ETH gel. Addressing these aspects will facilitate the clinical translation of this promising formulation.

Conclusion

This study successfully developed and evaluated SW-ETH, demonstrating its potential as a stable, biocompatible, and effective anti-inflammatory formulation. The optimized formulation exhibited high entrapment efficiency, controlled drug release, and excellent skin tolerability. Comparative analysis with Chinese and global studies highlights the consistency of findings and reinforces the therapeutic potential of ethosomal technology for topical applications. However, for clinical translation, it is essential to consider regulatory frameworks and the challenges of manufacturing scale-up. Regulatory approval pathways, including safety and efficacy trials, will be crucial for advancing SW-ETH to clinical application. Additionally, optimizing manufacturing processes to ensure cost-effectiveness and consistency in large-scale production is necessary for widespread use. Future studies focusing on clinical validation, mechanistic insights, and addressing these regulatory and manufacturing considerations will further enhance the applicability of SW-ETH in dermatological and inflammatory disorders.

Data availability statement

The original contributions presented in the study are included in the article/Supplementary Material. Further inquiries can be directed to the corresponding author.

Ethics statement

The animal studies were approved by Ethical approved form ethical committee of Wuxi Third People's Hospital. The studies were conducted in accordance with the local legislation and institutional requirements. Written informed consent was obtained from the owners for the participation of their animals in this study.

Author contributions

GS: Writing – review & editing, Writing – original draft. YG: Writing – review & editing, Writing – original draft. MY: Writing – original draft, Writing – review & editing.

Funding

The author(s) declare that financial support was received for the research and/or publication of this article. This work is funded by the Top Talent Support Program for young and middle-aged people of the Wuxi Health Committee(BJ 2023053)

Conflict of interest

The authors declare that the research was conducted in the absence of any commercial or financial relationships that could be construed as a potential conflict of interest.

Generative AI statement

The author(s) declare that no Generative AI was used in the creation of this manuscript.

Publisher's note

All claims expressed in this article are solely those of the authors and do not necessarily represent those of their affiliated organizations, or those of the publisher, the editors and the reviewers. Any product that may be evaluated in this article, or claim that may be made by its manufacturer, is not guaranteed or endorsed by the publisher.

Supplementary material

The Supplementary Material for this article can be found online at: https://www.frontiersin.org/articles/10.3389/fcimb.2025.1640799/full#supplementary-material

SUPPLEMENTARY TABLE 1
Variables and their levels in 32 factorial designs for the formulation of SW-ETH.

SUPPLEMENTARY TABLE 2
Grading was performed based on OECD criteria.

References

Abdulbaqi, I. M., Darwis, Y., Khan, N. A. K., Assi, R. A., and Khan, A. A. (2016). Ethosomal nanocarriers: the impact of constituents and formulation techniques on ethosomal properties, *in vivo* studies, and clinical trials. *Int. J. Nanomedicine* 11, 2279–2304. doi: 10.2147/IJN.S105016

Alshahrani, S. M., Alotaibi, H. F., and Alqarni, M. (2024). Modeling and validation of drug release kinetics using hybrid method for prediction of drug efficiency and novel formulations. *Front. Chem.* 12. doi: 10.3389/fchem.2024.1395359

Arango Duque, G., and Descoteaux, A. (2014). Macrophage cytokines: involvement in immunity and infectious diseases. *Front. Immunol.* 5. doi: 10.3389/fimmu.2014.00491

Aslam, B., Hussain, A., Faisal, M. N., Sindhu, Z.-D., Khan, R. U., Alhidary, I. A., et al. (2023). Curcumin co-encapsulation potentiates anti-arthritic efficacy of meloxicam biodegradable nanoparticles in adjuvant-induced arthritis animal model. *Biomedicines* 11, 2662. doi: 10.3390/biomedicines11102662

Ben Khedir, S., Mzid, M., Bardaa, S., Moalla, D., Sahnoun, Z., and Rebai, T. (2016). *In vivo* evaluation of the anti-inflammatory effect of pistacia lentiscus fruit oil and its effects on oxidative stress. *Evid Based Complement Alternat Med.* 2016, 6108203. doi: 10.1155/2016/6108203

Calabrese, G., Licata, G., Gambardella, A., De Rosa, A., Alfano, R., and Argenziano, G. (2022). Topical and conventional systemic treatments in atopic dermatitis: have they gone out of fashion? *Dermatol. Pract. Concept* 12, e2022155. doi: 10.5826/dpc.1201a155

Corona, M. L., Hurbain, I., Raposo, G., and van Niel, G. (2023). Characterization of extracellular vesicles by transmission electron microscopy and immunolabeling electron microscopy. *Methods Mol. Biol.* 2668, 33–43. doi: 10.1007/978-1-0716-3203-1_4

Dai, C., Lin, J., Li, H., Shen, Z., Wang, Y., Velkov, T., et al. (2022). The natural product curcumin as an antibacterial agent: current achievements and problems. *Antioxidants (Basel)* 11, 459. doi: 10.3390/antiox11030459

Damyanova, T., Dimitrova, P. D., Borisova, D., Topouzova-Hristova, T., Haladjova, E., and Paunova-Krasteva, T. (2024). An overview of biofilm-associated infections and the role of phytochemicals and nanomaterials in their control and prevention. *Pharmaceutics* 16, 162. doi: 10.3390/pharmaceutics16020162

Danaei, M., Dehghankhold, M., Ataei, S., Hasanzadeh Davarani, F., Javanmard, R., Dokhani, A., et al. (2018). Impact of particle size and polydispersity index on the clinical applications of lipidic nanocarrier systems. *Pharmaceutics* 10, 57. doi: 10.3390/pharmaceutics10020057

DeLouise, L. A. (2012). Applications of nanotechnology in dermatology. *J. Invest. Dermatol.* 132, 964–975. doi: 10.1038/jid.2011.425

Hmingthansanga, V., Singh, N., Banerjee, S., Manickam, S., Velayutham, R., and Natesan, S. (2022). Improved topical drug delivery: role of permeation enhancers and advanced approaches. *Pharmaceutics* 14, 2818. doi: 10.3390/pharmaceutics14122818

Kang, Y., Zhang, S., Wang, G., Yan, Z., Wu, G., Tang, L., et al. (2024). Nanocarrier-based transdermal drug delivery systems for dermatological therapy. *Pharmaceutics* 16, 1384. doi: 10.3390/pharmaceutics16111384

Kantor, R., and Silverberg, J. I. (2017). Environmental risk factors and their role in the management of atopic dermatitis. *Expert Rev. Clin. Immunol.* 13, 15–26. doi: 10.1080/1744666X.2016.1212660

Kim, J., Kim, B. E., Ahn, K., and Leung, D. Y. M. (2019). Interactions between atopic dermatitis and staphylococcus aureus infection: clinical implications. *Allergy Asthma Immunol. Res.* 11, 593–603. doi: 10.4168/aair.2019.11.5.593

Kirtane, A. R., Karavasili, C., Wahane, A., Freitas, D., Booz, K., Le, D. T. H., et al. (2022). Development of oil-based gels as versatile drug delivery systems for pediatric applications. *Sci. Adv* 8 (21), eabm8487. doi: 10.1126/sciadv.abm8478

Lee, Y. S., Chen, X., Widiyanto, T. W., Orihara, K., Shibata, H., and Kajiwara, S. (2022). Curcumin affects function of Hsp90 and drug efflux pump of Candida albicans. *Front. Cell. Infect. Microbiol.* 12. doi: 10.3389/fcimb.2022.944611

Li, Y., Xu, F., Li, X., Chen, S.-Y., Huang, L.-Y., Bian, Y.-Y., et al. (2021). Development of curcumin-loaded composite phospholipid ethosomes for enhanced skin permeability and vesicle stability. *Int. J. Pharm.* 592, 119936. doi: 10.1016/j.ijpharm.2020.119936

Lin, H., Lin, L., Sun, M., Liu, J., and Wu, Q. (2020). Topical delivery of four neuroprotective ingredients by ethosome-gel: synergistic combination for treatment of oxaliplatin-induced peripheral neuropathy. *IJN* 15, 3251–3266. doi: 10.2147/IJN.S233747

Loron, A., Gardrat, C., Tabary, N., Martel, B., and Coma, V. (2021). Tetrahydrocurcumin encapsulation in cyclodextrins for water solubility improvement: Synthesis, characterization and antifungal activity as a new biofungicide. *Carbohydr. Polymer Technol. Appl.* 2, 100113. doi: 10.1016/j.carpta.2021.100113

Lukhele, B. S., Bassey, K., and Witika, B. A. (2023). The utilization of plant-material-loaded vesicular drug delivery systems in the management of pulmonary diseases. *Curr. Issues Mol. Biol.* 45, 9985–10017. doi: 10.3390/cimb45120624

Mamun, A. A., Shao, C., Geng, P., Wang, S., and Xiao, J. (2024). Recent advances in molecular mechanisms of skin wound healing and its treatments. *Front. Immunol.* 15. doi: 10.3389/fimmu.2024.1395479

Mehmood, Y., Shahid, H., Ahmed, S., Khursheed, A., Jamshaid, T., Jamshaid, M., et al. (2024). Synthesis of vitamin D3 loaded ethosomes gel to cure chronic immune-mediated inflammatory skin disease: physical characterization, *in vitro* and ex vivo studies. *Sci. Rep.* 14, 23866. doi: 10.1038/s41598-024-72951-6

Nikhat, A., Hasan, N., Iqbal, Z., Kesharwani, P., and Talegaonkar, S. (2022). Enhanced transdermal delivery of lutein via nanoethosomal gel: Formulation optimization, *in-vitro* evaluation, and *in-vivo* assessment. *J. Drug Delivery Sci. Technol.* 73, 103447. doi: 10.1016/j.jddst.2022.103447

Pankajakasthuri Ayurveda Medical College Campus, and S, S (2021). Dermal irritation study of pankajakasthuri orthoherb cream/thermagel, a potent polyherbal anti-inflammatory and analgesic formulation for topical application in healthy New Zealand white rabbits. *TCR* 5, 1–7. doi: 10.24966/TCR-3735/100022

Panos, G. D., and Boeckler, F. M. (2023). Statistical analysis in clinical and experimental medical research: simplified guidance for authors and reviewers. *Drug Des. Devel Ther.* 17, 1959–1961. doi: 10.2147/DDDT.S427470

Peng, Y., Ao, M., Dong, B., Jiang, Y., Yu, L., Chen, Z., et al. (2021). Anti-inflammatory effects of curcumin in the inflammatory diseases: status, limitations and countermeasures. *Drug Des. Devel Ther.* 15, 4503–4525. doi: 10.2147/DDDT.S327378

Salamanca, C. H., Barrera-Ocampo, A., Lasso, J. C., Camacho, N., and Yarce, C. J. (2018). Franz diffusion cell approach for pre-formulation characterisation of ketoprofen semi-solid dosage forms. *Pharmaceutics* 10, 148. doi: 10.3390/pharmaceutics10030148

Schwartz, D. M., Kanno, Y., Villarino, A., Ward, M., Gadina, M., and O'Shea, J. J. (2017). JAK inhibition as a therapeutic strategy for immune and inflammatory diseases. *Nat. Rev. Drug Discov.* 17, 78. doi: 10.1038/nrd.2017.267

Sharifi-Rad, J., Rayess, Y. E., Rizk, A. A., Sadaka, C., Zgheib, R., Zam, W., et al. (2020). Turmeric and its major compound curcumin on health: bioactive effects and safety profiles for food, pharmaceutical, biotechnological and medicinal applications. *Front. Pharmacol.* 11. doi: 10.3389/fphar.2020.01021

Shinde, P., Page, A., and Bhattacharya, S. (2023). Ethosomes and their monotonous effects on Skin cancer disruption. *Front. Nanotechnol.* 5. doi: 10.3389/fnano.2023.1087413

Soury, R., Alhar, M. S. O., and Jabli, M. (2023). Synthesis, characterization, and application of dichloride (5,10,15,20-tetraphenylporphyrinato) antimony functionalized pectin biopolymer to methylene blue adsorption. *Polymers (Basel)* 15, 1030. doi: 10.3390/polym15041030

Sureshbabu, A., Smirnova, E., Tuong, D. T. C., Vinod, S., Chin, S., Moniruzzaman, M., et al. (2025). Unraveling the curcumin's molecular targets and its potential in suppressing skin inflammation using network pharmacology and *in vitro* studies. *Drug Dev. Res.* 86, e70058. doi: 10.1002/ddr.70058

Tampa, M., Neagu, M., Caruntu, C., Constantin, C., and Georgescu, S. R. (2022). Skin inflammation—A cornerstone in dermatological conditions. *J. Pers. Med.* 12, 1370. doi: 10.3390/jpm12091370

Touitou, E., Dayan, N., Bergelson, L., Godin, B., and Eliaz, M. (2000). Ethosomes - novel vesicular carriers for enhanced delivery: characterization and skin penetration properties. *J. Control Release* 65, 403–418. doi: 10.1016/s0168-3659(99)00222-9

Verma, P., and Pathak, K. (2010). Therapeutic and cosmeceutical potential of ethosomes: An overview. *J. Adv. Pharm. Technol. Res.* 1, 274–282. doi: 10.4103/0110-5558.72415

Wang, J., Zhang, C. S., Zhang, A. L., Changli Xue, C., and Lu, C. (2024). Chinese herbal medicine bath therapy for psoriasis vulgaris using topical calcipotriol as the comparator: A systematic review with meta-analysis and association rule analysis. *J. Ethnopharmacology* 330, 118166. doi: 10.1016/j.jep.2024.118166

Zhang, Y.-B., Wang, J.-F., Wang, M.-X., Peng, J., Kong, X.-D., and Tian, J. (2024). Nano-based drug delivery systems for active ingredients from traditional Chinese medicine: Harnessing the power of nanotechnology. *Front. Pharmacol.* 15. doi: 10.3389/fphar.2024.1405252

frontiers | Frontiers in Cellular and Infection Microbiology

TYPE Mini Review
PUBLISHED 14 August 2025
DOI 10.3389/fcimb.2025.1624036

OPEN ACCESS

EDITED BY
Biswajit Mishra,
Brown University, United States

REVIEWED BY
Tim Maisch,
University of Regensburg, Germany
Abdul Malik,
King Saud University, Saudi Arabia

*CORRESPONDENCE
Vikram Kumar
vikramyadav05@gmail.com;
vkumar3@jpr.amity.edu

RECEIVED 06 May 2025
ACCEPTED 17 July 2025
PUBLISHED 14 August 2025

CITATION
Tanu R, Chaudhary AA, Prakash G, Yasmeen N, Ali MAM, Raza N, Sharma PK, Kumar A, Yadav T and Kumar V (2025) Exploring the potential of photodynamic therapy in overcoming multidrug resistance: mechanisms, synergies, and clinical advancements in infectious diseases. *Front. Cell. Infect. Microbiol.* 15:1624036. doi: 10.3389/fcimb.2025.1624036

Exploring the potential of photodynamic therapy in overcoming multidrug resistance: mechanisms, synergies, and clinical advancements in infectious diseases

Ruchita Tanu[1], Anis Ahmad Chaudhary[2], Gagan Prakash[1], Nusrath Yasmeen[1], Mohamed A. M. Ali[2], Nadeem Raza[3], Pushpender K. Sharma[1], Akhilesh Kumar[1], Tejpal Yadav[4] and Vikram Kumar[4]*

[1]Amity Institute of Biotechnology, Amity University Rajasthan, Jaipur, Rajasthan, India, [2]Department of Biology, College of Science, Imam Mohammad Ibn Saud Islamic University (IMSIU), Riyadh, Saudi Arabia, [3]Department of Chemistry, College of Science, Imam Mohammad Ibn Saud Islamic University (IMSIU), Riyadh, Saudi Arabia, [4]Amity Institute of Pharmacy, Amity University Rajasthan, Jaipur, Rajasthan, India

Multidrug resistance (MDR) in bacterial and fungal pathogens poses a growing global health crisis, rendering many conventional antimicrobial therapies ineffective. The rise of MDR strains complicates treatment, prolongs illness, increases healthcare costs, and contributes to higher mortality rates. Mechanisms driving MDR include enzymatic drug inactivation, target modification, efflux pump activity, decreased permeability, and biofilm formation—often fueled by horizontal gene transfer and selective pressure from antimicrobial overuse. In response to the urgent need for novel therapeutic strategies, photodynamic therapy (PDT) has emerged as a promising, non-traditional approach. PDT utilizes a photosensitizing agent, light of a specific wavelength, and oxygen to generate reactive oxygen species (ROS) that inflict oxidative damage on microbial or cancer cells. This mechanism circumvents conventional resistance pathways, offering targeted, minimally invasive, and effective treatment for infections and malignancies. PDT is particularly adept at penetrating biofilms and resistant microbial populations, thus broadening its clinical applicability. In addition to direct microbial eradication, PDT may stimulate immune responses and demonstrates a favorable safety profile compared to traditional antibiotics or chemotherapy. Furthermore, advances in Antimicrobial Blue Light (aBL) and next-generation photosensitizers enhance PDT's effectiveness while minimizing resistance development. This review explores the biological mechanisms underlying MDR,

the principles and evolution of PDT, and its synergistic potential in managing infectious diseases. By addressing critical gaps in antimicrobial therapy, PDT stands out as a transformative modality in the ongoing battle against drug-resistant pathogens.

KEYWORDS

multidrug resistance, photodynamic therapy, reactive oxygen species, antimicrobial resistance, biofilm disruption, light-based therapies

1 Introduction

The World Health Organization (WHO) identifies antimicrobial resistance (AMR), including multidrug resistance (MDR), as one of the top ten threats to global public health. In 2019, bacterial AMR was directly responsible for an estimated 1.27 million deaths worldwide, with MDR strains playing a major role in this toll (World Health Organization, 2023). The U.S. Centers for Disease Control and Prevention (CDC) highlighted MDR organisms such as carbapenem-resistant Enterobacteriaceae and drug-resistant Candida auris as urgent threats in its 2019 AMR Threats Report, noting that these pathogens cause thousands of deaths each year in the United States alone (Centers for Disease Control and Prevention | CDC, 2025). Similarly, data from the European Centre for Disease Prevention and Control (ECDC) show rising rates of resistance to multiple antibiotic classes among pathogens like Escherichia coli, Klebsiella pneumoniae, and Pseudomonas aeruginosa across Europe. These findings emphasize the urgent need for innovative antimicrobial strategies to address MDR, particularly as the development of new antibiotics lags behind the pace of emerging resistance (Murray et al., 2022). Multidrug resistance (MDR) is a crucial and escalating risk factor for infections caused by bacteria and fungi. It describes how several antimicrobial drugs can be resisted by microbes, making traditional treatments useless. This process happens when microbes evolve defenses against medications that used to effectively kill them or stop their growth (Habboush and Guzman, 2025). As MDR strains proliferate, treatment choices get more complex, healthcare expenses rise, hospital stays lengthen, and morbidity and mortality rates sharply rise (Majumder et al., 2020). The bacterial and fungal pathogens that cause common illnesses like pneumonia, bloodstream infections, urinary tract infections, and invasive fungal diseases are among the many that exhibit multidrug resistance (MDR). The advent of MDR strains has broad ramifications, affecting global public health activities and patient outcomes (Bharadwaj et al., 2022; Tanwar et al., 2014).

Microorganisms utilize various strategies to develop MDR. These strategies can be generally classified as enzymatic inactivation, in which bacteria and fungi generate enzymes that either degrade or modify antimicrobial agents, thereby hindering their ability to bind to target sites (Chinemerem Nwobodo et al., 2022). Another significant mechanism is targeting modification, where microorganisms change the structure of the antimicrobial agent's target molecule, thereby reducing or completely eliminating the binding of the drug (Uddin et al., 2021). Efflux pumps play a vital role as well; these protein complexes actively expel antimicrobial agents from the microbial cell, decreasing their intracellular concentration and preventing access to their targets (Alenazy, 2022). Reduced permeability also contributes, as alterations in the microbial cell membrane or cell wall can lessen the entry of antimicrobial agents into the cell, limiting their access to target sites (Ghai and Ghai, 2018). Additionally, many microorganisms can develop biofilms, which are intricate communities of cells embedded in a self-produced matrix, offering a physical barrier that shields microorganisms from antimicrobial agents and immune responses (Rather et al., 2021). These mechanisms can be acquired via horizontal gene transfer (such as plasmids and transposons) or can emerge through spontaneous mutations. The widespread use of antimicrobial agents exerts selective pressure that fosters the evolution and proliferation of MDR strains (Reygaert, 2018).

There are many difficulties in treating MDR infections. The inability of conventional antibiotic treatments to completely remove the infection frequently results in longer disease duration, a higher risk of complications, and a higher death rate. Serious adverse effects may arise from the necessity of using substitute antimicrobial agents, which are frequently more toxic (Salam et al., 2023). Delays in diagnosing MDR strains can also make it more difficult to administer the right care, which can impair patient outcomes. Furthermore, the urgent need for innovative treatment approaches is highlighted by the limited supply of new antimicrobial medicines to address rising MDR strains. To tackle the problem of MDR infections, tactics like infection control procedures, antimicrobial stewardship programs, and the creation of novel medications and alternative treatments are essential (Ahmed et al., 2024; Huemer et al., 2020).

Photodynamic therapy (PDT) is a treatment method that employs a photosensitizing agent, light, and oxygen to provoke cell death and disrupt tissue. The foundation of PDT lies in the administration of a photosensitizer, an inert molecule that selectively concentrates in the target area, such as cancer cells or infected tissues. Following this, the tissue is subjected to light of a specific wavelength that aligns with the absorption characteristics of

the photosensitizer. Once the light activates it, the photosensitizer undergoes a photochemical process, transferring energy to adjacent oxygen molecules and producing reactive oxygen species (ROS), including singlet oxygen. These ROS are extremely toxic to cells and inflict oxidative damage to various cellular structures, resulting in cell death via apoptosis, necrosis, or autophagy. The focused nature of PDT reduces harm to nearby healthy tissues, making it a promising option for the treatment of various medical conditions (Aebisher et al., 2024; Cieplik et al., 2013).

The origins of PDT date back to the early 1900s when scientists noticed the harmful effects of particular dyes when exposed to light (Fernández-Guarino et al., 2010). In 1900, Oscar Raab found that acridine dyes could be lethal to paramecia when activated by light. Subsequently, in 1903, Niels Finsen was awarded the Nobel Prize in Physiology or Medicine for his innovative use of light to treat skin tuberculosis (Szeimies et al., 2001). However, the contemporary understanding of PDT began to take shape in the 1970s, primarily due to the contributions of Thomas Dougherty, who illustrated the effectiveness of hematoporphyrin derivative (HpD) in fighting experimental tumors (Aebisher et al., 2024). This early photosensitizer, HpD, demonstrated a tendency to concentrate in tumor cells and was successful in promoting tumor shrinkage when exposed to light. Since then, PDT has seen considerable progress, leading to the creation of more potent photosensitizers, enhanced light delivery mechanisms, and refined treatment strategies (Miranda et al., 2018). Today, PDT is utilized clinically to address various ailments, including certain cancer types, skin disorders, and infections. Ongoing studies are continuously investigating new applications for PDT, aiming to improve its effectiveness and safety (Garcia de Miranda et al., 2018). Among the clinically approved protocols, 5-aminolevulinic acid (5-ALA)-based photodynamic therapy (PDT) has become a gold standard, especially for treating dermatological conditions such as actinic keratosis, superficial basal cell carcinoma, and acne. 5-ALA is a prodrug that, when administered, leads to the intracellular accumulation of protoporphyrin IX (PpIX), a powerful endogenous photosensitizer. Once activated by red or blue light, PpIX generates cytotoxic reactive oxygen species. The approval of 5-ALA and its methyl ester derivative, methyl aminolevulinate (MAL), has significantly facilitated the widespread adoption of PDT in clinical dermatology, showcasing high selectivity, minimal invasiveness, and favorable cosmetic outcomes (Gholami et al., 2023; Fernández-Guarino et al., 2010; Guleng and Helsing, 2012).

PDT is emerging as a promising approach for tackling MDR in microbial infections and cancer due to its distinctive mode of action. In contrast to conventional antimicrobial or chemotherapeutic drugs that typically target specific cellular sites, PDT triggers cell death by generating ROS, which inflict extensive oxidative damage on various cellular components. This non-targeted assault complicates the ability of microorganisms or cancer cells to establish resistance mechanisms against PDT (de Carvalho Leonel et al., 2019). Photodynamic therapy (PDT) can effectively overcome the physical and biochemical barriers posed by biofilms and tumor microenvironments by generating reactive oxygen species (ROS) on-site. Because ROS generation occurs locally where the photosensitizer has concentrated and is activated by light, PDT can target and damage both surface and embedded cells within these protective structures. This capability addresses a significant challenge in treating multidrug-resistant (MDR) infections and solid tumors. The capability of PDT to bypass standard resistance pathways makes it a significant asset in the fight against MDR infections and cancers that do not respond to traditional treatments (Liu et al., 2015; Youf et al., 2021).

PDT presents various potential benefits over standard treatment approaches for both infections and cancer. To begin with, PDT allows for highly targeted delivery to diseased tissues, thereby reducing harm to adjacent healthy tissues. This is possible through the application of photosensitizers that preferentially gather in the affected area, combined with accurate light transmission to activate the photosensitizer. In addition, PDT demonstrates a wide range of efficacy, capable of eliminating numerous microorganisms such as bacteria, fungi, and viruses, along with various types of cancer cells. Furthermore, PDT can trigger a strong immune response, potentially boost its therapeutic effects and help to prevent disease recurrence. It is also typically well-tolerated with fewer overall side effects in comparison to conventional chemotherapy or antibiotics. Moreover, the likelihood of developing resistance to PDT is low, rendering it a viable option for the ongoing management of multidrug-resistant infections and cancers. These benefits position PDT as an appealing alternative or complementary therapy to traditional treatments, especially in scenarios where multidrug resistance poses a significant challenge (González et al., 2021; Guleng and Helsing, 2012; Liu et al., 2015; Pérez-Laguna et al., 2021a).

The alarming rise of MDR bacteria has significantly strained current antimicrobial therapies, necessitating the exploration of innovative strategies that challenge traditional resistance mechanisms. The antimicrobial potential of blue light has been recognized for over two decades. Early research showed that visible blue light at a wavelength of 405 nm could effectively kill methicillin-resistant Staphylococcus aureus (MRSA) *in vitro* (Enwemeka et al., 2008). This finding laid the foundation for the development of Antimicrobial Blue Light (aBL) therapies, which utilize the photoactivation of endogenous porphyrins within bacterial cells to produce reactive oxygen species (ROS). These ROS cause oxidative damage to essential biomolecules, including membranes, proteins, and DNA, ultimately leading to bacterial death. As shown in Figure 1, the mechanism involves the ROS-mediated breakdown of proteins, lipid peroxidation, DNA fragmentation, and membrane disruption. This broad-spectrum, multi-targeted approach reduces the risk of resistance development, making aBL a promising tool against multidrug-resistant (MDR) pathogens. Importantly, this mode of action is broad-spectrum and resilient against the development of resistance due to its multi-faceted approach. PDT represents another promising approach in this field, utilizing similar principles but employing exogenous

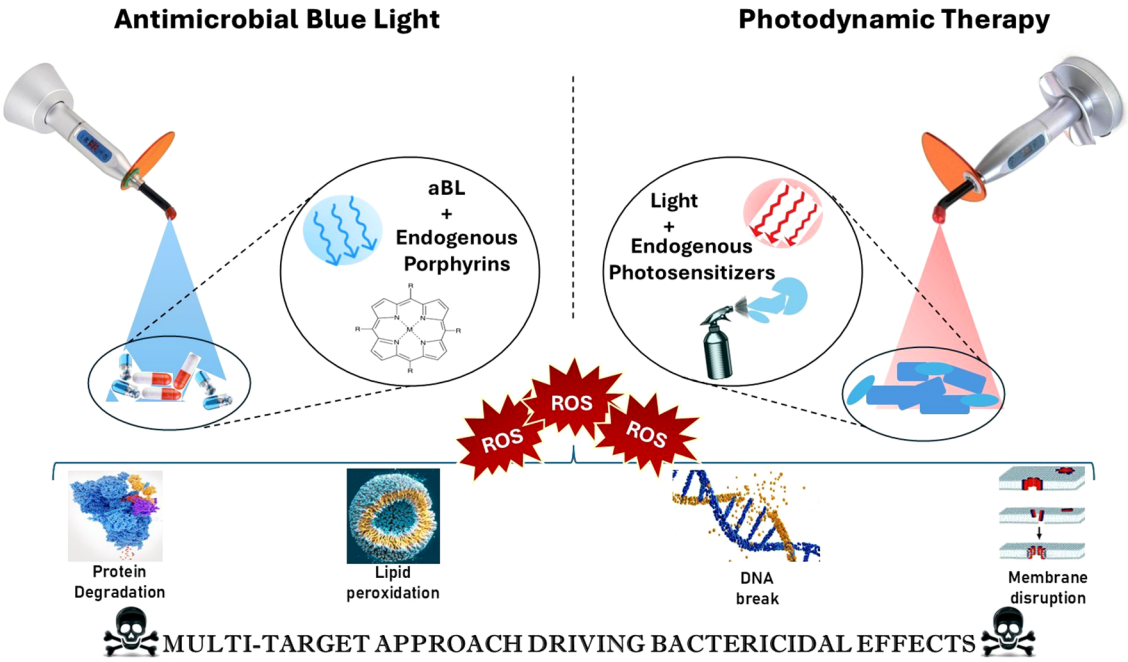

FIGURE 1
Mechanism of action of antimicrobial blue light (aBL) and photodynamic therapy (PDT) in bacterial inactivation. [Antimicrobial Blue Light (left) activates endogenous porphyrins in microbial cells, generating reactive oxygen species (ROS) that contribute to protein degradation and lipid peroxidation. Photodynamic Therapy (right) involves the use of exogenous photosensitizers activated by red light, leading to ROS generation that causes DNA damage and membrane disruption. Both approaches converge on a multi-target bactericidal mechanism through oxidative stress, ultimately enhancing microbial cell death].

photosensitizers that generate highly ROS when activated by a specific wavelength of light. These photosensitizers tend to accumulate in bacterial cells preferentially, allowing for selective destruction upon exposure to light (Cieplik et al., 2014; Leanse et al., 2023; Teng et al., 2023).

In this context, the terms "endogenous photosensitizers" and "endogenous porphyrins" are not entirely interchangeable. Endogenous photosensitizers include porphyrins as well as other chromophores naturally found in microbial cells, such as flavins and NADH. These molecules absorb blue light and generate reactive oxygen species (ROS) during antimicrobial blue light (aBL) therapy. On the other hand, exogenous photosensitizers—like methylene blue, SAPYR, and chlorin e6—are administered externally and activated by specific light wavelengths in photodynamic therapy (PDT). The light used in PDT can include blue, red, or near-infrared wavelengths. Both PDT and aBL therapies lead to oxidative damage in cellular membranes, lipids, proteins, and DNA. As a result, processes such as lipid peroxidation, protein degradation, and DNA fragmentation are not exclusive to one treatment modality; rather, they are shared consequences of ROS generation that depend on the type of sensitizer used and the amount of light applied (Cieplik et al., 2014; Przygoda et al., 2023).

Traditional antibiotic approaches, including β-lactams, macrolides, and fluoroquinolones, usually target critical microbial processes such as cell wall synthesis, protein translation, and DNA replication. However, the effectiveness of these antibiotics is increasingly compromised by bacterial resistance mechanisms, which include enzymatic degradation, efflux pumps, and modifications to the target sites, as shown in Figure 2. In response to the growing issue of antimicrobial resistance, new strategies have been developed to bypass or overcome these resistance mechanisms. These strategies include bacteriophage therapy, antimicrobial peptides (AMPs), anti-virulence agents that block quorum sensing, CRISPR-based antimicrobials, and light-based therapies such as photodynamic therapy (PDT) and antimicrobial blue light (aBL). Unlike traditional antibiotics, these innovative approaches operate through unique mechanisms, including physical disruption of membranes, generation of reactive oxygen species (ROS), and genetic interference, which decreases the likelihood of developing resistance. Traditional antibiotic strategies are increasingly challenged by bacterial resistance mechanisms as illustrated in Figure 2, including enzymatic degradation, alterations at target sites, efflux pumps, and reduced permeability. PDT circumvents these resistance mechanisms by attacking bacterial components through phototoxicity, demonstrating effectiveness even against multidrug-resistant (MDR) strains. By steering clear of conventional antibiotic targets such as ribosomes, DNA gyrase, and enzymes associated with the cell wall, PDT minimizes selective pressure and delays the emergence of resistance, making it an appealing alternative for the post-antibiotic era (Cieplik et al., 2013; Murray et al., 2022; Zhao et al., 2024).

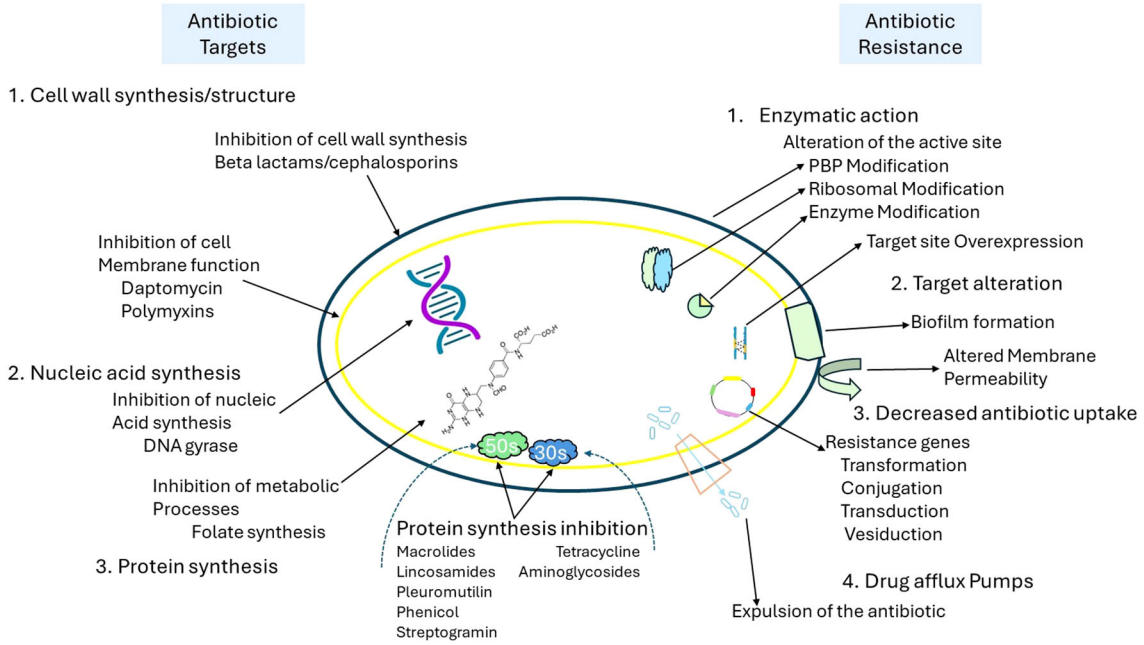

FIGURE 2
Overview of antibiotic targets and mechanisms of antibiotic resistance in bacteria. [This schematic illustrates key bacterial targets for antibiotics (left) and corresponding resistance mechanisms (right). Antibiotics act by inhibiting cell wall synthesis (e.g., beta-lactams), disrupting membrane function (e.g., daptomycin, polymyxins), inhibiting nucleic acid synthesis (e.g., DNA gyrase inhibitors), and blocking protein synthesis (e.g., macrolides, tetracyclines). In contrast, bacteria employ multiple resistance strategies, including enzymatic modification of antibiotic targets (e.g., PBP and ribosomal alterations), target site overexpression, biofilm formation, altered membrane permeability, reduced antibiotic uptake via genetic transfer mechanisms (e.g., transformation, conjugation), and drug efflux through specialized pumps that expel antibiotics from the cell].

2 Photodynamic therapy

2.1 Key components of PDT

2.1.1 Photosensitizers

Photosensitizers are molecules that become activated by light and produce reactive oxygen species (ROS) upon excitation. Ideal characteristics of these molecules include high singlet oxygen quantum yields, low toxicity in the absence of light, and an absorption profile that aligns well with therapeutic light sources. While wavelengths between 600 nm and 800 nm are often highlighted for their ability to penetrate deep tissues, they are not the best choice for all applications in photodynamic therapy (PDT). For example, recent studies have shown that photosensitizers like SAPYR can be effectively activated by blue light (approximately 460 nm) and act as exclusive Type-II singlet oxygen generators. This is particularly important in antimicrobial photodynamic therapy (aPDT), where deep tissue penetration is not as critical (Cieplik et al., 2013, 2015). It is important to distinguish between the therapeutic targets and requirements of tumor photodynamic therapy (PDT) and antimicrobial photodynamic therapy (aPDT). In tumor therapy, photosensitizers typically accumulate in cancerous tissue through the enhanced permeability and retention (EPR) effect or through targeted delivery. These photosensitizers remain inactive until activated by localized light exposure. In contrast, aPDT relies on rapid physicochemical interactions, such as cationic photosensitizers binding electrostatically to the negatively charged cell walls of bacteria, and does not require long-term retention. As a result, the design, activation wavelength, and pharmacokinetics of photosensitizers should be specifically tailored to their intended application. aPDT may benefit from shorter wavelengths (e.g., blue light) and surface-level targeting, while oncologic PDT focuses on achieving deeper tissue penetration and tumor selectivity (Cieplik et al., 2013).

2.1.2 Light activation

Effective photodynamic therapy (PDT) relies on light of a specific wavelength that matches the absorption peak of the chosen photosensitizer. Common light sources include lasers and light-emitting diodes (LEDs), which allow for adjustments in intensity and spectral output. Proper dosage is critical; insufficient light may not activate the photosensitizer effectively, while excessive exposure could harm surrounding tissues. The fluence rate and total light dose directly influence the generation of reactive oxygen species (ROS) and, therefore, the therapy's effectiveness. Notably, the depth of light penetration into tissues is dependent on its wavelength, with near-infrared light (650–800 nm) penetrating more deeply. A vital factor to consider is the number of absorbed photons, which fundamentally affects ROS production and the overall biological outcome (Algorri et al., 2023; Cieplik et al., 2015).

2.1.3 Oxygen-dependent mechanisms

The efficiency of PDT depends on the presence of molecular oxygen in tissues. A photosensitizer transforms oxygen molecules

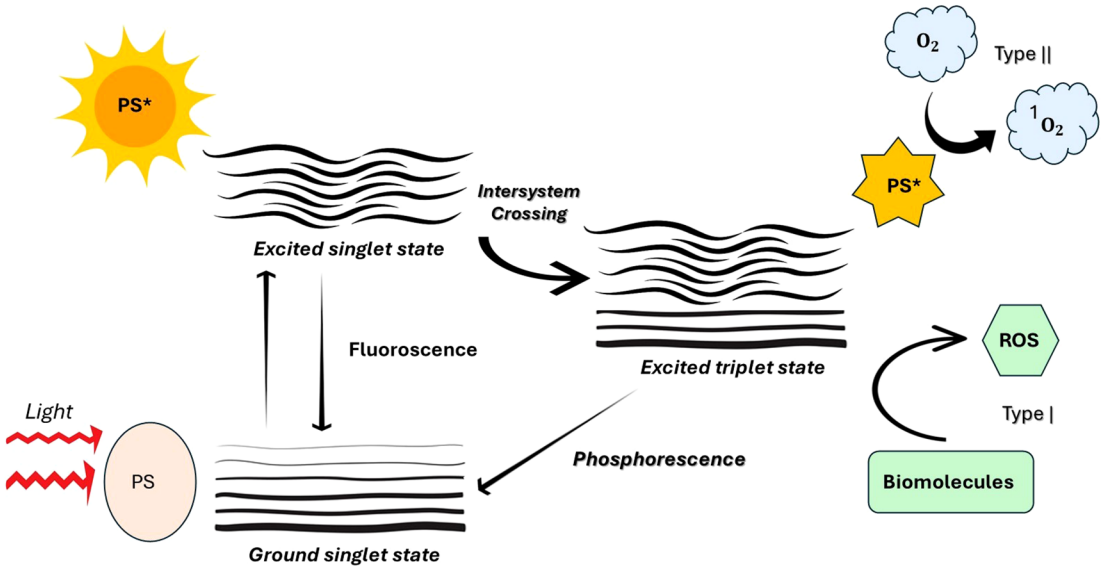

FIGURE 3
Photophysical and photochemical mechanisms of photosensitizer activation in photodynamic therapy (PDT). [Upon absorption of light, the photosensitizer (PS) transitions from the ground singlet state to an excited singlet state. It can return to the ground state by emitting fluorescence or undergo intersystem crossing to form an excited triplet state. From this triplet state, the PS can generate reactive oxygen species (ROS) through two pathways: Type I, involving electron transfer reactions that produce ROS (e.g., superoxide or hydroxyl radicals) that interact with biomolecules, and Type II, involving energy transfer to molecular oxygen (O_2) to produce singlet oxygen ($^1O_2$). Additionally, the excited triplet state may return to the ground state via phosphorescence. These ROS mediate the cytotoxic effects central to PDT].

into very reactive singlet oxygen by transferring energy to them when it is triggered by light. Cell death in target tissues is caused by this reactive species. Low oxygen levels, or hypoxia, can reduce PDT efficiency, therefore critical to maintain proper oxygenation throughout treatment (Cieplik et al., 2013).

The Figure 3 depicts the photodynamic process occurs through two main mechanisms: Type I and Type II. During excitation, the photosensitizer may either transfer electrons or hydrogen (Type I), resulting in the production of superoxide anions (O_2•−), hydrogen peroxide (H_2O_2), and hydroxyl radicals (•OH). While Type I is more effective under low-oxygen (hypoxic) conditions, it still necessitates the presence of molecular oxygen. Conversely, in the Type II pathway, energy is transferred directly to molecular oxygen, leading to the formation of singlet oxygen ($^1O_2$), which is a highly reactive and cytotoxic species. Both pathways contribute to oxidative stress and cell damage in targeted microbial or cancerous tissues (Harris and Rajasekar, 2025; Dube, 2024; Warszyńska et al., 2023).

Table 1. illustrates the effectiveness of different photosensitizers utilized in photodynamic therapy (PDT) targeting a variety of multidrug-resistant (MDR) pathogens. The chosen pathogens consist of both Gram-positive and Gram-negative bacteria, in addition to resistant fungal strains. Methylene Blue stands out due to its wide-ranging effectiveness and successful treatment against several resistant organisms, such as Staphylococcus aureus (MRSA), Klebsiella pneumoniae, and Candida albicans. Other photosensitizers, including Rose Bengal, Curcumin, and Hypericin, also showed significant results against pathogens like vancomycin-resistant Enterococcus faecalis and penicillin-resistant Streptococcus pneumoniae. The results of PDT showed a range of microbial inactivation from moderate to high, influenced by the type of organism, the photosensitizer used, and its resistance characteristics. This table highlights the flexibility of PDT in addressing conventional resistance mechanisms and reinforces its potential as a promising supplemental or alternative approach for tackling MDR infections (Aroso et al., 2021; Ghorbani et al., 2018).

2.2 Interaction of PDT with pathogens

2.2.1 Effects of PDT on bacterial and fungal cells

A novel antibacterial treatment called PDT uses the interplay of photosensitizers and light to create ROS. In both bacteria and fungus, these ROS cause oxidative stress, which harms cellular constituents like membranes and DNA. PDT successfully breaks down biofilms produced by bacterial infections caused by species such as Pseudomonas aeruginosa and Staphylococcus aureus, which are infamously resistant to traditional therapies (Suresh et al., 2024). By exposing the germs to the host's immune system, this disruption not only directly kills the bacteria but also makes them more vulnerable to subsequent treatments (Polat and Kang, 2021).

As seen with Candida species, PDT also affects fungal cells by weakening their cell walls and affecting their metabolic functions (Lima et al., 2019). In order to effectively combat bacterial infections, PDT also recruits neutrophils, which alters the immunological response (Malech et al., 2014). PDT's dual

TABLE 1 Selected photosensitizers and their characteristics for PDT applications.

No.	Photosensitizer	Chemical class	Charge	Absorption maximum	Bacterial targets	Reference
1	Methylene Blue	Synthetic Dye	Cationic	632 nm	Dental plaque, E. coli	(Ghorbani et al., 2018)
2	Toluidine Blue	Synthetic Dye	Cationic	410 nm	S. mutans, E. coli	(Ghorbani et al., 2018; Wainwright and Crossley, 2004)
3	Rose Bengal	Synthetic Dye	Anionic	532 nm	E. faecalis, P. aeruginosa	(Ghorbani et al., 2018; Nakonieczna et al., 2018)
4	Curcumin	Natural Compound	Neutral	547 nm	S. mutans, L. acidophilus	(Ghorbani et al., 2018; Wainwright and Crossley, 2004)
5	Hypericin	Natural Compound	Neutral	593 nm	S. aureus, E. coli	(Ghorbani et al., 2018; Maisch, 2007)
6	TMPyP (Porphyrin derivative)	Tetra-pyrrole	Cationic	446 nm	S. aureus, P. aeruginosa	(Ghorbani et al., 2018)
7	Zinc Phthalocyanine	Tetra-pyrrole	Neutral	670 nm	A. hydrophila, S. aureus	(Ghorbani et al., 2018; Wainwright and Crossley, 2004)
8	Chlorin e6	Tetra-pyrrole	Neutral	660 nm	S. aureus, E. coli	(Ghorbani et al., 2018; Maisch, 2007)
9	Fullerenes	Nanostructure	Neutral	532 nm	S. aureus, E. coli	(Ghorbani et al., 2018; Dai et al., 2009)
10	Titanium Dioxide	Nanostructure	Neutral	Near-UV (400 nm)	Water treatment	(Ghorbani et al., 2018; Dai et al., 2009)

mechanism of immune system stimulation and direct microbial death makes it an effective technique for fighting resistant microbial illnesses (Zhang et al., 2025).

2.2.2 Disruption of cellular membranes and genetic material

2.2.2.1 Cellular membrane distribution

PDT causes considerable harm to cellular membranes due to the oxidative stress produced by reactive oxygen species (ROS). Photosensitizers like polycation-containing hematoporphyrin tend to accumulate at negatively charged membrane glycans, resulting in lipid peroxidation and the breakdown of structural integrity (Przygoda et al., 2023).

Table 2. presents a comparative study of frequently researched photosensitizers utilized in antimicrobial PDT, detailing their chemical classifications, charge characteristics, absorption peaks, and targeted microorganisms. This compilation features synthetic dyes such as Methylene Blue and Toluidine Blue, in addition to natural substances like Curcumin and Hypericin. Importantly, the most effective photosensitizers tend to possess cationic or neutral charges, which enhances their affinity for negatively charged microbial membranes. The absorption maxima, which span from the visible to near-UV spectra, play a crucial role in ensuring optimal light activation and the generation of reactive oxygen species (ROS). Tetra-pyrrole compounds, including Chlorin e6 and Zinc Phthalocyanine, demonstrate strong absorbance within the red/near-infrared range, facilitating deeper tissue penetration. The properties of photosensitizers affect their effectiveness against different pathogens, such as E. coli, S. aureus, and P. aeruginosa. This table demonstrates how the choice of photosensitizers, guided by their physicochemical characteristics, can be customized according to the type of microbe and the site of infection, highlighting the adaptability of a PDT in clinical settings (González et al., 2021; da Fonseca et al., 2021; Dai et al., 2009; García et al., 2015; Ghorbani et al., 2018; Rubilar-Huenchuman et al., 2024; Wainwright and Crossley, 2004).

2.3 PDT in microbial treatment

The distinctions between the impact of PDT on microbial resistance and that of conventional therapies are essential and arise from their differing modes of action. Conventional therapies, including antibiotics and antifungals, generally focus on specific cellular functions or structures within microorganisms, such as the synthesis of cell walls, replication of DNA, or production of proteins. Microorganisms are capable of developing resistance to these treatments through various strategies, such as enzymatically deactivating the drug, modifying the drug's target, using efflux pumps to expel the drug from the cell, and decreasing cell permeability. These resistance mechanisms typically necessitate only a handful of genetic modifications, allowing for a relatively rapid emergence of resistance (Guo et al., 2018).

In contrast, PDT employs a non-specific oxidative approach. When energized by light, the photosensitizer produces highly ROS —like singlet oxygen—that inflict extensive damage to various cellular components, such as lipids, proteins, and nucleic acids. This broad, non-targeted assault makes it significantly more challenging for microorganisms to acquire resistance. Developing resistance would necessitate simultaneous and coordinated

TABLE 2 MDR pathogen sensitivity to PDT across diverse photosensitizers.

No.	MDR pathogen	Strain type	Resistance profile	Photosensitizer used	PDT outcome	Known resistance mechanism(s)	Reference
1	*Staphylococcus aureus* (MRSA)	Gram-positive	Methicillin-resistant	Methylene Blue	Significant reduction	Altered PBPs, Efflux pumps	(Dai et al., 2009; Reygaert, 2009)
2	*Pseudomonas aeruginosa*	Gram-negative	Carbapenem-resistant	Toluidine Blue O	Partial reduction	Efflux pumps, Porin loss, Enzymatic degradation	(Wainwright and Crossley, 2004)
3	*Acinetobacter baumannii*	Gram-negative	Carbapenem-resistant	Methylene Blue	Significant reduction	Efflux pumps, Enzymatic inactivation (OXA-type β-lactamase)	(da Fonseca et al., 2021)
4	*Enterococcus faecalis* (VRE)	Gram-positive	Vancomycin-resistant	Rose Bengal	Effective under low light dose	Altered target (D-Ala-D-Lac), Efflux pumps	(Rubilar-Huenchuman et al., 2024)
5	*Escherichia coli* (ESBL)	Gram-negative	Extended-spectrum β-lactamase producer	Curcumin	Moderate reduction	ESBLs (enzymatic inactivation), Efflux pumps	(Ghorbani et al., 2018)
6	*Klebsiella pneumoniae*	Gram-negative	Carbapenemase-producing (KPC, ESBL)	Methylene Blue	High inactivation rate	Enzymatic inactivation, Efflux pumps, Porin mutations	(Buchovec et al., 2022)
7	*Streptococcus pneumoniae*	Gram-positive	Penicillin-resistant	Hypericin	Effective inhibition	Altered PBPs, Efflux pumps (mefA)	(García et al., 2015)
8	*Enterococcus faecium*	Gram-positive	Vancomycin-resistant	Methylene Blue	Significant reduction	Target modification (vanA/vanB), Efflux pumps	(Dai et al., 2009)
9	*Klebsiella aerogenes*	Gram-negative	Carbapenem-resistant	Methylene Blue	Effective inhibition	Enzymatic inactivation (AmpC β-lactamase), Efflux pumps	(Buchovec et al., 2022)
10	*Candida albicans*	Fungal	Fluconazole-resistant	Methylene Blue	Significant reduction	Efflux pumps (CDR1, MDR1), Ergosterol target alteration	(Dai et al., 2009; de Carvalho Leonel et al., 2019)
11	*Cryptococcus neoformans*	Fungal	Amphotericin B-resistant	Methylene Blue	Effective inhibition	Membrane alterations, Efflux pumps (ABC transporters)	(Dai et al., 2009)
12	*Staphylococcus epidermidis*	Gram-positive	Methicillin-resistant	Methylene Blue	Significant reduction	Altered PBPs, Efflux pumps	(García et al., 2015)
13	*Enterobacter cloacae*	Gram-negative	Carbapenem-resistant	Methylene Blue	Effective inhibition	Enzymatic inactivation, Porin loss, Efflux pumps	(Buchovec et al., 2022)
14	*Proteus mirabilis*	Gram-negative	Ampicillin-resistant	Methylene Blue	Significant reduction	β-lactamase production, Efflux pumps	(García et al., 2015; Reygaert, 2018)

10.3389/fcimb.2025.1624036

alterations in multiple cellular pathways to defend against the oxidative harm induced by ROS. Although some microorganisms may show a degree of tolerance by boosting antioxidant production or enhancing DNA repair mechanisms, the emergence of strong resistance to PDT is deemed much less probable compared to conventional therapies due to the intricate and multifaceted nature of PDT's cytotoxic actions. This distinction is a primary reason why PDT is being investigated as a viable option to address the escalating issue of multidrug resistance (Liu et al., 2015; Surur, et al., 2024).

3 Mechanisms of multidrug resistance and how PDT overcomes them

3.1 MDR in microbial infections

MDR among microbes poses a significant threat to global health. Microorganisms acquire the ability to withstand multiple antimicrobial treatments through different mechanisms, complicating the treatment of infections. Gaining insight into these resistance mechanisms is essential for developing new strategies to address MDR and maintain the efficacy of current medications (Salam et al., 2023).

The main mechanisms of multidrug resistance (MDR) include efflux pumps, enzymatic degradation, modification of target sites, reduced permeability, and biofilm formation. These mechanisms can vary across different microbial strains, and not all pathogens listed in Table 2 necessarily utilize efflux pumps. The excessive use of antibiotics promotes the dissemination of these resistance mechanisms, highlighting the urgent need for innovative therapeutic solutions (Ahmed et al., 2024; Elshobary et al., 2025).

3.2 PDT as a potential solution

PDT overcomes prevalent MDR strategies through its distinct mode of action. Unlike traditional antimicrobial or chemotherapy agents that focus on particular cellular targets, PDT operates by producing ROS, resulting in extensive oxidative harm to various cellular elements. This non-specific approach effectively evades resistance mechanisms like enzymatic breakdown and modified target sites, as the ROS directly harm critical cellular components irrespective of any resistance factors present. Furthermore, PDT can counteract the impact of efflux pumps, a prevalent mechanism of MDR, by producing ROS within the cells. The production of these intracellular ROS damages crucial cellular components, regardless of the concentration of the medication. In addition, the oxidative stress induced by PDT can harm or deactivate the proteins of efflux pumps, which further boosts its effectiveness against MDR strains. This multifaceted strategy positions PDT as a viable alternative to conventional therapies in the fight against MDR (Alwaeli et al., 2015; Alfei et al., 2024; Liu et al., 2015).

Figure 4 depicts the established ways in which bacteria develop resistance to traditional antibiotics, including the use of efflux pumps, enzymatic drug inactivation, and modifications to antibiotic target sites. In contrast, the figure also demonstrates that photodynamic therapy (PDT) combats microbes by generating reactive oxygen species (ROS), which inflict widespread oxidative damage on bacterial membranes, proteins, and genetic material. Notably, there are no known cases of stable or heritable resistance to PDT. While some bacteria may temporarily adapt by increasing their tolerance to oxidative stress, this response does not equate to the genetically encoded resistance seen with antibiotics. Because PDT's oxidative damage targets multiple cellular components and bypasses conventional resistance pathways, it stands out as a promising approach for managing multidrug-resistant infections (Feng et al., 2022, 2022; Tavares et al., 2010).

Exploring non-traditional pathways to target microbial cells presents a promising opportunity to address antimicrobial resistance and create innovative therapeutic strategies. Conventional antimicrobial agents typically aim at specific bacterial functions, such as the synthesis of cell walls, DNA replication, or protein synthesis. Nevertheless, microorganisms are capable of developing resistance mechanisms that can make these agents ineffective. Non-traditional methods emphasize disrupting microbial survival through alternative means, like targeting virulence factors, interfering with quorum sensing, or inhibiting metabolic pathways critical for their survival. Another strategy involves photodynamic therapy, where the production of reactive oxygen species causes damage to various cellular components. These methods bypass existing resistance mechanisms and suggest a potential solution to the escalating challenge of AMR (Murugaiyan et al., 2022; Feng et al., 2022).

4 Photodynamic therapy against multidrug-resistant microorganisms

4.1 PDT for resistant bacterial infections

PDT has proven effective against a wide range of bacteria, which includes both Gram-positive and Gram-negative strains, as well as those resistant to antibiotics. While there are significant differences in the cell wall composition between Gram-positive and Gram-negative bacteria—specifically, the outer membrane of Gram-negative bacteria can hinder the absorption of certain substances—PDT has shown potential against both groups. The ROS produced during PDT can inflict damage on various cellular components regardless of cell wall structure, resulting in bacterial inactivation. This extensive spectrum of activity makes PDT a significant asset in addressing infections caused by various pathogens (Sperandio et al., 2013).

The ability of PDT to combat antibiotic-resistant bacteria is especially remarkable. Mechanisms of antibiotic resistance, including efflux pumps, enzymatic breakdown, and modifications

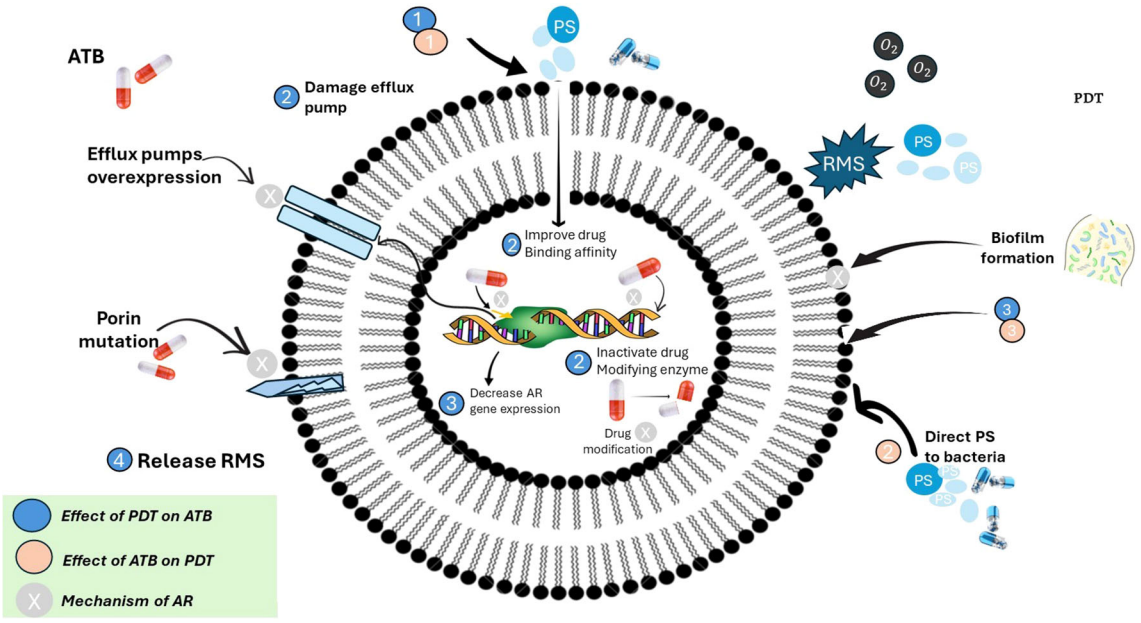

FIGURE 4
Interplay between photodynamic therapy (PDT), antibiotics (ATB), and antimicrobial resistance (AR) mechanisms in bacteria. [This schematic illustrates the complex interactions between antibiotics (ATB), photodynamic therapy (PDT), and bacterial antimicrobial resistance (AR). Antibiotic resistance mechanisms (indicated by beige circles) include overexpression of efflux pumps, porin mutations, drug-modifying enzymes, and biofilm formation, all of which reduce antibiotic efficacy. PDT (blue circles) exerts its effect through reactive molecular species (RMS), particularly reactive oxygen species (ROS), which can: (1) damage efflux pumps, (2) inactivate drug-modifying enzymes, (3) disrupt biofilms, (4) release RMS to reduce AR gene expression and improve antibiotic binding affinity. Conversely, antibiotics can enhance PDT by directing photosensitizers (PS) to bacterial targets. The figure emphasizes a synergistic strategy where PDT can overcome antibiotic resistance, and antibiotics can potentiate PDT effectiveness. Color-coded legend: blue = effect of PDT on antibiotics; beige = effect of antibiotics on PDT; grey = intrinsic mechanisms of antibiotic resistance].

of target sites, often make conventional antibiotics ineffective. Nevertheless, PDT can bypass these issues by producing ROS that induce widespread oxidative damage to a range of cellular components. Furthermore, PDT can penetrate resistant cells found within biofilms, effectively addressing the protective barrier that contributes to antibiotic resistance. Research has indicated that PDT can successfully eliminate antibiotic-resistant bacterial strains such as methicillin-resistant Staphylococcus aureus (MRSA), vancomycin-resistant Enterococci (VRE), and multidrug-resistant Pseudomonas aeruginosa, underscoring its potential as an innovative treatment approach to tackle the rising challenge of antibiotic resistance (Liu et al., 2015).

4.2 PDT in fungal infection

PDT has demonstrated encouraging outcomes in the fight against Candida species and other resistant fungi, presenting a possible alternative to standard antifungal treatments. Fungal infections, particularly those caused by Candida species, pose a significant threat, especially for individuals with weakened immune systems. The rise of antifungal-resistant strains makes treatment approaches even more challenging. The action mechanism of PDT, which includes the production of ROS, can effectively target fungal cells regardless of their resistance traits. ROS can harm fungal cell membranes, cell walls, and internal components, resulting in cell death. PDT has proven effective against various Candida species, including Candida albicans, along with other resistant fungi such as Aspergillus species. Therefore, PDT stands out as a useful method for treating fungal infections that do not respond to traditional antifungal medications (Hung et al., 2021; Rodríguez-Cerdeira et al., 2021a; X. Wu and Hu, 2022).

5 Synergy between PDT and antibiotics

Combination therapies that include PDT present a promising approach for increasing effectiveness against resistant bacterial and fungal strains. By pairing PDT with other antimicrobial agents, such as traditional antibiotics or antifungals, synergistic effects can be achieved, leading to better elimination of resistant microorganisms. The logic behind these combination therapies is that PDT can undermine the resistance mechanisms of microorganisms, making them more vulnerable to the actions of additional antimicrobial agents. For instance, PDT can break down biofilms, which can help antibiotics penetrate the biofilm matrix more effectively. Moreover, PDT can impair efflux pumps, resulting in higher intracellular levels of antibiotics. Additionally, the integration of PDT with immunomodulatory agents can enhance the host's immune response, further improving the elimination of resistant microorganisms (Akhtar et al., 2024; Pérez-Laguna et al., 2021b).

6 Clinical evidence and case studies

Photodynamic therapy (PDT) has shown effectiveness in treating various resistant infections in both clinical and preclinical studies. For instance, PDT using methylene blue has been successfully applied to wounds infected with methicillin-resistant Staphylococcus aureus (MRSA). This treatment resulted in faster healing and a reduction of over 80% in bacterial load (Dai et al., 2009). PDT has proven effective in treating Pseudomonas aeruginosa infections in burn wounds and ulcers, as well as addressing fungal infections like oral and vaginal candidiasis caused by Candida albicans (MaChado-de-Sena et al., 2014; Rodríguez-Cerdeira et al., 2021b). Additionally, PDT has been utilized in the treatment of fungal keratitis, onychomycosis, and localized cutaneous leishmaniasis, yielding encouraging results and few adverse effects (Ramos et al., 2016; Hung et al., 2021).

6.1 Pre-clinical and clinical studies in PDT

6.1.1 Preclinical innovations in PDT

Next-era photosensitizers and targeting techniques are revolutionizing PDT through enhancing precision and efficacy against multidrug-resistant pathogens. Indium phosphide (InP) quantum dots generate bactericidal superoxide radicals, eradicating MDR Staphylococcus aureus in murine wounds without harming mammalian cells, at the same time as hybrid nano systems like silver nanoparticle-rhodamine B complexes leverage photothermal-photodynamic synergy to get rid of 98% of E. coli and MRSA inside 5 mins of light exposure. Stimuli-responsive companies, which includes pH-activated porphyrin-metallic natural frameworks, selectively release ROS in acidic contamination microenvironments, sparing healthful tissues. targeting techniques further refine PDT's specificity: cationic polymers like Amberlite resin-changed Rose Bengal triumph over hydrophobicity to improve Gram-negative bacterial focused on, and antibody-conjugated photosensitizers, including anti-Pseudomonas monoclonal antibodies guiding chlorin e6, reduce lung infection bacterial loads by means of four-log in preclinical fashions. Combinatorial strategies extend these outcomes—gold nanorods permit concurrent photothermal therapy and PDT to eliminate Acinetobacter baumannii biofilms at reduced light doses, even as PDT-mediated disruption of efflux pumps in Klebsiella pneumoniae restores susceptibility to colistin *in vitro*, resensitizing pathogens to traditional antibiotics. These innovations together decorate PDT's potential as a focused, multifunctional weapon towards resistant infections (Lee et al., 2022; G. Wu et al., 2024).

6.1.2 Clinical innovations in PDT

Advances in photodynamic therapy (PDT) emphasize new photosensitizers and enhanced delivery methods, while targeting real-world multidrug-resistant infections. In instances of onychomycosis, MAL-PDT has completed therapy fees of as much as 90%, outperforming traditional antifungals in sufferers mistaken for systemic remedies. Methylene blue-based photodynamic therapy (PDT) has demonstrated significant benefits in clinical studies for patients with persistent ulcers infected with Staphylococcus aureus. This therapy accelerates wound closure, reduces bacterial counts, and enhances tissue repair. For instance (Dai et al., 2009),patients who received PDT achieved more than 80% bacterial clearance and experienced faster epithelial healing within 10 days. In contrast, those treated with mupirocin showed a slower recovery. Important clinical advancements include the use of device coatings and the integration of photodynamic therapy into textiles. PDT has additionally proven efficacy towards viral pathogens like cutaneous HPV and HSV by way of interfering with viral replication cycles, and in parasitic illnesses which includes localized leishmaniasis, wherein topical PDT has finished 100% treatment quotes without the systemic side outcomes related to conventional medicinal drugs. collectively, these advances underscore the extensive-spectrum and flexible applications of PDT in combating multidrug-resistant and hard-to-treat infections (Ramos et al., 2016; G. Wu et al., 2024).

7 Challenges and limitations of photodynamic therapy

Even with its potential benefits, the broad implementation of PDT encounters numerous obstacles. A major challenge is light penetration, as the light must reach the photosensitizer for activation, which is especially difficult for infections or tumors located deeper within the body. Approaches to address this challenge include utilizing higher light doses (with safety considerations), employing photosensitizers that respond to longer wavelengths of light (which can reach deeper tissues), or applying alternative light delivery techniques such as interstitial illumination (Wainwright and Crossley, 2004). The properties of photosensitizers also present challenges; optimal photosensitizers should have high selectivity for targeted cells, low toxicity to surrounding healthy tissues, and effective activation from easily accessible light sources. Moreover, although the risk of developing resistance to PDT is generally perceived to be lower than that associated with conventional antimicrobials due to its multi-targeting nature, it remains a potential issue that should be monitored and examined. Lastly, the financial aspect and availability of PDT are vital factors influencing its general acceptance. PDT equipment and photosensitizers can be costly, and specialized knowledge is necessary to administer the treatment. Enhancing the cost-effectiveness and expanding the availability of PDT could make it a more feasible treatment choice for patients globally (Ahmed et al., 2024; Shi et al., 2019).

8 Future directions and innovations

The prospects for PDT in treating MDR infections are encouraging, with several innovative pathways emerging. Progress in the development of photosensitizers, especially through advancements in nanotechnology and new formulations, is improving the targeting of microbial cells while minimizing side effects on healthy tissues. This enhanced selectivity broadens the

therapeutic window of PDT. Additionally, there is an exploration of PDT's potential in personalized medicine, where treatment protocols and photosensitizers are customized to align with the infection's specific characteristics and the patient's needs, maximizing effectiveness and reducing off-target impacts (Hamblin and Hasan, 2004; Liu et al., 2015). The combination of PDT with other therapeutic approaches, such as traditional antibiotics or immunomodulatory agents, shows great potential for boosting treatment efficacy against resistant strains. Current trends in both clinical and preclinical research involve the examination of new photosensitizers, improved light delivery techniques, and novel treatment protocols for various MDR infections, setting the stage for PDT to play a significant role in combating antibiotic resistance (Harris and Rajasekar, 2025; Miranda et al., 2018).

9 Conclusion

In conclusion, PDT offers a promising and novel solution to address the increasing issue of MDR in microbial infections. Its distinct mode of action, which involves the production of reactive oxygen species to cause extensive cellular damage, enables it to bypass many of the resistance mechanisms that make traditional antibiotics and antifungals ineffective. As research and development progress in optimizing PDT methods and photosensitizers, its application in existing clinical settings becomes more practical. PDT can be used alongside conventional treatments, particularly for localized MDR infections or as a strategy to eliminate resistant strains. In the future, PDT shows great potential as a sustainable and adaptable option in the battle against MDR, providing hope in a scenario where antimicrobial resistance continues to rise. Ongoing research, clinical studies, and technological innovations are essential to fully realize the capabilities of PDT and to establish it as a fundamental element of future antimicrobial approaches.

Author contributions

RT: Writing – original draft, Formal analysis, Data curation, Conceptualization, Investigation, Validation, Writing – review & editing, Methodology. AC: Methodology, Writing – review & editing, Conceptualization, Writing – original draft. GP: Writing – review & editing, Formal analysis, Data curation, Writing – original draft, Conceptualization, Methodology. NY: Writing – review & editing. MA: Writing – review & editing. NR: Writing – review & editing. PS: Writing – review & editing. AK: Writing – review & editing. TY: Writing – review & editing. VK: Investigation, Software, Conceptualization, Writing – original draft, Resources, Visualization, Funding acquisition, Methodology, Validation, Writing – review & editing, Formal analysis, Project administration, Data curation, Supervision.

Funding

The author(s) declare financial support was received for the research and/or publication of this article. The funding was provided by the Deanship of Scientific Research at Imam Mohammad Ibn Saud Islamic University (IMSIU) for supporting this work through Research Grant No. IMSIU-DDRSP2501.

Acknowledgments

Authors would like to thank the Amity University Rajasthan, Jaipur for providing the needful facilities.

Conflict of interest

The authors declare that the research was conducted in the absence of any commercial or financial relationships that could be construed as a potential conflict of interest.

Generative AI statement

The author(s) declare that no Generative AI was used in the creation of this manuscript.

Publisher's note

References

Aebisher, D., Serafin, I., Batóg-Szczęch, K., Dynarowicz, K., Chodurek, E., Kawczyk-Krupka, A., et al. (2024). Photodynamic therapy in the treatment of cancer-the selection of synthetic photosensitizers. *Pharm. (Basel Switzerland)* 17. doi: 10.3390/PH17070932

Ahmed, S. K., Hussein, S., Qurbani, K., Ibrahim, R. H., Fareeq, A., Mahmood, K. A., et al. (2024). Antimicrobial resistance: Impacts, challenges, and future prospects. *J. Medicine Surgery Public Health* 2, 100081. doi: 10.1016/J.GLMEDI.2024.100081

Akhtar, F., Misba, L., and Khan, A. U. (2024). The dual role of photodynamic therapy to treat cancer and microbial infection. *Drug Discov. Today* 29. doi: 10.1016/J.DRUDIS.2024.104099

Alenazy, R. (2022). Drug efflux pump inhibitors: A promising approach to counter multidrug resistance in gram-negative pathogens by targeting acrB protein from acrAB-tolC multidrug efflux pump from escherichia coli. *Biology* 11. doi: 10.3390/BIOLOGY11091328

Alfei, S., Schito, G. C., Schito, A. M., and Zuccari, G. (2024). Reactive oxygen species (ROS)-mediated antibacterial oxidative therapies: available methods to generate ROS and a novel option proposal. *Int. J. Mol. Sci.* 25. doi: 10.3390/IJMS25137182

Algorri, J. F., López-Higuera, J. M., Rodríguez-Cobo, L., and Cobo, A. (2023). Advanced light source technologies for photodynamic therapy of skin cancer lesions. *Pharmaceutics* 15, 2075. doi: 10.3390/PHARMACEUTICS15082075

Alwaeli, H., AlKhateeb, S. N., and AlSadi, A. (2015). Long-term clinical effect of adjunctive antimicrobial photodynamic therapy in periodontal treatment: A randomized clinical trial. *Lasers Med. Sci.* 30, 801–807. doi: 10.1007/s10103-013-1426-y

Aroso, R. T., Schaberle, F. A., Arnaut, L. G., and Pereira, M. M. (2021). Photodynamic disinfection and its role in controlling infectious diseases. *Photochemical Photobiological Sci.* 20, 1497. doi: 10.1007/S43630-021-00102-1

Bharadwaj, A., Rastogi, A., Pandey, S., Gupta, S., and Sohal, J. S. (2022). Multidrug-resistant bacteria: their mechanism of action and prophylaxis. *BioMed. Res. Int.* 2022, 5419874. doi: 10.1155/2022/5419874

Buchovec, I., Vyčaitė, E., Badokas, K., Sužiedelienė, E., and Bagdonas, S. (2022). Application of antimicrobial photodynamic therapy for inactivation of *acinetobacter baumannii* biofilms. *Int. J. Mol. Sci.* 24, 722. doi: 10.3390/ijms24010722

Centers for Disease Control and Prevention | CDC. (2025). Available online at: https://www.cdc.gov/index.html (Accessed April 10, 2025).

Chinemerem Nwobodo, D., Ugwu, M. C., Oliseloke Anie, C., Al-Ouqaili, M. T. S., Chinedu Ikem, J., Victor Chigozie, U., et al. (2022). Antibiotic resistance: The challenges and some emerging strategies for tackling a global menace. *J. Clin. Lab. Anal.* 36. doi: 10.1002/JCLA.24655

Cieplik, F., Pummer, A., Regensburger, J., Hiller, K. A., Späth, A., Tabenski, L., et al. (2015). The impact of absorbed photons on antimicrobial photodynamic efficacy. *Front. Microbiol.* 6. doi: 10.3389/FMICB.2015.00706/BIBTEX

Cieplik, F., Späth, A., Leibl, C., Gollmer, A., Regensburger, J., Tabenski, L., et al. (2014). Blue light kills Aggregatibacter actinomycetemcomitans due to its endogenous photosensitizers. *Clin. Oral. Investigations* 18, 1763–1769. doi: 10.1007/S00784-013-1151-8

Cieplik, F., Späth, A., Regensburger, J., Gollmer, A., Tabenski, L., Hiller, K. A., et al. (2013). Photodynamic biofilm inactivation by SAPYR - An exclusive singlet oxygen photosensitizer. *Free Radical Biol. Med.* 65, 477–487. doi: 10.1016/j.freeradbiomed.2013.07.031

da Fonseca, A., de, S., Mencalha, A. L., and de Paoli, F. (2021). Antimicrobial photodynamic therapy against Acinetobacter baumannii. *Photodiagnosis Photodyn. Ther.* 35. doi: 10.1016/J.PDPDT.2021.102430

Dai, T., Huang, Y. Y., and Hamblin, M. R. (2009). Photodynamic therapy for localized infections – state of the art. *Photodiagnosis Photodyn. Ther.* 6, 170. doi: 10.1016/J.PDPDT.2009.10.008

de Carvalho Leonel, L., Carvalho, M. L., da Silva, B. M., Zamuner, S., Alberto-Silva, C., and Silva Costa, M. (2019). Photodynamic Antimicrobial Chemotherapy (PACT) using methylene blue inhibits the viability of the biofilm produced by Candida albicans. *Photodiagnosis Photodyn. Ther.* 26, 316–323. doi: 10.1016/j.pdpdt.2019.04.026

de Miranda, R. G., and Colombo, A. P. V. (2018). Clinical and microbiological effectiveness of photodynamic therapy on primary endodontic infections: a 6-month randomized clinical trial. *Clin. Oral. Investig.* 22, 1751–1761. doi: 10.1007/s00784-017-2270-4

Dube, E. (2024). Antimicrobial photodynamic therapy: self-disinfecting surfaces for controlling microbial infections. *Microorganisms* 12, 1573. doi: 10.3390/MICROORGANISMS12081573

Elshobary, M. E., Badawy, N. K., Ashraf, Y., Zatioun, A. A., Masriya, H. H., Ammar, M. M., et al. (2025). Combating antibiotic resistance: mechanisms, multidrug-resistant pathogens, and novel therapeutic approaches: an updated review. *Pharmaceuticals* 18, 402. doi: 10.3390/PH18030402

Enwemeka, C. S., Williams, D., Hollosi, S., Yens, D., and Enwemeka, S. K. (2008). Visible 405 nm SLD light photo-destroys methicillin-resistant Staphylococcus aureus (MRSA) in *vitro*. *Lasers Surg. Med.* 40, 734–737. doi: 10.1002/LSM.20724

Feng, Y., Tonon, C. C., and Hasan, T. (2022). Dramatic destruction of methicillin-resistant Staphylococcus aureus infections with a simple combination of amoxicillin and light-activated methylene blue. *J. Photochem. Photobiology. B Biol.* 235. doi: 10.1016/J.JPHOTOBIOL.2022.112563

Fernández-Guarino, M., Harto, A., and Jaén, P. (2010). Studies of methyl aminolevulinate photodynamic therapy for actinic keratosis. *Actas Dermo-Sifiliográficas (English Edition)* 101, 315–322. doi: 10.1016/S1578-2190(10)70641-7

García, I., Ballesta, S., Gilaberte, Y., Rezusta, A., and Pascual, Á. (2015). Antimicrobial photodynamic activity of hypericin against methicillin-susceptible and resistant Staphylococcus aureus biofilms. *Future Microbiol.* 10, 347–356. doi: 10.2217/FMB.14.114

Ghai, I., and Ghai, S. (2018). Understanding antibiotic resistance via outer membrane permeability. *Infection Drug Resistance* 11, 523–530. doi: 10.2147/IDR.S156995

Ghorbani, J., Rahban, D., Aghamiri, S, Teymouri, A, and Bahador, A (2018). Photosensitizers in antibacterial photodynamic therapy: an overview. *Laser Ther.* 27 (4), 293. doi: 10.5978/ISLSM.27_18-RA-01

Gholami, L., Shahabi, S., Jazaeri, M, Hadilou, M, and Fekrazad, R (2023). Clinical applications of antimicrobial photodynamic therapy in dentistry. *Front Microbiol.* 13, 1020995. doi: 10.3389/fmicb.2022.1020995

González, I. A., Palavecino, A., Núñez, C., Dreyse, P., Melo-González, F., Bueno, S. M., et al. (2021). Effective Treatment against ESBL-Producing *Klebsiella pneumoniae* through Synergism of the Photodynamic Activity of Re (I) Compounds with Beta-Lactams. *Pharmaceutics* 13, 1889. doi: 10.3390/pharmaceutics13111889

Guleng, G. E., and Helsing, P. (2012). Photodynamic therapy for basal cell carcinomas in organ-transplant recipients. *Clin. Exp. Dermatol.* 37, 367–369. doi: 10.1111/J.1365-2230.2011.04248.X

Guo, Y., Tian, X., Wang, X., and Xiao, Z. (2018). Adverse effects of immunoglobulin therapy. *Front. Immunol.* 9. doi: 10.3389/FIMMU.2018.01299

Habboush, Y., and Guzman, N. (2025). "Antibiotic resistance," in *StatPearls*. (Treasure Island (FL): StatPearls Publishing).

Hamblin, M. R., and Hasan, T. (2004). Photodynamic therapy: a new antimicrobial approach to infectious disease? *Photochem. Photobiol. Sci.* 3 (5), 436–450. doi: 10.1039/b311900a

Harris, J. J., and Rajasekar, A. (2025). Efficacy of antimicrobial photodynamic therapy (a-PDT) as an adjunct to scaling and root planing on clinical parameters…: A randomized controlled clinical trial. *Odontology*. doi: 10.1007/s10266-025-01106-4

Huemer, M., Mairpady Shambat, S., Brugger, S. D., and Zinkernagel, A. S. (2020). Antibiotic resistance and persistence-Implications for human health and treatment perspectives. *EMBO Rep.* 21. doi: 10.15252/EMBR.202051034

Hung, J. H., Lee, C. N., Hsu, H. W., Ng, I. S., Wu, C. J., Yu, C. K., et al. (2021). Recent advances in photodynamic therapy against fungal keratitis. *Pharmaceutics* 13. doi: 10.3390/PHARMACEUTICS13122011

Leanse, L. G., Marasini, S., dos Anjos, C., and Dai, T. (2023). Antimicrobial resistance: is there a "Light" at the end of the tunnel? *Antibiotics (Basel Switzerland)* 12. doi: 10.3390/ANTIBIOTICS12091437

Lee, I., Moon, J., Lee, H., Koh, S., Kim, G. M., Gauthé, L., et al. (2022). Photodynamic treatment of multidrug-resistant bacterial infection using indium phosphide quantum dots. *Biomaterials Sci.* 10, 7149–7161. doi: 10.1039/D2BM01393B

Lima, S. L., Colombo, A. L., and de Almeida Junior, J. N. (2019). Fungal cell wall: emerging antifungals and drug resistance. *Front. Microbiol.* 10. doi: 10.3389/FMICB.2019.02573

Liu, Y., Qin, R., Zaat, S. A. J., Breukink, E., and Heger, M. (2015). Antibacterial photodynamic therapy: overview of a promising approach to fight antibiotic-resistant bacterial infections. *J. Clin. Trans. Res.* 1, 140. doi: 10.18053/jctres.201503.002

MaChado-de-Sena, R. M., Corrêa, L., Kato, I. T., Prates, R. A., Senna, A. M., Santos, C. C., et al. (2014). Photodynamic therapy has antifungal effect and reduces inflammatory signals in Candida albicans-induced murine vaginitis. *Photodiagnosis Photodyn. Ther.* 11, 275–282. doi: 10.1016/j.pdpdt.2014.03.013

Maisch, T. (2007). Anti-microbial photodynamic therapy: useful in the future? *Lasers Med. Sci.* 22, 83–91. doi: 10.1007/S10103-006-0409-7

Majumder, M. A. A., Rahman, S., Cohall, D., Bharatha, A., Singh, K., Haque, M., et al. (2020). Antimicrobial stewardship: fighting antimicrobial resistance and protecting global public health. *Infection Drug Resistance* 13, 4713–4738. doi: 10.2147/IDR.S290835

Malech, H. L., Deleo, F. R., and Quinn, M. T. (2014). The role of neutrophils in the immune system: an overview. *Methods Mol. Biol. (Clifton N.J.)* 1124, 3. doi: 10.1007/978-1-62703-845-4_1

Murray, C. J., Ikuta, K. S., Sharara, F., Swetschinski, L., Robles Aguilar, G., Gray, A., et al. (2022). Global burden of bacterial antimicrobial resistance in 2019: a systematic analysis. *Lancet* 399, 629–655. doi: 10.1016/S0140-6736(21)02724-0

Murugaiyan, J., Anand Kumar, P., Rao, G. S., Iskandar, K., Hawser, S., Hays, J. P., et al. (2022). Progress in alternative strategies to combat antimicrobial resistance: focus on antibiotics. *Antibiotics (Basel Switzerland)* 11. doi: 10.3390/ANTIBIOTICS11020200

Nakonieczna, J., Wolnikowska, K., Ogonowska, P., Neubauer, D., Bernat, A., and Kamysz, W. (2018). Rose bengal-mediated photoinactivation of multidrug resistant pseudomonas aeruginosa is enhanced in the presence of antimicrobial peptides. *Front. Microbiol.* 9. doi: 10.3389/FMICB.2018.01949

Pérez-Laguna, V., García-Luque, I., Ballesta, S., Rezusta, A., and Gilaberte, Y. (2021a). Photodynamic therapy combined with antibiotics or antifungals against microorganisms that cause skin and soft tissue infections: A planktonic and biofilm approach to overcome resistances. *Pharmaceuticals* 14, 603. doi: 10.3390/PH14070603

Pérez-Laguna, V, Barrena-López, Y, Gilaberte, Y, and Rezusta, A. (2021b). *In vitro* effect of photodynamic therapy with different lights and combined or uncombined with chlorhexidine on *Candida* spp. *Pharmaceutics* 13(8), 1176. doi: 10.3390/pharmaceutics13081176

Polat, E., and Kang, K. (2021). Natural photosensitizers in antimicrobial photodynamic therapy. *Biomedicines* 9, 584. doi: 10.3390/BIOMEDICINES9060584

Przygoda, M., Bartusik-Aebisher, D., Dynarowicz, K., Cieślar, G., Kawczyk-Krupka, A., and Aebisher, D. (2023). Cellular mechanisms of singlet oxygen in photodynamic therapy. *Int. J. Mol. Sci.* 24. doi: 10.3390/IJMS242316890

Ramos, U. D., Ayub, L. G., Reino, D. M., Grisi, M. F. M., Taba, M. Jr., et al. (2016). Antimicrobial photodynamic therapy as an alternative to systemic antibiotics: results

from a double-blind, randomized, placebo-controlled clinical study on type 2 diabetics. *J. Clin. Periodontol* 43, 147–155. doi: 10.1111/jcpe.12498

Rather, M. A., Gupta, K., and Mandal, M. (2021). Microbial biofilm: formation, architecture, antibiotic resistance, and control strategies. *Braz. J. Microbiol : [Publication Braz. Soc. Microbiology]* 52, 1701–1718. doi: 10.1007/S42770-021-00624-X

Reygaert, W. (2009). Methicillin-resistant staphylococcus aureus (MRSA): molecular aspects of antimicrobial resistance and virulence. *Am. Soc. Clin. Lab. Sci.* 22, 115–119. doi: 10.29074/ASCLS.22.2.115

Reygaert, W. C. (2018). An overview of the antimicrobial resistance mechanisms of bacteria. *AIMS Microbiol.* 4, 482. doi: 10.3934/MICROBIOL.2018.3.482

Rodríguez-Cerdeira, C., Martínez-Herrera, E., Fabbrocini, G., Sanchez-Blanco, B., López-Barcenas, A., El-Samahy, M., et al. (2021a). New applications of photodynamic therapy in the management of candidiasis. *J. Fungi (Basel Switzerland)* 7. doi: 10.3390/JOF7121025

Rubilar-Huenchuman, M., Ortega-Villanueva, C., González, I. A., and Palavecino, C. E. (2024). The effect of photodynamic therapy on enterococcus spp. and its application in dentistry: A scoping review. *Pharmaceutics* 16, 825. doi: 10.3390/PHARMACEUTICS16060825

Salam, M. A., Al-Amin, M. Y., Salam, M. T., Pawar, J. S., Akhter, N., Rabaan, A. A., et al. (2023). Antimicrobial resistance: A growing serious threat for global public health. *Healthcare (Basel Switzerland)* 11. doi: 10.3390/HEALTHCARE11131946

Shi, X., Zhang, C. Y., Gao, J., and Wang, Z. (2019). Recent advances in photodynamic therapy for cancer and infectious diseases. *Wiley Interdiscipl. Rev.: Nanomed. Nanobiotechnol.* 11 (5), e1560. doi: 10.1002/wnan.1560

Sperandio, F., Huang, Y.-Y., and Hamblin, M. (2013). Antimicrobial photodynamic therapy to kill Gram-negative bacteria. *Recent Patents Anti-Infective Drug Discov.* 8, 108–120. doi: 10.2174/1574891X113089990012

Suresh, N., Joseph, B., Sathyan, P., Sweety, V. K., Waltimo, T., and Anil, S. (2024). Photodynamic therapy: An emerging therapeutic modality in dentistry. *Bioorganic Medicinal Chem.* 114. doi: 10.1016/J.BMC.2024.117962

Surur, A. K., de Oliveira, A. B., De Annunzio, S. R., Ferrisse, T. M., and Fontana, C. R. (2024). Bacterial resistance to antimicrobial photodynamic therapy: A critical update. *J. Photochem. Photobiol. B.* 255, 112905. doi: 10.1016/j.jphotobiol.2024.112905

Szeimies, R. M., Dräger, J., Abels, C., and Landthaler, M. (2001). Chapter 1 History of photodynamic therapy in dermatology. *Compr. Ser. Photosciences* 2, 3–15. doi: 10.1016/S1568-461X(01)80105-8

Tanwar, J., Das, S., Fatima, Z., and Hameed, S. (2014). Multidrug resistance: an emerging crisis. *Interdiscip. Perspect. Infect. Dis.* 2014. doi: 10.1155/2014/541340

Tavares, A., Carvalho, C. M. B., Faustino, M. A., Neves, M. G. P. M. S., Tomé, J. P. C., Tomé, A. C., et al. (2010). Antimicrobial photodynamic therapy: study of bacterial recovery viability and potential development of resistance after treatment. *Mar. Drugs* 8, 91. doi: 10.3390/MD8010091

Teng, J., Imani, S., Zhou, A., Zhao, Y., Du, L., Deng, S., et al. (2023). Combatting resistance: Understanding multi-drug resistant pathogens in intensive care units. *Biomedicine Pharmacotherapy = Biomedecine Pharmacotherapie* 167. doi: 10.1016/J.BIOPHA.2023.115564

Uddin, T. M., Chakraborty, A. J., Khusro, A., Zidan, B. R. M., Mitra, S., Emran, T., et al. (2021). Antibiotic resistance in microbes: History, mechanisms, therapeutic strategies and future prospects. *J. Infection Public Health* 14, 1750–1766. doi: 10.1016/J.JIPH.2021.10.020

Wainwright, M., and Crossley, K. B. (2004). Photosensitising agents - Circumventing resistance and breaking down biofilms: A review. *Int. Biodeterioration Biodegradation* 53, 119–126. doi: 10.1016/J.IBIOD.2003.11.006

Warszyńska, M., Repetowski, P., and Dąbrowski, J. M. (2023). Photodynamic therapy combined with immunotherapy: Recent advances and future research directions. *Coordination Chem. Rev.* 495, 215350. doi: 10.1016/J.CCR.2023.215350

World Health Organization. (2023). Antibacterial agents in clinical development: An analysis of the antibacterial clinical development pipeline. Geneva: World Health Organization. https://www.who.int/publications/i/item/9789240079643

Wu, X., and Hu, Y. (2022). Photodynamic therapy for the treatment of fungal infections. *Infection Drug Resistance* 15, 3251–3266. doi: 10.2147/IDR.S369605

Wu, G., Xu, Z., Yu, Y., Zhang, M., Wang, S., Duan, S., et al. (2024). Biomaterials-based phototherapy for bacterial infections. *Front. Pharmacol.* 15. doi: 10.3389/FPHAR.2024.1513850

Youf, R., Müller, M., Balasini, A., Thétiot, F., Müller, M., Hascoët, A., et al. (2021). Antimicrobial photodynamic therapy: latest developments with a focus on combinatory strategies. *Pharmaceutics* 13. doi: 10.3390/PHARMACEUTICS13121995

Zhang, J., Chen, Y., Wang, S., Weng, Y., Liu, Y., Li, D., et al. (2025). The efficacy of 5-aminolevulinic acid photodynamic therapy in inducing cell death in multidrug-resistant trichophyton mentagrophytes: an *in vivo* and *in vitro* study. *Photodiagnosis Photodyn. Ther.* 104599. doi: 10.1016/J.PDPDT.2025.104599

Zhao, W., Wang, L., Zhang, M., Liu, Z., Wu, C., Pan, X., et al. (2024). Photodynamic therapy for cancer: mechanisms, photosensitizers, nanocarriers, and clinical studies. *MedComm* 5, e603. doi: 10.1002/MCO2.603

Frontiers in
Cellular and Infection Microbiology

Investigates how microorganisms interact with their hosts

Explores bacteria, fungi, parasites, viruses, endosymbionts, prions and all microbial pathogens as well as the microbiota and its effect on health and disease in various hosts.

Discover the latest Research Topics

See more →

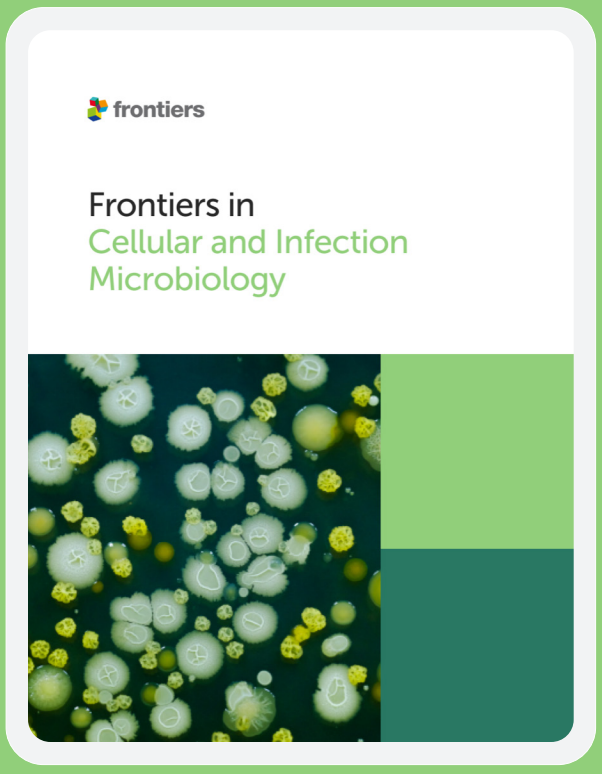

Frontiers

Avenue du Tribunal-Fédéral 34
1005 Lausanne, Switzerland
frontiersin.org

Contact us

+41 (0)21 510 17 00
frontiersin.org/about/contact